DEVELOPMENT OF MODELLING AND TESTING FOR ANALYSIS OF DEGRADATION OF NI-YSZ ANODE IN SOLID OXIDE FUEL CELLS

By

JOHN GEOFFREY MAILLARD

A thesis submitted to the University of Birmingham for the degree of DOCTOR OF PHILOSOPHY

Centre for Fuel Cells and Hydrogen

School of Chemical Engineering

College of Engineering and Physical

University of Birmingham

November 2016

Acknowledgements

A large number of acknowledgments are necessary to show my gratitude towards those who have helped me reach this stage of my research. Firstly to my supervisor Robert Steinberger-Wilcken's, who has helped steer my focus towards a meaningful outcome, as well as significant aid reviewing my thesis structure and language, I am eternally grateful. Your often stoic response to changes in fortune helped balance an otherwise turbulent journey. To Ahmad El-Kharouf, who has given considerable time helping give advice for the best course of action and has helped me clear through my thoughts of many occasions to focus on the more important end result, I thank you. James Andrews has given continued advice in all things modelling throughout my PhD, and has always made time to discuss matters. His helped in developing the code for particle analysis proved greatly appreciated. I would also like to thank the contributions of Dr. Waldek Bujalski who sadly passed away early on in my PhD and was my original supervisor. To all my colleagues who have aided me in various way I wish give my thanks for all help and advice, each piece of help however small is truly appreciated. Bob Sharpe the technician has on more than one occasion given his time and help to allow me to focus on my research whilst he toiled away on equipment I needed. Without his help it is unlikely I would have finished. Dr. Evans Mogire helped resolved an ongoing issue by sparing his time and knowledge with me, and without which I may lost months more of my time. To my colleague and friend Amrit, who persistently encouraged me and resolutely believed in my capabilities, I am incredibly grateful.

To my family, I wish to thank them for each and every day they've supported me, a PhD is a significant endeavour of not just one's mind and energy but equally ones spirit and emotional endurance. They have constantly stood beside me and I wouldn't be here without all their help. To my housemate Dom, being able to escape from work whilst home was easily achieved through his friendship, allowing for each day to be faced that little bit refreshed for the next day. And to Emma, more than once the rewards that awaited me for achieving the goal of submitting a thesis could not overcome the duress and emotional destress that accompanied it. However, being with you and sharing my life with you makes me want to excel and overcome any obstacle, and knowing that achieving this goal would mean more for the both of us meant that I was always motivated, and even at my lowest having you beside me meant I was never alone facing it.

Abstract

The ability to predict the lifetime performance of an SOFC can give guidelines for where improvements can be made in terms of production, operating parameters and cell design.

Microstructural analysis of Ni-YSZ anode samples under varying steam and temperature regimes was investigated to determine trends in the anode Ni particle growth. Increasing the steam content produced larger mean Ni radii for a given temperature. Higher operating temperatures (900°C) were shown to have a significant accelerating effect on the particle size change.

Further analysis of the microstructural data highlighted profiles for Ni-pore contact angle θ values, as well as Triple Phase Boundary points and overlap length which both showed a decrease over time, highlighting differences in the rate of performance loss in the anode.

Using models derived for the degradation mechanisms combined with a particle packing model, Matlab® coding was developed to predict the Ni particle growth rate and the relative change in conductivity and TPB length per unit volume. Ni particle growth rate predictions were compared to experimental results and showed good correlation. The data can be used to help design accelerated testing procedures for SOFC anodes to determine the long term performance of a given anode composition.

Table of Contents

CHAPTER 1 Introduction 1

1.1 The Solid Oxide Fuel Cell 1

1.2 SOFC Degradation 7

1.3 Thesis Objective 13

CHAPTER 2 State of the Art 17

2.1 Materials Available for use in SOFC Operation 17

2.1.1 Electrolyte Materials 17

2.1.2 Anode Materials 25

2.1.3 Cathode Materials 31

2.1.4 SOFC Interconnect Materials 39

2.2 Initial Ni-YSZ Microstructure and Material Selection 47

2.3 Transformation in Microstructure 52

2.3.1 Nickel Oxide Reduction 60

2.3.2 Nickel Volatisation 73

2.4 Measurement and Analysis Techniques 77

2.4.1 Imaging Analysis (SEM, FIB-SEM, Tomography) 77

2.4.2 Parameter Extraction for Model Development 82

2.4.3 Modelling 87

CHAPTER 3 Experimental Set-up and Methodology 92

3.1 Experimental Set-up 93

3.2 Sample Preparation and Polishing 99

3.3 Image Processing and Data Development 116

CHAPTER 4 Microstructural Analysis of Ni-YSZ SOFC Anode Samples with SEM and EDX Imaging 123

4.1 Nickel Area and Porosity Analysis and Comparison 125

4.2 Nickel and Pore Radius Comparison and Analysis 130

4.3 Conclusions 143

CHAPTER 5 Particle Radius Modelling for TPB and Conductivity Predictions 146

5.1 Vassen Model 147

5.2 Nakajo et al Ni radius predicting model 151

5.2.1 Nickel particle radius predicting equation 151

5.2.2 Comparisons of Model with Literature and Experimental Data 152

5.3 Gao Ni Particle Radius Modelling 160
5.3.1 Nickel Radius Predicting Equation 161
5.3.2 Comparisons of Models with Literature and Experimental Data 166
5.3.3 Conclusions on Radius Modelling Equations 169
5.4 Chen et al Percolation Model for TPB Length and Conductivity Estimation 170
5.4.1 Non-dimensional Comparison of Model 182
5.4.2 Chen Model Combined with Gao and Nakajo model 186
5.5 Particle Radius Estimation and Parameter Evaluation Conclusion 190
CHAPTER 6 Image Analysis and the Determination of Triple Phase Boundary (TPB) points 191
6.1 Microstructural 191
6.1.1 Percolation 192
6.1.2 Image Analysis 193
6.1.3 Laplacian Adjacency Matrix 194
6.1.4 Identifying Nickel-Pore Contacts 195
6.1.5 Theta Value and Lengths 196
6.2 Comparisons of SEM and ImageJ Images with Image analysis Output 199
6.3 TPB Identification 202
6.4 Modelling Results and Discussions 202
6.5 Conclusions 209
CHAPTER 7 Conclusions and Further Work 211
7.1 Discussion of the Value of the Work Presented Here 211
7.2 Further Work 216
Appendix 235

List of Figures

Figure 1-1. Cross-sectional diagram of SOFC layers. The dark grey layer represents the interconnect, the green the anode material and in this case the support layer, the white is the electrolyte and the light grey is the cathode. 3
Figure 1-2 Example diagram of SOFC operating principal [1]. Oxygen ions travel from the cathode through the electrolyte and combine with the hydrogen on the anode side to form steam. 4
Figure 1-3 Example of SOFC APU unit from Delphi. [2] The unit provides electricity and heat inside of long-haul trucks. 6
Figure 1-4 Long term testing of an SOFC stack with an LNG/H_2/H_2O anode fuel mixture. 18 individual cells made up the stack (U1-18), the current draw j was kept at 0.5 Acm^{-2} unless interrupted, the power P was >2.5kW at all times and the two thermocouples T9/10 measured 700°C [11]. 11
Figure 1-5 Accelerated testing example plot showing change in operating voltage over time, highlighting how normal testing time periods can be compared to accelerated tests. 14
Figure 2-2 An Arrhenius plot of some of the most common oxide ion conductors, showing a log plot of the conductivity multiplied by degrees Kelvin over the inverse of the temperature [22]. 18
Figure 2-3 An example of oxygen diffusion through a cubic fluorite YSZ structure via the vacancy diffusion mechanism. The vacancy would shift from 1st position to 2nd [27]. 20
Figure 2-4 Depiction of a cubic perovskite crystal structure. An example of potential material usage would be A) Sr, B) as Ti and X) as O. Image adjust from source [50]. 23
Figure 2-5 Crystal structures of perovskite $ABO_{3-\delta}$ samples showing a) an example with an oxygen vacancy and b) showing the hopping of an oxide ion along vacancies in the direction of oxygen migration. Image adapted from reference [121]. 35
Figure 2-6 A 500x500 μm Image of a ToF-SIMS analysis of an ZrO-Ni interface and the surrounding Si causing a reduction in contact. Brighter regions denote areas of strong signal for the given element [9]. 51
Figure 2-7 Environmental Scanning Electron Microscopy (ESEM) image of sample with section A the YSZ region, B the necklace region of adhering Ni particles and C the Ni electrode [211]. 55
Figure 2-8 Suggested model for NiO reduction by Jeangros et al [228]. The blue represent NiO progressively being reduced to the red Ni metal, highlighting how varying reduction paths can affect the access to the NiO material. 62
Figure 2-9 Visual representation of varying effects of temperature on reduction procedure [230]. The grey region is Ni metal and the green NiO. Option a) is reduction at a low temperature, where gradual reduction lead to encapsulated Ni metal disconnected from each other, whilst in b) higher temperature reduction allowed for percolated networks to form. 64
Figure 2-10 Porosity type formations [234]. The ideal formation is a connected series of channels; the least ideal is the isolated which reduces material percolation whilst not offering any path for gaseous transport. 66
Figure 2-11 Ni radii from various experimental testing of SOFC anodes presented for comparison of Ni particle radius growth rates for given temperature, fuel and material composition over time. See Table 2-7 for references. 70
Figure 2-12 Normalised experimental testing of SOFC anodes presented for comparison of Ni particle radius growth rates for given temperature, fuel and material composition over time. See Table 2-7 for references 71

Figure 2-13 Percentage loss of nickel mass over time from SOFC-LIFE data [243] for its given analysis route (XRF or SEM) and respective operating conditions. 75
Figure 2-14 Comparison of reported Ni volatility from SOFC-LIFE [243] and Holzer's [216] on Ni volume loss for a given anode composition and operating conditions. 76
Figure 2-15 Visual description of particle size measurement techniques, highlighting how the Discrete PSD_D, Intercept method and Continuous PSD_C establish the area of pores/particles [216]. 79
Figure 2-16 Values for Active TPB lengths (in μm μm^{-3}) based on Ni volume fraction and NiO Wt%, highlighting their effect on total percolation in the microstructure [249]. 83
Figure 2-17 Chart comparing the rate of change of normalised ASR against the change of TPB density [221]. The outlying value is due to a poor choice of sintering inhibiter compared to the other values used in this paper. 84
Figure 2-18 Ni wettability on YSZ surface shown through two coarsening particles [293]. As the particles are exposed to high temperatures they deform and eventually combine on the wetting surface of the YSZ, here represented by the light grey surface. 91
Figure 3-1 Quartz tube and furnace for anode sample testing. Fuel gas enters from the left hand side, passes over the samples which are resting across a alumina plate. 92
Figure 3-2 Schematic drawing of rig with MFCs, CEM and Cori-flow delivering fuel to the quartz tube rig. Nitrogen purges the system on start-up, after which hydrogen (and possibly steam) pass through the controlled evaporating mixer and into the quartz tube sitting inside of a furnace. 93
Figure 3-3 Process pathway for samples showing the procedure of preparing for testing and analysis. This includes initial segmentation, testing and removal and mounting for imaging. 95
Figure 3-4 Example of samples having been exposed for 250h at 800°C to 97/3 H_2/H_2O prior to having 2 samples taken for analysis and subsequently being returned to the furnace for the other samples continued exposure. 97
Figure 3-5 Thermal distribution in the quartz tube furnace with pure hydrogen flowing at 100 ml/min at 800ºC. Inlet and outlets are room temperature, whilst the section of the furnace where samples are located is at the intended operating condition. 99
Figure 3-6 Comparisons of varying degrees of dense layer formed by the same polishing procedure of similar/same batch, cutting procedure, testing environment and mounting. Samples were tested at 800°C in 100% H_2 for a) 250h, b) 500h, c) 750h and d) 1000h respectively. Images taken via optical microscopy. 102
Figure 3-7 Progressive SEM inspection of area with dense vs. non-dense layer of a sample reduced at 700°C for 24h in 100% H_2 a) x50 mag BSE, b) x400 mag BSE c) x1200 mag BSE and d) x2400 mage BSE/SE mix. 103
Figure 3-8 Non-dense layer EDX analysis of sample reduced at 700°C in 100% H_2 for 24h a) Ni-Zr EDX overlap, b) SEM EDX, c) Ni, d) Zr, e) Al and f) O. 105
Figure 3-9 Dense layer EDX analysis of sample reduced at 700°C in 100% H_2 for 24h, a) Ni-Zr joint image, b) EDX background image, c) carbon EDX, d) Ni , e) O and f) Zr. 106
Figure 3-10 EDX image of area of broken sample showing discrete Ni/YSZ phases with O predominately visible overlapping YSZ phase. Sample was reduced at 800°C for 24h in 100% H_2 A) Ni-Zr -O EDX overlap, b) plain EDX, c) O, d) Zr, e) Ni. 108
Figure 3-11 Comparison of Surface of freshly sawn samples in BSE and SE mode. Sample was reduced at 800°C for 24h in 100% H_2. Images clearly show the shearing affect of the diamond saw on the surface of the sample. 109
Figure 3-12 Investigation of non-sheared section of freshly sawn sample. Sample was reduced at 800°C for 24h in 100% H_2. As the surface resembles that of non-sheared/freshly broken samples it eliminated the diamond saw as an issue. 110

Figure 3-13 x5000 mag comparison of a sample operated at 900C in 20-80% H_2/H_2O mixture for 250h versus a virgin green sample imaged as polished. Notable differences in particle size and porosity are visible. 112
Figure 3-14 x5000 mag comparison of a sample operated at 900C in 20-80% H_2/H_2O mixture for 250h versus a virgin green sample imaged as polished. The section shows comparison between Ni-Zr and Ni-Zr-O overlap EDX images for the reduced sample in a) and c) and for the virgin sample in b) and d). 113
Figure 3-15 Route for sample data utilisation. Sample images are generated and then processed through ImageJ. These are subsequently either analysed via Matlab to determine TPB lengths and other values or the distributions are calculated and input into predictive models. 117
Figure 3-16 EDX sample examples for those used in imaging stage. Sample tested at 900°C for 250h in a 20-80% H_2/H_2O mixture. a) is for Ni, b) Zr, c) a BSE image and d) the resultant overlapping image. 118
Figure 3-17 Example of ImageJ black and white thresholding and subsequent watershedding of same sample as Figure 3-16. Images show Ni for a) & b) and pores for c) & d). The sample was tested at 900°C for 250h in a 20-80% H_2/H_2O mixture. 120
Figure 3-18 Histograms of Ni and Pore for a given sample. The curve shows the mean and standard deviation for the given plot. The sample was tested at 900°C for 250h in a 20-80% H_2/H_2O mixture. 121
Figure 4-1 Nickel area percent for the selected temperature and fuel regimes. Each time frame shows the average of two samples. Each sample was evaluated through 12 images covering random sections of the sample. 126
Figure 4-2 Pore area percent for sample temperature and fuel regimes. Each time frame shows the average of two samples. Each sample was evaluated through 12 images covering random sections of the sample. 126
Figure 4-3 Normalised nickel area percentage for sample temperature and fuel regimes. Samples normalised relative to Zr mean value of 50% and porosity and nickel are adjusted proportionally. 128
Figure 4-4 Suggested linear relationship between porosity and nickel content. Values have a linear line of best fit placed to highlight their trends. The as collected relationship between Ni and porosity is close to the expected normalised relationship. 129
Figure 4-5 Mean Ni particle radius (μm) for samples sets. Each time frame shows the average of two samples. Each sample was evaluated through 12 images covering random sections of the sample. 131
Figure 4-6 Mean Pore radius (μm) for samples sets. Each time frame shows the average of two samples. Each sample was evaluated through 12 images covering random sections of the sample. 131
Figure 4-7 Correlation between Ni content and mean Ni particle radius. A linear line of best fit has been applied to the sample values for the mean Ni radius relative to its Ni content percentage. 133
Figure 4-8 Correlation between porosity and mean pore radius. A linear line of best fit has been applied to the sample values for the mean pore radius relative to its porosity. 133
Figure 4-9 Ni particle radius normalised relative to their Ni content. Values are adjusted according to the relative amount of Ni greater or less than the average of 34 percent. 134
Figure 4-10 Graphic highlighting the general trend of effect of steam and temperature on Ni particle radius that have been normalised according to their Ni content. 135

Figure 4-11 Number of Ni particles over Ni area and pores and porosity. The relative spread of samples indicates a lack of correlation between the two factors for both Ni particles and pores. 136
Figure 4-12 Number of Ni particle for given data set. Each time frame shows the average of two samples. Each sample was evaluated through 12 images covering random sections of the sample. 137
Figure 4-13 Number pores for given data set. Each time frame shows the average of two samples. Each sample was evaluated through 12 images covering random sections of the sample. 138
Figure 4-14 Comparison between mean nickel radius values (μm) and particle number and mean pore radius values (μm) and pore number. Linear lines of best fit have been applied to both sample sets showing a strong correlation for Ni and a weak/non-existent one for porosity. 139
Figure 4-15 Example histograms of Ni particle radius, showing two samples and their relative size distributions for their 250, 500, 750 and 1000 hours samples. 140
Figure 4-16 Ni particles normalised to 0.38μm radii over temperature setting. The value of 0.38 μm was determined from initially reduced samples average Ni particle radius. Note that the figure does not highlight which samples are largest and which are smallest of 250h, 500h, 750h and 1000h. 143
Figure 5-1 Geometric model of agglomeration process for two Ni particles. The flux $\boldsymbol{jv}$ of vacancies travels from the larger B particle to the smaller A particle, simultaneously increase the size B. 147
Figure 5-2 Nakajo et al's model for Ni particle increase compared to available literature, as presented in source [277]. 0.04/0.04 refers to a 4% H_2, 4% H_2O 92% Ar mixture..... 153
Figure 5-3 Comparison of Nakajo et al's model for normalised Ni radius predictions. Values are normalised to their initial particle radius 155
Figure 5-4 Experimental data versus Nakajo model equations. Samples normalised to 0.38 μm Ni particle radius. Note the relative inaccuracy in predicting Ningbo samples tested under varying conditions. 157
Figure 5-5 Experimental data versus Nakajo model adjusted for Ningbo cells. Samples normalised to 0.38 μm Ni particle radius. Note the superior fit to the sample data points compared to the unadjusted model equation. 159
Figure 5-6 Gao model versus Faes and Tanasini data [17, 19]. The equation uses fitting parameters to produce a highly comparable prediction of the particle growth 167
Figure 5-7 Gao model versus Vassen data showing Ni particle radius growth over time [237]. 167
Figure 5-8 Gao model versus experimental data. Similar to other literature the equation does a good job of estimating the growth of the particles relative to their temperature and starting particle size. 168
Figure 5-9 Anode microstructure type cluster example. A type represent fully percolated networks connecting the YSZ material with the current collecting medium. B and C types represent either un-connected networks or ones without contact to the YSZ electrolyte material. 172
Figure 5-10 Percolation thresholds based on particles size ratio r_{el}/r_{io} and electrolyte volume fractions φ_{el} [303]. The upper bound represents compositions where high ionic percolation existing whilst the lower bound is for electronic percolation. The mid-region represents the optimal volume ratio to provide high percolation for both materials. 176
Figure 5-11 Example of k and l particles overlapping and visual of neck radius r_c.. and resultant contact angles θ produced. 179

Figure 5-12 Nondimensional $\boldsymbol{\lambda TPB, effV}$ for varying set electrolyte particle sizes. The Ni radius has been set to 1.2 and highlights how at around the same size the performance is best but as the YSZ size gets larger or smaller you see a reuction in effective TPB length per unit volume. 183
Figure 5-13 Nondimensional $\boldsymbol{\lambda TPB, effV}$ comparison of varying volume loadings. Samples with similar to slightly more YSZ show best performance with those samples heavily favouring one material showing reduced values. Not the drop of values to 0 in the extreme settings is a result of the percolation model as the Ni radius changes over time. 184
Figure 5-14 Nondimensional $\boldsymbol{\lambda TPB, effV}$ comparison of different $r_{Ni\infty}$ values. This figure shows how a smaller value of $r_{Ni\infty}$ compared to the YSZ mean particle size results in the best possible $\boldsymbol{\lambda TPB, effV}$. 185
Figure 5-15 Variation of resistivity with varying volume loading. As expected a higher quantity of Ni reduces the overall resistivity in the sample, which particularly large relative increases above 50% loading. 186
Figure 5-16 Relative effective TPB change based on Gao/Nakajo radius predictions and Chen percolation model. The drop seen in 900°C 20-80% H_2/H_2O and 900°C 97-3% H_2/H_2O is present in all Nakajo models and relates to the change in mean Ni particle radius to a value larger than the mean YSZ particle radius. 187
Figure 5-17 Relative effective conductivity (S/m) based on combined Gao/Nakajo radius predictions and Chen percolation model using equations Equation 5-37 & Equation 5-38... 189
Figure 6-1 Diagram of Euclidean distance between two particles to determine if in contact. The respective x,y coordinates are used to determine if the distance d between the samples is less than or equal to the combined radius values. 194
Figure 6-2 For determining the nature of contacting circles a Laplacian adjacency matrix was applied with a) example image of circular particles and b) the respective Laplacian adjacency matrix representing contacts. 195
Figure 6-3 Diagram describing the nature of contact angle and overlap length. The distance between intersecting points P and O represent the overlap length for the pore and Nickel contact. 196
Figure 6-4 Diagram showing the radius of each circle to the intersecting point P and the tangent lines at those points. The resultant angles above and below are shown by φ and Ξ respectively. 197
Figure 6-5 Depiction of triangle created by $Ni\theta_{1/2}$ and $Pore\theta_{1/2}$ and that created by the tangents to the radius at the point of intersection P. 198
Figure 6-6 Comparison of original cropped SEM image and it with overlapping circles. Channels can be seen to form a collection of connected smaller pores often surrounding the nickel particles. 200
Figure 6-7 Comparison of colour thresholding, black and white creation of Ni particles (and pores with YSZ) and watershed image with circle-generation overlap model. 201
Figure 6-8 Mean Ni θ values for samples sets over time. Each time frame shows the average of two samples. Each sample was evaluated through 12 images covering random sections of the sample. 203
Figure 6-9 Mean Ni θ values adjusted for variation in Ni area percent for samples sets over time. Each time frame shows the average of two samples. Each sample was evaluated through 12 images covering random sections of the sample. 204
Figure 6-10 TPB points divided by respective Ni area %/porosity ratio over time for a given temperature (°C) and fuel composition (H_2/H_2O). The curve is a power law fitting of the data to show general trends. 206

Figure 6-11 TPB overlap length adjusted according to Ni area percent vs. porosity ratio for a given temperature (°C) and fuel composition (H_2/H_2O). The curve is a power law fitting of the data to show general trends. 208
Figure 7-1 Example of TPB effective length modal predictions for use in accelerated testing. The significantly shorter time taken for the higher temperature and steam content testing to reach the plateau can be used to potentially predict longer term performance of a variety of samples. 215

List of Tables

Table 2-1 DC conductivities of materials developed as anodes for SOFCs at 800°C, as presented by Shaikh et al [12]. 27
Table 2-2 Composition and Thermal expansion coefficient (CTE) for certain cathode materials [113]. Values similar to YSZ's CTE of 10.5 x10^{-6} [114] are desirable to prevent mechanical stress during thermal cycling. 33
Table 2-3 Description of key properties of potential metallic interconnect materials, including Cr based alloys (CrBA), ferritic stainless steels (FSS), austenitic stainless steels (ASS) and Fe and Ni based super alloys (FeBSA, NiBSA) [156]. 41
Table 2-4 Comparison of some of the available coatings techniques and their properties, including electronic conductivity, Cr inhibition, oxidation reduction rate and deposition complexity [120]. 44
Table 2-5 SOFC compositional table of NiO/YSZ & Ni/YSZ weights and volumes including porosity degradation testing data from literature [186]. 49
Table 2-6 NiO and Ni molar mass and volume comparison table [222]. 60
Table 2-7 SOFC testing data from literature covering fuel, operating temperature, duration, material composition, current and nickel growth. 67
Table 3-1 Chart for intended experimental runs of NiO samples for a given temperature and H_2/H_2O fuel composition. More-extreme ends of the spectrum were selected for testing to see results with limited testing runs possible. 97
Table 3-2 Comparison of different material polishing guidelines from Buehler polishing manual. The abrasive size relates to the coarseness of the polishing pads, load the pressure applied, as well as rotational speed and time. 100
Table 3-3 Polishing procedure for variable comparison. Tests were done relative to the polish pad used and compared variables of pressure, rotational speeds and the orientation (was alignment of the sample perpendicular or parallel with the pads rotation). 115
Table 4-1 Relative change in Ni content for normalised sample sets with time. Fluctuating samples showed both increases and decreases in their analysis. 130
Table 4-2 Numerical changes in Ni particle radius from 250h to 1000h. the 800°C value shoes a decrease between 250h and 1000h. 141
Table 5-1 Data values for Nakajo calculations. 152
Table 5-2 Data Values used in Gao modelling equations 166
Table 5-3 Fitting parameters used for various experiments. 169
Table 5-4 Data values used in Chen model. 181
Table 6-1 Mean θ values and relative standard deviation. 205
Table 6-2 R^2 values relative to sample set for TPB points fitting curves. 207
Table 6-3 R^2 values relative to sample set for TPB overlap length fitting curves. 209

Nomenclature

Symbol	Description
$a_{ed,el}$	Cross-sectional area per contact between and electrode and electrolyte particle (m^2)
C	Vacancy concentration
C_r	Solute concentration at a plane interface in a matrix in equilibrium with particle of infinite radius
C_f	Vacancy concentration for a flat surface
D_s	Atomic surface diffusion coefficient ($m^2\ s^{-1}$)
$D_{v,s}$	Vacancy surface diffusion coefficient ($m^2\ s^{-1}$)
$Ea_{D_{an}}$	Activation energy of anode degradation ($J\ mol^{-1}$)
$g(t)$	Growth restricting value for maximum nickel size
$\bar{J}$	Diffusive flux or flow ($mol\ m^{-2}\ s^{-1}$)
k_B	Boltzmann constant ($J\ K^{-1}$)
$k_{0D_{an}}$	Rate constant for Ni particle grain growth
I	Contact perimeter between overlapping particles (m)
M_{mol}	Molar mass ($g\ mol^{-1}$)
n	Sintering mechanism exponent
$n_{Ni_k}^V$	Number of specific particle size per unit volume
P_{ed}	Percolation probability of electrode particles
P_{el}	Percolation probability of electrolyte particles
r	Radius of particle (m)
r_c	Neck radius of two overlapping particles (m)

$r_{Ni(0)}$	Initial mean Ni particle size (m)
$r_{Ni\infty}$	Max mean Ni particle size (m)
r_{YSZ}	Radius of YSZ particle (m)
R	Universal gas constant (8.314 J mol-1 K^{-1})
ΔS	Surface diffusion area change (for vacancy flow)
S_{edk}^{ter}	Effective contact surface area between el-particles per particle layer (m^2)
S	Geometric cross-sectional area of composite electrode (m^2)
S_{ed_k}	Surface area fraction of all electrode particles (of size k) (m^2)
t	Time (s)
T_{ref}	Reference temperature (K)
T_s	Temperature set point for cell (K)
V	Volume of material (m^3)
V_m	Molar Volume (cm^3 mol^{-1})
$\bar{x}$	Diffusion distance (m)
x_{H_2}	Hydrogen partial pressure
x_{H_2O}	Steam partial pressure
$\bar{Z}$	Average coordination number for all solid particles
$Z_{ed,ed}$	Average coordination number for all electrode particles
$Z_{el,el}$	Average coordination number for all electrolyte particles

Greek letters	
β	Fitting parameter (relationship between largest and smallest Ni

	radii relative to mean radius
ζ_{ed_k}	Fraction of the number of particles of a specific electrode type k out of all particles
δ	Thickness of boundary between particles (m)
δ_s	Thickness of inter-atomic spacing (2.5A)
γ	Surface energy (J m^{-2})
λ_{TPB}^{V}	TPB length per unit volume (m)
$\lambda_{TPB,eff}^{V}$	Effective TPB length per unit volume (m)
$\tilde{\lambda}_{TPB,eff}^{V}$	Non-dimensional effective TPB length per unit volume
θ	Contact angle between two particles
μ	Bruggeman factor
$\tilde{\sigma}_{ed}^{ter,eff}$	Dimensionless effective inter-particle conductivity
$\tilde{\sigma}_{ed}^{tra,eff}$	Dimensionless effective intra-particle conductivity
$\sigma_{ed}^{ter,eff}$	Effective inter-particle conductivity (S m^{-1})
$\sigma_{ed}^{ter,o}$	Intrinsic conductivity of the particle interface (S m^{-1})
$\sigma_{ed}^{tra,eff}$	Effective intra-particle conductivity (S m^{-1})
$\sigma_{ed}^{tra,o}$	Intrinsic material conductivity (S m^{-1})
σ_m^0	Total bulk material conductivity (S m^{-1})
σ_m^{eff}	Total effective conductivity (S m^{-1})
Φ_g	Porosity
ψ_{ed}	Volume fraction of Ni particles
ψ_{el}	Volume fraction of YSZ particles

ψ_{ed}^{o}	Volume fraction of electrode particle of size k
ψ_{ed}^{c}	Percolation threshold for Ni electrode particles
ψ_{el}^{c}	Percolation threshold for YSZ electrolyte particles
$\psi_{ed_k}^{o}$	Relative volume fraction of particle k electrode to all electrode particles
Ω	Mean atomic (or molar) volume of the particle, or volume element (m^3)

CHAPTER 1 Introduction

Fuel cell technology dates back to as early as 1838, when William Grove described his version of a phosphoric acid fuel cell (PAFC), and in the same year Christian Friedrich Schönbein wrote about his early fuel cell design. Subsequent work over the next hundred years by researchers such as Ludwig Mond, Friedrich Wilhelm Ostwald and Walther Nernst helped the progressive understanding of fuel cells. Francis Bacon is attributed with significant advancements to fuel cells, having built a functional 5kw unit in 1939, and eventually helped develop an alkaline fuel cell (AFC) (also referred to as a Bacon fuel cell). This technology was further developed and eventually it was incorporated into the space craft for the Apollo missions. Nernst's work in the fields of electrochemistry and thermodynamics led to an experiment where he noted that whilst zirconia is an insulator at room temperature it is an ionic conductor when red hot. This discovery took until the 1930s to be implemented in laboratory practice by Baur and Preis. Subsequent developments have been made in the field of SOFC research, with Siemens Westinghouse work on Tubular SOFCs being a major contributor in the field for a number of years before they pulled out of the area, leading the way for SOFC research to become increasingly focused in research institutes and many smaller companies internationally.

1.1 The Solid Oxide Fuel Cell

Solid Oxide Fuel Cells (SOFCs) are a potential avenue for a more sustainable fuel utilisation than via existing technologies due to an improved efficiency in energy

generation. By converting the hydrogen or hydrocarbon fuels electrochemically, rather than by conventional combustion, they allow for a more efficient use of the potential energy of the fuels they use whilst also producing reduced or zero harmful emissions compared to conventional fuels. SOFCs operate in temperature ranges anywhere from 600°C to 950°C, with the 600-650°C range often being referred to as Intermediate Temperature (IT)-SOFCs. This temperature range is needed to allow for sufficient ionic conductivity through the ceramic electrolyte material. Their components are predominately made of ceramic or mixed ceramic/metallic materials, capable of withstanding the high operating temperatures required. Unlike many other types of fuel cells, SOFCs are capable of directly utilising hydrocarbon fuels, efficiently generating electricity and producing only steam and CO_2 as emissions. The high temperature removes the need for expensive platinum group metal catalyst commonly used in Polymer Electrolyte Fuel Cells (PEFCs), allowing for less expensive catalysts such as Ni. Overall, this gives SOFCs certain flexibilities and cost reducing features making them ideal for potential heating and electrical applications.

Figure 1-2 shows a basic diagram of the operating mechanism of an SOFC. Hydrogen fuel gas travels through the anode and reacts with oxygen ions travelling through the electrolyte to form water (which is present as steam). The ions created on the cathode side allow for the transport of electrons through the system and thus generate electricity.

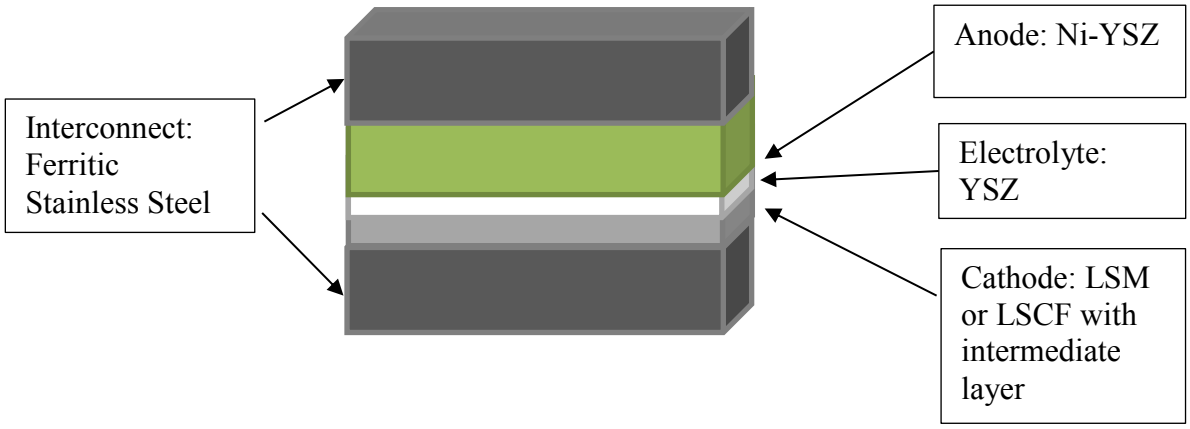

Figure 1-1. Cross-sectional diagram of SOFC layers. The dark grey layer represents the interconnect, the green the anode material and in this case the support layer, the white is the electrolyte and the light grey is the cathode.

Variations of the processes in the anode take place depending on the composition of fuel gas used. The Triple Phase Boundary points (TPB points) are the locations where the ions, electrons and hydrogen protons meet to be able to form the steam and complete the circuit for electricity generation.

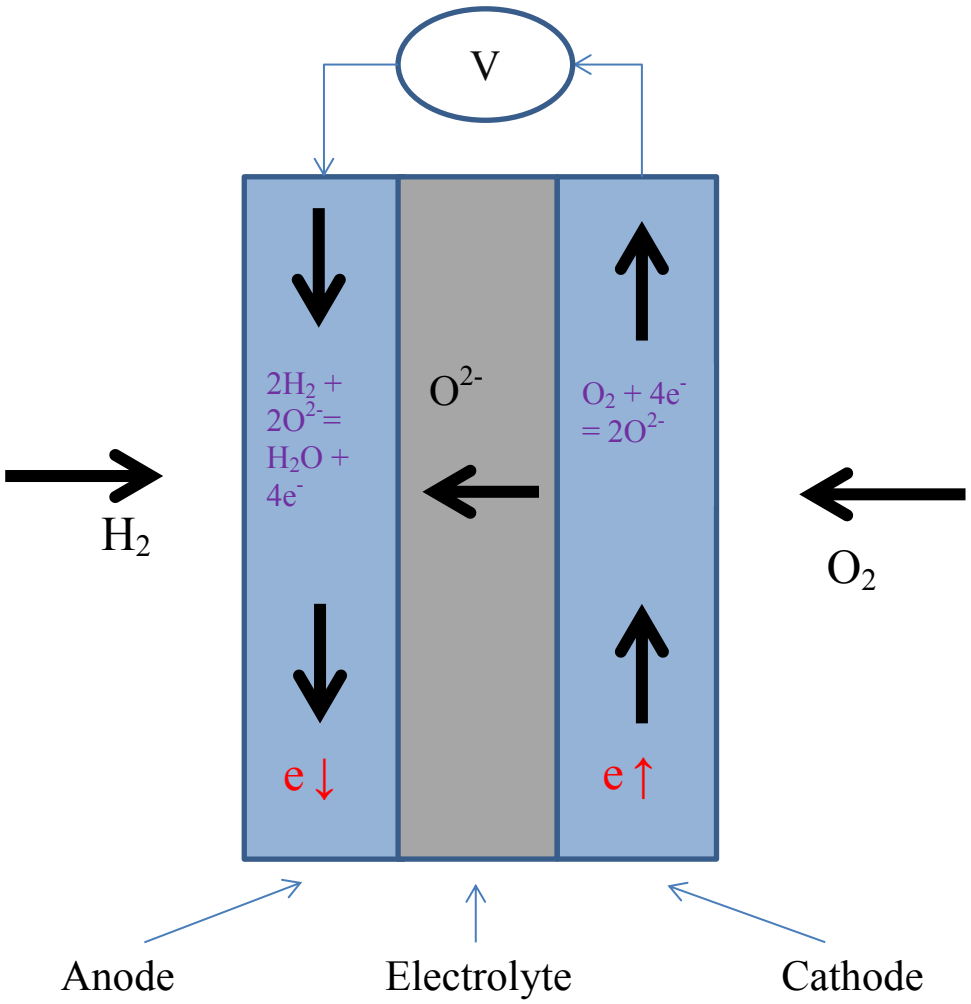

Figure 1-2 Example diagram of SOFC operating principal [1]. Oxygen ions travel from the cathode through the electrolyte and combine with the hydrogen on the anode side to form steam.

The difference in the way an SOFC operates can offer significant advantages compared to current incumbent technologies. Areas for application include stationary and mobile power generation. For stationary applications the replacement of conventional power generation units requires the fuel cells to provide reliable, efficient electricity, with the additional benefits of being cleaner, quieter, capable of

heat generation and more fuel flexible. For mobile applications, being able to quickly deliver the required electricity and (potentially) heat to the customer are key, with its relatively cleaner emissions and silent operation far more desirable in enclosed environments or in locations where air cleanliness is paramount. For example, currently in the market of Auxiliary Power Units (APUs) for trucks in the U.S, diesel powered engines provide the electricity and heating for the passengers during long haul driving, which can be 10's of hours of electricity generation between stops. Anything from powering fridges and TVs to heating or cooling the vehicles during extreme weather need power. For many drivers the APUs allow for heat or electricity when stationary, as engine idling is illegal in a number of states across the US. Not only does the SOFC APU offer a more efficient solution, especially if used for heat generation, but due to its lack of moving parts the relative silence could be beneficial for those drivers who suffer from the noise associated with, as well as cleaner generation compared to, a diesel unit. These SOFC APUs however have to be capable of long hours of operation (10,000-20,000 hours, depending on application) as well as a frequent start-up/shut-down cycles during their lifetime.

Figure 1-3 Example of SOFC APU unit from Delphi. [2] The unit provides electricity and heat inside of long-haul trucks.

To achieve these requirements improvements in the understanding of SOFCs and their ancillary equipment (such as blowers, fuel delivery systems, pre-reformers) is required to meet the desired targets. The U.S Department for Energy DoE and the Solid State Energy Conversion Alliance (SECA) have outlined desired outcomes for the performance of SOFCs, and include lifetime performance degradation of less than 0.2%/1000h over 40,000 hours, and total efficiencies over 60% [3]. In particular SOFCs components lose performance over time as the high temperature, fuel composition, contaminates and the cycling undergone all contribute to progressive degradation. Currently one of the significant limitations to commercial implementation of SOFCs is the rate of loss of performance in SOFCs systems, unlike PEFCs which currently focus more on cost reduction (via reduced materials cost) for commercial implementation. The benefits of the high operating temperatures, which allow for cheaper materials and more fuel flexibility compared to other fuel cells, also lead to faster degradation rates. Mitigating the mechanisms which lead to less loss of

performance allowing for longer operation and thus a more cost effective product. However, understanding the vast array of degradation phenomena which occur in the cells is both complicated to understand and simple effects are difficult to extract.

SOFCs as a novel and emerging field have seen significant research undertaken to both improve the performance and understanding of the fuel cells as well as looking into the ways in which this technology can help augment the existing power generation market. Research can focus on areas covering cost reduction, reliability, improved performance, improved manufacturing techniques, various analytical techniques, contaminant resistance and alternative applications [4-7] Looking to improve the lifetime of cells and stacks through an increased understanding of degradation and overall robustness often incorporates many of these fields.

1.2 SOFC Degradation

Fuel cells are subjected to a number of degradation mechanisms influenced by operating conditions such as temperature and fuel composition, contaminates in either the fuel or fabrication materials as well mechanical/structural issues. Degradation is most commonly reported as a loss of electrochemical performance. A major contribution is microstructural change. SOFCs at stack level can be very susceptible to mechanical issues due to the rigidity of ceramics, which has the logical effect in limiting most SOFCs to be used in more stationary applications meaning the most common forms of degradation are based on internal influences (rather than external ones like vibrations from shaking). Each component of an SOFC will be subjected to degradation mechanisms, and each field represents one of interest for

maximising the long term efficiency of the unit. For this study the SOFC anode, which of the components has perhaps the most regularly research material composition i.e. (Nickel-Yittria Stabilised Zirconia (Ni-YSZ cermet)), was chosen for further research due to available data in literature.

SOFC anode degradation can be attributed to 3 overall mechanisms which can lead to its loss in performance and eventually catastrophic failure. These mechanisms include anode deactivation/passivation, thermomechanical issues, and transportation of anode material. Anode deactivation/passivation occurs when the active Ni sites are blocked or otherwise impeded thus reducing the TPB density. The most common forms of this degradation are carbon formation and from fuel impurities such as those seen in sulphur poisoning. The nature of how these processes take place, and attempts to mitigate or resolve them have been the ongoing focus of research to help product commercialisation (due to being able to avoid hydrogen procurement and instead directly operate off natural gas lines). With thermomechanical mechanisms we see mechanical failure due to temperature gradients which leads to mechanical failure of the cell. This is more common in stack level testing, where the thermal gradients can lead to severe thermal mismatch, eventually leading to crack formation etc. Redox cycling is the other most common cause of thermomechanical issues, where the expansion and contraction caused by nickel metal shifting between its larger oxide state and its pure metal state leading to mechanical stress. If oxygen enters the fuel stream or an interruption to the stream occurs and air gets access then significant damage can occur to the cell/stack. Both of these issues again have seen significant focus in recent years, with computational modelling helping with the former and microstructural analysis and initial cell microstructure optimisation helping

with the latter. Lastly, with material transportation we see a tendency to reduce free surface energy causing a change in Ni particle size and morphology. The Ni atoms are transported via diffusion and condensation/evaporation mechanisms, allowing for sintering and coarsening to occur, leading to an increase in mean Ni particle size. This leads to a loss of Ni-Ni connectivity (percolation), changes the contact angle of the TPB and decreases the specific surface area of the anode microstructure. All of this leads to an overall loss of conductivity. The exact mechanism via which this loss is incurred is still unclear. It is known to be attributed to nickel particle agglomeration in the Ni-YSZ cermet, but a clear understanding of the individual effects of the operating conditions (temperature and steam content), as well as the effects of the initial microstructure are on the long term performance loss. Most long term tests involve complete cells, and so the attributed gradual degradation cannot solely be placed as being a sole result of the microstructural changes in the anode or the other components. Due to the loss of performance in the anode as a result of particle growth, microstructural analysis could allow the segmentation and fuller understanding of how these changes lead to overall degradation in the cell.

Long term degradation is predominately associated Ni particle growth, agglomeration and volatisation. This is commonly attributed to diffusion. Anode performance is based on the effectiveness of the TPB and the more of these locations and the less resistance to their individual functions leads to a higher generation of current for a given voltage. As hydrogen molecules diffuse through the cermet the continuous nickel phase conducts electronically whilst the YSZ conducts ionically. The oxygen ions from the cathode combine with the hydrogen molecules, releasing electrons which then travel via the nickel particles to the interconnect material and through to

the cathode to create the oxygen ions. In the anode, the porosity affects the diffusion rate for hydrogen and water molecules (mass flow), whilst the electronic and ionic conductivity determine the rate of reaction in the anode (charge flow).

At operating conditions, the Ni particles can sinter, influenced by the relative environmental features such as steam partial pressures and temperature. Over an extended period of time the Ni would normally agglomerate into one large metallic mass however the cermet in which the Ni is present creates a form of backbone which suppresses this. Over time the Ni will agglomerate to a point wherein it will shift most of the smaller Ni particles into larger grains. This has the cumulative effect of reducing the TPB points, reducing the potential electronically conducting pathways (thus increasing electronic resistance), as well as changing the porosity in the cell (normally leading to larger pores in some areas whilst removing some in other sections). Understanding how these changes occur, and what the major determinates and the rates of alteration are, is an important field for the improvement of SOFC testing and development, especially if combined with accelerated testing. Methods to improve long-term performance of anodes include careful control of mean particle size distribution (PSD) of Ni particles, sintering procedures, and operating conditions which reduce growth of Ni particles and Ni volatilisation through optimal steam content and flow rates. Impurities in the original powder and/or fuel stream can lead to a significant drop in performance, and pre-treatment for removal of impurities can lead to improved lifetime of the anode[8-10]. An example of stack performance degradation is given in Figure 1-4. It shows the operating temperature, current and voltage as well as overall power for the stack over 6000hours. The work, undertaken

at Forschungszentrum Jülich, is a comparison of a number of different cells and their respective power out and operating temperature. The degradation is represented by the overall loss of voltage over time.

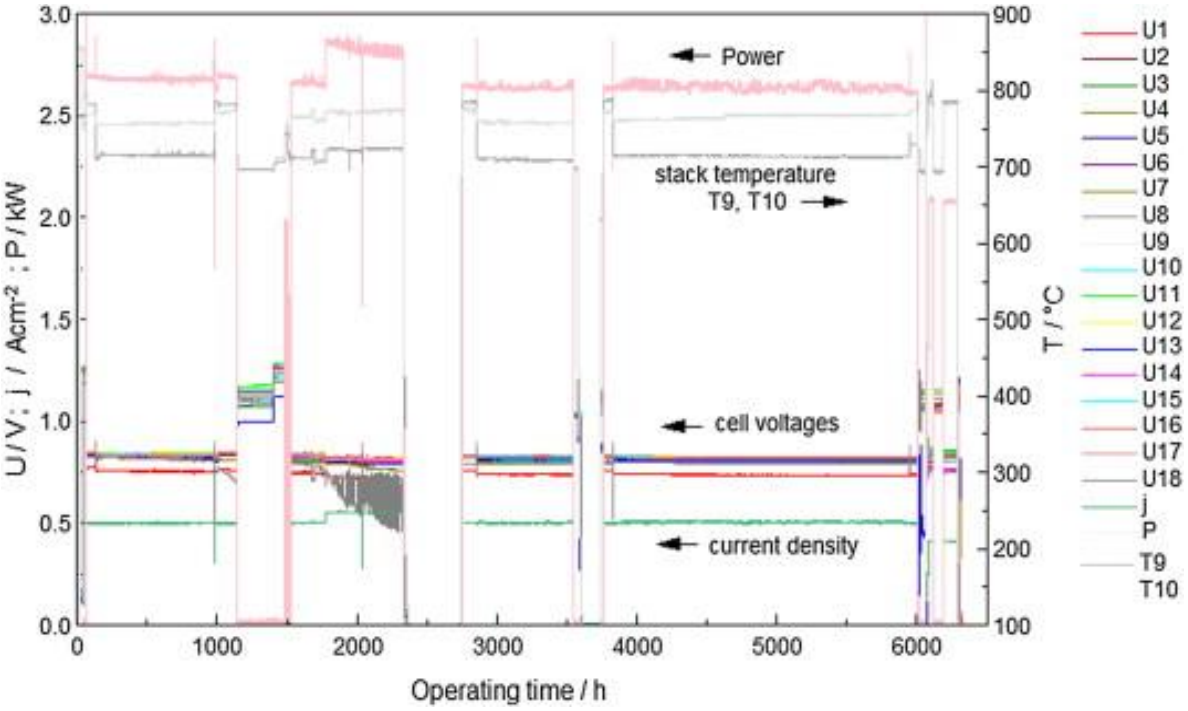

Figure 1-4 Long term testing of an SOFC stack with an LNG/H_2/H_2O anode fuel mixture. 18 individual cells made up the stack (U1-18), the current draw j was kept at 0.5 Acm^{-2} unless interrupted, the power P was >2.5kW at all times and the two thermocouples T9/10 measured 700°C [11].

Data regarding the microstructural changes that take place in an SOFC are often limited in their scope (due to time or equipment constraints). The significant permutations of material utilisation in the cell manufacture can lead to non-comparable data. The most common material selection for SOFCs are Nickel–Yittria Stabilised Zirconia (Ni-YSZ) anodes, YSZ electrolytes, Lanthanum Strontium Manganate (LSM) cathodes and ferritic stainless steel interconnects [12, 13].

Electrolyte degradation is often either mechanical, i.e. the cell delaminates or cracks, or loses ionic conductivity, normally caused by a shift from the higher ionic conductivity of the cubic phase to the less conductive tetragonal phase. LSM as well as Lanthanum strontium cobalt ferrite (LSCF) are the two most common cathode materials. The cathode can suffer similar mechanical failure as the electrolyte, where delamination and similar effects can lead to near if not complete failure of the cell. However, currently the major focus looks to deal with contamination by particles in air stream, migration of constituent atoms through the electrode, and contamination by dissociation from the steel interconnects (used for current collection and fuel channels in many cells). Significant research looking to mitigate the chromium poisoning has been undertaken, most of it looking at ceramic spinel coatings of the interconnect to improve the lifetime of the cell cathode.

The use of a variety of different ceramic components such as Scandia and Ceria dopants instead/alongside of Yittria have shown promise as alternative material composition for lowering the operating temperature to help reduce degradation rates as they offer higher ionic conductivity. Much of the research into alternative material compositions in anodes, however, looks to mitigate anode deactivation, but often introduces new obstacles to overcome in terms of product commercialisation. Different ceramic materials which make up the anode SOFCs should theoretically provide the same backbone support for the Ni (if used), and thus the analysis of Ni could prove beneficial to a multitude of different anode materials. As Ni is commonly used in cermet materials with alternative ceramic components to YSZ.

1.3 Thesis Objective

Whilst understanding how initial microstructures are affected by operating temperatures and conditions could benefit the optimisation of the manufacturing process, it is in the task of accelerated testing in which this data could prove even more useful. Accelerated testing is studying the particular materials or components of machinery or equipment in a compressed timeframe and/or extreme environments to allow for cost effective testing of items to determine their approximate lifetime in a reduced length of time. Originally used extensively for military equipment as a means of determining the lifetime of weapons and equipment, it is now a commonly utilised technique in many mechanical and electronic fields [14]. The technique commonly utilises higher than normal operating temperatures for testing components. This generally leads to an accelerated rate of degradation for the component or item. It may also operate under significantly increased operating parameters (pressure, flow rate, etc.) with the aim to draw a compressed timeline of the particular item under normal operating conditions (which would produce a baseline lifetime as shown in Figure 1-5).

However SOFC fuel cell components normally operate in temperature ranges from 600-900°C, so a ramped temperature may not give a linear response to operating at elevated temperatures. In particular many of the ceramic materials in the SOFC undergo phase changes above 1000°C, causing significant degradation as the cells perform and respond differently than under normal operating conditions. Additionally, SOFC components do not have moving components in the same way a combustion engine does or a trigger on a gun, which could normally be cycled repeated to

determine lifetime usage for certain components. This all leads to SOFCs being unable to be tested by the standard methods for accelerated testing protocols.

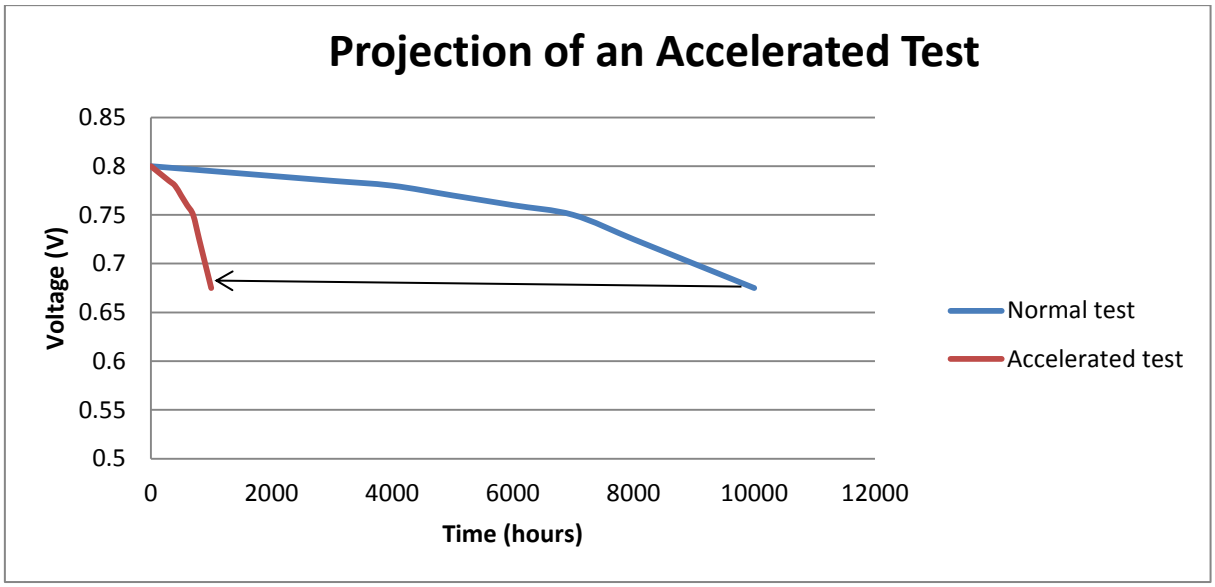

Figure 1-5 Accelerated testing example plot showing change in operating voltage over time, highlighting how normal testing time periods can be compared to accelerated tests.

Recent work by Weber et al [15] has highlighted the inherent complexities of testing complete fuel cells at “aggravated” testing regimes, due to the potentially different degradation mechanisms all having an impact on the overall degradation in the cell. Cathode materials experience a low amount of moisture present in the air stream due to environmental humidity; this has been augmented in accelerated testing for the cathode to establish the relative lifetime of that component. However, in anode fuel streams water is generally present as steam, since it is formed in the reactions taking place at the TPB, so that relatively small increase in the volumes of steam may lead to only minor increases in degradation rates (compared to the cathode). Literature

has suggested steam and temperature have important roles to play in the degradation rate in SOFC anodes [16-19]. With this information is it believed that higher operating temperatures and steam content may lead to an increased rate of degradation for SOFC anode materials. In particular, it is thought that higher temperatures and steam content will have a significant influence on the rate of growth/change of Ni particles in the anode, and the subsequent degradation in the cell. Thus if we know that a cell operated at higher temperature and steam content reaches a value for its mean particle size distribution a certain degree faster than one operating at lower operating conditions (whether steam or temperature), a novel design or material combination could be tested at these higher extremes to indicate the longer term performance change over time expected at lower conditions. If these conditions can be linked with more standard operating values then it opens up the opportunity to achieve faster test protocols, saving valuable time and money for laboratory and industrial researchers.

By developing a portfolio of data regarding the impacts of temperature and steam, an effect model will be developed to predict with a degree of accuracy the change in Ni particle radii, and from these further estimates of performance change will be projected. By furthering the understanding of the microstructural impacts of fuel and temperature conditions better optimised microstructures and operating conditions can be outlined to help improve the overall robustness of the SOFC systems. Also new developments or changes could be evaluated through this model to help determined expected outcomes for the longevity and overall effectiveness of the cell.

This thesis will report on the results of exposure tests of Ni-YSZ anode samples under varying steam content atmospheres. This data will be analysed for trends or patterns and further utilised in modelling. The microstructural data will be evaluated to determine TPB points based on 2D imaging. The models will utilise the same operating conditions to predict the change in mean Ni particle size over time, which can further be utilised to determine changes in TPB length and conductivity in the anode.

CHAPTER 2 State of the Art

2.1 Materials Available for use in SOFC Operation

As each type of fuel cell is distinctly defined by its type of electrolyte, so too is each type of SOFC heavily defined by its electrolyte choice. As the focus of this research is investigating Ni-YSZ anodes, it is also worth understanding how different materials are being investigated to work around or compensate for Ni-YSZ deficiencies as well as if there may be possible similarities in how this research can be applied to others.

2.1.1 Electrolyte Materials

Requirements for a suitable electrolyte are that it must be stable in both oxidising and reducing atmospheres whilst having suitably high ionic conductivity. It must have a low electronic conductivity as well as also being capable of gas tightness when applied as a thin layer between the anode and cathode [21]. The thermal expansion coefficient (CTE) of all other SOFC components (anode, cathode, interconnects) are chosen such that they match the electrolyte CTE so as to not cause any mechanical stress on this key component during thermal cycling. The thickness of the electrolyte influences the ohmic resistance and thus its capability of being as thin as possible is a key issue in increasing SOFC performance.

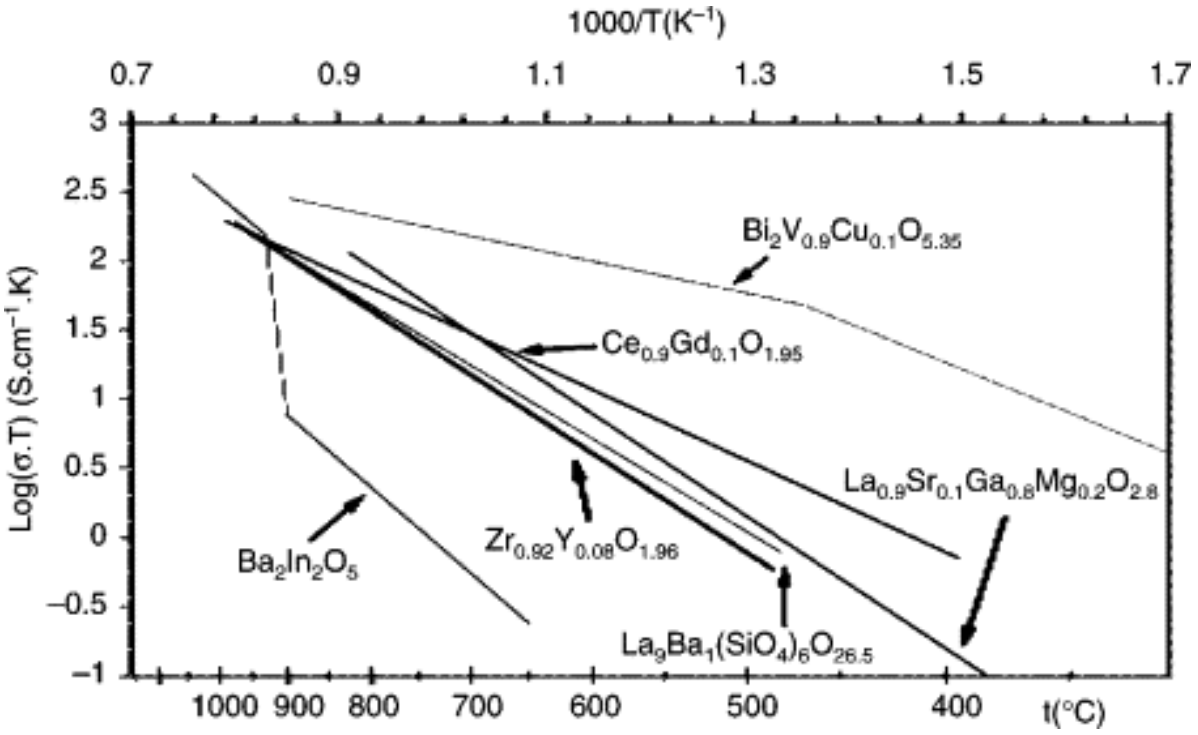

Figure 2-1 An Arrhenius plot of some of the most common oxide ion conductors, showing a log plot of the conductivity multiplied by degrees Kelvin over the inverse of the temperature [22].

The Bismuth oxide shown in Figure 2-1 highlights its superior ionic conductivity compared to most others, however due to its high sensitivity to reducing environments it is unsuitable for a fuel cell electrolyte [22], thus reinforcing the fact that multiple aspects need to be considered when choosing the electrolyte.

For transfer of the oxygen ions through the electrolyte (and the anode and cathode), an unoccupied site must be available providing a path with minimum obstruction. These unoccupied sites exist in the form of vacancies on the oxygen sublattice, provided by interstitial oxide ions or via oxide ion vacancies. For pure oxides such as ZrO_2 and CeO_2, the relative number of existing defects is low, which is why most

materials used for SOFC ionic conduction have the aliovalent dopants added, as the difference in charge needs defects in the form of interstitials or vacancies to maintain the electroneutrality in the material. As the ionic conductivity rises linearly with dopant concentration [21], it would be logical to assume that a value close to 50-50 mol% would result in the optimum conductivity, however, this maximum value is reached significantly earlier, and is often below 10 mol% for Zr systems, as seen in Arachi et al's work [23]. This has been attempted to be explained by authors [23-26], and is usually attributed to mismatch in size between the dopant and host cation.

For cubic fluorite structures (MO_2), a metal cation in a tetravalent state is needed such as Zr^{4+} or Ce^{4+}. Dopants such as the aliovalent (cations having a different charge to the given material such as Zr^{4+}) trivalent cations (Y^{3+}) are added to the ZrO_2 to stabilise it allowing the formation of cubic fluorite structures at lower temperatures. Ceria (CeO_2) can form fluorite structures without the need for dopants to stabilise it. The advantage of the cubic phase over the tetragonal one available to YSZ is the greater freedom and thus ease of movement for the ions in the lattice structure, and this is generally true for all electrolyte materials which have a favourable phase. Figure 2-2 shows an example of how the ions transport themselves in the cubic lattice structure. Also, any change between cubic and tetragonal phase during thermal cycling need to be avoided to reduce mechanical stress and rapid degradation of the electrolyte layer.

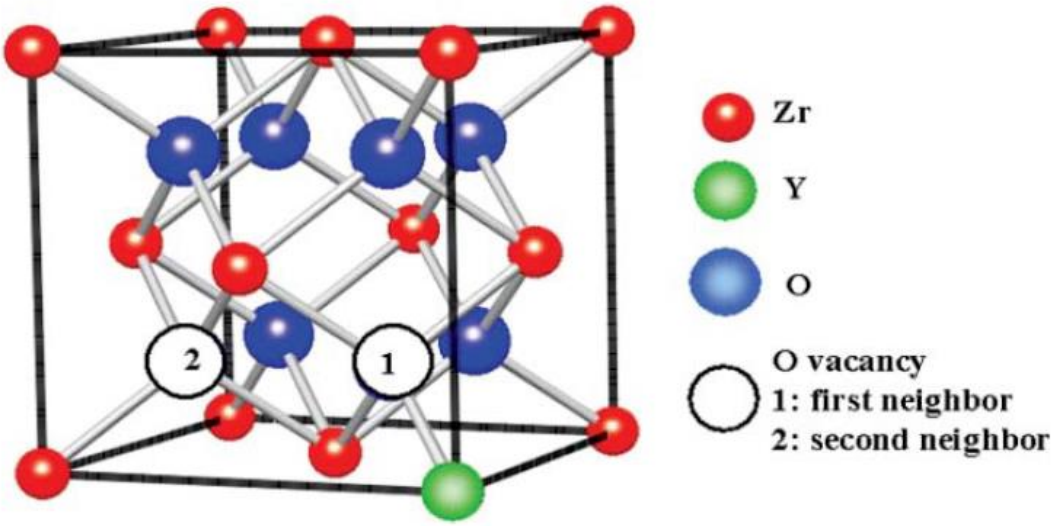

Figure 2-2 An example of oxygen diffusion through a cubic fluorite YSZ structure via the vacancy diffusion mechanism. The vacancy would shift from 1st position to 2nd [27].

2.1.1.1 Scandia

Scandia stabilised Zirconia (ScSZ) is applied for investigating intermediate temperature systems (600-800°C), as it provides a higher ionic conductivity compared with YSZ. As with yittria stabilised zirconia, it is used to help maintain the cubic phase, however it is found that for dopant concentrations less than 10% significant ageing occurs in the electrolyte upon annealing at 1000°C [28]. Some material combinations also include Ce alongside the Scandia as a dopant as it also helps with stability [29], and has encouraged research into so called “co-doping” materials, such as Y [30], Yb [31], Ho [32].

2.1.1.2 Ceria

Ceria has been proposed as an alternative to zirconia for the electrolyte material, in particular for low to intermediate temperature SOFCs, as like Scandia doped Zr it has a higher conductivity in these regions [33]. It has the same fluorite structure as found in Zr. To improve conductivity a variety of dopants have been investigated including Sm, Gd, La, Y and Ca [33-36]. Ceria based cells can be reduced in low oxygen partial pressure environments, such as those found on the anode side. This can lead to electronic conductivity, thus reducing the efficiency of the cell by internal short-circuiting across the electrolyte. To avoid this feature it is recommended that the cells are operated at low enough temperatures (<600°C) to avoid electronic leakage [37], although thin coatings of Zr can be used to prevent this [38].

2.1.1.3 Perovskite and Perovskite Related Electrolytes

Perovskite oxide materials generally take the form of ABO_3, as shown in Figure 2-3 The A and B components need to cumulatively reach a +6 charge and how they do this can vary and thus gives rise to a large number of combinations (+1/+5, +2/+4,+3/+3, etc). Due to the fact that they are capable of being both good ionic and electronic conductors they are often used in SOFC electrodes [39], and ones used specifically for the electrolyte need to be designed to mitigate the aspect of electronic conductivity. Much like fluorite structures they can be designed to have an optimal number of unoccupied sites or beneficial defect chemistry. In ABO_3 perovskites a system exists where a relationship between the A and B cations creates a “critical triangle” [40], which influences the electric properties of the material. Thus care in

terms of both cation size matching is necessary for appropriate electrolyte suitability [41].

Commonly used or researched perovskite materials include $LaAlO_3$ and doped $LaGaO_3$ (which includes $La_{0.8}Sr_{0.2}Ga_{0.8}Mg_{0.2}O_{3-\delta}$ (LSGM) [42, 43] and (La, Sr)(Ga, Mg, Co)O_3 (LSGMC) [44]). They are more stable than ceria based electrolytes in reducing atmospheres but have a higher associated cost due to the gallium oxide and a high sintering temperature [22]. Also of interest are TiO_3 based electrolytes, which show high transport numbers among lower temperature perovskites [45].

Brownmillerites can be described as an oxygen-defective perovskite in terms of its structure, and most of the relevant research on this material focuses on maintaining its cubic phase through substitution [46]. It also is unstable in wet atmospheres as well as reactive with CO_2. It has the feature of being protonically conductive below ~600°C, which makes it potentially more appealing for low temperature SOFCs [47-49]

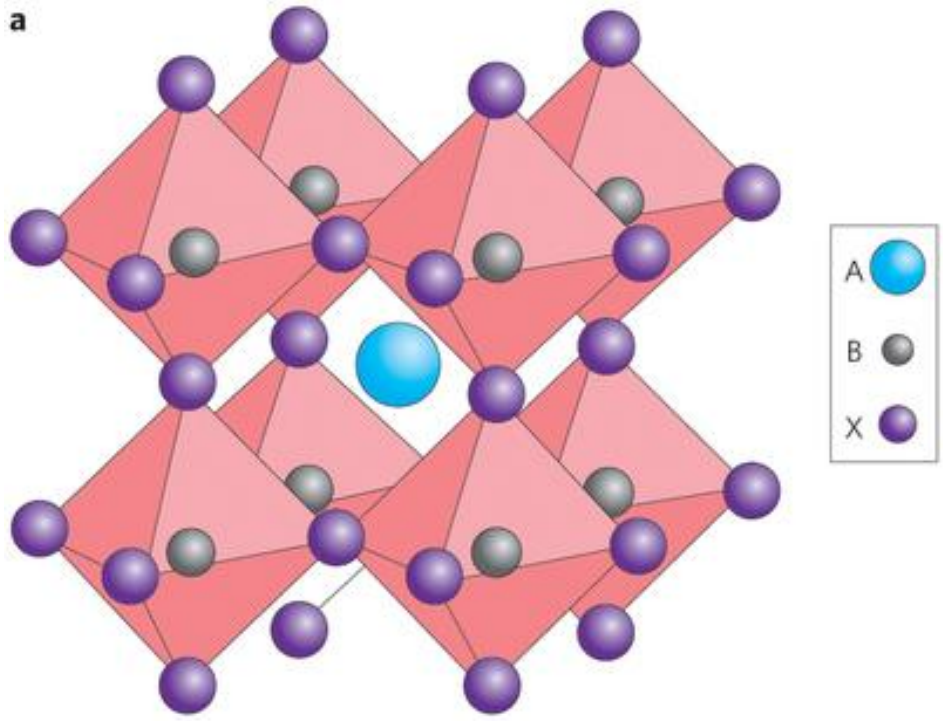

Figure 2-3 Depiction of a cubic perovskite crystal structure. An example of potential material usage would be A) Sr, B) as Ti and X) as O. Image adjust from source [50].

Pyrochlores have a perovskite related structure, and thus can function as suitable electrolyte materials, however they suffer from a limited functional oxygen partial pressure range [51]. They do, however, intrinsically come with oxygen vacancies for transportation [22]. They include materials such as gadolinium titanate ($Gd_2Ti_2O_7$)[52] or $Y_2Zr_2O_7$ [53].

Lastly there exist high-temperature proton conducting perovskites, which operate like the lower temperature polymeric fuel cells, but at relatively elevated temperatures >400°C. The most common of these are barium based, and as the activation energy for migration in protons is lower than for oxide ions they can provide higher relative

conductivities. However, stability is an issue and reactivity with common gases in the form of H_2O and CO_2 can lead to issues [54].

2.1.1.4 Novel Electrolyte Materials

A number of non-fluorite/perovskite crystal structure electrolyte materials exist and can include a large number of distinctly different materials which provide similar desirables but in very different ways. These are often newly discovered materials which, if optimised further, could improve on the current standard (YSZ), which is further along in terms of its development. These include materials like lanthanum apatite silicates [55], which offer significantly improved ionic conductivity at intermediate temperatures but current synthesis mechanism require very high temperatures (1300°C), and thus alternative methods are a focus of research [56]. Another example is $La_2Mo_2O_9$ (LAMOX) compounds which offer a different crystal structure to those commonly found in the fluorite/perovskite materials whilst still offering potentially high ionic conductivity [57]. CTE values for LAMOX are normally higher than those found in most electrode materials [58], and need to be optimised accordingly. Also, a phase change present at higher temperatures from the lower temperature cubic into a monoclinic phase results in a loss of conductivity which careful control of dopants and substitutions seek to mitigate [59].

2.1.1.5 YSZ Electrolyte Degradation

As the most commonly used electrolyte material in SOFCs, YSZ degradation has long been an area of investigation. Barring the potentially devastating effects of impurities in the bulk powders, the major loss in performance in electrolytes is due to

the permanent loss of oxygen ion vacancies, and that over time, depending on temperature and initial phase composition, can cause these higher conducting phases to change into the lower conducting variants. The most common explanation for the loss of ionic conductivity relies on the chance for a phase change of the YSZ from its initial phase (cubic) into a tetragonal phase [60-63]. Work was done on YSZ yittria balancing and found 9.5/10 mol% to be optimum due to lack of tetragonal phases which have lower ionic conductivity. At these values the cubic phase is stable and has a much lower degradation rate [60, 61, 63]. Haering et al [28] suggested that ageing promotes tripoles, which are more stable than dipoles. However the precise reason for this trend is unknown.

Impurities can lead to problems at grain boundaries, giving rise to formation of glassy phases not reported at high temperature, but could be true for lower temperature [63-65]. One problem found is that Si is a serious containment [66] and thus methods of removal of Si is one potential way to increase long term performance. Most impurities are found in initial powders [8, 9]. Different methods for cleaning the impurities from YSZ samples (in particular Si) have been suggested [67, 68]. Careful control of dopants, their composition, the sintering procedure and temperature can all help control loss of performance in a given electrolyte.

2.1.2 Anode Materials

As Ni-YSZ is the core focus of the thesis it is covered in more detail later, however like the electrolyte section it is worth understanding the various anode materials under investigation in the field of SOFC research.

The core requirements for a good anode material include:

- High electronic conductivity
- Good ionic conductivity
- Thermal and chemical stability
- Reduction stability
- Thermal expansion values match those of other materials, specifically the electrolyte
- Catalytic function for choice of operating fuel.

A comparison of DC conductivities for various anode materials is shown in Table 2-1, along with other relevant data points such as their cost or operating temperature where important. It is worth noting that the table is geared towards highlighting the potential performance at 800°C which favours some more than others as conductivity is not always linear in its performance relative to temperature.

Table 2-1 DC conductivities of materials developed as anodes for SOFCs at 800°C, as presented by Shaikh et al [12].

Materials	DC conductivity (S cm^{-1})	Advantages/Disadvantages	References
$Sc_{0.1}Y_{0.1}Zr_{0.6}Ti_{0.2}O_{1.9}$	0.14	Operate at high temperature	[69]
$La_{0.8}Sr_{0.2}Fe_{0.8}Cr_{0.2}O_3$	0.5	Low conductivity	[70]
$La_{0.8}Sr_{0.2}Cr_{0.95}Ru_{0.05}O_3$	0.6	Expensive	[71]
$(La_{0.7}Sr_{0.3})_{1-x}Cex–Cr_{1-x}NixO_3$	5.03	Carbon deposition	[72]
$Sr_{0.88}Y_{0.08}TiO_3$	64	High operating temperature	[73]
$CrTi_2O_5$	177	Expensive	[72]
Ni–YSZ	250	High operating temperature	[74]
$Ti_{0.34}Nb_{0.66}O_2$	340	Expensive	[75]
$LaSrTiO_2$	360	Compatibility issues	[12]
Ni–SDC	573	Coke formation	[74]
Ni–GDC	1070	Coke formation, electronic performance degradation	[74]
Cu–CeO_2	5200	Improved electronic conductivity	[76, 77]
Cu–GDC	8500	Good thermal expansion and electronic performance	[78]

2.1.2.1 Ceria, CGO Based Anodes

Ceria and copper have seen significant interest as an alternative to zirconia and nickel, respectively [79-81]. Copper has the advantage of being a relatively inert metal and thus better suited for carbonaceous fuels, as well as having a high electronic conductivity [82]. As previously mentioned, ceria has shown good conductivity for intermediate temperature fuel cells and is commonly seen as a doped ceramic component, often with Gadolinium (CGO) [83], combined with a variety of electronically conductive materials such as Ni, Cu and Co. Gadolinium-doped ceria (CGO) $Ce_{0.9}Gd_{0.1}O_{1.95}$ has also shown carbon deposition resistance [84]. Work has been done on Ni-GDC anode materials for different operating fuels including ethanol [85], as well as modelling research into suitability and electrochemical activity for internal steam reforming (including Au/Ni-GDC based cells) [86]. Iron as a dopant is quite common alongside Ni, and work involving GDC cermets has shown promise in areas that use bi-metallic anodes for lower temperature operation [87]. The iron acts to reduce cell overpotential, and may help with coarsening at lower temperatures. Other areas focus on novel manufacturing techniques alongside very different materials selections such as the solution combustion synthesis (SCS) method for producing a CeMnFO (CMF) anode material for SOFC [88]. $Ni_{1-x}CO_x$-CGO is another example of CGO, where alloying the Co and Ni has resulted in improvements to the overall performance [89].

2.1.2.2 Scandia Based Anodes

Scandia-ceria-doped zirconia electrode and electrolyte materials have been investigated owing to their improved ionic performance at reduced operating temperature [90-92]. Scandia based cells offer the opportunity to lower the operating temperature of the cells to an intermediate level (600-800°C), which, as previously mentioned, can help improve the long-term stability of the cells. For Sc based anode materials the literature seems to have similar performance to its YSZ counterpart cermet. Sumi et al [93] showed improved performance for ScSZ-Ni anodes for humidified methane in a 2500 hour test, due to the formation of whisker-like graphite rather than the amorphous graphite formed on normal YSZ anodes. Kishimoto et al [94] conducted a study on ScCe based Ni cermet materials. They found that their cermet material had issues with the reduction of NiO to Ni metal during reduction, suffering a phase change from cubic to tetragonal phase, rending the performance significantly reduced from onset of operation. Somalu et al [95] studied Ni/10ScSZ and Ni/10Sc1CeSZ fabrication and characterisation of a cermet anode. Sc based electrodes performed better with regards to electronic conductivity and electrode polarisation when doped with Ce, and both materials exhibited improved tolerance towards carbon deposition compared to Ni-YSZ.

2.1.2.3 Perovskite Based Anodes

Perovskites based anodes have the advantage of structural stability under redox cycling, a significant improvement on the relatively limited resistance that Ni-YSZ

ones have. They have limited activity to hydrocarbon cracking as well as resistance to sulphur and other fuel impurities, however their electronic conductivity is lower than that found in NI-YSZ anodes, and are thus sometimes used in composite anodes to balance for this. By careful selection of appropriate dopants as described previously in the perovskite electrolyte section, you can create a mixed ionic-electronic conductor (MIEC). Most of the focus on new materials deals with carbon tolerance [96] and the ability to cope with impurities such as sulphur as previously discussed. Perovskite materials represent an interesting area of focus [97], as their lack of Ni circumvents issues for the standard Ni-YSZ anode. However, they inherently have lower electronic conductivity, and so a lot of research looks to find a composition where the conductivity is high whilst still offering their inherent benefits [98]. LaSrCrMn anode materials have been looked at, which show good redox stability at high temperatures, but poor catalytic activity compared to Ni. Nanocomposite formation of the cermet showed improved performance/lower electrode polarisation resistance [99]. LaSrCrMn perovskite anode materials have been tested with methane with a specific interest in the influence of lattice oxygen stoichiometry. As with other studies in this field the material shows great promise if a significant improvement in performance is possible [100]. Development of a LaSrTiO^{-} YCeO (LST-YDC) composite anode uniquely found that when 0.5% H_2S was present in syngas a power increase was noted, however, more than 0.5% did lead to issues [101]. Using various perovskites can also offer different opportunities with electrolyte materials [102], as they also share similar CTEs and can have similar application/manufacturing techniques/procedures.

$SrTiO_3$, when exposed to a reducing atmosphere or certain dopants shifts from Ti^{4+} to Ti^{3+} ions. This strips oxygen from the lattice, creating oxygen vacancies and electrons which greatly increase the ionic and electronic conductivity of the material [103]. Having the perovskite formula ABO_3, when doping the A site with trivalent cations such a La^{3+}, there is an increase in electronic conductivity due to the increased charge on the donor [104]. This performance has seen further improvements through partially replacing the Ti^{4+} with cations such as Ga^{3+}. Due to the coordination flexibility of Gallium it improves the redox stability and as well as the overall reduction process [105].

2.1.2.4 Manufacturing Improvements for SOFC Anodes

Alongside different material compositions, varied methods of manufacturing have seen interest to either improve overall performance or reduce cost/time. This includes novel approaches such as solution precursor plasma spraying [106], atomic layer deposition [107] and wet impregnation/infiltration technique based composites [108-110], many of which show equal or greater performance than conventional manufacturing techniques like tape casting due to factors such as being able to extend the TPB length and increase overall microstructural control.

2.1.3 Cathode Materials

Focus in the area of cathode research and development generally looks to resolve the most pressing issues in the field, and can include the designing of new compositions and microstructures to overcome current limitations, improving the

understanding of the oxygen transport mechanisms in different types of cathode materials, as well as the effect of operational conditions (such as temperature and thermal cycling) on those materials. The design requirements for SOFC cathodes [111] include:

- High electronic conductivity (preferably more than 100 S/cm in an oxidising atmosphere);
- Minimum mismatch between the coefficient of thermal expansion (CTE) values of the cathode and other sections of the cell, examples of which can be seen in Table 2-2 ;
- Good ionic conductivity;
- Chemical compatibility with the electrolyte and interconnect materials;
- Sufficient porosity for O_2 gas diffusion;
- Good stability under an oxidising atmosphere;
- High catalytic activity during oxygen reduction reaction.

Part of the reason for cathodes being the focus of interest in lower operating temperatures specifically is a result of the fact that the rate of increase in cathodic polarisation resistance is larger than the respective ohmic polarisation increase for a comparable drop in temperature, and thus becomes the dominant limiting effect on cell performance [112].

Table 2-2 Composition and Thermal expansion coefficient (CTE) for certain cathode materials [113]. Values similar to YSZ's CTE of 10.5 x10^{-6} [114] are desirable to prevent mechanical stress during thermal cycling.

Composition	**CTE ($10^{-6}K^{-1}$)**
$La_{0.99}MnO_3$	11.2
$La_{0.69}Sr_{0.30}MnO_3$	12.8
$LaMnO_3$	12.5
$La_{0.7}Sr_{0.3}MnO_3$	11.8, 12.0
$La_{0.9}Ca_{0.1}MnO_3$	10.6
$La_{0.7}Ca_{0.3}MnO_3$	10.5

2.1.3.1 Perovskite Cathodes

As discussed previously in the electrolyte portion of this section, the perovskite materials have a general formula of ABO_3, where A and B represent cations which cumulatively possess a net charge of +6 [115]. The A sites are occupied mainly by rare earth metals and alkaline earth metals. These metals are lower valence cations, and can be either a single metal cation or a mixture of different metal cations (La, Sr, Ca, etc). These cations have a larger ionic radii compared to the B site cations. The B sites are occupied by higher valence transmission metal cations (again either a single metal or a mixture of metals) which possess a smaller ionic radius. Example B site cations include Ti, Cr, Co and Fe. The A-sites are coordinated by 12 oxide ions and the B sites are coordinated by 6 oxide ions, as shown Figure 2-4. It is the octahedral symmetry around the transition metal cations which promotes a

semiconducting band structure which gives perovskite materials its high relative electronic conductivity at high temperatures [114].

$La_{1-x}Sr_xCoO_{3-\delta}$ (LSC) is the first reported perovskite material to have be used as cathodes in SOFCs [116], and LSC is a good MIEC conductor but displays a high thermal and chemical expansion relative to the ~10.5 x10-6/K seen in YSZ which makes it difficult to use for SOFC purposes. Strontium doped lanthanum manganite (LSM) became the most commonly used material for SOFC cathodes after 1973, as its relative robustness (in terms of chemical and thermal stability [117, 118]) and overall suitability for higher temperature operation encouraged intensive research. Lanthanum manganite benefits from Sr doping in terms of increased electronic conductivity (as $LaMnO_3$ is an intrinsic p-type conductor [117]), changing the crystal structure from orthorhombic to rhombohedral upon doping, as well as helping to suppress the chemical reaction which can take place between the $LaMnO_3$ based cathodes and YSZ at high temperatures [114]. However, at those higher temperatures it is particularly vulnerable to chromia poisoning from steel interconnects. Chromia poisoning is also a serious concern for a number of other cathode materials, and a number of solutions have been investigated with spinel coatings of the interconnect being one of the more common resolutions to this problem [119, 120].

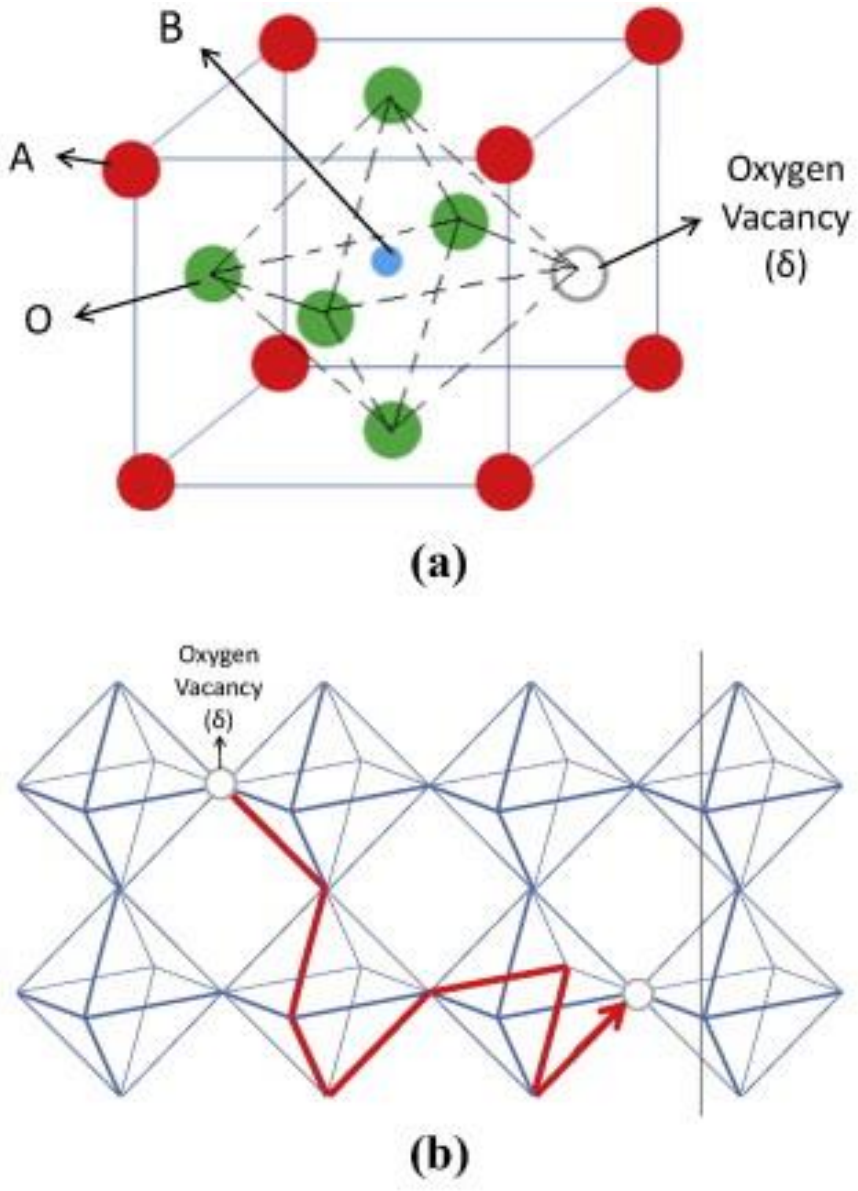

Figure 2-4 Crystal structures of perovskite $ABO_{3-\delta}$ samples showing a) an example with an oxygen vacancy and b) showing the hopping of an oxide ion along vacancies in the direction of oxygen migration. Image adapted from reference [121].

From a stability point of view, with rare earth transition metal perovskites, the largest ions are most desirable, which in this case is La^{3+} [122] and part of the reason why

lanthanum based cathode materials are so prominent in SOFCs. The La_2O_3 component can react with the Zr in zirconia-based-electrolytes to form lanthanum zirconate. When the A site has deficiencies in the ABO_3 formula, it is less reactive to the YSZ.

$La_{0.8}Sr_{0.2}FeO_3$ (LSF) offers potential as a lower temperature cathode material compared to LSM due to the significant increase seen in the overpotential of LSM when operating at lower temperature (500°C) [123]. It has shown good long term stability and high relative power output (~0.9 W/cm^2 at 750°C) [124-128], however it does suffer from a lower electronic conductivity.

$La_{(1-x)}Sr_xFe_yCo_{(1-y)}O_3$ (LSCF) has a less severe CTE mismatch and is thus popular with manufacturers, as the ferroelastic nature of the rhombohedral lattice mitigates the CTE mismatch with the electrolyte [122]. LSCF with a ceria layer is often used to prevent reaction with YSZ [129, 130]. LSCF has a much higher CTE [131] than compared to those seen in Table 2-2, and thus different potential electrolyte materials are necessary. Due to thermal expansion coefficient compatibility and stability LSCF is suited for use with GDC electrolytes [132, 133]. Which makes it a desirable choice for lower temperature SOFCs, as $La_xSr_{(1-x)}CoO_3$ (LSC) alone, whilst having a higher conductivity than LSM, suffers from cobalt diffusion and some mechanical issues [125, 133-135]. LSCF suffers from reactions with YSZ electrolytes and is not suitable to be placed directly on it, thus some research has looked into placing ceria based interlayers between the LSCF and YSZ to allow for combined usage [136].

A large number of variants exist for lanthanum based cathode materials, many showing promise but are still in earlier stages of their development. For example $(La_{0.5}Sr_{0.25}Ca_{0.25})MnO_3$ (LSCM) cathode materials have shown long term experimental performance (5000h) alongside a samarium doped ceria (SDC) interlayer [137]. Porosity formation caused by Mn & Ca diffusion from the cathode was noted, though performance remained stable. However, below 800°C the cell voltage saw significant losses, which was ascribed to the formation of a dense layer formed of La, Ca and Mn which prevented O_2 supply to the electrode reaction sites.

2.1.3.2 Non-Lanthanum Based Cathodes

Lanthanum is the most commonly used cathode material but, praseodymium, strontium, gadolinium and yittria have all seen attention for alternative cathode materials.

Praseodymium cathodes have seen some interest in the field, in particular $Pr_xCa_{(1-x)}MnO_3$ (PCM) has shown a very high electrical conductivity with a lower cathode potential and reactivity to YSZ [138, 139]. Other variants including strontium doped praseodymium manganate (PSM) have seen attention but have had reactivity issues with zirconia [140].

Gadolinium based cathodes have seen interest for SOFC applications, unsurprisingly these show particular promise when used alongside Gd based electrolytes from a thermal expansion perspective. $Gd_xSr_{(1-x)}CoO_3$ (GSC) shows low resistances at

temperatures around 700°C [141], and an overpotential one order of magnitude lower than LSM at 1000°C (whilst at 800°C) [142]. It can however react with YSZ, in particular with increasing Sr content. Strontium doped gadolina manganate (GSM) equally does not react with GDC but does with YSZ and has a reasonable CTE for GDC [143].

Strontium based cathodes have seen interest as an intermediate temperature cathode material (500-800°C). In particular strontium-doped samarium cobaltite, $Sm_{1-x}Sr_xCoO_3$ (SSC), is a good MIEC and has a high oxygen vacancy concentration showing promise as a potential cathode material [144]. The interest in SSC has also resulted in composite cathodes being investigated, [112, 145, 146], for example a SSC/Co_3O_4 composite showed a 40% increase in cell performance through an enhancement of the open-circuit voltage as well as the oxygen surface-exchange rate. However SSC is less well suited for higher temperatures due to its reactivity with YSZ and SSZ, and does not perform as well as GSC and strontium doped neodymium cobaltite (NSC) [147]. Other variants of strontium doped cathode materials have been investigated including bismuth and neodymium [148]. NSC has shown comparable properties to GSC with a GDC electrolyte [20] and $Bi_2Sr_2CaCu_2O_8$ (BSCCu) has shown good resistance properties on GDC for lower temperature operation [141].

Yittria-doped cathode variants exist and $Y_{(1-x)}Sr_xCo_yFe_{(1-y)}O_3$ (YSCF), $Y_{(1-x)}Ca_xCo_yFe_{(1-y)}O_3$ (YCCF) and $YBa_2Cu_3O_7$ (YBCu) have shown suitability for intermediate temperature fuel cell application (~800°C) alongside SDC electrolytes. They have higher overpotential than LSCF but lower than LSC [20]. For YCCF a

spinel-type oxide can form with a YSZ electrolyte during fabrication but was shown to have negligible growth during operation [149], suggesting a compatible fit for YSZ materials also.

2.1.4 SOFC Interconnect Materials

Ceramic interconnects are the original interconnect material, mainly due to the high operating temperatures of SOFCs. But development into intermediate temperature has opened the possibility for metallic interconnect materials. Irrespective of material, when analysing the suitability of a given material, a number of factors need to be considered [150-152], including:

- Maintaining a high electrical conductivity – Acceptable area specific resistance (ASR) is considered to be well below $0.1\Omega cm^2$
- Close match to SOFC components coefficient of thermal expansion (CTE).
- Good stability in both reducing and oxidising atmospheres. (adequate stability in terms of dimensions, microstructure, chemistry and phases at operating temperature in both oxidising and reducing atmospheres up to 40,000h (service lifetime).
- Good compatibility with other SOFC ceramic components.
- Impervious to oxygen and hydrogen to prevent direct combination of oxidant and fuel during operation
- No reaction or interdiffusion between interconnect and its adjoining components.

- Good resistance to oxidation, sulfidation and carbon formation.
- Adequate strength and creep resistance at high temperatures.
- Low cost, as well as easy to use in fabrication and shaping.

2.1.4.1 Ceramic Interconnects (Lanthanum Chromites)

Historically, the most common interconnect material for high temperature SOFCs (~1000^{0}C) is $LaCrO_3$ (varying compositions). Its values lie with the following features [151, 153]:

- It has a high electrical conductivity under SOFC operating conditions
- It has a very high melting point of ~2783K.
- It is stable in both cathodic and anodic environments making it suitable for both anode and cathode sides.
- A CTE value of $9.5x10^{-6}$ K^{-1} closely matches that of YSZ ($10.5x10^{-6}$ K^{-1})

$LaCrO_3$ has certain disadvantages as a interconnect material, however:

- It is a ceramic material, which limits the geometry of interconnects which can be fabricated.
- It is difficult to sinter to a high relative density, and is thus difficult to process as a hermetic $LaCrO_3$ layer.
- La is an expensive rare earth metal

Ultimately because of the added costs and complexity other materials have been investigated. But importantly for the investigation of IT-SOFCs (600-800°C) is that the reduced operating temperatures open up opportunity for metallic based interconnects, which can be relatively less expensive and easier to fabricate/manufacture.

2.1.4.2 Metallic Interconnects

Metallic interconnects have a number of advantages, in particular they can have high electrical and thermal conductivity, low cost, ease of fabrication, are readily available as well as having adequate mechanical strength [154, 155]. Table 2-3 highlights a number of these features for the most commonly investigated metal interconnect materials.

Table 2-3 Description of key properties of potential metallic interconnect materials, including Cr based alloys (CrBA), ferritic stainless steels (FSS), austenitic stainless steels (ASS) and Fe and Ni based super alloys (FeBSA, NiBSA) [156].

Alloys	Matrix structure	CTE$\times 10^{-6}$/K	Oxidation resistance	Mechanical strength	Manufactur-ability	Cost
CrBA	BCC	11.0–12.5 (RT-800°C)	Good	High	Difficult	Very expensive
FSS	BCC	11.5–14.0 (RT-800°C)	Good	Low	Fairly readily	Inexpensive
ASS	FCC	18.0–20.0 (RT-800°C)	Good	Fairly high	Readily	Inexpensive
FeBSA	FCC	15.0–20.0 (RT-800°C)	Good	High	Readily	Fairly expensive
NiBSA	FCC	14.0-19.0 (RT-800°C)	Good	High	Readily	Expensive

Chromium based alloys can operate in temperatures up to 900-1000^{0}C and they have very high electrical conductivity compared to other oxides, but invariably lead to

chromium poisoning for the cathode side and excessive chromia growth (which causes spallation after thermal cycles) due to the high chromium content [152, 155]. Also, oxide dispersion strengthened alloys are more difficult and costly to fabricate. These factors make it highly unlikely to be used for large scale SOFC interconnects.

Ni-Cr based alloys show high oxidation resistance as well as electrical conductivity and have high mechanical strength [157-159]. However they have a relatively large CTE compared to the anode/electrolyte/cathode material values seen in SOFCs, and are some of the more expensive materials in terms of cost [160].

Fe and Ni super-alloys are both face centred cubic (FCC), which means that their CTEs are sufficiently different to cause issues during operation with standard YSZ components. Alternative ceramics alongside alloys with lowered CETs would be the most likely way to manage to incorporate these super-alloys into use as interconnect materials, despite having many suitable features for operation as an interconnect material [156].

Stainless steels offer the lowest cost option for interconnect materials. Ferritic and austenitic steels are the two most suited types due to their mechanical properties and low cost relative to other stainless steels. Due to the fact that body centre cubic (BCC) structures have a lower CTE than FCC ones [153] (and closer to YSZ's CTE), ferritic stainless steels offer the most suitable choice for interconnects [119]. A minimum Cr content of 20-25 mol% is needed to develop a protective layer in the form of Cr_2O_3 scales [4]. Also ferritic alloys benefit from simpler processing methods [154, 161, 162]. Chromia scales can however grow to such high levels as to raise the

ASR to unacceptable ranges when operated at intermediate temperatures. Vaporisation of Cr can lead to severe degradation of the electrical properties of the SOFC on the cathode triple phase boundary layer [163]. This has led to the development of coatings to mitigate excessive chromia scale growth and Cr poisoning, whilst still taking advantage of the CTE and reduced cost of ferritic steels.

Gas sealant options used to prevent gas permeation can influence the suitability of a specific interconnect material. Interactions with the SOFC components and its suitability for the chosen operating conditions has led to a number of options being investigated [164].

Cost however tends to be the most limiting factor and most of the research and development has focused on ferritic stainless steels for use as interconnects. Thus a large amount of research has gone into developing coatings and techniques for improved operation and longevity alongside reduced cost.

2.1.4.3 Coatings

Coatings should be able to suitably mitigate or improve the ferritic steels whilst also remaining cost effective. For a coating to be viable it should have the following characteristics [156].

1. Diffusion coefficients of Cr and O in the coating should be as small as possible so that the transport of chromium and oxygen can be effectively hindered.

2. It should be chemically compatible and stable with respect to substrate, electrodes, sealing materials and contact pastes.
3. It should be thermodynamically stable in both oxidising and reducing atmospheres over the applied temperature range.
4. It must have low ohmic resistance to maximise electrical efficiency.
5. CTE should be well matched to substrate so that the coating is resistant to spallation during thermal cycling.

A selection of suitable material types are presented in Table 2-4, highlighting the materials respective conductivity, Cr mitigation, oxidation reduction and processing simplicity.

Table 2-4 Comparison of some of the available coatings techniques and their properties, including electronic conductivity, Cr inhibition, oxidation reduction rate and deposition complexity [120].

Comparison of different coating materials in terms of capability of improving electronic conductivity, Cr migration inhibition and oxidation rate reduction as well as simplicity of the coating process.

Coating material	Electronic conductivity	Cr migration inhibition	Oxidation rate reduction	Simplicity of deposition
REOs	Fair	Poor	Good	Good
Perovskites	Good	Fair	Poor	Fair
Spinels	Good	Good	Fair	Good
Composite spinels	Good	Good	Good	Good
MCrAlYO	Highly depends on composition	Good	Good	Poor

2.1.4.3.1 Reactive Element Oxides

Reactive element oxides (REO)s are regarded as the first generation of steel interconnects coating material [120]. Based off elements such as Y, La and Ce, they can reduce the oxidation rate and ASR of the substrate [165]. However due to the thin and porous layer that they coat the substrate with, they offer no Cr poison mitigation, and are thus unsuited for the long term role of the coating [120].

2.1.4.3.2 Perovskite Coatings

On top of the properties already attributed to perovskites they are capable of some mitigation of Cr poisoning. They have a number of possible application techniques, but many suffer from an inefficient deposition method (multiple/uneven coatings). Importantly, they do not help reduce oxidation rates. $LaCrO_3$, [166, 167] LSM [168]. LSCF [169], LSC & LSF [170] are all examples of tested perovskite coatings used for SOFC steel interconnects.

2.1.4.3.3 MAlCrYO coatings

Metal (M) AlCrYO is normally used on coatings for gas turbines and other high temperature applications, but the addition of Mn and/or Co can provide suitability for interconnect coating applications [171]. A low ASR can be achieved, as it is effective in reducing Cr release from the surface of the interconnect.

2.1.4.3.4 Nitride Coatings

Nitride coatings have low resistance and high temperature stability (also high wear resistance) [172]. Limitations include high capital cost and low deposition rate. Also importantly, nitride is not quite stable at temperatures above 600°C [156].

2.1.4.3.5 Spinels

Spinel coatings have the general formula AB_2O_4, with the A and B sites being either divalent, trivalent or quadrivalent cations in tetrahedral or octahedral sites and anions in the form of oxygen on a face centred cubic (FCC) lattice site [120]. Spinels have good electrical conductivity and importantly good Cr mitigation abilities. They have simple and effective methods of processing, but suffer from moderate oxidation reducing properties. RF sputtering, screen printing, slurry coating, plasma spraying, electro-deposition and anodic electro-deposition of aqueous solution followed by heat treatment have all been used to coat steel substrates [120, 158, 173-176].
$NiO/(Ni,Fe,Cr)_3O_4$ [177], $(Co,Mn)_3O_4$, $(Cu,Mn)_3O_4$ [120] and $Mn_{0.9}Y_{0.1}Co_2O_4$ [178] are all examples of potential spinel coatings.

Composite spinels, formed with reactive oxide elements, offer improved oxidation rate reduction over normal spinels, without any notable drawbacks (except perhaps cost) [179]. This is because the spinels produced have a denser, finer grain structure resulting in a more protective spinel [180]. Electro-deposition is the method of choice for composite spinels, which allows a single stage process which provides uniform application of the solution [120].

Of the available techniques, spinels (and composites) are the only coatings which can adequately reduce the Cr poisoning for the cathode, and if composite, can also improve oxidation rate reduction.

2.2 Initial Ni-YSZ Microstructure and Material Selection

The initial microstructure of Ni-YSZ anodes is considered a critical part of SOFC anode performance [181] . In particular the particle size distribution and fabrication method can heavily determine long term performance. Due to the nature of balancing the electrical conductivity of the Ni, the ionic conductivity of the YSZ and the gas permeability of the pores most Ni-YSZ anodes look to use approximately 60-50 wt% NiO and 50-40 wt% YSZ for their electrodes. NiO reduces by roughly 40% volume, which gives the cells ~30 vol% porosity [182].

Typically, anode compositions consist of 8 mol% YSZ, but some work has investigated alternative compositions of anode material. Jiang et al's [181, 183] report design and optimisation of a Ni/ 3mol%YSZ (or Ni/TZ3Y). TZ3Y was found to have different properties to Ni-8YSZ, but the long term stability of 8YSZ has led to it being the most prominent choice as electrolyte material and is the most commonly incorporated as the ceramic component of the anode for thermal coefficient matching (TEC) [12]. The research highlighted the most critical parameter determining the anode performance was the particle size and the size distribution of NiO and TZ3Y powders. YSZ is critical in its particle ratio size relative to the Ni particles, and in its relation to Ni particle coarsening. Work by Tu and Stimming [184] found that YSZ is

added in order to support the Ni particles, to inhibit coarsening of the Ni, and to provide a CTE which is similar to that of the zirconia based electrolyte. Its degradation rate is marginal compared to the growth rate of Ni particles [185]

The effect of pore formers in initial microstructure is naturally important as the H_2 oxidation reaction is limited by two electrode processes thus optimising the microstructure will affect both of these. For hydrogen species transport to Ni surfaces a greater porosity is useful, whilst for charge transfer at the electrolyte/electrode interface a Ni/YSZ volume is better, which is generally inversely proportional to each other. Pore formers are often chosen to increase porosity, and these are selected for parameters such as optimal shape, aspect ratio etc. Work looking into various means of pore generation have suggested materials such as polystyrene particles to produce the optimal percolation paths/pore channels for operation of an anode supported cell [186].

Table 2-5 SOFC compositional table of NiO/YSZ & Ni/YSZ weights and volumes including porosity degradation testing data from literature [186].

Solid content								Including porosity		
Wt%		Vol%		Wt%		Vol%		Vol%		
NiO	YSZ	NiO	YSZ	Ni	YSZ	Ni	YSZ	YSZ	Ni	Pore
10	90	8.95	91.05	8.03	91.97	5.47	94.52	91.05	5.262	3.688
20	80	18.11	81.89	16.42	83.58	11.51	88.49	81.89	10.65	7.46
30	70	27.49	72.51	25.19	74.81	18.24	81.76	72.51	16.16	11.33
40	60	37.10	62.9	34.38	65.62	25.76	74.24	62.9	21.8	15.3
50	**50**	**46.94**	**53.06**	**44.00**	**56**	**34.23**	**65.77**	**53.06**	**27.6**	**19.34**
60	**40**	**57.02**	**42.98**	**54.10**	**45.9**	**43.84**	**56.16**	**42.98**	**33.53**	**23.49**
70	30	67.36	32.64	64.71	35.29	54.84	45.16	32.64	39.60	27.76
80	20	77.96	22.04	75.86	24.14	67.55	32.45	22.04	45.84	32.12
90	10	88.84	11.06	87.61	12.39	82.41	17.59	11.06	52.23	36.61

Component	Mol.-wt.	Density (g cm^{-3})	Molar volume (cm^3)
Ni	58.69	8.907	6.589
NiO	74.69	6.67	11.198
8YSZ	131.42	5.90	22.27

Early work in the field of Ni particle optimisation [187] investigated 4 different anode types including fine Ni cermet (0.5-1um particles), coarse Ni cermet (2-3um) , a porous Ni-paste anode and Ni-felt anode. The fine Ni cermet produced the best cell performance and most research indicates that smaller Ni particles lead to a more optimal long term performance and degradation resistance. The polarisation characteristics of the anode are highly dependent on its morphology. The apparent activation energy has a distinct tendency towards lower values for fine cermets than that for coarse cermets [187]. Kim et al [188] highlighted the potential of a composite of nano-crystallised NiO deposited onto YSZ versus commercially produced powders as a method of improving anode durability. This study showed an improved suppression of anode degradation and enhanced long term and redox stability of the unit at elevated temperatures, which was attributed to the fine initial Ni particle size which allowed for a more percolated Ni pathway during sintering. Other work looks to

highlight the potential of in-situ formation of Ni particles in the anode in the hopes to improve long term performance [189] through a more controlled microstructure. Many Ni-YSZ anodes make use of an anode functional layer (AFL) with the intended role to facilitate a greater TPB density nearer the electrolyte surface [190], Analysis of the samples worked on by Faes et al [17] has suggested that no different degradation mechanisms take place between the anode functional layer and the support layer.

Impurities in the initial powders used for manufacture and in the gas streams can lead to significant if not catastrophic failure. Investigating the effect of impurities such as Mn, Si and Ti in H_2-H_2O mixtures in the anode (Al, Na, Mg Ca and K can also be found in some samples), was shown to lead to performance loses as the impurities were able to block the TPB layers even in tiny quantities [10, 191, 192]. It highlights the critical importance of high purity Ni for the electrode (where for example 99.995% purity Ni was shown to be 10 times better than 99.8%Ni in terms of lower polarisation resistances [192]). A Time-of-flight secondary ion mass spectrometry (Tof-SIMS) scan issued in Figure 2-5 to show how Si can act to reduce contact between the Ni and Zr phases via. fuel impurities (sulphur, tar, etc) can also cause serious issues in cells, especially when they combine/react with trace impurities present from the initial powder mixture (such as Si) [193]. The effects of the impurities were shown to be significant on the performance of the cells. However they did also find with their cells that those units which were operating at OCV before testing (for 440-332 hours) showed minimal degradation compared to tests which started immediately after initial characterisation of the cells. Further work [194] attempting to improve the degradation resistance of the anode was directed at improved manufacturing methods leading to a more controlled Ni particle size distribution. The suggestion for

the mechanism taking place was that impurities in the cell material whilst running at OCV form crystals that future impurities in the fuel are more likely to be drawn to thus preventing degradation from impure fuel streams. Whether this effect would be prevalent over 10s of thousands of hours is still unclear.

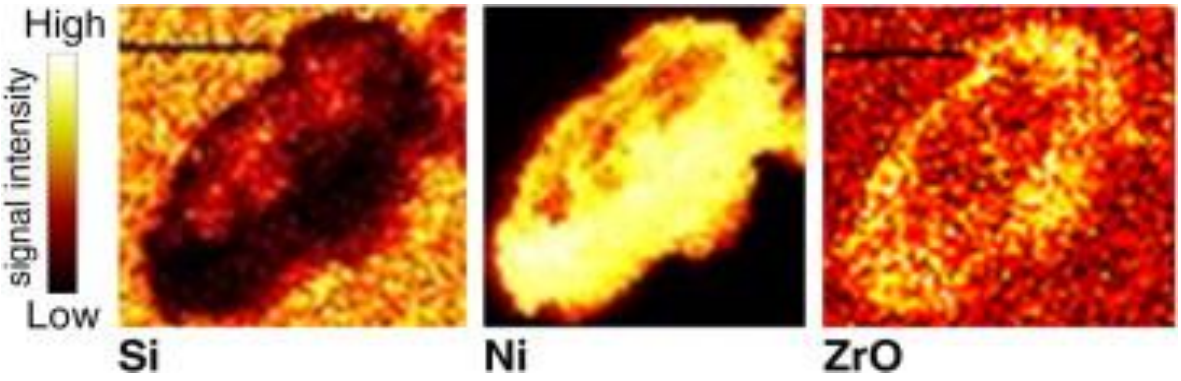

Figure 2-5 A 500x500 µm Image of a ToF-SIMS analysis of an ZrO-Ni interface and the surrounding Si causing a reduction in contact. Brighter regions denote areas of strong signal for the given element [9].

Some research focuses on the use of novel designs of patterned Ni anodes in an attempt to improve understanding of boundary kinetics [195-200], in the hope of furthering understanding of Ni particles in SOFCs. The data has especially seen use for modelling purposes where the values which are difficult to obtain, such as rate kinetics, are necessary for modelling reactions inside the SOFC.

Other areas aim to investigate different manufacturing and fabrication techniques to help improve degradation resistance. Designs such as the electroless technique prepared by Basu et al [201, 202] [203], which involves creating a YSZ core which is surrounded by Ni particles, in particular look to change the way the microstructure is

formed to mitigate the normal routes of degradation. This allows in theory for the use of less Ni without compromising on electrical conductivity. This structure appears to undergo significantly less degradation when compared to a conventionally fabricated anode undergoing redox cycling.

Barring the potentially devastating effects of impurities in the bulk YSZ powders[66], the major loss in performance in electrolytes is due to the permanent loss of oxygen ion vacancies, and that over time, depending on temperature and initial phase composition, the higher conducting phases can change into lower conducting phases[61, 63, 65, 204]. Careful control of dopants, their composition, the sintering procedure and temperature can all help control loss of performance in a given electrolyte.

2.3 Transformation in Microstructure

As with any area relating to SOFC research, investigating and understanding the change in the anode, and in particular the Ni particles, has been a focus of research for a number of years. Early work by Simwonis [16] is one of the earliest papers looking to test, analyse and model anode degradation in H_2O/H_2 mixtures. A significant portion of later modelling work is based on these early attempts to understand Ni agglomeration and coarsening in cells. Agglomeration in the cell occurs through sintering which includes grain growth and densification and occurs in two distinct phases: in the earlier phase local bonding is created through neck formation, and in the later stage pore rounding and pore shrinkage occur. In both

stages the bulk volume of the sintering particles shrinks [205]. The driving force is minimisation of the free surface enthalpy of the particle agglomerate.

5 mechanisms are possible to allow for sintering to occur.

- Volume diffusion (migration of vacancies)
- Grain-Boundary diffusion
- Surface diffusion
- Viscous and plastic flow (caused by surface tension)
- Evaporation /condensation of atoms on surface

The equation references as describing the sintering mechanism present is from Kuczynski [206]

$$\left(\frac{2r_c}{2r}\right)^n \sim t \qquad \textbf{Equation 2-1}$$

Where r_c is the radius of the neck of the overlapping particles. r is the particle radius, n is the sintering exponent mechanism and t is the sintering time. The mechanism factors change depending on the suggested phenomenon, so viscous/plastic flow corresponds to n=2, for evaporation/condensation n=3, for volume diffusion is n=5 and for surface diffusion is n=7. Experimental work done to compare this validate agreed with the predominant mechanism for sintering in a metal powder to be volume diffusion [65] in the earlier stages.

Coarsening is when the larger particles grow at the expense of smaller ones, and is described as Ostwald Ripening. In Ostwald Ripening the thermodynamically driven process takes place where the more energetically stable larger particles grow in size

whilst the smaller particles diffuse due to concentration gradients into the larger ones before being consumed completely assuming no physical/energetic restrictions. Surface energy minimisation is known to drive Ni particle coarsening, and previously, albeit not in YSZ cermets, it was shown that the shape of the Ni particles formed into larger spherical particles [207, 208].

The effect of steam partial pressure in the fuel stream has generally been agreed to be an important determinant in the rate of Ni agglomeration. Some work found that at 600ºC, there was no effect from steam, whereas at higher operating conditions, steam accelerates the rate of degradation, as expected [209]. Others have suggested temperatures as high as 700ºC have limited impact on the degradation process, whilst 800ºC was shown to induce significant degradation, deeming it to be a thermally activated process or processes, albeit under high steam partial pressures (80%-20% H_2O-H_2) [210]. In the former study, when the obtained data was fitted with two time constants, at least two growth processes were identified. The perceived loss in conductivity was related to Ni particle growth and loss of Ni percolation.

In experiments done by Aaberg et al [211], Ni wires were pressed onto YSZ substrates, which when exposed to various humidified hydrogen atmospheres and run at anodic overpotentials led to Ni particles being transported towards the electrolyte surface forming a “necklace” that increased TPB length, as seen in Figure 2-6. This highlighted the importance of contacting and percolation in improving the activation of cells, without the potentially convoluting microstructural distribution environment that doing these tests in a cermet might generate i.e. separating one impacting factor from another.

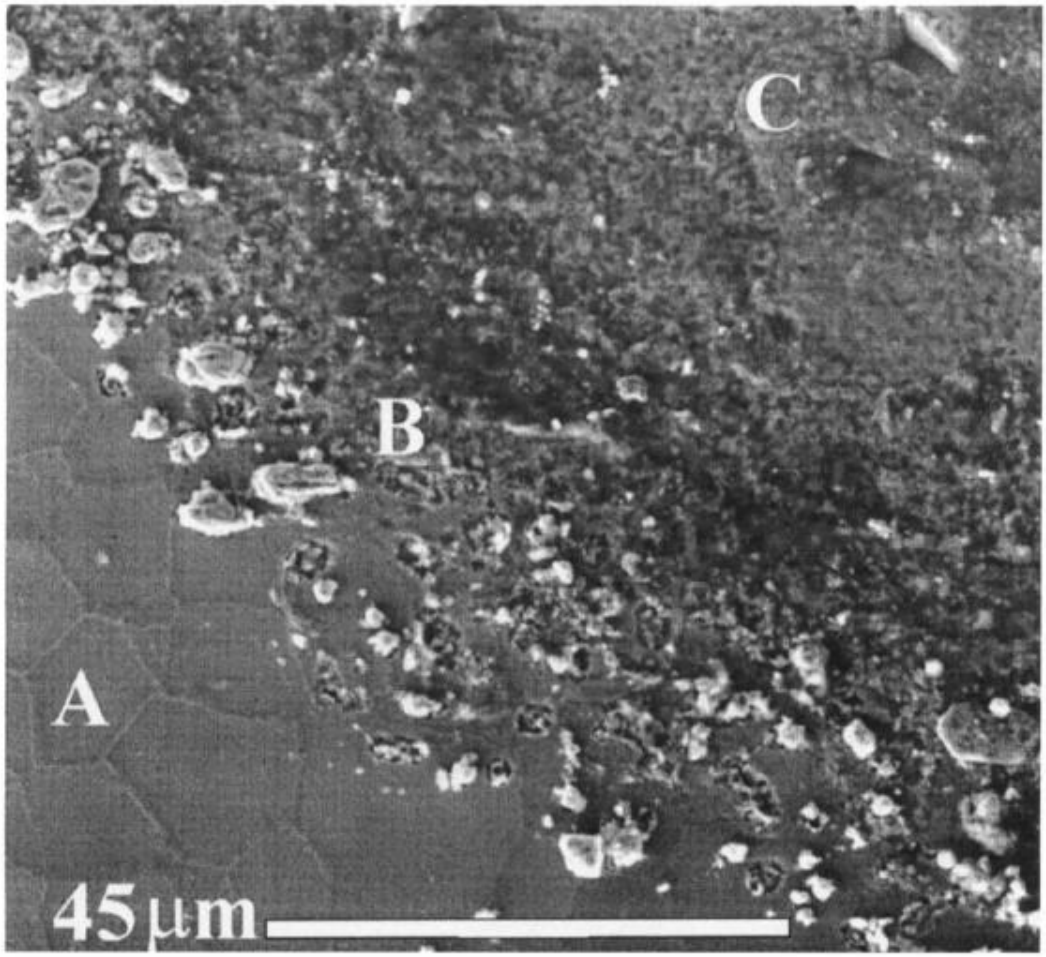

Figure 2-6 Environmental Scanning Electron Microscopy (ESEM) image of sample with section A the YSZ region, B the necklace region of adhering Ni particles and C the Ni electrode [211].

Sehested et al's early work on Ni catalysts in industrial reformers has been used to give an insight into some mechanisms potentially present in Ni-YSZ anode materials [212]. Whilst in most cases the data is less representative due to its lower temperatures of 500ºC and high pressure (30Bar), it is often used as a referencing point on the basic reactions of steam and Ni. Continued examination into Ni particle behaviour on different supports [213] presented an increased Ni particle sintering

with higher P_{H2O}/P_{H2} ratios (10:1). Their equations for particle sintering assume particle migration and coalescence as the mechanism (which similarly uses the value n as seen in Equation 2-1), whilst at higher temperatures Ostwald ripening was suggested to dominate. So for temperatures <700°C where the particle migration and coalescence dominates the value used is $n \geq 7$, whilst for temperatures above this Ostwald ripening (atomic migration) is more likely to dominate and $n \leq 7$, thus speeding the sintering process. Ni volatility appears to be a significant issue in some research, however, its exact mechanism seems to be unclear, despite the understanding of Ni volatility in water vapour mixtures being an established field [214].

Later work building on previous studies for the Component reliability of solid oxide fuel cell systems for commercial operation (CORE-SOFC) project looked to test performance and degradation of SOFCs under a number of operating conditions [215]. With a variety of temperatures, fuel compositions and current densities tested it represents one of the earliest detailed investigations of SOFC performance and degradation. Data analysis revealed a critical cell voltage of ~750mV, above which the degradation rates were trivial but below which they were significant. Different ageing behaviour is seen with different testing procedures. Previously Mogensen's work with Linderoth had indicated back in 2000 that high steam and current values lead to larger degradation rates. Certain samples underwent activation in the first 50 hours of operation, as so measurements on their loss of performance were taken after this change in activity. Results were often misleading or were in disagreement with expected results. Impedance analysis made it clear when the cells loss in

performance was due to cathodic failure rather than anode degradation. Some of the data indicated that a superior performing cell had a larger than average Ni particle size increase after testing, contrary to the suggestion that agglomeration negatively impacts on performance. However this larger particle size and initial superior performance does not necessarily represent its long term performance over 1000's of hours. What might have been an initial redistribution of particles leading to overall improvements (due to poor microstructure design for example), may in the long term lead to similar overall performance degradation. It highlighted that even minor operational differences could potentially lead to vastly differing individual performances from the cells. Thus care should be taken to ensure that outside factors which can impact on the cell performance are minimised whilst also keeping experimental operating conditions as close to their intended function/purpose.

Research has suggested that Ni coarsening is driven by particle curvatures indicated by dihedral angles between Ni, YSZ and pore phases [18]. It is hypothesised that this growth occurs mainly due to diffusion and particle agglomeration constrained by a pinning mechanism related to the YSZ phase. The decrease in Ni phase size after extended periods of time may be the result of a second process connected to a mobility-induced decrease in the YSZ phase size or non-uniform curvature resulting in a net decrease in Ni phase size. Decrease in YSZ phase size due to mobility of Zr and Zr^{4+} may result in a decrease of Ni phase size at longer operational times.

The suggestion of a plateau at which Ni agglomeration peaks inside of the YSZ core structure has been reported in some work [17]. Though the particular time scale for this is dependent on the fuel composition, initial particle size and microstructure as

well as temperature, some suggest that the initial ~100 hours are where significant degradation occurs [216]. Faes et al [17, 19] have reported that no morphological changes in the anode support versus the functional layer during operation, and that they found that phase proportions from unreduced to reduced samples correlated reasonably well with those expected theoretically.

Very high current densities have been reported to lead to rapid degradation or even catastrophic cell failure in some cases [217]. In cells tested up to 20% H_2O it was found that performance steadily decreased. However in 30% and 40% steam environments cells suffered significant degradation and then seemingly complete failure, likely caused by a significant loss of Ni percolation in the cells. The cells may have also suffered in particular with high steam content due to low porosity affecting the TPB layer. They saw longer performance in higher nickel content cermets, correlating in at least some way to Ni phase connectivity [218]. The authors had previously done similar work on an anode supported cell with similar results.

Porous Ni pellets pressed against a dense YSZ pellet have been used to help understand morphological changes in the TPB layer [219]. Lower voltages resulted in greater local H_2O concentration which formed an interlocking effect between Ni and YSZ as well as a redistribution of densified Ni layer along the TPB. With the potentially higher humidity at the TPB compared to the bulk phase, the authors suggested that local morphological changes were due to enhanced surface diffusion of Ni and the vaporisation-deposition mechanism of $Ni(OH)_2$ driven by the gradient of H_2O outwards from the TPB to the bulk gas environment.

Recent short term testing of steam effects on anode materials at higher temperatures (1000-1200°C) investigated thresholds for significant microstructural degradation. For values of ≥10% H_2O at 1200ºC or ≥40% H_2O at 1000ºC, there was notable degradation in their samples [220]. Whilst 50 hours of testing does not truly represent a sufficient time to deduce degradation in anode materials, it does suggest that steam and temperature have either a cumulative effect or constructive effect (as in waves). The authors have suggested an alternative degradation mechanism involving YSZ particles being encompassed by the volatile Ni (in $Ni(OH)_2$ form), especially under the high humidity stream (and thus may or may not happen with lower humidity environments) . It was suggested that NiO_2 generates more easily at the boundaries between the YSZ and the Ni interface.

Work on reducing sintering effects has been studied by Khan et al [221] through the use of inhibitors in the microstructure. Their attempt at long term degradation involved 1000°C testing in 25%H_2/75% N_2. The tests look to be done over 750 hours for each respective sintering inhibitor combination. Humidification was introduced by mixing with 12% and 20% water vapours at ~150 hours and 300 hours into the experiment. The initial introduction of H_2O into the fuel stream is shown to improve the Area Specific Resistance (ASR) in the system. 10wt% GDC added to the 60/40wt% NiO/YSZ was shown to have the most significant improvement in reducing ASR increase (from 0.0059 h^{-1} for Ni-YSZ to 0.0009 h^{-1} for 10wt% GDC) which was compared to a TPB density change of (0.00121 um^{-2} h^{-1} for Ni-YSZ to 0.00037 um^{-2} h^{-1}).

2.3.1 Nickel Oxide Reduction

Freshly sintered anodes will contain nickel in its oxide state inside of the anode. This needs to be reduced a) to improve electrical conduction through the anode material and b) to improve or otherwise completely generate the porosity for gas transport in the anode. NiO reduction from the oxide to the metal state Ni follows Equation 2-2 [17] where the values for reduction in volume $\Delta V_{reduction}$ are found in Table 2-6 showing the values of NiO and Ni in terms of molar mass M_{mol} and molar volume V_m.

$$\Delta V_{reduction} = \frac{\left(V_{m,Ni} - V_{m,NiO}\right)}{V_{m,NiO}} \qquad \textbf{Equation 2-2}$$

Table 2-6 NiO and Ni molar mass and volume comparison table [222].

	NiO	**Ni**
M_{mol} **(g mol^{-1})**	74.71	58.71
V_m. **(cm^3 mol^{-1})**	11.32	6.60

The volume contraction from the oxide state should match reasonably closely with mercury porosimetry measurements. This value should be equivalent to a volume loss of 41% from the respective loss of oxygen in the NiO [223], and an equivalent mass loss of 21%. By working out the respective radius of NiO and Ni we know that Ni is roughly 0.835% the radius of NiO. Working out the respective areas produced from each radii gives a total of ~30% porosity produced in a 2D image from the reduction, which equates to roughly 15% in a 50/50 NiO/YSZ green mixture.

Work by Richardson et al [224] used in-situ X-ray diffraction to study the reduction process in porous NiO. The results indicated that without water present in the gas (hydrogen) the reduction followed a series of steps: (1) initial reduction of NiO and the appearance of Ni clusters; (2) increased reduction of NiO as the size of the clusters increase; and (3) NiO disappears and Ni appears in concert until reduction slowed at a fractional conversion of about 80%. With added water this reduction process slowed down (which was enhanced at lower temperature). These experiments were however done at a low temperature range compared with Ni-YSZ anodes (175-300°C), and so may present a different reduction process than those commonly present in SOFC anodes.

Work by R. Sharma [225] used environmental transmission electron microscopy (ETEM) to help determine nano-structural and kinetic information regarding the microstructure of their sample. In particular it allowed for in-situ temperature and/or temperature resolved analysis, which is particularly important for understanding the dynamics in NiO-YSZ reduction.

Jeangross over a number of years [226-229] has done work investigating NiO reduction. Much of the work describes the process for using energy-filtered environmental TEM to successfully describe quantative local measurements of both the chemistry and microstructure in a NiO-YSZ anode [227]. A suggested activation energy for NiO reduction of ~70kJ/mol was determined from their analysis, which was comparable to other literature values. In their work the temperature was raised up to 600°C under reducing gas to analyse the change in microstructure. A model for the suggested reduction method of NiO was given from theirs and previous work. Initial

at a) hydrogen adsorbs and dissociates onto two Ni atoms, with an oxygen vacancy beside them, then b) at around 350-400°C the Ni clusters increase in size and hydrogen adsorbs directly onto the surface then desorbs as water. In c) the pores from within larger particles whilst smaller ones shrink to allow for the volume loss which is created from the reduction process. Steam present begins to block or restrict access to active sites. In d) some of the NiO is restricted by Ni layers which prevents access further which is exacerbated by steam, lastly in e) the system has reach 600°C and surface energy minimisation cause the smaller grains to become part of larger grains.

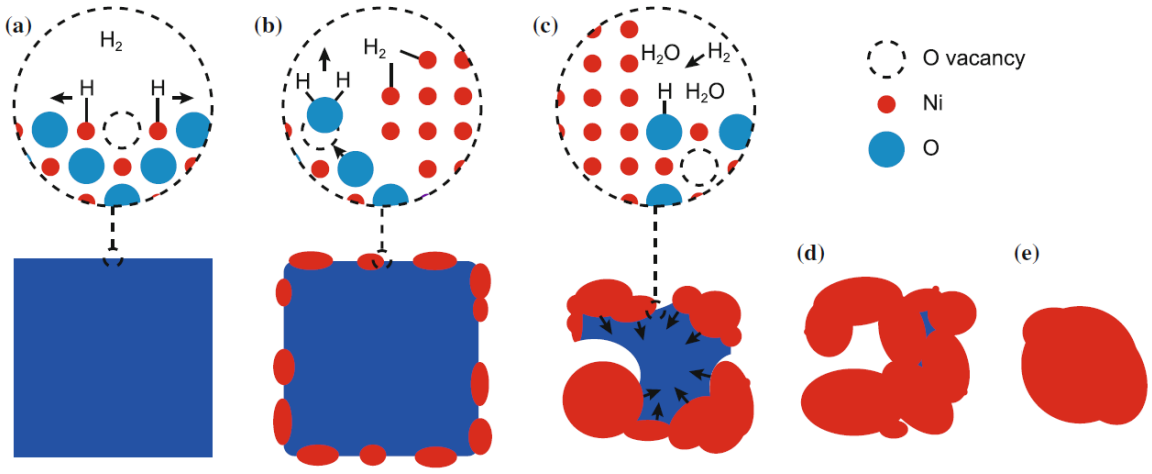

Figure 2-7 Suggested model for NiO reduction by Jeangros et al [228]. The blue represent NiO progressively being reduced to the red Ni metal, highlighting how varying reduction paths can affect the access to the NiO material.

Further work on the effect of NiO/NiO grain boundaries and how they change during reduction [229]. The initial NiO/NiO interface can affect which sites are most likely to be reduced and form percolated networks during activation. Incoherent NiO/NiO

boundaries detach during activation. Small impurities are investigated and the oxide films created from elements such as Si and Al lead to supported Ni nanoparticles that precipitate from volatile Ni hydroxide which re-deposit on its surface. It has shown that a fully dense Ni layer can form over NiO if the reduction takes place at high temperature with a low H_2-H_2O ratio feed gas. [223], which would impede or halt the further reduction of that cluster of Ni particles. Work done by Zhu et al [230] investigated the impact of initial reduction temperature and highlighted a clear performance improvement through reducing at higher temperatures, as the initial reduction process still left a percolated network; whereas slower reduction temperatures allow for segregation of particles, as shown in Figure 2-8. The highest reduction temperature investigated was 700°C and was superior to 650°C, 600°C and Room Temperature. The silver edge represents reduce Ni metal and the green sections shows NiO

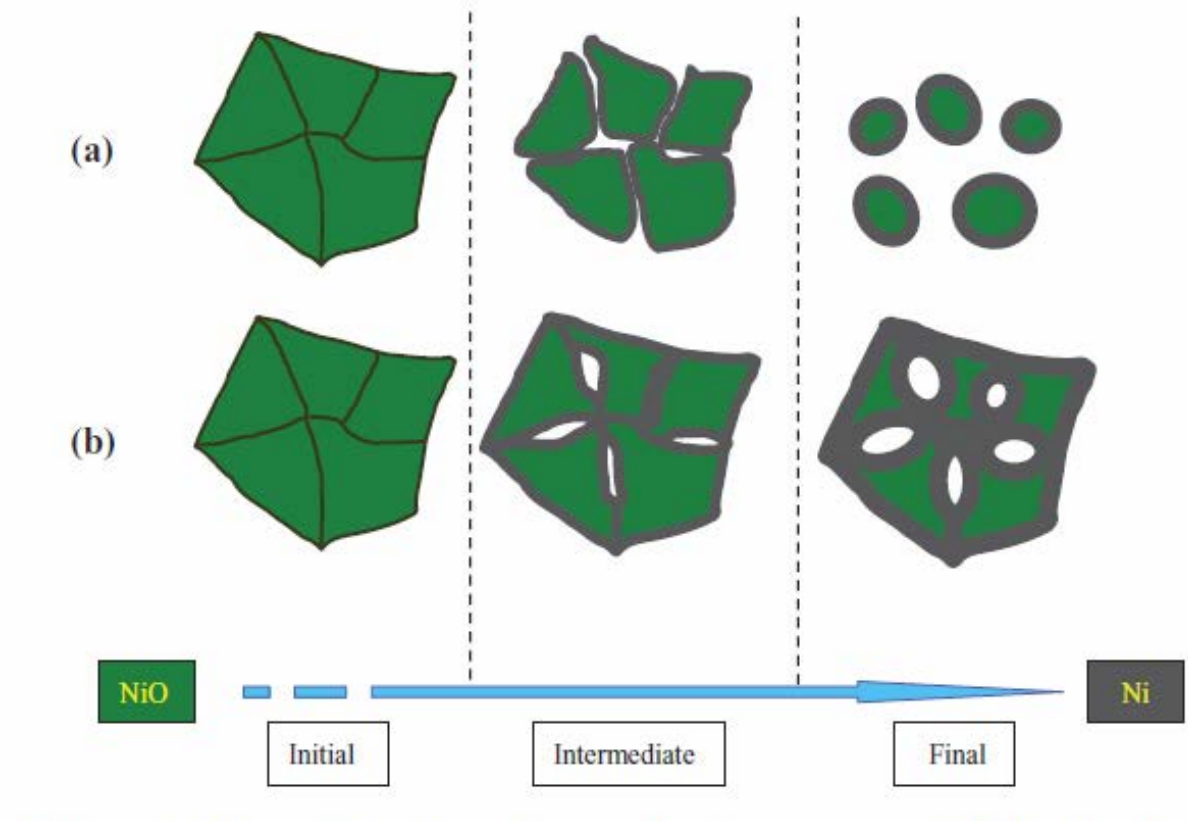

Figure 2-8 Visual representation of varying effects of temperature on reduction procedure [230]. The grey region is Ni metal and the green NiO. Option a) is reduction at a low temperature, where gradual reduction lead to encapsulated Ni metal disconnected from each other, whilst in b) higher temperature reduction allowed for percolated networks to form.

Previous studies indicated that the reduction profile for NiO was impeded by the YSZ support, leading to a slower reduction process [231]. More recent studies have suggested that the macroscopic network in which the NiO is found is indirectly affected by the YSZ [232, 233] through gas/mass transportation limitations. Simonsen et al's work tried to clarify which process is the cause for the limited reduction process. NiO crystallites incorporated into YSZ were determined not to be

the cause due to the relatively low degree of incorporation, but may still have an impact, however small, on the inhibitive effect on the reduction process. Thermogravimetric analysis (TGA) of their samples matched previous investigations into the inhibitive effects of YSZ to the reduction process, however ETEM did not show this reduction in Ni particle growth in its analysis. As the samples were only analysed in a nearly 2D environment the impact of gas/mass transportation limitations could be the cause of this difference seen in the TGA analysis. It was noted that the variations in cell compositions and preparation mechanisms could lead to a more pronounced effect from the NiO-YSZ chemical reactions than those observed in these tests, however they were compared against relatively similar cells to those most commonly used in the SOFC field. The comparison between reduction at lower temperatures ~300°C and higher temperatures ~800°C showed no difference with ETEM, leading to the belief that the collapse of nano-pores and coarsening of the Ni particles is seen as the cause of a slowing reduction process.

The formation of porosity in the cell and the shapes that are created will be dependent on the manner in which the NiO reduces and the relative particle size of NiO to YSZ. A number of different styles of pore can form in the cell, including channels, dead ends, ink bottles and isolated pores. Isolated pores serve no purpose as gas can neither enter nor escape and are entirely undesirable. Channels present the idealised path for gaseous fuel as they offer the least resistance, whilst ink bottles and dead ends can at least potentially provide access to sites for reactions. Figure 2-9 shows an example of the pore styles and how they might influence fluid flow.

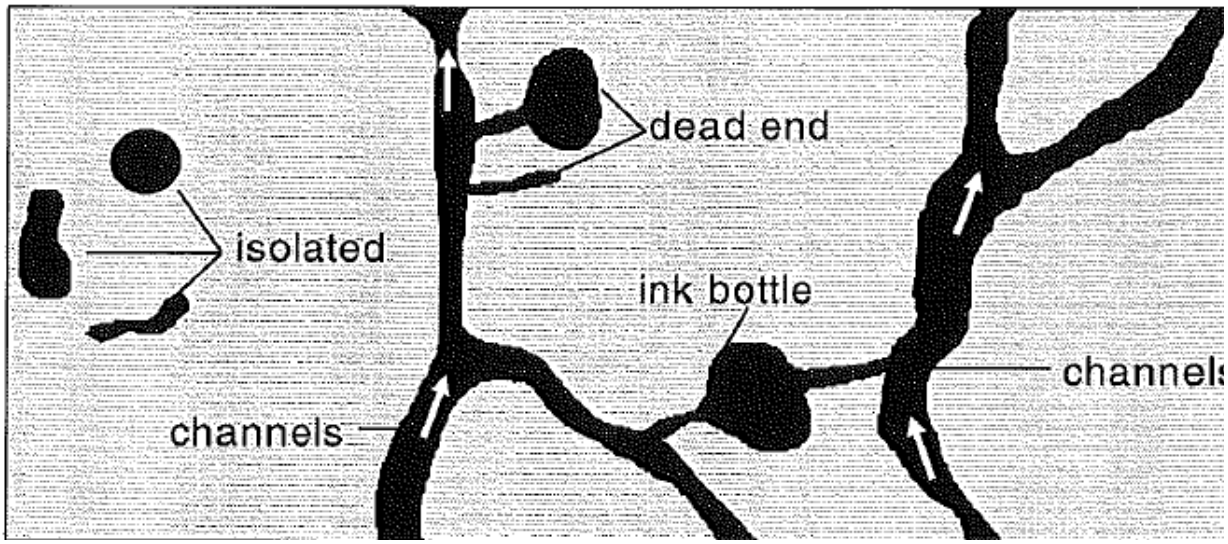

Figure 2-9 Porosity type formations [234]. The ideal formation is a connected series of channels; the least ideal is the isolated which reduces material percolation whilst not offering any path for gaseous transport.

The data available covering anode degradation has been collated in Table 2-7, and highlights the fuel composition, operating temperature, test duration, anode material composition, electrical operation and Ni particle growth rates where available.

Table 2-7 SOFC testing data from literature covering fuel, operating temperature, duration, material composition, current and nickel growth.

Fuel composition	Temperature (°C)	Test Duration (hours)	Material Composition	Current draw (A/cm^2)	Nickel growth (um)	Refer-ence
40-60% H_2O/H_2 for all and 10-90% H_2O/H_2 for 1100°C and 1200°C	1000, 1100 and 1200	50h	Ni-(8%)YSZ	OCV		[220]
10-40% H_2O/H_2	800	~80	Ni-(8%)YSZ, various percentage distribution. Electrolyte supported		1.38 – 1.75	[217, 218, 235]
5-50% (varying) H_2O/H_2	750-850	~300	Ni-(8%)YSZ			[215]
40-60% H_2O/H_2 and some other compositions	750	300-700h	Ni-(8%)YSZ	OCV & 0.75A/cm^2		[193]
3-97% H_2O /H_2 120ml/min	850	0, 24, 200, 1000	Ni-(8%)YSZ		0.29-0.35 and 0.32-0.38	[17, 19]
CO_2 +H_2 (CH_4 +H_2O)	750,850,950	1500h	Ni-YSZ			[236]
60-40% H_2O/H_2 (varied across 3 experiments) 60-40 H_20-H_2/N_2, 97-3% N_2-H_2	950	2000h+	Ni-CGO		0.28 - 0.38	[216]

20-80% H_2/H_2O	700 and 800	300, 1000, 3000	Ni-(8%)YSZ			[210]
3-4-93% $H_2O/H_2/Ar$	1000	4000h	Ni-(8%)YSZ		2 – 2.6, 1.02-1.25	[16, 237]
97-3% H_2O/H_2	1000	4000	Ni–(3%)YSZ		1.54+/-0.55 – 2.7 +/-0.84	[238]
50-50% H_2/N_2	927, 1008	211, 1015	Ni-(8%)YSZ	0.5 A/cm^2 and 0.3 A/cm^2	Range of 0.1/ 1-0.1/1 and 0.1/1-1/10	[239]
15-85% H_2/N_2	800	600	Ni-(8%)YSZ/ Ni–(3%)YSZ (50%-50%)		0.7-0.9	[240]
97-3%, 50-50% and 15-85% H_2/H_2O	750, 1000	300	Ni-(8%)YSZ		Normalised 1 up to 1.375	[241]

The data presented in Table 2-7 is structured in a way to highlight the significant variation present in either operating parameters or composition differences in existing literature. If there was interest to visually compare the grain growth rates we could either look to compare radii normalised to their initial “as reduced” starting values or simply plot the recorded values, and both have merit.

Figure 2-10 shows a collection as presented Ni radii and their evolution over time for given operating conditions. These are mean values, and as such represent the entire distribution of the samples as best presented. Some of the data is only capable of showing particles of a certain size, and thus especially for the initial values may

overestimate the mean size. What is most notable from this set of data is that for the majority a plateau development becomes visible for the samples. This is often in the first 250h and certainly in the first 1000h. Due to the variance present in the samples and the relatively large distributions the std. deviations are often quite wide for the given data points.

The various data from papers does agree with the suggestions of temperature and steam content being the direct influencing factors on Ni grain growth. Holzer et al's [216] data suggests a much more rapid increase due to the presence of steam, as does Jiang [183]. Simwonis [16, 237] and Tanasini [19] on the other hand see much more gradual inclines due to the relative absence of H_2O in the inlet fuel stream. Faes et al's [17] samples despite different initial mean Ni radii reach very similar values, which suggests similar conditions and mass distributions will likely reach the same end result.

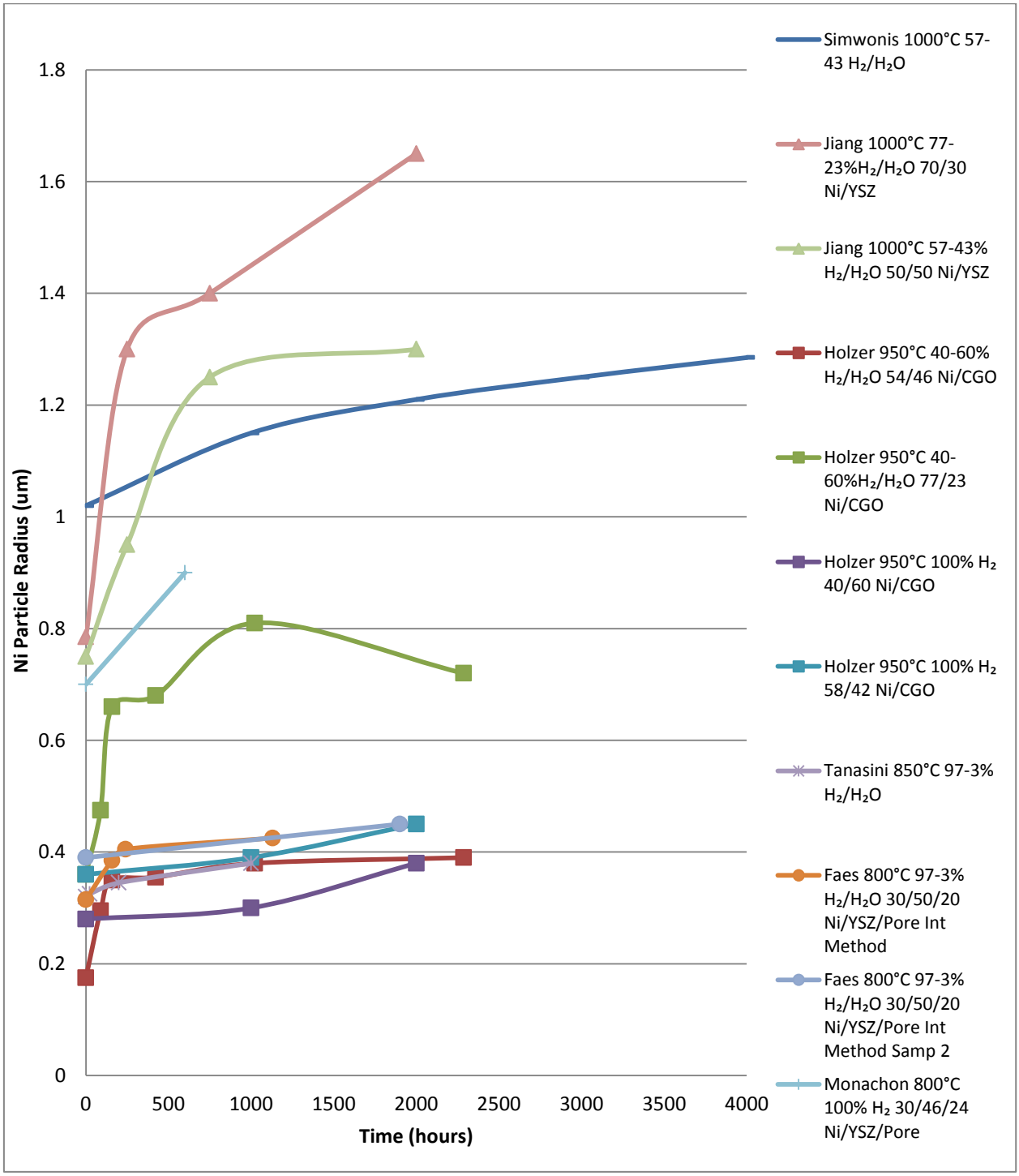

Figure 2-10 Ni radii from various experimental testing of SOFC anodes presented for comparison of Ni particle radius growth rates for given temperature, fuel and material composition over time. See Table 2-7 for references.

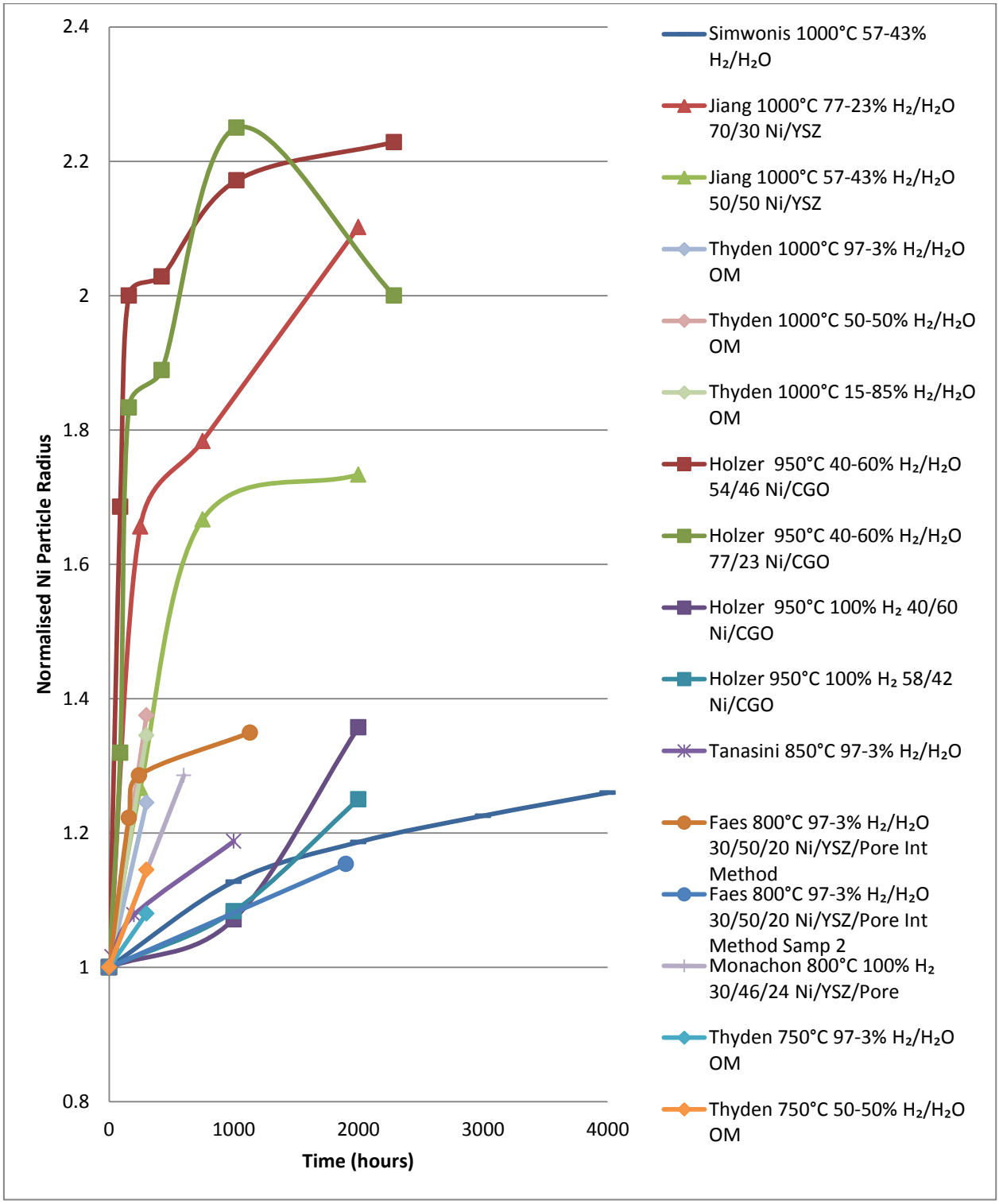

Figure 2-11 Normalised experimental testing of SOFC anodes presented for comparison of Ni particle radius growth rates for given temperature, fuel and material composition over time. See Table 2-7 for references

The normalised data highlights that for some samples with relatively large initial mean radii the actual percentage growth is relatively small over the exposure time. This is especially true of Simwonis' data set [16]. On the opposite end Holzer's [216] high Ni content, high steam (60%) 950°C test results in sizeable increase in normalised radii, with Jiang's [238] high relative steam ratio test values also showing significant increases. It is worth noting that all 3 data sets have relatively high steam contents (i.e. not humidified hydrogen) and high operating temperatures of 1000°C and 950°C.For the high steam content Holzer tests it is also worth noting that a significant loss of Ni volume content was recorded (roughly 40% of the total value), which would have most likely been smaller particles and thus heavily skew the data in favour of a larger relative mean value. Jiang's values saw an increase in Ni content, which could have been down to previously undetectable small particles forming larger ones during testing, leading to a significant increase in mean values. Thyden's [242] high temp (1000°C) high humidity 50% and 85% H_2O show very step gradients, but the relatively short test time of 300h and only 1 data point prevent further analysis.

Ideally, a max mean Ni particle radius would be clearly highlighted from existing data. Due to the variation in initial Ni radii size distributions, the YSZ (or electrolyte) particles, and the porosity, the ability for a specific mechanism to affect the grain growth rate may be impeded/improved. As previously mentioned in the normalised data the highest data sets have mitigating factors which could explain their particularly large increase. Outside of these extremes you see values where a maximum radius value for an "average" Ni-YSZ cell (that is, 50/50 Ni/YSZ with a rough porosity of >20%) could be reasonably similar. Given the suggestion of a set

YSZ grain size and a known porosity, a theoretical max value for the Ni radii could be determined, but as with the nickel oxide powders, the ceramics used in the fabrication process will have a distribution and the sintering will help guide to a desired percolation throughout the sample but not necessarily uniform sizes for the grains.

2.3.2 Nickel Volatisation

Nickel volatisation, as previously mentioned, is a potential mechanism for loss of performance in the anode side of the SOFC. With loss of Ni volume, Ni percolation is lost and thus TPB length will eventually suffer. Whilst the effects of Ni loss are often mentioned in research [221], the exact cause or quantification of this loss is often difficult to describe

.

The Solid Oxide Fuel Cell Integrating Degradation Effects into Lifetime Prediction Models (SOFC-LIFE) project [243] data suggested that as generally agreed for 800°C the overall degradation was the same for samples with high (80%) and low (3%) steam contents irrespective of current drawn (0-0.7A/cm^2). However they found that at 700°C their cells underwent significant degradation in the form of increased resistivity, though surprisingly this was noticeable at lower steam content. Ni weight content was established to have dropped by roughly 5% over 3000 hours at 80% steam, with roughly 4% seen at 3%, though both values followed a similar profile. With the 80% versus the 3% steam content the only notable difference is that the flow rates for steam were 5l/h and 1.03 l/h respectively. Imaging analysis of the

700ºC and 80% sample shows incredibly uniform PSD compared to the 3 other testing parameters at 300h, 1000h and 3000h. Whether this uniformity was a very early response to the testing parameters or to do with the initial microstructure wasn't clear but presents an interesting anomaly. The samples for 700ºC with 3% steam were found to have a very dense inner microstructure compared to the other samples, leading to very different average Ni weight percentages in the dense phase compared to the exterior.

Figure 2-12 shows a comparison of the data for 1000h analysis of nickel mass loss from the samples. Solid lines represent calculations from Image Analysis whilst dot-dash lines represent X-ray fluorescence (XRF) data. 2 sets of samples were investigated for 800ºC and 1 set for 700ºC with 3% and 80% analysed with XRF and image analysis for a total of 12 points. The total weight loss was given in terms of initial starting percentage and then final percentage. This data has then been converted into total relative Ni weight loss. The error margins on much of the data are particular wide in places, which could potentially lead to very different looking plots. However there are a few potential points which can be drawn from the data. All samples are seen to have undergone mass loss. For 800ºC the samples seem to undergo more loss for higher steam contents, which suggests that studies which find higher steam content to lead to faster degradation may be suffering more significant volatisation in these conditions. However at 700ºC the inverse was true for steam content, with the 3% suffering more severely. In the figure the values for 700ºC with 3% have been averaged from the dense and non-dense phases for a (very) rough estimate of the average weight loss. Their data also showed that the rate of loss was significant in the initial 1000 hours, however afterwards it was considerably

slower/negligible, which suggests that like the Nickel which is limited in agglomeration and sintering due to the YSZ backbone, may also have a max percentage of Ni which can be removed from the sample before the energy demand to drive the hydroxide volatisation becomes too high.

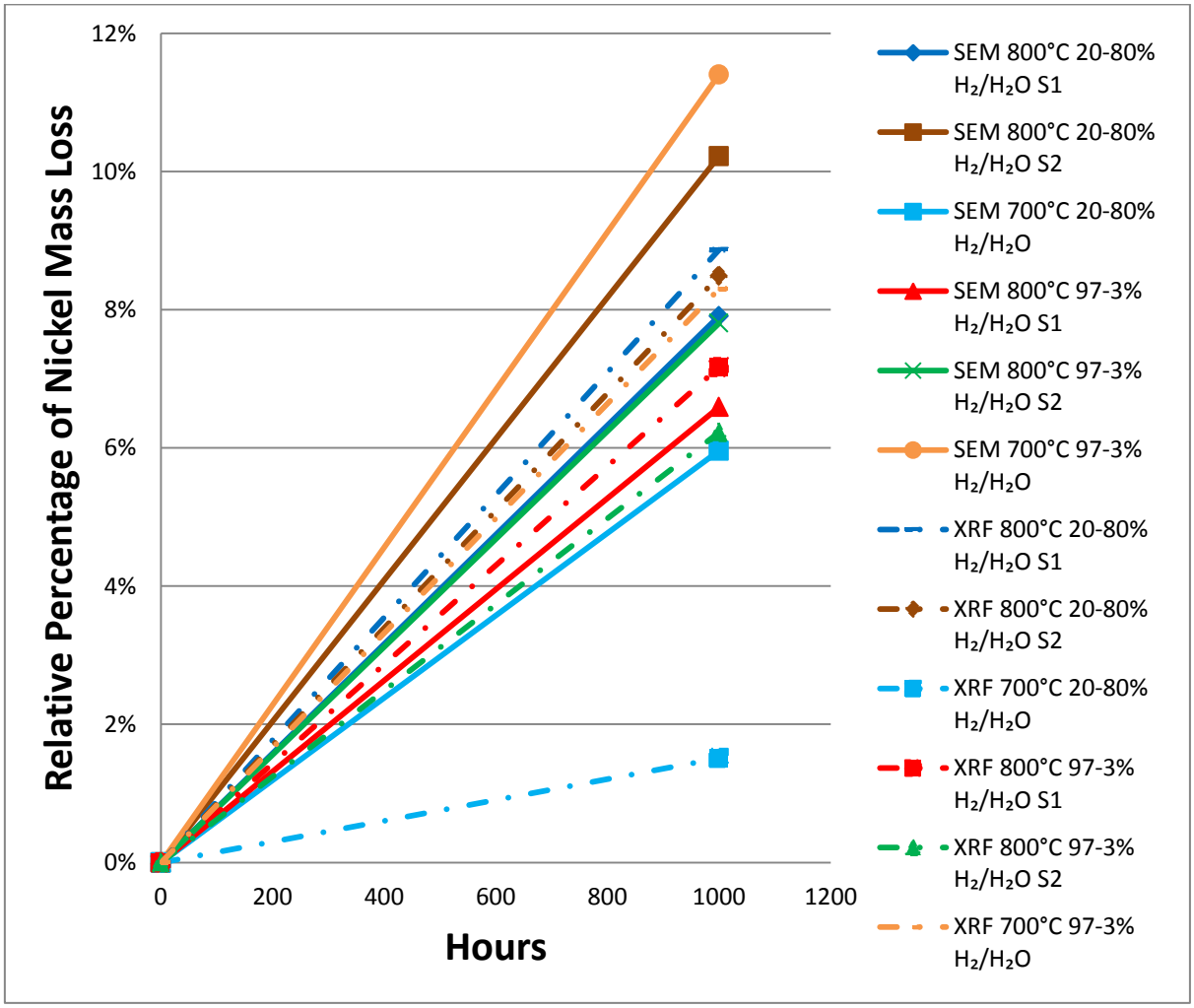

Figure 2-12 Percentage loss of nickel mass over time from SOFC-LIFE data [243] for its given analysis route (XRF or SEM) and respective operating conditions.

Figure 2-13 shows a comparison of SOFC-LIFE data to Holzer et al's [216] data which have reported Ni volatility. It is important to note that Holzer et al have a CGO based ceramic component rather than YSZ, and this was likely the influencing factor in the large quantity volatisation.

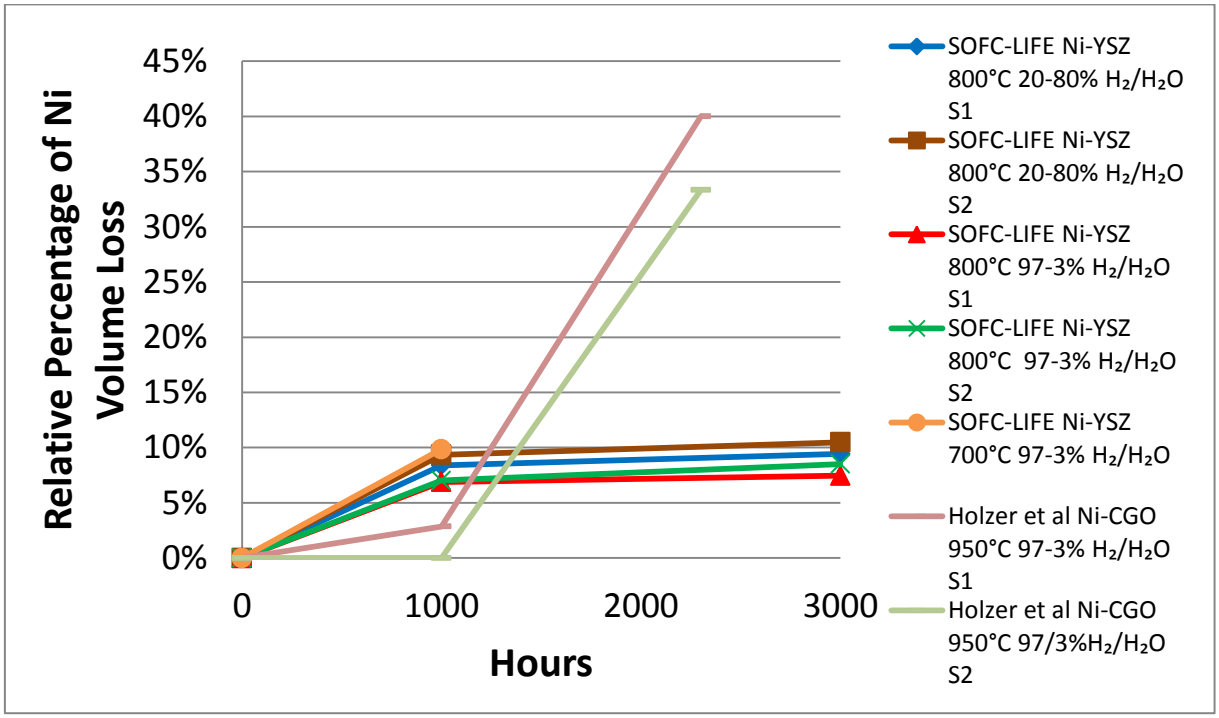

Figure 2-13 Comparison of reported Ni volatility from SOFC-LIFE [243] and Holzer's [216] on Ni volume loss for a given anode composition and operating conditions.

Work done by Chen et al [244] involving Ni-CGO anodes with ScSZ electrolyte cells on cathode supports ran a number of cells through 5 electrochemical cycles to investigate the degradation on their samples. The testing time encompassed a total of 9 hours, but very high current densities (and thus high H_20 levels). Their flow rates were 5.66% H_2 in Ar at 53ml/min, with a pure H_2 run for cycle 5, all at 800ºC. Their

analyses indicates that Ni_2-OH complexes could have been formed due to the high current densities, which can lead to nickel reoxidation, as their research supports, as well as Ni volatisation. Whilst there is a less than uniform loss of Ni from each analysed sample a median value places the total loss at ~14%.

Samples having been subjected to steam reforming mixtures in a 750°C-850ºC temperature range and low to high current densities were also investigated for Ni particle coarsening [236]. The report described a 30% increase in Ni particle size for a 750ºC sample and a 22% increase for 850ºC sample. This was attributed to an estimated loss of 40% of Ni from their 850ºC sample due to volatisation.

2.4 Measurement and Analysis Techniques

Degradation in Ni-YSZ anodes can be determined via a number of different techniques. Often because of the complexity of the systems analysed, a multitude of data extraction methods are used. Visual and electrochemical analysis are regularly used in conjunction with different post-testing techniques. In-situ visualisation of the microstructure is incredibly difficult due to the high operating temperatures of SOFCs

2.4.1 Imaging Analysis (SEM, FIB-SEM, Tomography)

Imaging of samples remains a critical aspect of data collection from testing, and different techniques exist to prepare and present these samples. Once mounted, the images then have to be quantified via state of the art imaging techniques. SEM [245] image formation is dependent on elastic and inelastic interactions. Inelastic

interaction results in primary beam electrons transferring substantial energy to the atoms in question, leading to the generation of secondary electrons (SE) which can be used for imaging of samples. Elastic interactions lead to back scattered electrons (BSE). The back scattered electrons yield is dependent upon the atomic number of the atoms in the sample (thus samples with very different atomic number will show the greatest contrast in the sample whereas similar ones will be harder to differentiate)

Scanning Electron Microscopy (SEM) imaging has for a long time been the basis for imaging of SOFC samples, whether anode, cathode or electrolyte. Sample preparation can be incredibly important for error minimisation in imaging, to ensure the quality of images being taken is accurate for further analysis [240]. Previously there was a shift away from using normal acceleration voltages of 10-20kV commonly used in SEM due to the similar back scattering coefficients of Ni and YSZ (requiring a sputtered coating to reduce the brightness of Ni [16, 246].It became more common for low acceleration voltages (<1kV) to be used [242], which can allow for greater distinction between the phases. Due to the potential variance in experimental procedures used by individual research groups an attempt to present a standardised method was suggested by Holzer et al [216, 247] for determining the change in Ni particle growth. The work covered a number of important aspects of anode investigation such as PSD and suggestions for grey-scaling in microscopic analysis. Different methods for calculation of particle size measurement have been utilised when analysing images [19]. These techniques include Discrete PSD, the Intercept Method and Continuous PSD, as seen in Figure 2-14

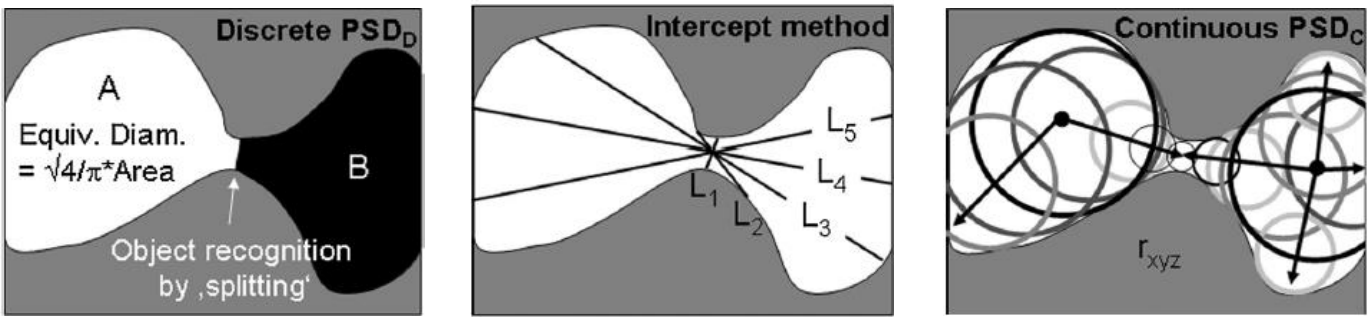

Figure 2-14 Visual description of particle size measurement techniques, highlighting how the Discrete PSD_D, Intercept method and Continuous PSD_C establish the area of pores/particles [216].

SEM only produces 2D images of the intended sample, which, if solely used in measurements and calculations, can lead to errors. This has lead researchers to investigate the use of tomography and 3D reconstruction for producing 3D structures. SOFC analysis has seen a considerable increase in the use of tomographical techniques for detailed investigation of microstructure, with further use in modelling [6, 235, 248-256].

Use of Focused Ion Beam (FIB) technology originally allowed single beam instruments the use of an Ion beam current to allow combined nanoscale milling and imaging. More recently it was used in combination with an ion column and an electron gun to mill and image separately using scanning electron microscope (FIB-SEM). FIB-SEM analysis has been used for a number of years to establish 3D properties of samples [257] Bansal et al [258], and Wilson et al [259] used FIB-SEM on an SOFC in some of the earliest usages for 3D reconstruction. FIB-SEM can be used to build a 3D microstructure to investigate parameters such as the electrical

conductivity and percolation in the cell [249], material fractions, surface areas, particle size and distribution, pore size, phase conductivity, and triple-phase boundary density [260]. Investigations of effects of thermal cycling [261], as well as studying the microstructural changes undergone during redox cycling [252] have also used FIB-SEM Much of the information gathered can be combined with modelling tools to help create a more detailed picture of the in-situ workings of an SOFC. Iwai et al [235] used dual beam FIB-SEM with EDX to analyse a sample to build a 3D reconstruction of the anode microstructure. This was used for TPB density and tortuosity evaluation. The TPB was determined using the volume expansion and centroid methods, and tortuosity was analysed with a random walk calculation and the Lattice Boltzmann method. In both cases the difference between both values was ~3% and both were deemed equally suitable for calculations of the sample parameters. Their sample sizes (roughly 19 x 8 x 6 μm) where determined to be too small for conductivity calculations for Ni or YSZ.

The Imperial College fuel cell group has successfully built up research in the field of FIB-SEM and tomography with SOFC samples and materials [255]. Their research centre had issues recreating the work done by Wilson et al [259], specifically due to specimen charging, image shadowing and re-deposition of sputtered material. All of these can lead to erroneous interpretation of the image so they developed their FIB lift-out technique for both single and dual beam instruments. A number of limitations had to be overcome such as Ni twinning phenomena which presents Ni in such a way that Ni and YSZ greyscale histogram data can overlap. Single and Dual beam analysis is possible, though single beam analysis suffers from some manual operation limitations, unlike dual beam. Multiple sample volumes should be taken

from the bulk to ascertain an accurate measurement of the overall microstructural distribution [254]. Improvements in the imaging process [262] allowed for movement away from features such as their lift out techniques, allowing for completely automated processes. Combination with electrochemical simulation has further increased the predictive capabilities of their analysis. Shearing [253] also found that H_2 concentration had seemingly little impact compared to temperature in terms of ASR resistance.

The nanotomographical studies done on SOFC anodes can help understand the distribution of particles in the functional layer vs. substrate [263]. Nano computer x-ray tomography (CT) has been used as an analysis technique, and has a particular advantage over FIB-SEM due to its non-destructive nature [264]. Earlier work by Izzo et al [265] investigated half-cells involving porosity from voxel counting and tortuosity from Laplace equation solving used in modelling mass transport and electrochemical reactions at pore scale. Work was followed up in 2010 by Grew et al [266]. An example of particularly relevant work by Galinski et al [267] covered Ostwald ripening in Ni/CGO, in the temperature ranges of 500-1100°C. Specific investigation into the effects of temperature alone on the Ni grain coarsening, suggested nearly a 50% increase in average grain size (0.44 to 0.66 μm) over 500h.

Analysis of Cathode microstructure using tomography has also been undertaken [268] to obtain parameters such as tortuosity, surface area and volume fractions which has seen further development with finite element modelling (FEM) using COMSOL®. Analysis of mixed ionic/electronic conducting (MIEC) materials has applications in anode materials (especially Perovskites). Similar analysis can be

done on both electrodes such as correlating three-dimensional microstructure and polarisation resistance [269].

2.4.2 Parameter Extraction for Model Development

With SOFCs, certain parameters are difficult to obtain, such as PSDs, or potentially face accuracy issues with common place techniques such as mercury porosimetry (which struggles with very small pores). Often, more than one technique is available for establishing these values, either experimentally or through modelling.

2.4.2.1 TPB Calculations

Kenney et al [270] worked on cathode microstructure using two different techniques for establishing TPBs with percolating networks. A grid based counting technique and an analytical technique. The grid based technique created a 3D Cartesian grid over the structure and counted contacting edges for LSM/YSZ/pores which were part of percolating networks. So a voxel square with edges contacting two phases that were not its own were measured in the xy, xz and yz directions, summed and then these values were compared against the relevant particles to determine if they were part of a percolating network to give the TPB length. This technique has also been subsequently used by a number of other authors [248, 249]. The analytical technique determined TPBs through use of the known values of their coordinates in the system and subsequently determined the availability of TPBs in percolating networks. The analytical technique assumed that all pores belonged to a percolating network. This

was based on data showing that the porosity was 99% percolating in volume fractions of 25% porosity and above.

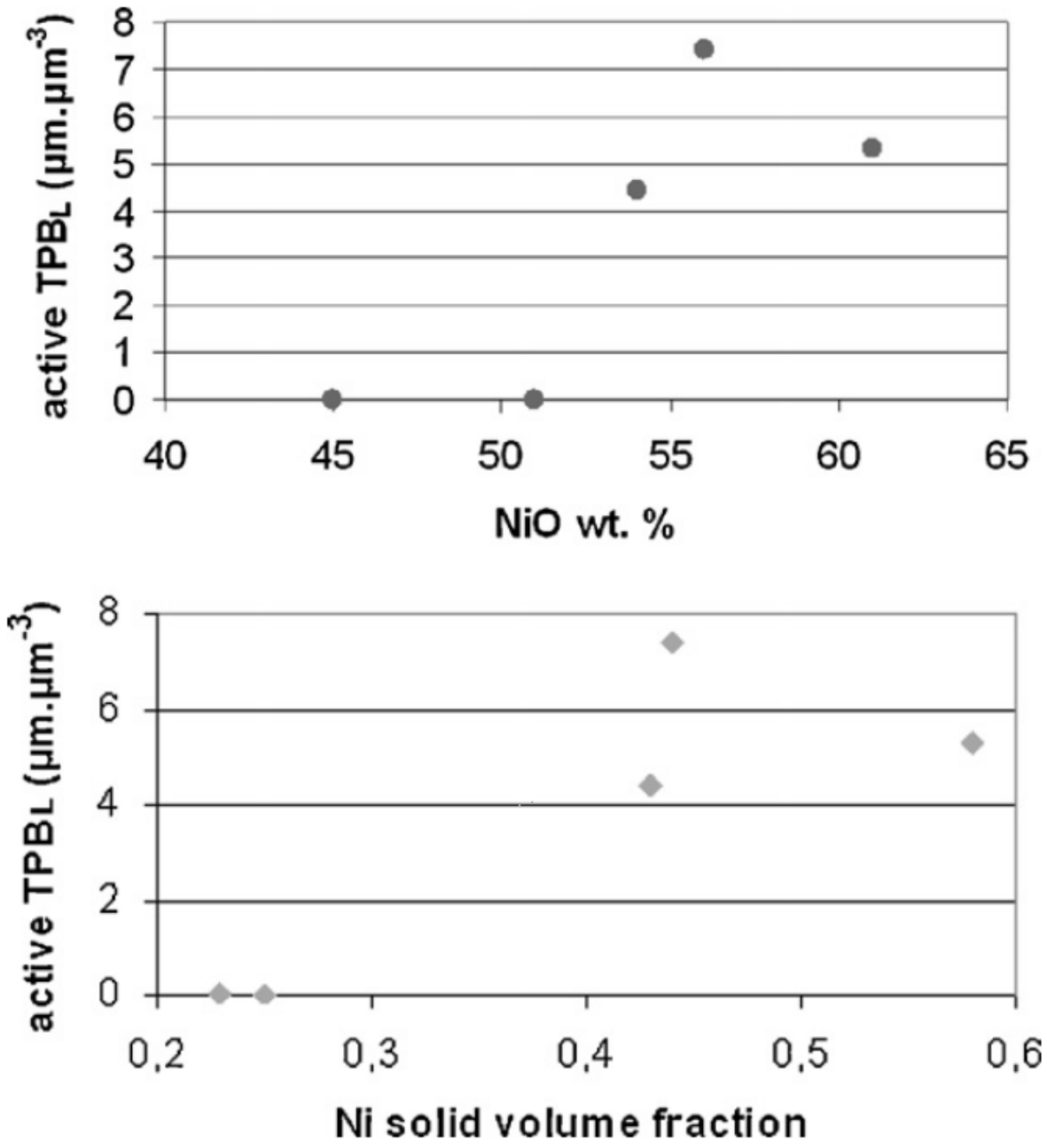

Figure 2-15 Values for Active TPB lengths (in µm µm^{-3}) based on Ni volume fraction and NiO Wt%, highlighting their effect on total percolation in the microstructure [249].

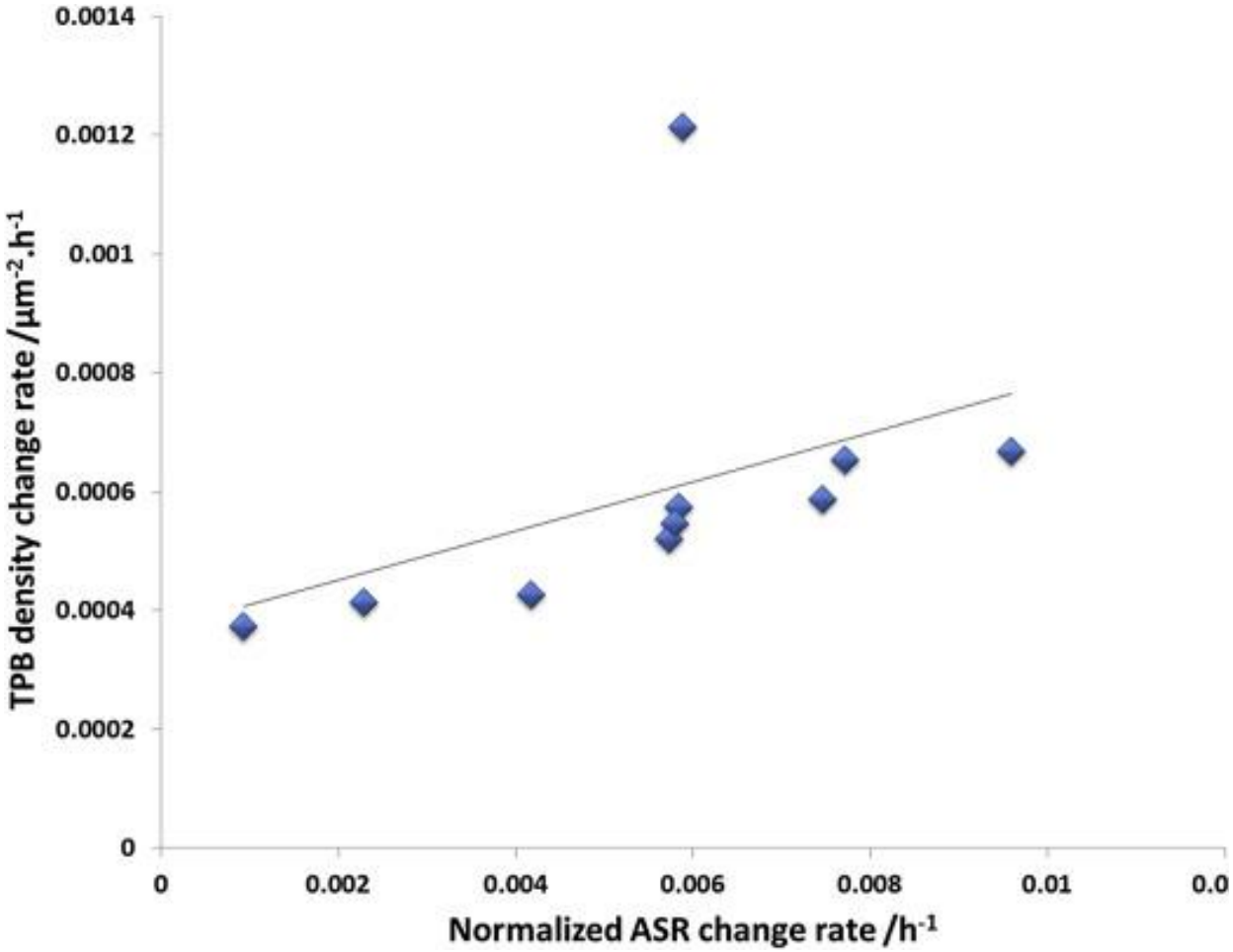

Figure 2-16 Chart comparing the rate of change of normalised ASR against the change of TPB density [221]. The outlying value is due to a poor choice of sintering inhibiter compared to the other values used in this paper.

More recently Khan et al [221] utilised their calculations to determine a link between the ASR and the TPB density change thus allowing them to predict the lifetime of the cell, as seen in Figure 2-16. They also used a technique with energy-dispersive X-ray spectroscopy (EDX) for imaging the respective phases in the anode layer. The TPB density was determined over 7x7 pixel areas in their images, and the total number of TPBs in the area was used to determine the TPB density. An outlying

value is present in the graph but otherwise shows a clear trend for increasing ASR change with TPB change.

2.4.2.2 Porosity

Dealing with porosity in these investigations can be done in a number of ways. Some authors have simply used a rough value of 1.0 - 2.6 μm as the value for average pore size [271] [272] , which appears to be a reasonable approximation for their studies but can lead to inaccuracies where used to determine other properties. Cannarozzo [273] et al determined average pore size as a function of particle size and volume fraction. When the Knudsen diffusion values, which is when the scale length of the system is equal to or less than the mean free path of the particles travelling through the system, fall into the transition regime diffusion (which is when the length scale is comparable to the mean free path of the particles and where a high frequency of collisions with pore walls and other molecules occur), the Bosanquet relation is best used to calculate the diffusion coefficient in the pores. The relationship combines the Knudsen $D_K^{-1}$and binary mixture diffusion D_{12}^{-1} coefficients, as seen in Equation 2-3. For hydrogen diffusing through very small pores, there may be circumstances where the free molecular flow regime dominates, and the Bosanquet relation is not necessarily the best option,

$$D^{-1} = D_{12}^{-1} + D_K^{-1} \qquad \text{Equation 2-3}$$

Pore percolation is the percentage of open porosity versus the total porosity. The open porosity allows a complete path for gas molecules to travel. Whilst this path

needs to reach the electrode fuel domain the inverse (i.e. the electrolyte surface) is not necessarily mandatory for open porosity. The gas simply needs to be able to reach an active TPB site for utilisation. This is important when analysing the imaging for samples as it can lead to over estimates in TPB density, as not all TPB points are percolated sufficiently in electronic, ionic and mass transportation pathways.

Tortuosity is related to pore size and can be described as a retardation factor to flow in porous media [274]. This value is important for calculations such as effective diffusivity and permeability, which are important values for comprehensive models describing fuel cell operation. A number of techniques can be used depending on available information to determine the tortuosity in the cells. A homogenisation approach/technique, which produced averaged properties for real material with complex geometry and anisotropic properties, has shown to give reasonable results [249], whilst the Lattice Boltzmann Method (LBM) is commonly used and is viable for SOFC analysis [275]. However, Iwai et al [235] compared a random walk method and LBM and found they gave similar tortuosity values (less than ~3% difference).

Work by Zalc et al [276] highlighted that tortuosity factors are independent of the diffusion mechanism for most void fractions when an equivalent Knudsen diffusivity is correctly defined. By using a more rigorous Knudsen length scale a more accurate method for determining of tortuosity factors is possible.

2.4.3 Modelling

Modelling of SOFCs can be done in 1D, 2D, 3D as well as in a number of alternative computational methods. It can cover simply calculations for fuel consumption down to TPB boundary calculations and nano-scale chemistry. Anode degradation modelling often aims to incorporate the change in Ni particle size and location through sintering, agglomeration, coarsening and volatisation into polarisation resistance changes and thus performance degradation. This involves understanding changes in porosity due to Ni transportation as well as the percolation loss in the anode. YSZ as a ceramic component is generally modelled as inert for calculation purposes, which for <900°C calculations appears to be an appropriate assumption [61]. Perhaps one of the earliest degradation models was created by Simwonis et al [16] which derived equations for Ni particle agglomeration relative to operating conditions based on their microstructural analysis. Following on from this work Vassen et al [237] developed a more in-depth model to try and predict Ni particle behaviour In the anode. However due to a lack of readily available data to compare against, these models were specifically designed to work with the limited data they had at the time. Due to the variability in initial microstructure, cell composition, fuel composition operating conditions, as well as relatively small but potentially highly influential issues such as minor containments in the cell or fuel streams, a wealth of data is necessary for any one model to likely accurately predict all or most fuel cell degradation behaviour.

Nakajo et al's [277-281] detailed work on SOFC stacks models multiple facets of SOFC degradation, incorporating thermomechanical, electrochemical and operational degradation. Anode degradation modelling is based on a modified model

of Vassen's work, and is incorporated into a percolation model to determine TPB length and thus electrochemical performance on the anode side.

A study conducted by Chen et al [282] focussed on the development of a functional model for Ni coarsening in anodes. Their model investigates the possibility of limited YSZ mobility and complete immobility. The latter is found to match their experimental data better. It is found that the TPB contact angles can have a strong effect on microstructural evolution. In particular, reducing the contact angle of Ni on YSZ yields less TPB reduction. This is due to the smaller Ni-YSZ interfacial energy available. Work using a level set method to help characterise the three dimensional structure can be achieved with FIB-SEM reconstruction [283]. From the reconstruction the method has estimated surface tension forces from the calculated mean contact angles. The contact angles determined varied from those in Chen et al's work, especially for YSZ and pores as these had large standard deviations.

Various work has been done on agglomeration kinetics in SOFC anodes, such as the quantitative mode by Gao et el. [284]. It uses Fick's law of diffusion for the transport of the Ni particles, with the Gibbs-Thomson relation for vacancy concentration and coordination number theory for nickel percolation. Other analysis of SOFC anodes has been achieved through the use of phase field modelling to help develop the microstructure in the anode. Work done by Abdeljawad et al [285] built on previous studies [286] and using data from a number of sources [287] for values and information on SOFCs was used in Ni-YSZ anode modelling. In their opinion cells with a particle radius for YSZ equal to or less than 0.5um and a particle radius for Ni less than YSZ will last longest, assuming the YSZ radius remains constant. Particle

size distributions remain an important aspect of analysis in modelling. Some work [270] has suggested that dealing with a wide range of particle size distributions rather than a single average value can help prevent potential errors, especially with pore volume measurements. BET adsorption measurements and mercury intrusion porosity measurements must be extremely sensitive in order to measure the low surface area and pore volumes in anode microstructures.

Sanyal et al [288] developed particle-resolved simulations for prediction of electrode conductivities. The work was completed through two models, a discrete element model (DEM) and a random particle packing model. These models would generate microstructures and similarly to work done by Chen et al [289] in terms of percolation theory. Effective conductivities based on percolation theory and coordination number can be evaluated from Equation 2-4, where σ_m^{eff} is the total effective conductivity, σ_m^0 is the total bulk material conductivity, ϕ_g is the porosity, ψ_m is the volume fraction of m material and P_m is the percolation probability of material m. The equation is obviously dependant on the value of the Bruggeman factor μ, and in the work done by Sanyal et al they discuss the effects of the Bruggeman factor, highlighting that the more commonly referenced value of 1.5 may be too low, and thus overestimate the effective conductivity for the electrodes. The study recommended a value of 3.5 which they validated through comparisons with Iwai et al [235] and Wang et al [290] which both felt the value of 1.5 was less suited for their models.

$$\sigma_m^{eff} = \sigma_m^o\left[\left(1-\phi_g\right)\psi_m P_m\right]^{\mu} \qquad \textbf{Equation 2-4}$$

Also of note was their evaluation of the coordination number. In their work the simulations run resulted in an averaged value of 6.7 for $\bar{Z}$, which is slightly higher than the more commonly referenced value of 6. The value represents the number of contacts between the particle in a randomly packed bed model and other particles. It is used for modelling of percolation and other predictive parameters such as conductivity.

Certain models have attempted to make use of the detailed reaction chemistry from studies on patterned electrodes such as that by Mizusaki et al [195, 197]. Computational models to describe the behaviour at the TPB layer in SOFC patterned electrodes have been investigated [291, 292]. They encompass the electrochemistry, transport and elementary chemistry. Values generated in their research are some of the most detailed covering the chemistry inside an SOFC anode.

Wang and Atikson [293] have looked at modelling the microstructural evolution through the use of Cellular Automaton (CA), which allows for the prediction of microstructural changes based on reduction of energy levels. The work highlights that at least in the early stages the wettability of Ni on YSZ is heavily defining on the microstructural evolution, where better wettability leads to slower coarsening in the cell. The wettability of the Ni particle is the degree to which the adhesive force of the YSZ causes the Ni to spread across its surface whilst the cohesive force within the Ni particle looks to keep away from the YSZ surface.

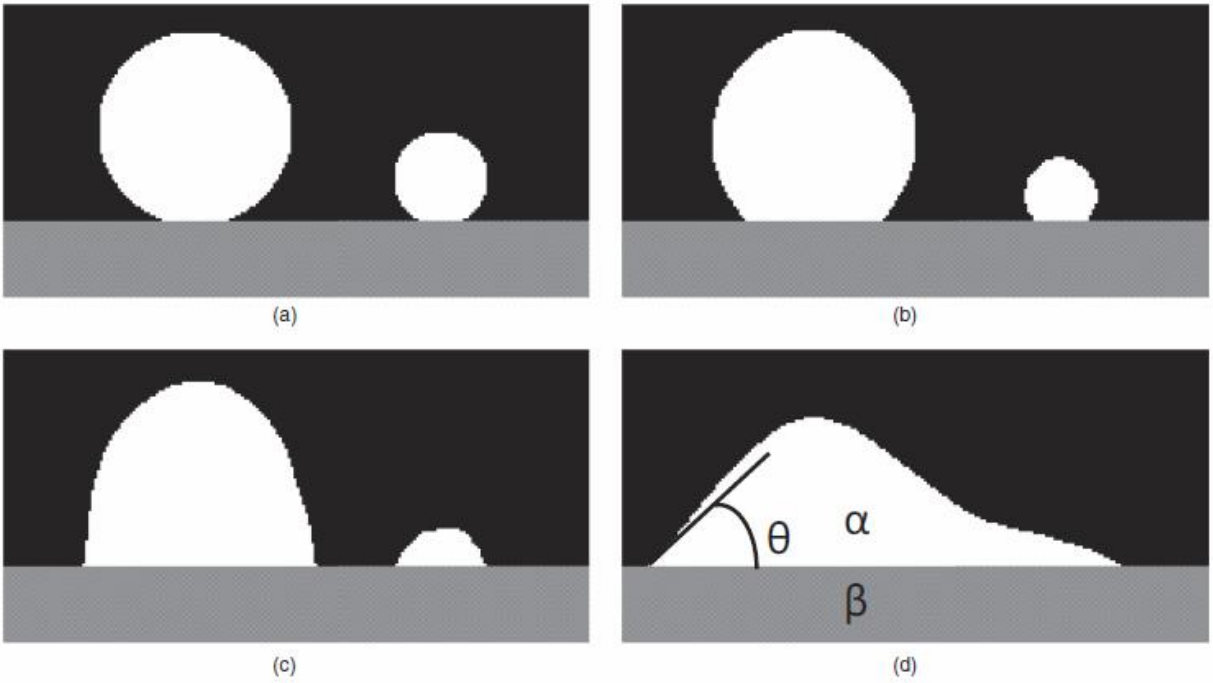

Figure 2-17 Ni wettability on YSZ surface shown through two coarsening particles [293]. As the particles are exposed to high temperatures they deform and eventually combine on the wetting surface of the YSZ, here represented by the light grey surface.

CHAPTER 3 Experimental Set-up and Methodology

A rig has been designed and constructed to obtain data regarding Ni-YSZ sample transformation over a variety of operating conditions. It is designed to operate the samples in only temperature and fuel (gas exposure) under varied conditions. This rig is operated inside of a furnace supplied by Vecstar, and is henceforth referred to as the Vecstar rig. A quartz tube and sample holder was designed for holding a number of samples simultaneously in the given testing environment. The quartz tube allows contained exposure to high temperatures and air or hydrogen and steam mixtures. Figure 3-1 shows the tube and furnace without the mass flow controller system.

Figure 3-1 Quartz tube and furnace for anode sample testing. Fuel gas enters from the left hand side, passes over the samples which are resting across a alumina plate.

Hydrogen and nitrogen gases are delivered via Mass Flow Controllers (MFCs) whilst water is delivered to a Cori-flow meter (through a filter to ensure purity) and converted to steam in a Bronkhorst Controlled Evaporating Mixer (CEM) alongside the hydrogen and nitrogen which is then fed into the quartz tube shown in Figure 3-2. The gases travel over the samples where they are reduced and the remaining hydrogen and steam are evacuated from the outlet to a water trap and then the atmosphere.

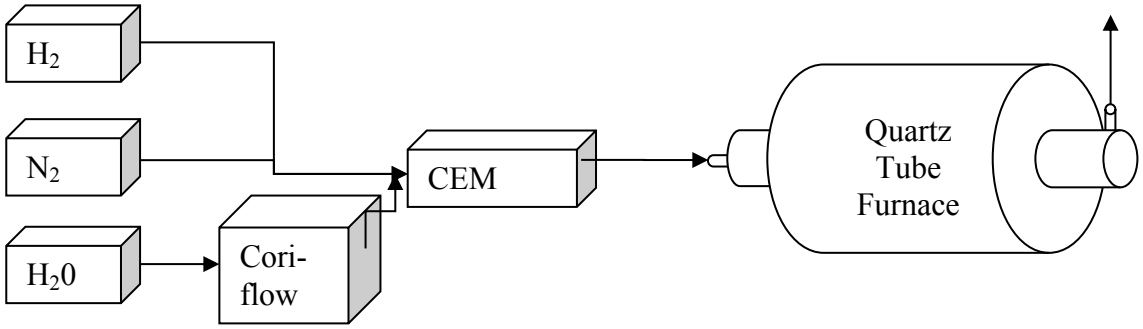

Figure 3-2 Schematic drawing of rig with MFCs, CEM and Cori-flow delivering fuel to the quartz tube rig. Nitrogen purges the system on start-up, after which hydrogen (and possibly steam) pass through the controlled evaporating mixer and into the quartz tube sitting inside of a furnace.

3.1 Experimental Set-up

Multiple 100 cm^2 planar anode supports with functional layer were purchased from Ningbo Institute of Materials Technology and Engineering (NIMTE). These Ni-YSZ samples were then segmented into roughly 1 cm^2 sections with a diamond saw. Care

was taken to slice the samples to be as uniformly sized as possible. These samples were rinsed with ethanol and then air dried before being placed into the quartz tube. The 10x10cm square planar samples produced a large number of smaller sections, and batches of 8 were used for each parameter test. The quartz holder inside of the tube was approximately 30cm long and supported an alumina plate on which the samples rested along the length of the holder tube. The holder section also attached to the quartz plug on one side of the tube itself to create the seal, thus only the inlet and outlet ports allowed fluid transport. Once the samples were secure, insulation was placed around the rims on the inlet and outlet sides to help ensure temperature control. Thermocouple measurements were taken at various locations within the furnace to confirm constant temperature within the location of the samples; however they were not taken within the tubes whilst operating with gas as those temperatures due to the risks of explosion with hydrogen.

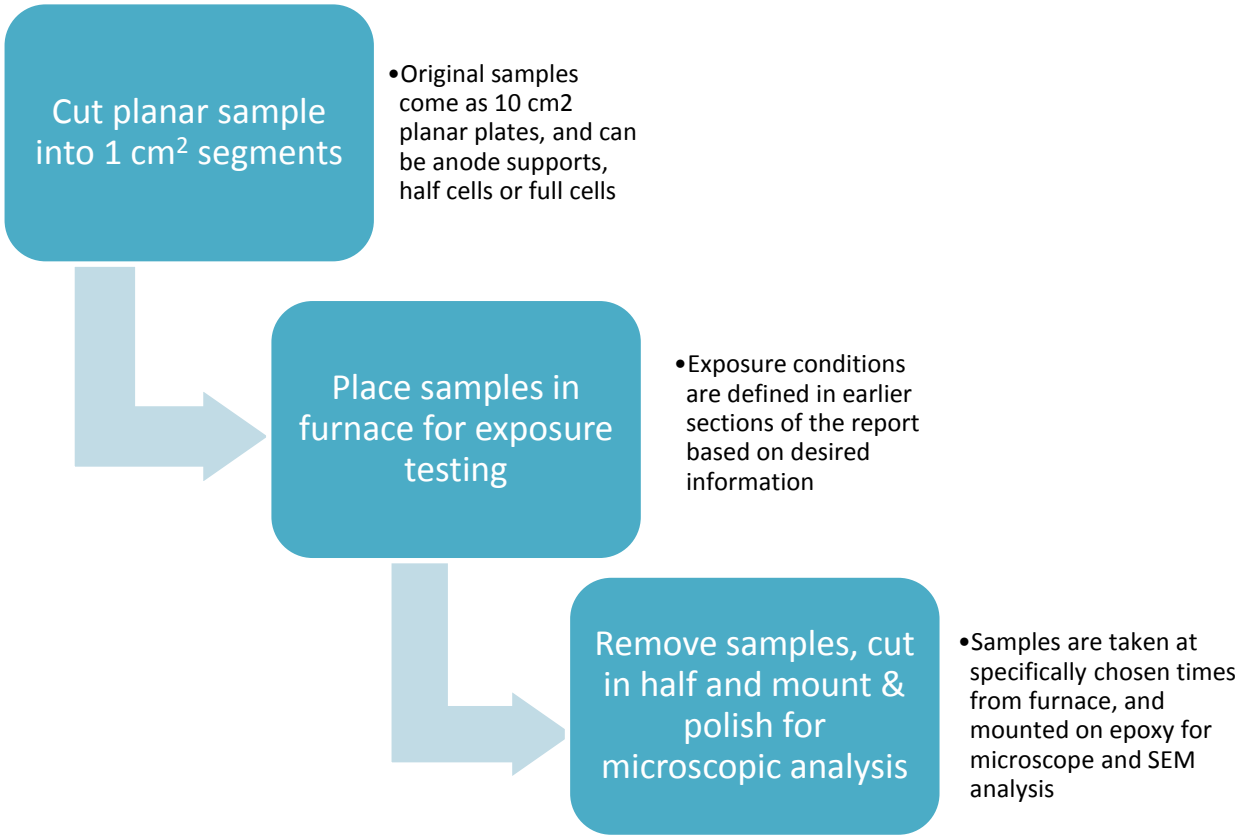

Figure 3-3 Process pathway for samples showing the procedure of preparing for testing and analysis. This includes initial segmentation, testing and removal and mounting for imaging.

For temperature only dependant testing the samples were exposed only to air as well as initially reduced in a hydrogen environment and then exposed to nitrogen for a comparison of NiO versus Ni growth rates. Samples exposed to air were run for similar lengths of time as those run in hydrogen. Samples reduced in hydrogen then exposed to nitrogen were run for 4 and 24 hour periods only. For gas and temperature dependant testing the samples were exposed to various levels of steam and hydrogen in the furnace for set temperature levels. Virgin samples were kept

aside from the initial batch of segment planar cells and prepared with the exposed samples for analysis as shown in Figure 3-3. Time exposures of 250h, 500h, 750h and 1000h were chosen to investigate the microstructure changes. Steam contents of 0, 3, 50 and 80 volume percent were chosen, as these presented examples of lower steam content more commonly seen in experiments (3%) to be compared to extreme steam contents (80%) which might highlight processing procedures for accelerated testing. Volume of gas was adjusted for 100ml/min delivery at all set-ups. Temperatures of 700°C, 800ºC and 900ºC were chosen as shown in Table 3-1. Two samples were taken out of the furnace for each interval, and 1 set of complete runs was done for each temperature/fuel combination. The furnace was ramped up at 10°C per minute which normally results in a roughly 1 to 2 hour heat up period. Samples were exposed to nitrogen during ramp up and then subsequently exposed at their operating temperature, once stable, to hydrogen for reduction of nickel oxide for 4 hours before the 250h interval commencement. After reaching the specified time interval the furnace was gradually coole down over approximately 8 hours; when below 100°C the hydrogen gas was switched off and once sufficiently close to room temperature the quartz tube would be opened and the two samples taken from random locations on the plate would be put into petri dishes for subsequent cutting, mounting and polishing. Then the remaining samples would be returned to the furnace as previously described and the process would continue until the 1000h sample was completed and a new batch would commence. Figure 3-4 Shows 8 samples after the initial 250h period reduced and on the alumina plates supported on the quartz holder.

Table 3-1 Chart for intended experimental runs of NiO samples for a given temperature and H_2/H_2O fuel composition. More-extreme ends of the spectrum were selected for testing to see results with limited testing runs possible.

Temp (°C)/ Fuel (H_2/H_2O)	**100%**	**97-3%**	**50-50%**	**20-80%**
700	X	N/A	N/A	X
800	X	X	X	X
900	N/A	X	N/A	X

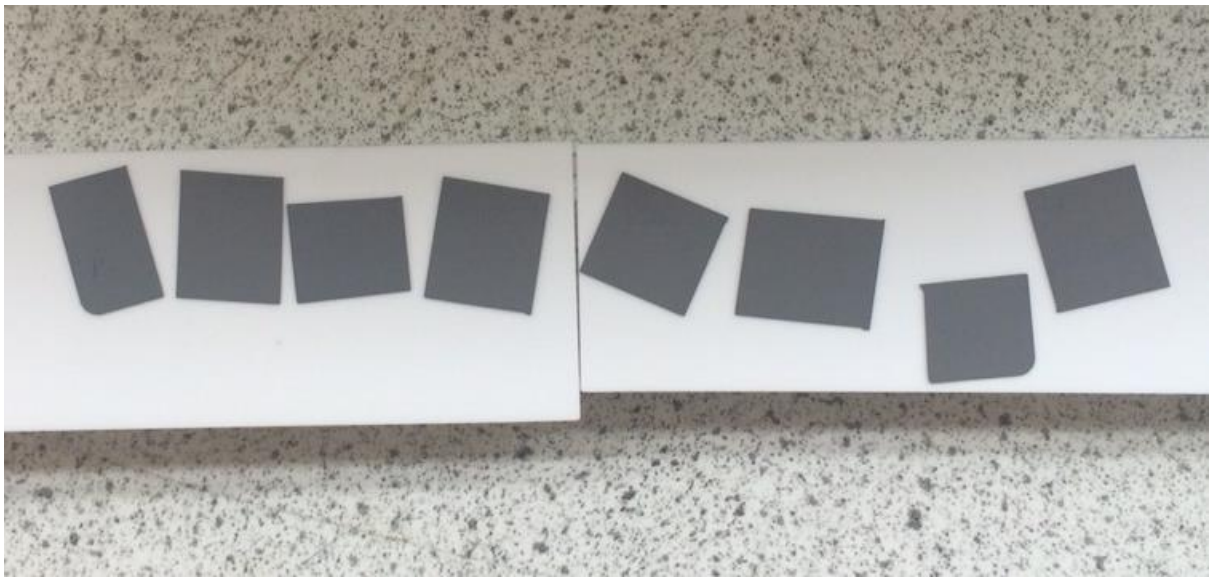

Figure 3-4 Example of samples having been exposed for 250h at 800°C to 97/3 H_2/H_2O prior to having 2 samples taken for analysis and subsequently being returned to the furnace for the other samples continued exposure.

Comsol® modelling was used to establish whether a uniform testing environment was present in the tube to provide repeatable data. Mass flow, heat transfer and fluid velocity were inspected to see if all cells in the sample holder would experience similar conditions. Figure 3-5 shows that the temperature distribution in the furnace accurately provided the heat specified in the area of the tube where the holder was situated. Inlets and outlets on the tube were modelled to be at room temperature, whilst the inside section was deemed insulated. Clearly the insulation placed around the furnace entrance and exit would not perfectly trap all heat in the furnace but neither would the sections outside of the furnace be at room temperature once operating and thus this minor inconsistency can be ignored. This is backed by the previously mentioned thermocouple tests. Fluid transport is shown to be uniform through the quartz for the 100 ml/min flow rate ensuring anode samples indeed received the required levels of steam and hydrogen.

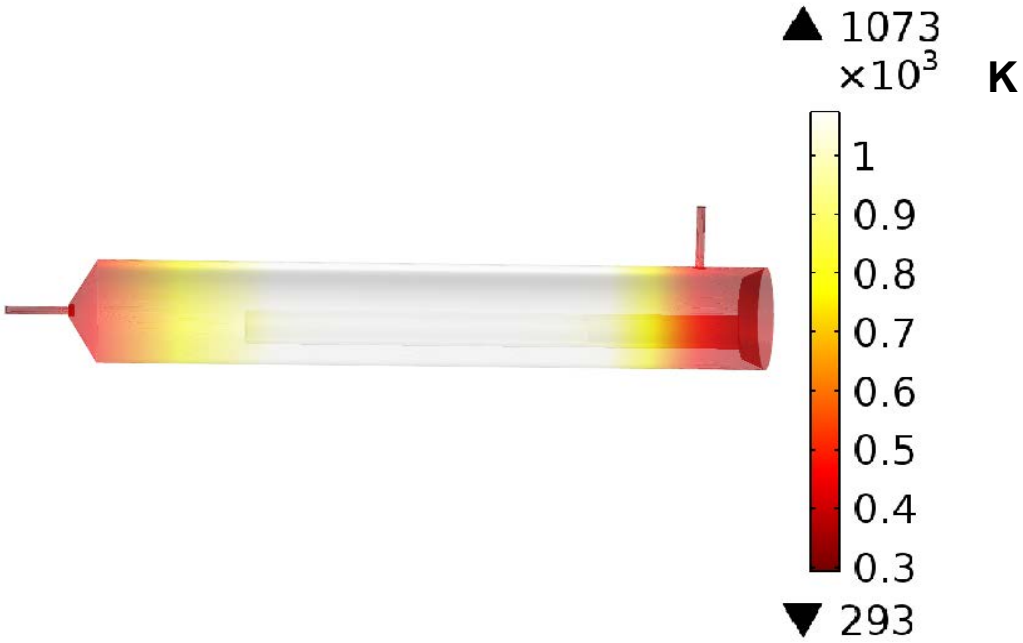

Figure 3-5 Thermal distribution in the quartz tube furnace with pure hydrogen flowing at 100 ml/min at 800ºC. Inlet and outlets are room temperature, whilst the section of the furnace where samples are located is at the intended operating condition.

3.2 Sample Preparation and Polishing

The standard procedure for preparing samples involves sectioning, mounting, grinding and polishing [183, 240]. Samples needed to be analysed cross-sectionally to allow for gradients or changes in microstructure to be seen, and so a diamond saw was used to segment the samples for subsequent mounting in epoxy resin EpoThin™ Epoxy 2 Resin and Hardener. Sectioning involves slicing the sample to produce the cross sectional area of interest, which has been achieved cutting with a diamond saw blade. Grinding and polishing are both achieved on the Buehler rotating

pad, and represent different levels of finish, with grinding being up to ~5 μm according to Buehler's manual and polishing down to 0.05 μm.

Table 3-2 Comparison of different material polishing guidelines from Buehler polishing manual. The abrasive size relates to the coarseness of the polishing pads, load the pressure applied, as well as rotational speed and time.

Zr				Ni				Polymer/Resin			
Abrasive size	Load (N)	RPM	Time	Abrasive size	Load (N)	RPM	Time	Abrasive size	Load (N)	RPM	Time
45μm	36 N	120-150	Until flat	30 μm	22 N	200-300	Until flat	P400	18 N	200-250	Until flat
9μm	27 N	120-150	04:00	9 μm	27 N	100-150	05:00	P600	18 N	200-250	00:30
3μm	27 N	120-150	03:00	3 μm	27 N	100-150	03:00	P1200	18N	200-250	00:30
1μm	44 N	120-150	05:00	1 μm	27 N	100-150	02:00	P1500	18N	200-250	00:30
				0.05 μm	27 N	80-150	02:00	3 μm	22 N	100-120	04:00
								0.05 μm	13N	100-120	04:00

Buehler provides their polishing equipment with a manual for suggested polishing procedures for various materials. Included are guides for specific materials as seen in Table 3-2 Ni-YSZ cermets are a combination of these materials, and whilst mounted in the resin represent a trio of quite different materials. A suggested polishing procedure which accommodates the hardness of the Zr materials with the smaller particle size and softness of the Ni/Polymer was devised from these

guidelines. Initial grinding at 125μm and 70μm were done until the sample was fully exposed from the resin, and then gradually worked down through 45, 15, 9, 3, 1, 0.3 and 0.05 μm. Times were similar in length to those suggested in the Table 3-2, with an increased amount of time spent polishing at finer grades. A mechanical polishing arm was used to apply pressure and rotation to the samples. Some sample may have required longer periods due to an insufficient finish in some cases.

Initially an in-house polishing and grinding procedure was used which had been successful with other SOFC samples and thus deemed a useable starting point. In the process of attempting to successfully polish a reproducible and comparable finish, issues surfaced wherein a seemingly dense middle layer was formed. This issue was apparent on some samples and to varying degrees, as seen in Figure 3-6. These images are taken via an optical microscope (Zeiss AXIO Lab.A1) with a Q-Imaging Micropublisher 3.3 RTV camera along with ImagePro image capturing software. When this anomaly was originally noticed a list of potential causes was outlined and analysed to confirm or eliminate these items.

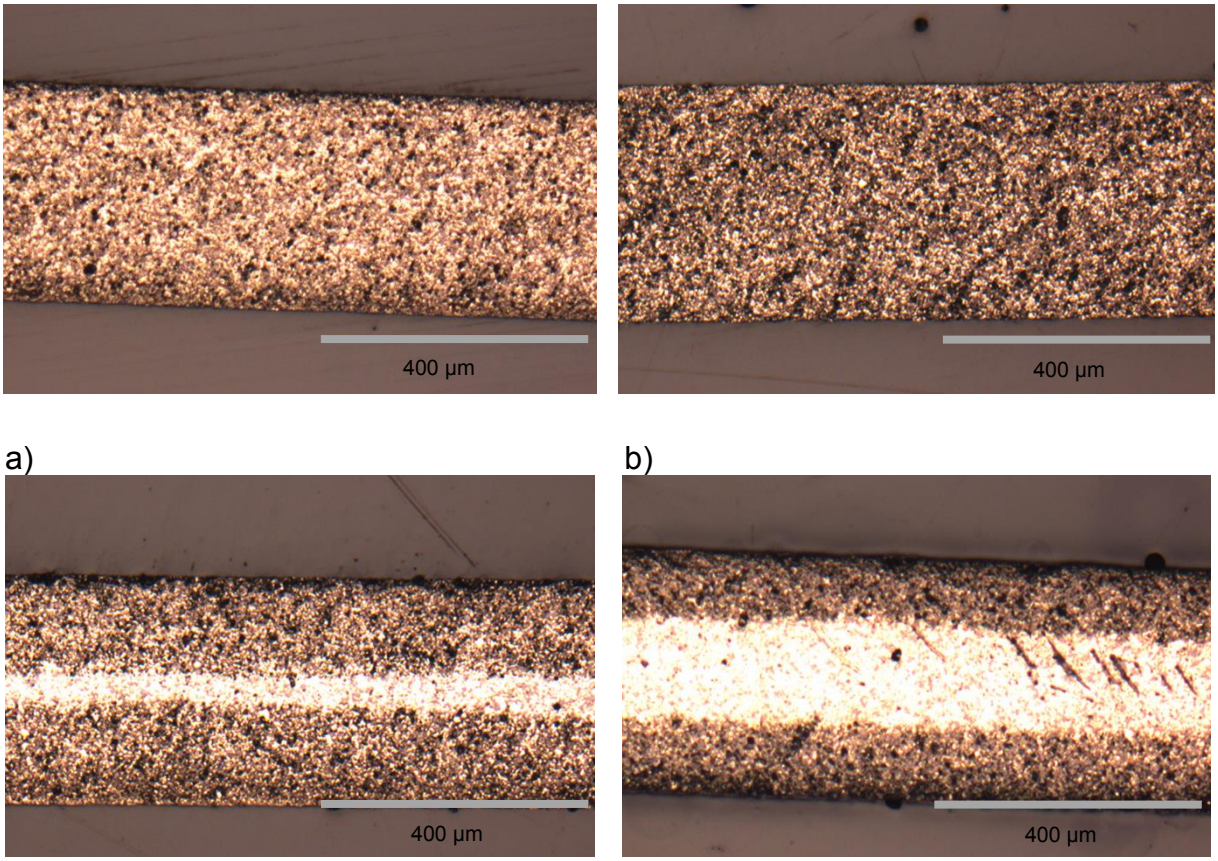

Figure 3-6 Comparisons of varying degrees of dense layer formed by the same polishing procedure of similar/same batch, cutting procedure, testing environment and mounting. Samples were tested at 800°C in 100% H_2 for a) 250h, b) 500h, c) 750h and d) 1000h respectively. Images taken via optical microscopy.

Potential causes of dense layer

- Feature either not removed or created through disproportionate allocation of pressure to samples during hand polishing
- NiO layer forming in edge or centre of samples
- Ni diffusion through sample via steam –Ni-hydroxide transportation.

Whilst it was quickly determined that the brightness in the bright field of the optical microscope was caused by a lack of porosity/high surface density of Ni/YSZ rather than due to a different phase, EDX was undertaken to be certain.

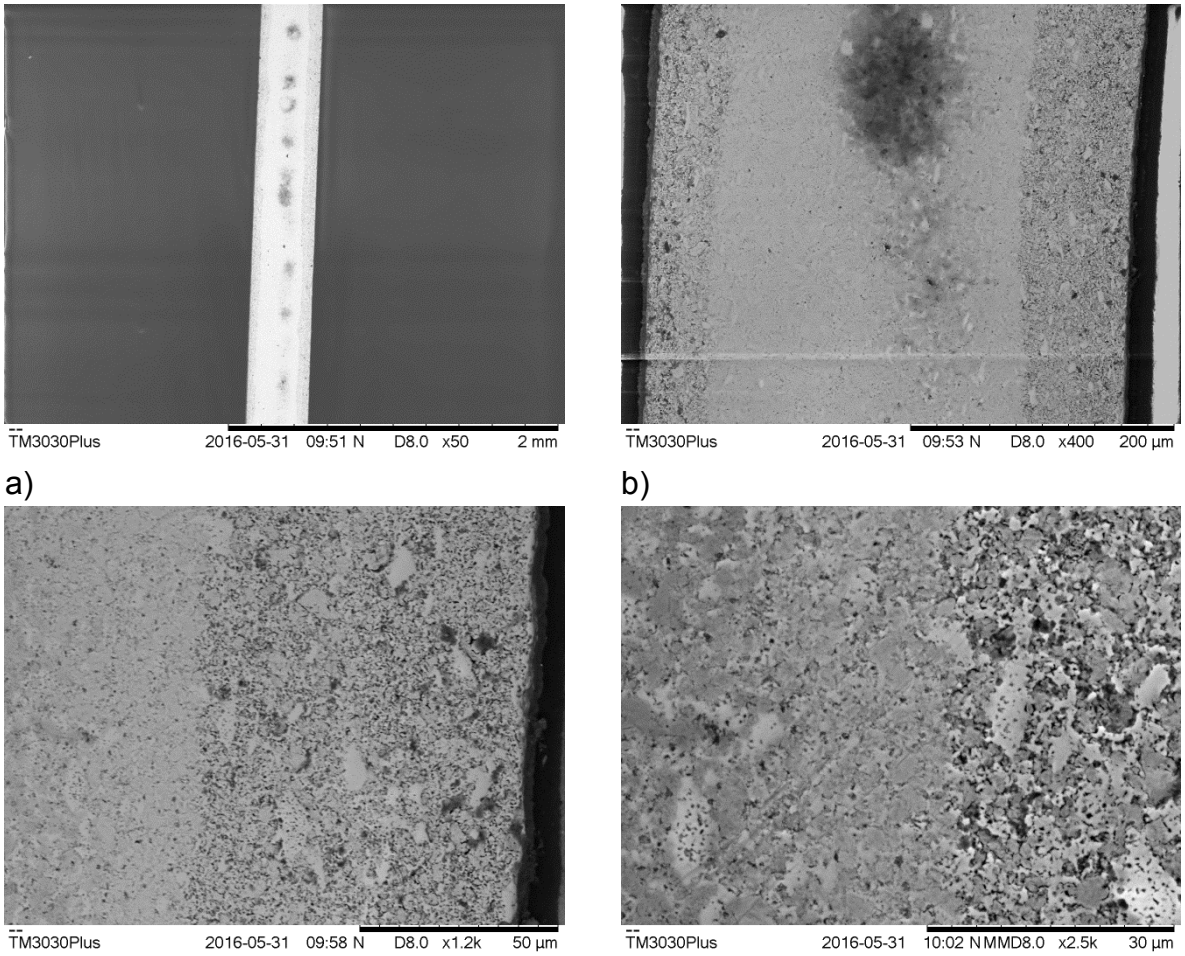

Figure 3-7 Progressive SEM inspection of area with dense vs. non-dense layer of a sample reduced at 700°C for 24h in 100% H_2 a) x50 mag BSE, b) x400 mag BSE c) x1200 mag BSE and d) x2400 mage BSE/SE mix.

In Figure 3-7 the progressive imaging of a boundary between the two layers is shown, the dark patch present in these images is in relation to the resin itself and is not a feature in other samples (but was analysed to ensure it wasn't in any capacity

an influencing factor). Imaging shows that a very dense layer is present in the central (left hand side) portion of the image. BSE/SE mixed imaging shown in 3.9 d) shows limited reduction between the slightly lighter phase of YSZ and the surrounding nickel phase. EDX was performed to ascertain elemental distribution in each section.

For analysis of the non-dense layer, Figure 3-8 shows the oxygen distribution relative to the other elements. Carbon was present as a blanket coverage with no distinct high density areas. Aluminium is used in the final polishing stage of the process and can deposit on the surface of the samples. Notable here it is present as a darker phase, and is highlighted in the EDX images through e) and f), where areas of high O concentration overlap perfectly with Al present. The sample holders are also Al and thus a light layer is visible on most samples as well. Importantly for this analysis the regions of Ni are limited/void of O, confirming fully reduced Ni metal

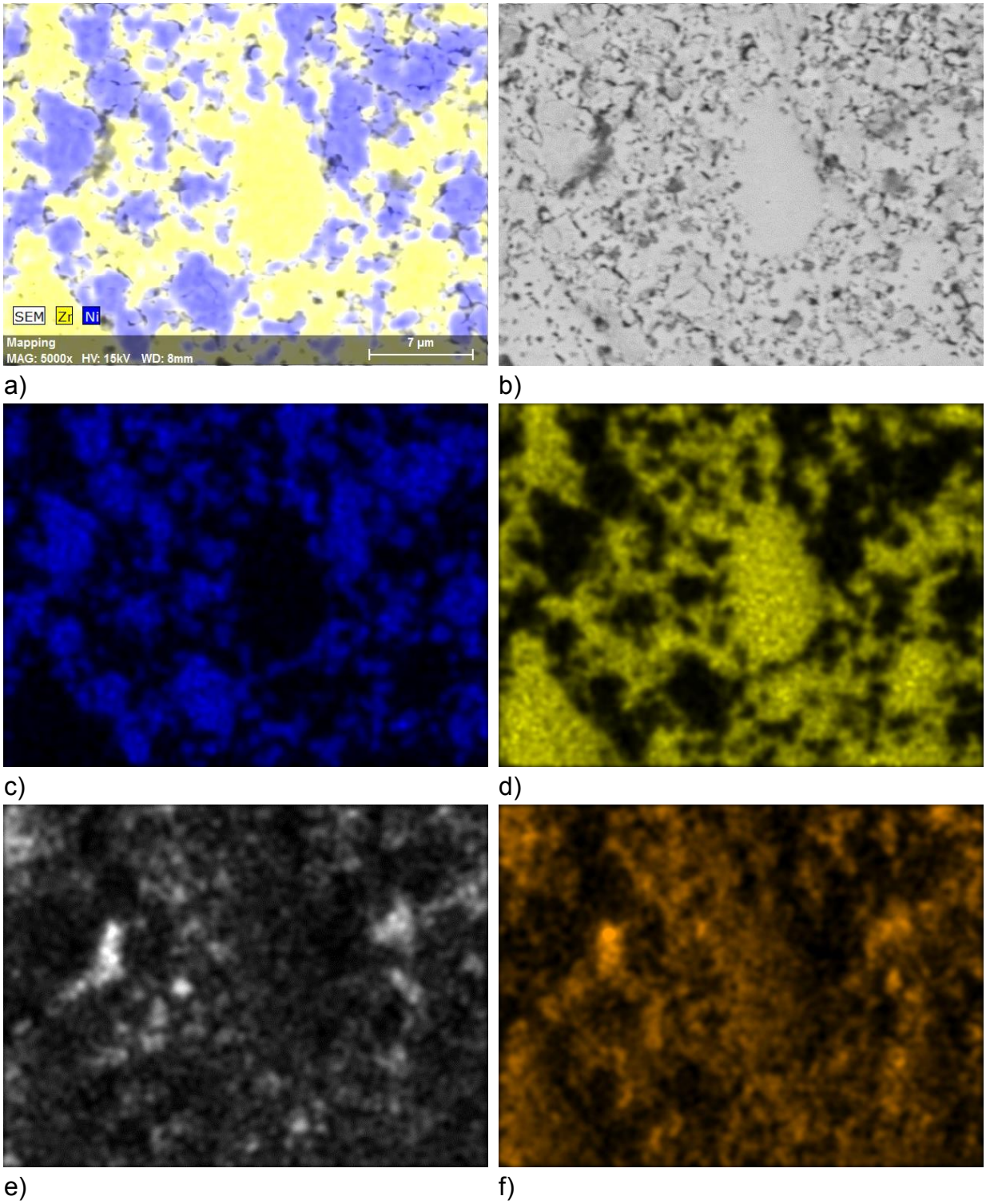

Figure 3-8 Non-dense layer EDX analysis of sample reduced at 700°C in 100% H_2 for 24h a) Ni-Zr EDX overlap, b) SEM EDX, c) Ni, d) Zr, e) Al and f) O.

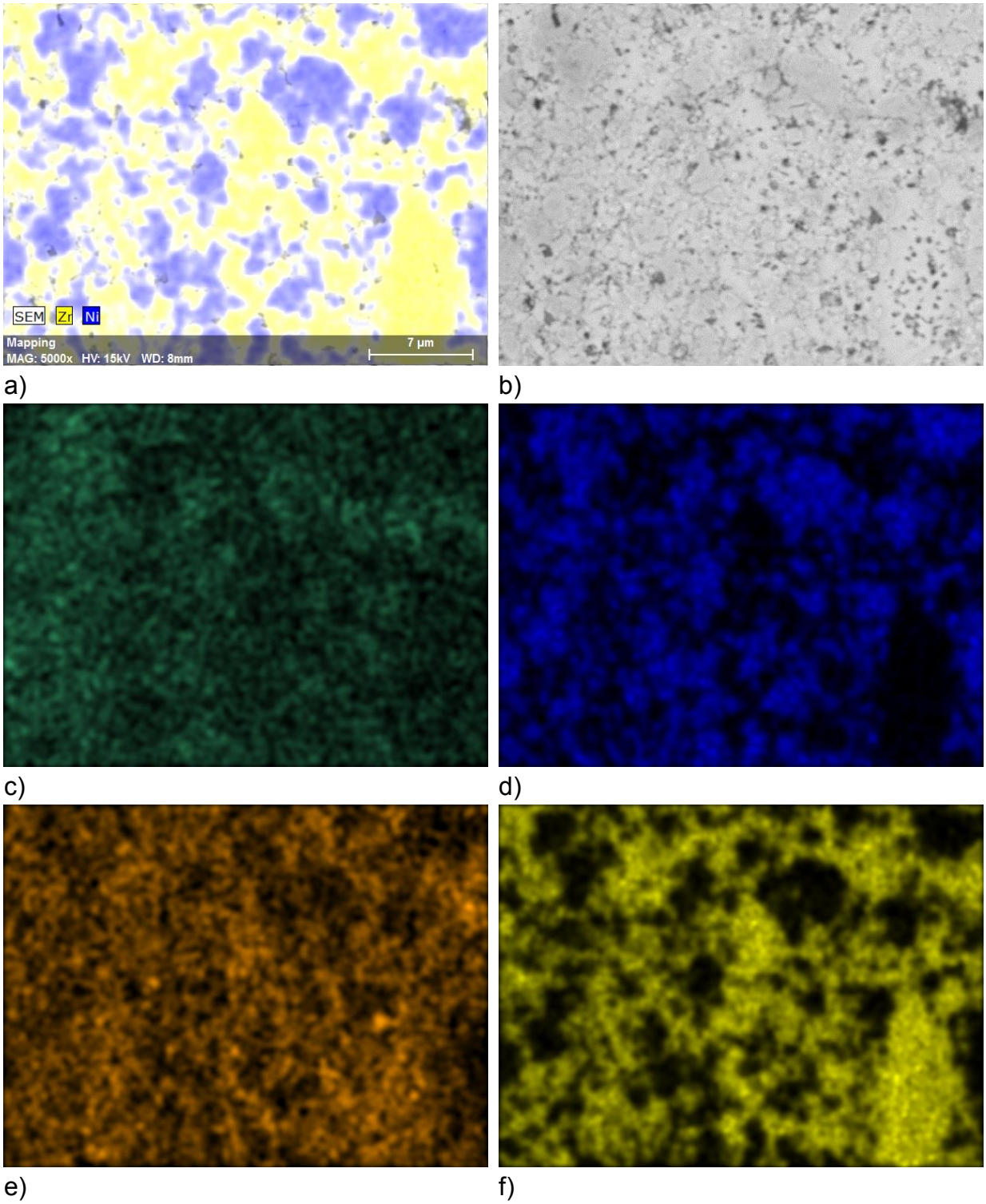

Figure 3-9 Dense layer EDX analysis of sample reduced at 700°C in 100% H_2 for 24h, a) Ni-Zr joint image, b) EDX background image, c) carbon EDX, d) Ni , e) O and f) Zr.

Investigating the denser layer present in Figure 3-7 with EDX imaging resulted in drifting which occurred on all dense sections of samples. This resulted in less clear imaging than previously. Whilst the oxygen profile does mirror the Zr profile as shown in Figure 3-9, the appearance of oxygen does overlap on points with Ni. It is also important to note that the resin present in the sample mount will contain oxygen and thus due to the polishing process small quantities will be distributed over the sample. The drifting present could be a sign of lack of conduction through the sample, which would indicate an unreduced section, but as the oxygen profile could neither confirm nor deny its state further investigation was necessary.

Because initial imaging could not clarify the issue, determining whether sectioning was causing an issue in the sample was investigated. Figure 3-10 is the EDX imaging of a section of a freshly broken reduced sample which was not sheared by the diamond blade. What is immediately clear from these images is that whilst small bits of O appear to overlap in areas where there is Ni, this is almost definitely due to drifting in the sample, and almost exclusively it is present in areas of Zr in the sample.

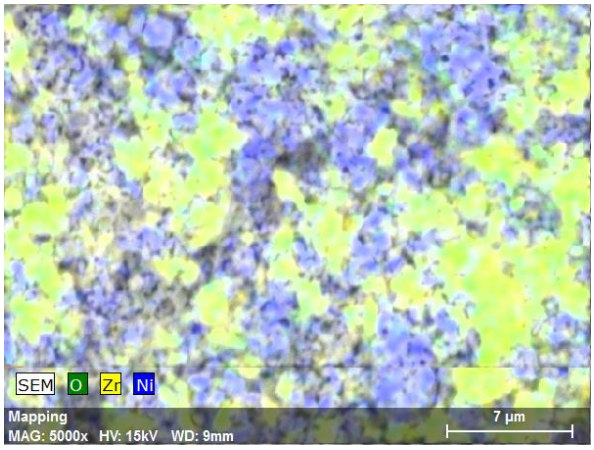

a)

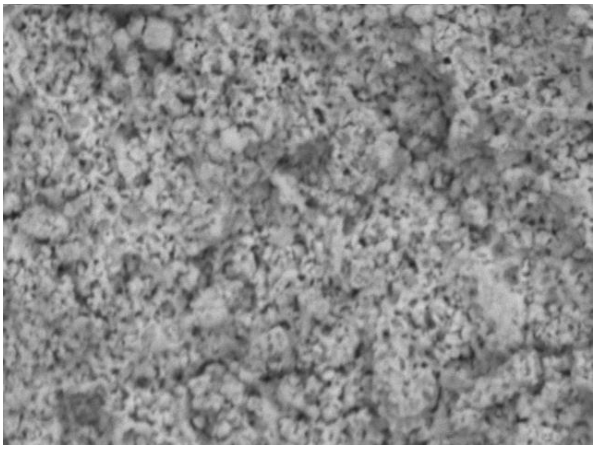

b)

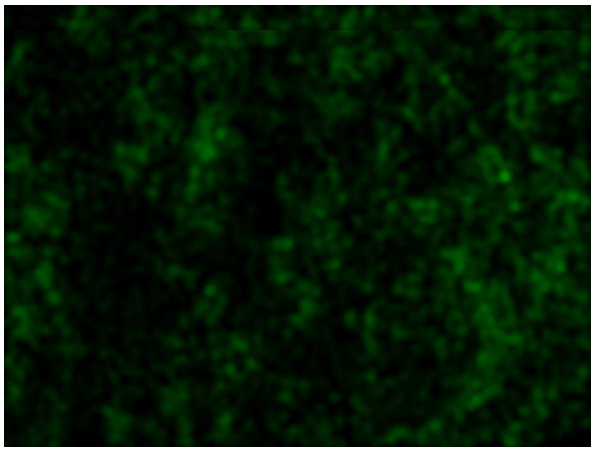

c)

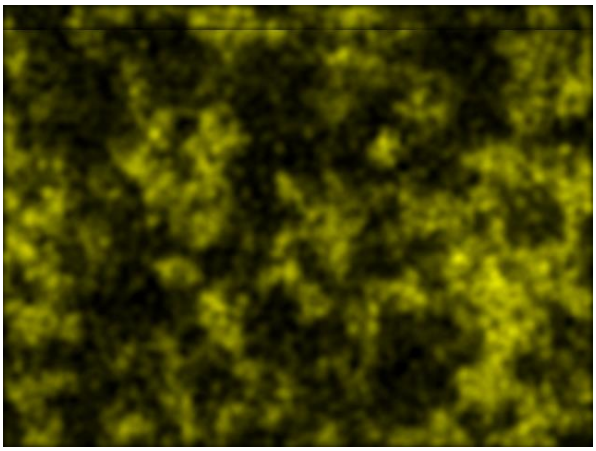

d)

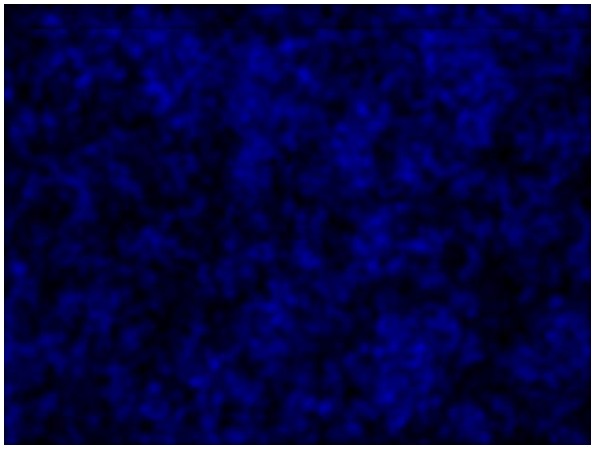

e)

Figure 3-10 EDX image of area of broken sample showing discrete Ni/YSZ phases with O predominately visible overlapping YSZ phase. Sample was reduced at 800°C for 24h in 100% H_2 A) Ni-Zr -O EDX overlap, b) plain EDX, c) O, d) Zr, e) Ni.

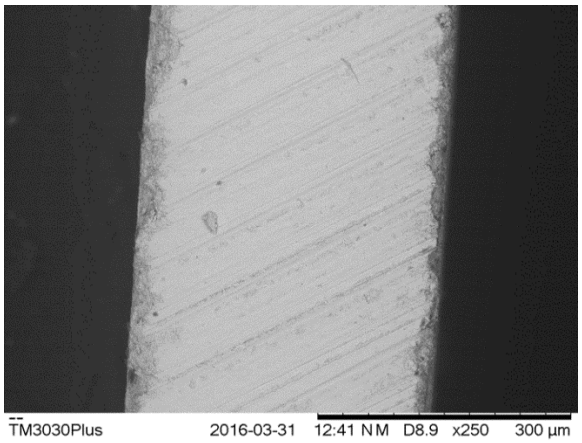

a) BSE x250 mag diamond saw

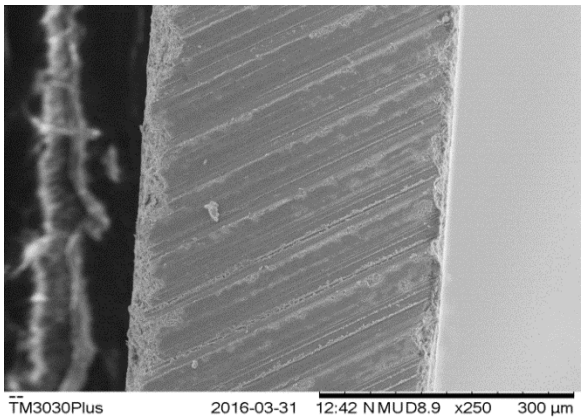

b) SE x250 mag diamond saw

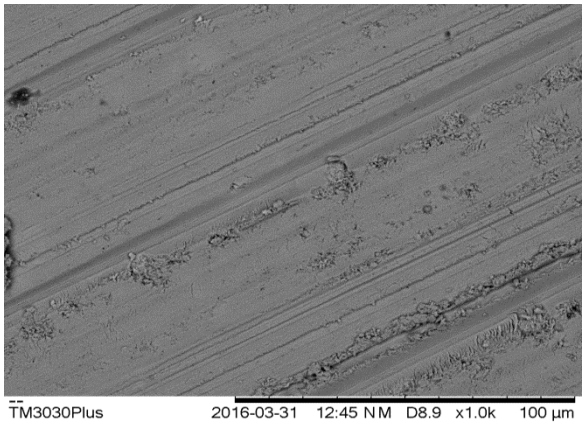

c) BSE x1000 mag diamond saw

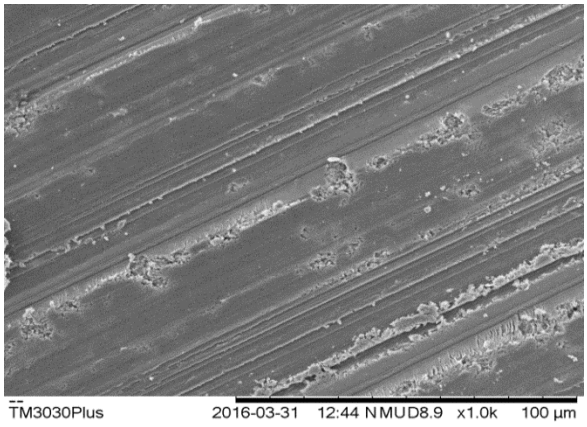

d) SE x1000 mag diamond saw

e) BSE x5000 mag diamond saw

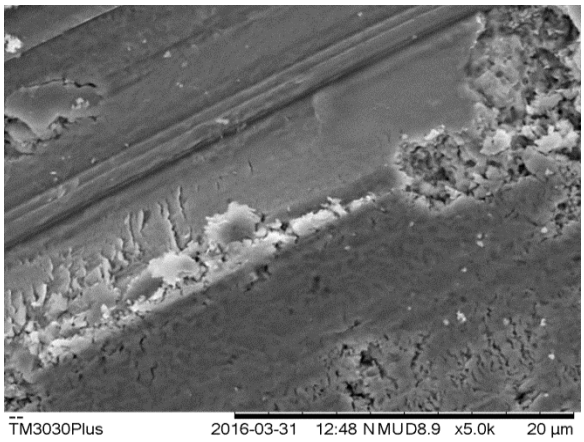

f) SE x5000 mag diamond saw

Figure 3-11 Comparison of Surface of freshly sawn samples in BSE and SE mode. Sample was reduced at 800°C for 24h in 100% H_2. Images clearly show the shearing affect of the diamond saw on the surface of the sample.

Next investigation of a freshly sawn sample was undertaken to see what the surface change looked like, i.e. did the change run deeply through the sample and were there any noticeable irregularities. From Figure 3-11 it is visibly clear that the edges, much like those of polished samples, are lower than the surface of the sample. This results in it not having been smoothed/sheared by the diamond saw. Also worth noting is the small pockets of un-sheared areas in images e) and f). This area was investigated further and was shown to have a very similar microstructure to that seen by freshly sawn samples, as shown in Figure 3-12. EDX imaging shows that the porous sections of the freshly cut sample appear to be very similar to those of polished samples, importantly the porosity is located concentric to Ni particles predominately. As the pores are formed from the NiO reduction this is what it should appear as.

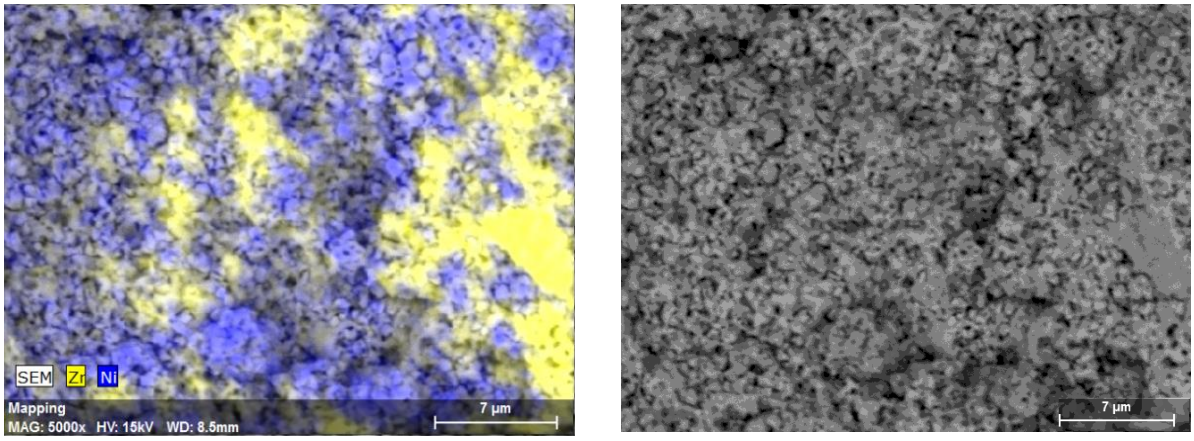

a) EDX image at X5000 mag of Ni-Zr overlapping with SEM

b) EDX image at X5000 mag from SEM

Figure 3-12 Investigation of non-sheared section of freshly sawn sample. Sample was reduced at 800°C for 24h in 100% H_2. As the surface resembles that of non-sheared/freshly broken samples it eliminated the diamond saw as an issue.

Topographical analysis was done on samples without resin mounting and imaged on their sides rather than cross-sectionally. Two separate samples were imaged to look at their different microstructure; one virgin NiO sample, and one reduced sample. Figure 3-13 shows the SE and BSE images of the respective samples. Issues with a lack of porosity are clearer in the BSE images. Figure 3-14 shows the varying distribution of the NiO and Ni reduced samples, respectively. As neither sample could be prepared in such a way to avoid drifting completely, oxygen is expected over the entirety of the image, however if the combined overlapping Ni, Zr and O SEM images for both figures are inspected in Figure 3-14 a) and c) it is immediately apparent that oxygen is significantly more present in the Virgin sample than the reduced sample. NiO-YSZ virgin samples which were polished had a repeatedly uniform solid distribution across its surface (unlike that present on reduced Ni-YSZ samples), which suggested it could be to do with porosity in the centre of reduced samples being filled by sheared Zr/Ni grains.

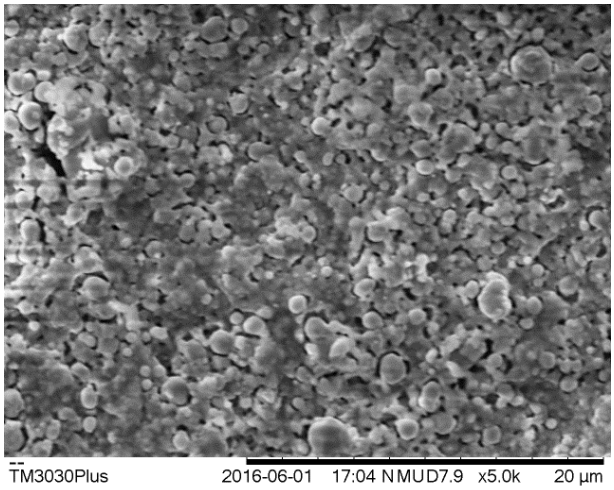

a) 900°C 250h reduced sample SE

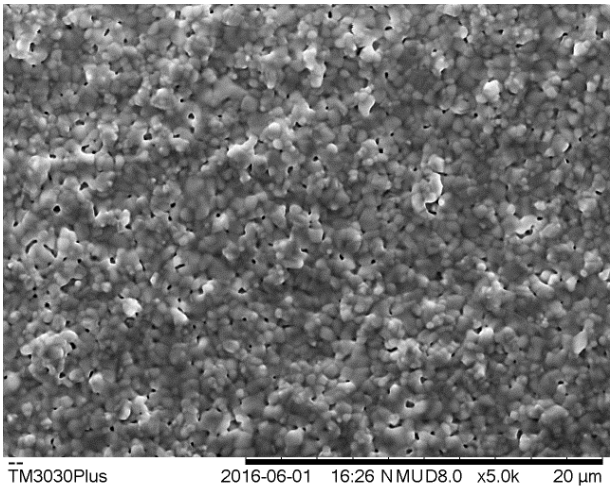

b) Virgin Sample SE

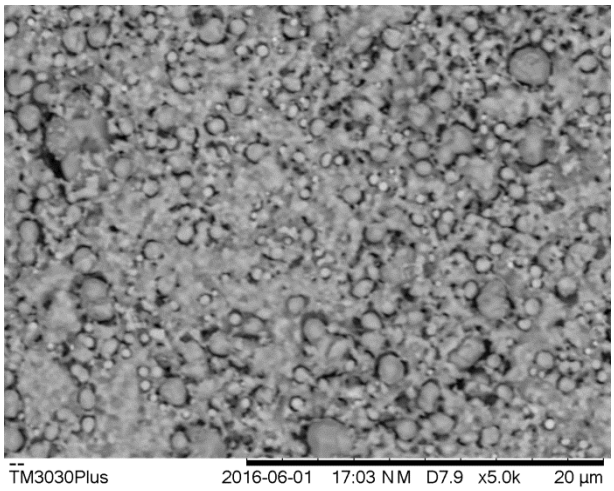

c) 900°C 250h reduced sample BSE

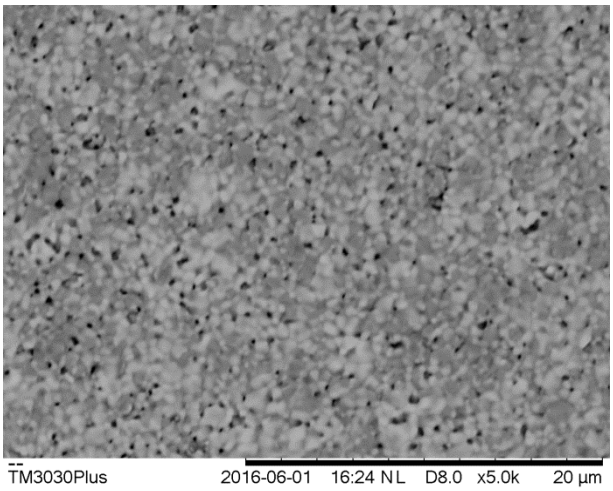

d) Virgin Sample BSE

Figure 3-13 x5000 mag comparison of a sample operated at 900C in 20-80% H_2/H_2O mixture for 250h versus a virgin green sample imaged as polished. Notable differences in particle size and porosity are visible.

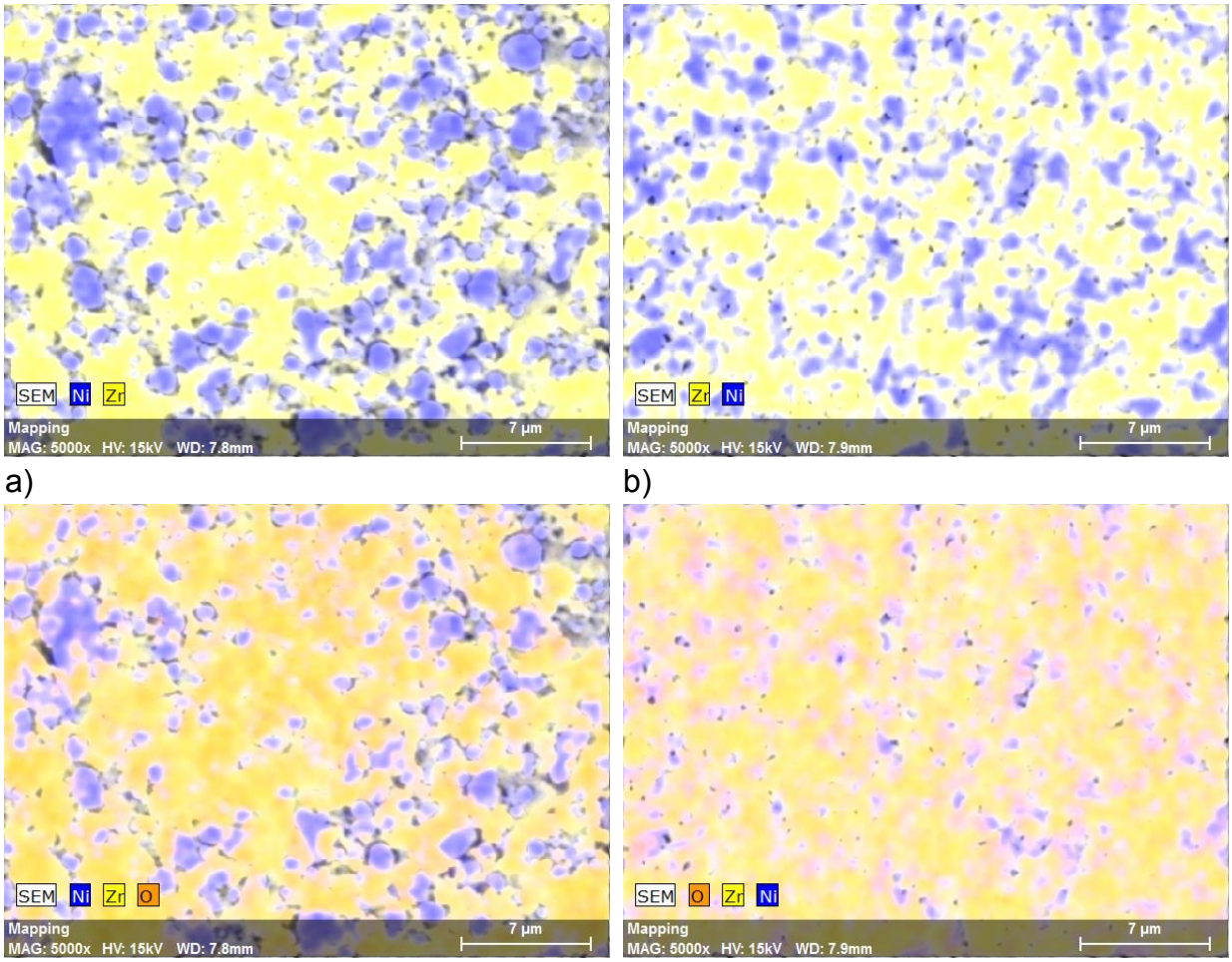

Figure 3-14 x5000 mag comparison of a sample operated at 900C in 20-80% H_2/H_2O mixture for 250h versus a virgin green sample imaged as polished. The section shows comparison between Ni-Zr and Ni-Zr-O overlap EDX images for the reduced sample in a) and c) and for the virgin sample in b) and d).

Lastly looking over the disproportional application of pressure on the mounted samples, initially when the only option available was hand polishing, care was taken to adhere as rigorously as possible to specified time frames, in the hope this would allow for reasonably similar levels of polishing force. Later on, the availability of a machine polishing head for the same apparatus allowed for much more controlled application of force on up to 4 samples at a time (previously the limit was 2 in each

hand). This allowed for a series of tests covering a range of different pressures to ascertain what impact if any the pressure was causing. High levels of pressure (30N and above) appeared to cause an increase in the relative coverage of the sample in terms of dense/non-dense. However lower levels (10N and below) of pressure did not remove the dense layers.

Issues depending on the location and set up of the samples in the quartz tube furnace as prepared should not be an influencing factor, as full cells from Ningbo (Ni-YSZ-LSCF) were tested for comparison, with 0.4 l/min hydrogen flow directly to the anode side on a 4x4cm^2 active area cell. The cells were reduced for a minimum of 4-5 hours (on top of subsequent testing). These samples also had dense areas present after polishing, but were sectioned as previous anode supports had been.

When looking at the whole preparation process an analysis of all the variables which could impact on the surface of the sample was investigated: pressure, orientation (the directional facing of the sample during polishing i.e having the sample length perpendicular to the direction of the polish pad or parallel), length of polished stage, initial starting coarseness of polishing, and initial cutting/sectioning, as shown in Table 3-3 These factors were analysed and no repeating negative features were ascribed to the variations.

Table 3-3 Polishing procedure for variable comparison. Tests were done relative to the polish pad used and compared variables of pressure, rotational speeds and the orientation (was alignment of the sample perpendicular or parallel with the pads rotation).

Test No	Pressure	Orientation	Speeds (rpm)
diamond saw sectioned sample			
125µm	Normal/ low P		150
70 µm	Hand polish/ Medium P		150
45µm	High, Medium, Low and Hand P	Single/mixed	50, 150, 300, 500
	Low P	Single/mixed	150
	Hand polish	Single/mixed	150
30µm	Hand polish	Mixed	250-400, 100-150
15µm	High P	Single/mixed	50, 150, 300, 500
	Low P	Single/mixed	150
	Hand polish	Single/mixed	150
9µm	Low P	Mixed	150
	Hand polish	Mixed	150
3µm	Low P	Mixed	150
	Hand polish	Mixed	150
1µm	Low P	Mixed	150
	Hand Polish	Mixed	150
0.3µm	N/A	N/A	N/A
0.05µm	N/A	N/A	N/A

In an attempt to clarify the issue, polishing aid was found from Dr. Evans Mogire, who manages Buehler's centre at the Warwick Manufacturing Group (WMG) and has considerable expertise in the field of polishing. After investigation his professional opinion was that the resultant dense layer was a microstructural issue present in the

samples, and not the result in any way from the polishing methodology. This was in agreement with the previous analysis, that in certain sections of some samples a denser region was present. Thus the current polishing procedure was sufficient for imaging and the dense layer was an anomaly of the testing samples and procedures. Given that full cells were tested electrochemically and capable of delivering suitable performance, these samples were deemed sufficiently reduced to provide data for Ni particle analysis.

3.3 Image Processing and Data Development

After the samples had been physically prepared through testing and subsequent moulding/polishing as shown in Figure 3-3 , the sample particle populations were extracted from the image in two ways. Firstly for both, the initial sample underwent SEM analysis, where an EDX image highlighting the Ni and Zr phases (Yittria has a similar peak to Zr and would overlap) was produced which represented the Ni, YSZ and pores in the image. From this, two routes were selected of which one was used for reconstruction in a 2D Matlab® model to help interpret the values and parameters for the sample and its respective images. This could then be used to help determine the change in performance of the cell via TPB changes. The second method looked at particle distribution changes, equating the change in area to a relative change in radius. This result was then used alongside Matlab coding looking to estimate the change in TPB length and conductivity in the anode. A mean particle radius is implemented for comparison, and predictive models describing its change over time

in varying temperature and fuel composition were compared against the test data. Figure 3-15 shows the pathway for generating the data used in both processes.

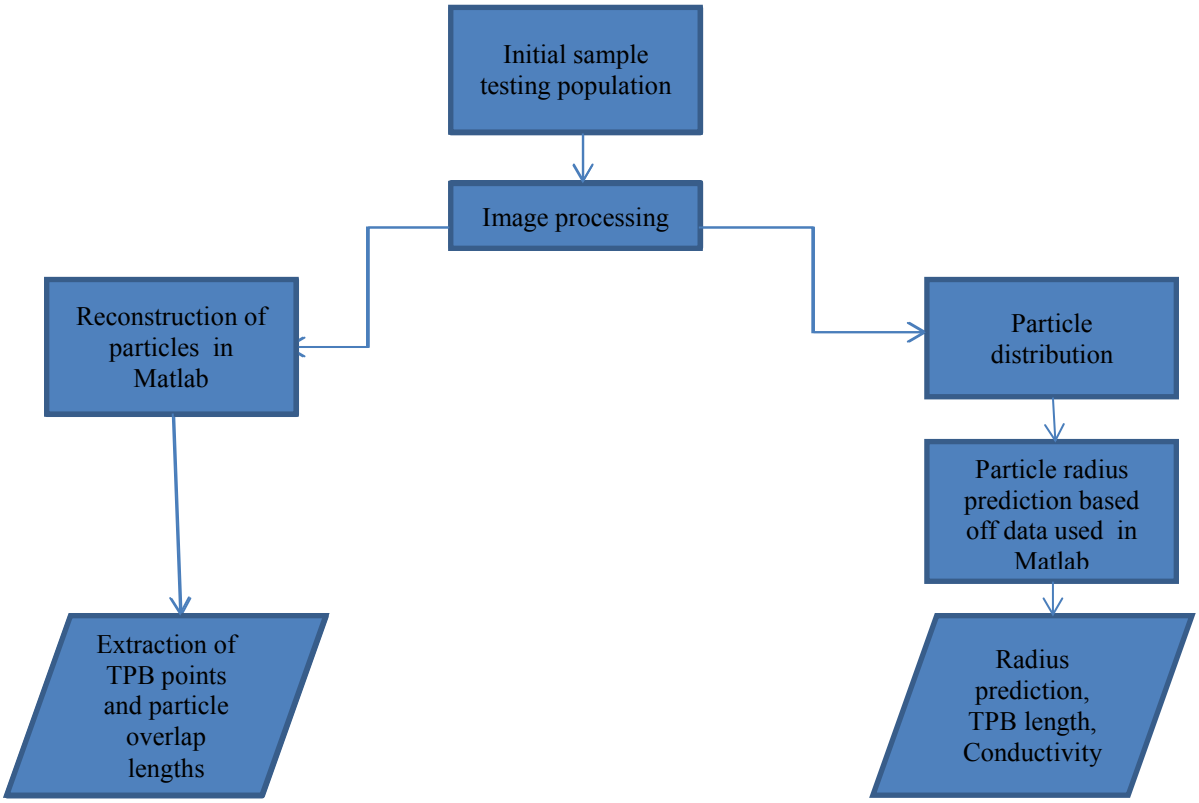

Figure 3-15 Route for sample data utilisation. Sample images are generated and then processed through ImageJ. These are subsequently either analysed via Matlab to determine TPB lengths and other values or the distributions are calculated and input into predictive models.

Samples were loaded into a benchtop Hitachi TM3030 SEM. The working distance was generally established to be as close as reasonably possible whilst allowing room for EDX and the not perfectly square dimensions of the samples so as not to damage the equipment. Normally this results in roughly a 8mm working distance. Operating parameters were a 5000x magnification and 15kV beam energy over a 3 minute

imaging time. Carbon and oxygen were present over the coverage of the sample, as the polishing process would likely spread the resin (in very small quantities) and oxygen would be present alongside the zirconia and porosity (pore phase).

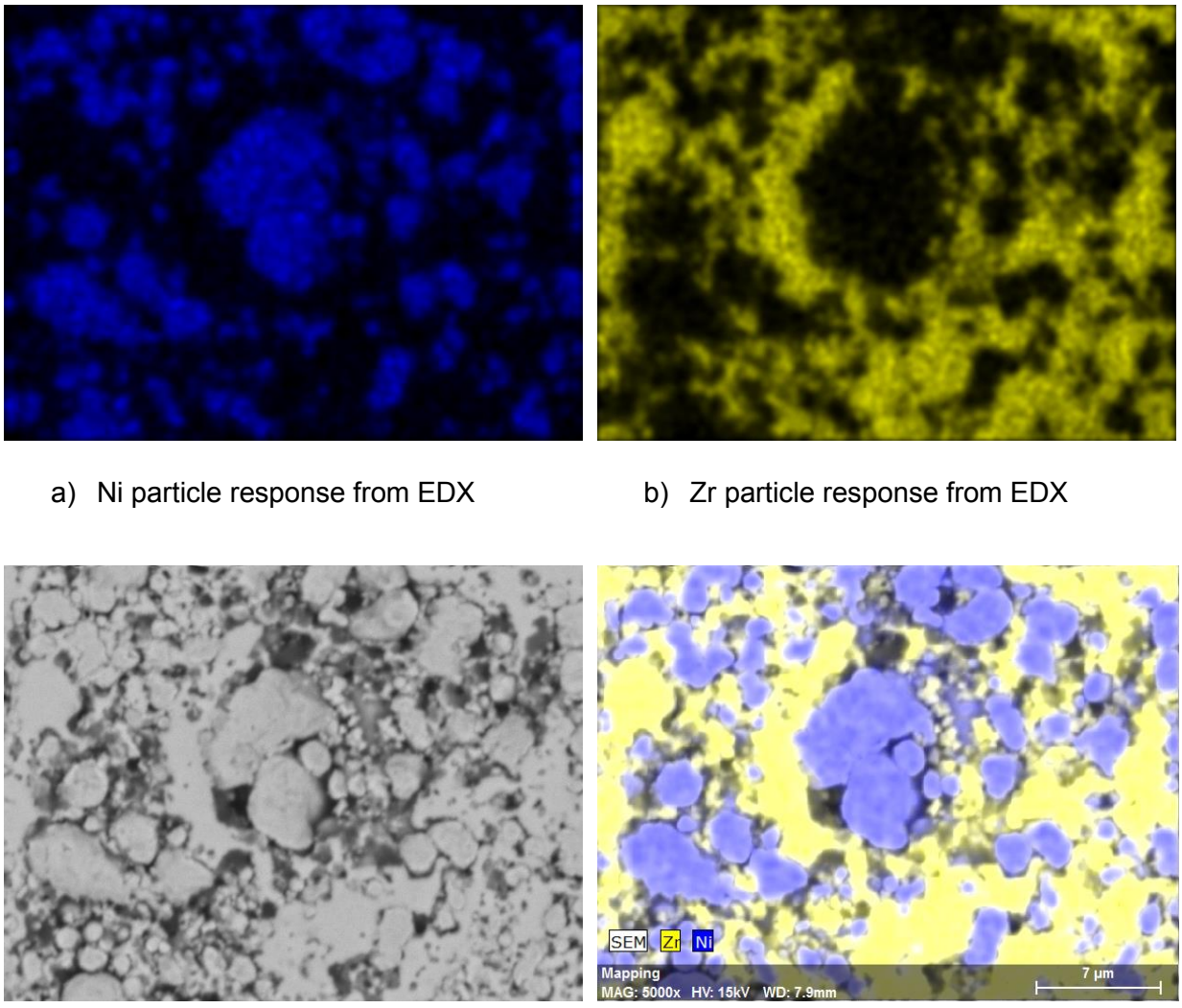

a) Ni particle response from EDX

b) Zr particle response from EDX

c) EDX BSE

d) combined overlap of a), b) and c)

Figure 3-16 EDX sample examples for those used in imaging stage. Sample tested at 900°C for 250h in a 20-80% H_2/H_2O mixture. a) is for Ni, b) Zr, c) a BSE image and d) the resultant overlapping image.

For the purposes of analysis the carbon and oxygen responses were omitted from the mass imaging analysis but checked upon initially to ensure no unusual issues.

Figure 3-16 shows the comparison between the visual responses on the EDX a) and b), initial image c) and eventual combined overlap d).

Once the EDX images had been generated they were converted and analysed with ImageJ software. The software is capable of thresholding the specific phases such that their total area can be summed, and after thresholding can be watershedded to provide values of particles areas, which can then be used to generate particle radius distributions and x,y coordinates for Matlab coding. The thresholding uses the Otsu method algorithm, as previously had been shown to be effective for SOFC microstructural analysis [294]. During analysis the images are cropped to remove the scale bars and labels, but were retain in Figure 3-17 for reference. This results in an area of 32.8 μm x 20.5 μm for each image. The watershedding process looks to find logical segmentation points in the imaged binary particles and especially for Ni particles presents a visually comparable segregation method. Figure 3-17 shows the black and white images of the Ni and pores extracted from Figure 3-16. It is important to note that the generated data shows the area for each individual particle and their x,y centre coordinates. This is then converted into a radii value under the assumption of circular particle shape. This is suitable for Ni analysis, as naturally they form spherical particles over time, the pore shape however can vary as discussed previously. The channels which can form in the reduction process are more likely encompass the Ni particles after initial reduction, and over time form larger circular pores as Ni particles form larger particles at the expense of smaller ones. However for the analysis it was assumed the pore values were sufficiently represented by the circular comparison. The process produced a Discrete PSD from which a mean was established.

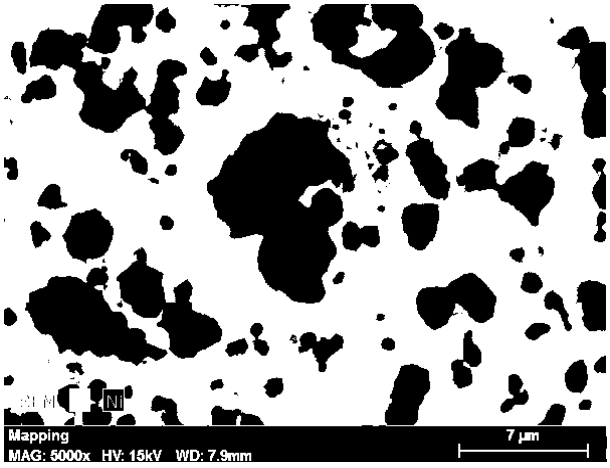

a)Ni thresholding

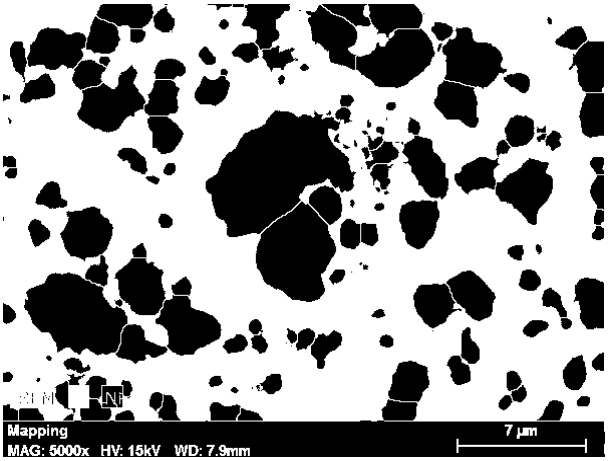

b)Ni particles post watershedding

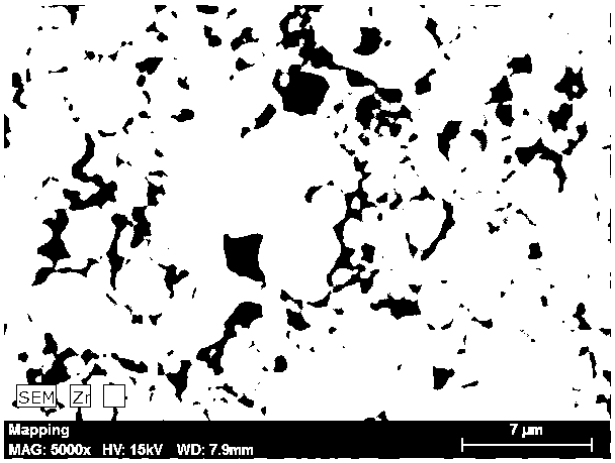

c)Pore thresholding

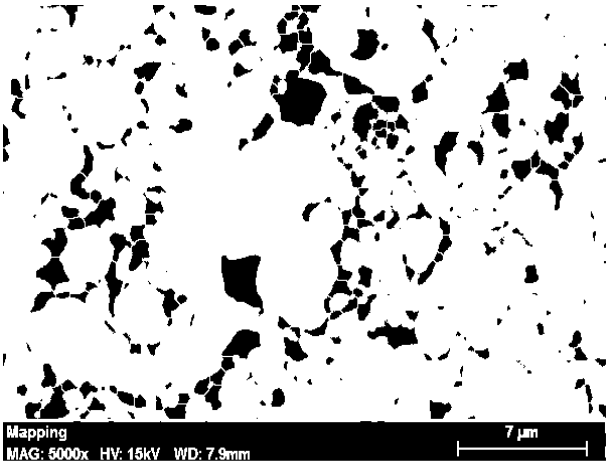

d) Pores post watershedding

Figure 3-17 Example of ImageJ black and white thresholding and subsequent watershedding of same sample as Figure 3-16. Images show Ni for a) & b) and pores for c) & d). The sample was tested at 900°C for 250h in a 20-80% H_2/H_2O mixture.

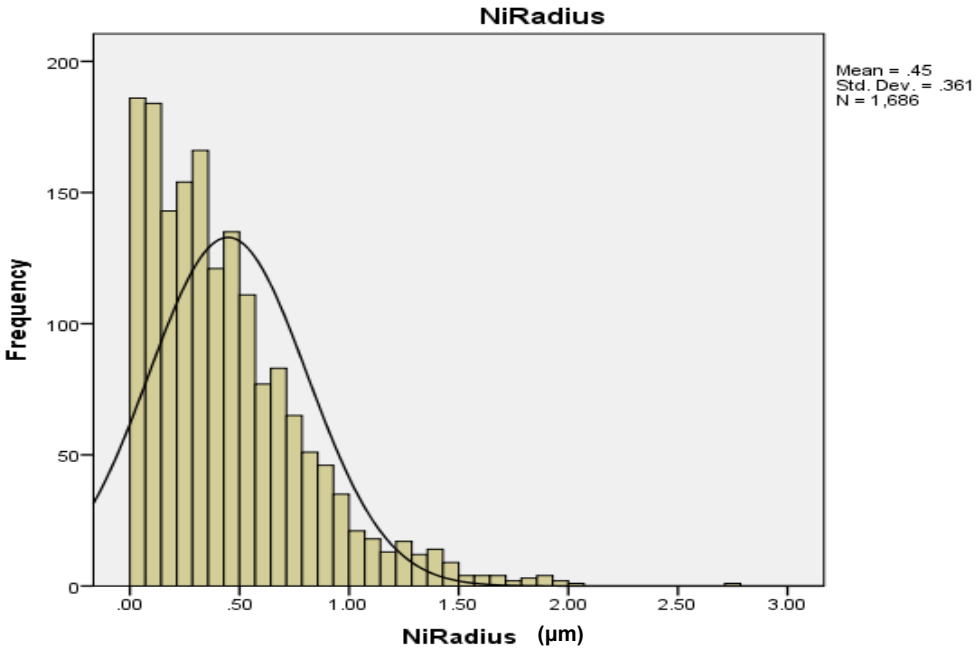

a) Histogram of Ni particle radius (µm) distribution

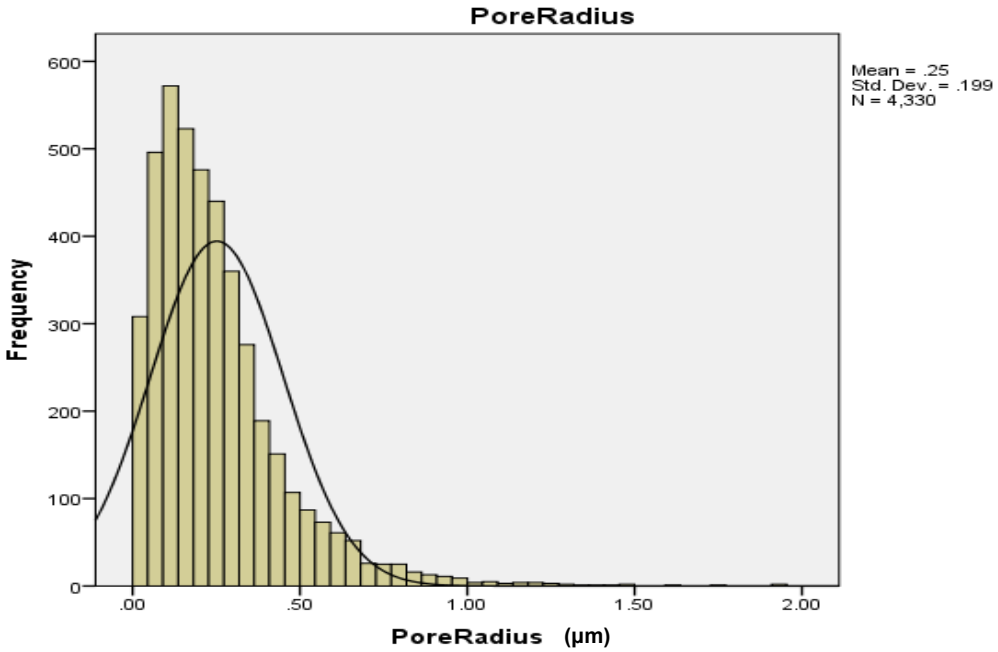

b) Histogram of Pore radius (µm) distribution

Figure 3-18 Histograms of Ni and Pore for a given sample. The curve shows the mean and standard deviation for the given plot. The sample was tested at 900°C for 250h in a 20-80% H_2/H_2O mixture.

The histograms produced from the ImageJ analysis result in values for both a mean pore/particle radius as well the standard deviation. These can be compared against each other to see what correlations (if any) are present when various factors change in the operating setup of the samples. The data is processed using the IBM SPSS statistics data editor, as shown in Figure 3-18.

CHAPTER 4 Microstructural Analysis of Ni-YSZ SOFC Anode Samples with SEM and EDX Imaging

Nickel particles inside of the anode can coarsen and agglomerate over time leading to a loss in electrical conduction due to a reduction in percolating pathways for electron transfer and thus increased resistance in the system. Equally, mass transport limitations can be caused by a reduction in porosity or percolating pores. Due to these effects there is interest in understanding the longer term changes that an anode undergoes based on its operating temperature and the fuel composition. Some literature suggests one mechanism over the other for being the major determinate in the rate of Ni particle size increase/transport. The aim of this work was to further clarify or add to the understanding of these processes.

As mentioned in the methodology chapter, 8 samples were distributed along the inside of a quartz tube inside of a furnace where they were exposed at constant temperature to a set fuel composition. They were reduced for 4 hours in 100% H_2 before commencing the 1000h testing procedure. 2 samples were taken for each 250h interval and these were sectioned, mounted and polished for SEM and EDX analysis. The images were process by ImageJ software and the data was analysed with IBM SPSS and MS Excel.

Certain assumptions have been made regarding the cell testing, 1) All samples are exposed to the same composition and volume of gas. 2) The temperature inside of

the quartz tube is constant and uniform. 3) The exposure times are sufficient to allow for complete reduction of the NiO. Modelling work done on the quarts tube and its operation support this, as well as the regularly referenced reduction time of 1-2 hours [215, 216, 219, 230] versus the 4 used during these experiments.

The analysis process should provide data on Ni particle radii, the total percentage of area of Ni in the images relative to YSZ and porosity, as well as the total number of pores and Ni particles. The hypothesis based on existing literature is that the larger particles will coarsen via loss of smaller particles, and this should cause a shift in the distribution of particles and thus the mean values should get larger over time. Temperature and steam content should influence these values and thus higher temperature or steam sample sets should have relatively larger mean values over time. The Ni content value should remain relatively constant. Unless a notable amount of Ni decline is seen over time there is unlikely to be significant volatisation of Ni particles out of the sample. A larger value for Ni content is likely to provide a larger mean Ni radius value for that image set, as for larger Ni particles to be present either smaller YSZ particles or less YSZ would need to be in the section analysed assuming constant porosity. Thus looking at the samples relative to a constant value of YSZ is likely to be necessary for accurate appreciation of any significant changes. The number of particles and pores in a sample are expected to decrease over time for a given test as the smaller particles coarsen into larger ones.

Assuming the mean Ni radii values change with the Ni content present in a given image then a value for the mean radii should be adjusted relative to the Ni content for appreciable comparison between samples. The relative change in samples from

250h to 1000h should highlight trends where visible. The Ni content is important to appreciate the distribution in these cells, and as the amount of YSZ should remain constant throughout all samples (both in content and size distribution), normalising to these values allow for a more accurate evaluation of any notable features within samples. The particle numbers, depending on their relationship with Ni content, should show decline in numbers inversely proportional to the increase in Ni radius. The pore number, pore radius and porosity will all be analysed in a similar fashion to the Ni values, to see how they progression of those values change over time relative to the Ni values.

4.1 Nickel Area and Porosity Analysis and Comparison

Analysing Ni area percentage from Figure 4-1, the initial data extraction shows the variation and differences over temperature ranges and fuel compositions appear relatively negligible. In theory, if the cells have fully reduced and there is no volatisation then it would be expected that this value be consistent throughout the samples. The 100%H_2 at 700°C sample shows the highest relative amount of Ni content in their samples, as well as the lowest relative porosity. Imaging of the samples suggests that the NiO began the reduction process but after a reduction in volume (seen as area in 2D), this process was restricted from significant reduction, as the samples have very similar relative Ni/porosity to the 24h reduced 800°C samples.

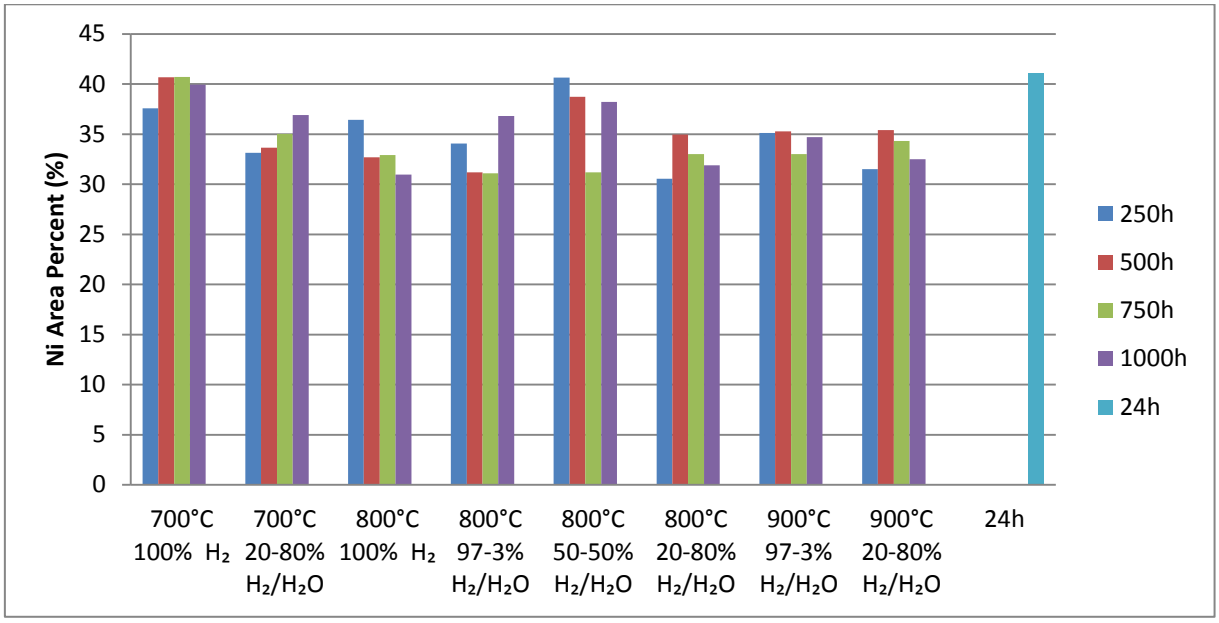

Figure 4-1 Nickel area percent for the selected temperature and fuel regimes. Each time frame shows the average of two samples. Each sample was evaluated through 12 images covering random sections of the sample.

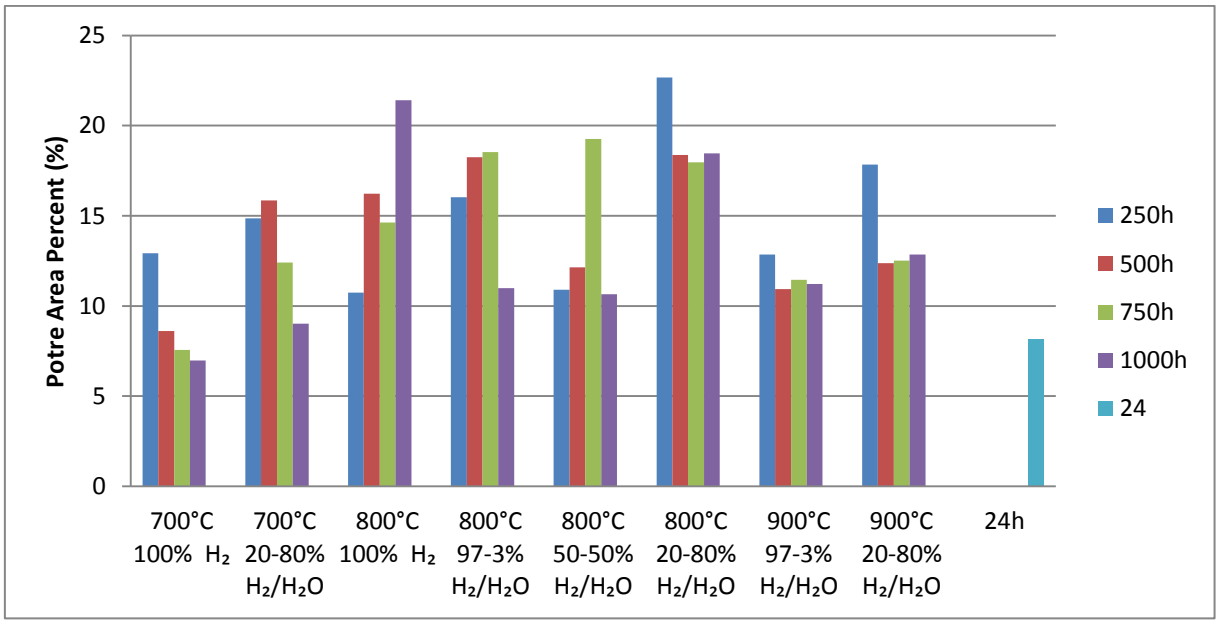

Figure 4-2 Pore area percent for sample temperature and fuel regimes. Each time frame shows the average of two samples. Each sample was evaluated through 12 images covering random sections of the sample.

When total average values for the nickel, porosity and zirconia were taken, a mean value of ~50% for the zirconia area became apparent. As the initial composition of the cells was not given for the purchased samples, this value of 50% YSZ does match up with very common mixture compositions from literature, suggesting a 50%-50% volume split of NiO and YSZ in the Green sintered state. Bearing this in mind some of the data contained less or more YSZ in the imaging process and thus a normalised representation of the data was achievable by correcting this value to 50% (as this was the value used in the manufacturing process) and altering the porosity and Ni accordingly by normalising it, as shown in Figure 4-3. This process involved adjusting the values of the porosity and nickel equally in a negative correlation to the YSZ, thus if the ratio of YSZ/Ni/porosity was 0.55/0.35/0.10 it would be adjusted to give 0.500/0.389/0.111. As before, the relative amount of Nickel is fairly consistent. As more Nickel cannot be created inside of the cell, and coarsening should only move the Nickel from smaller particles to fewer larger particles then the only real trend of note would be if the total Ni area was lessening over time for samples. Bearing in mind the potential errors present in the data, which are discussed later in the conclusions section, the only samples with a downward trend are 800°C 100%H_2 and 97%/3% H_2/H_2O. That being said the trend, whilst notable for 100%H_2, could simply be a result of only analysing a 56x35 μm area for each sample. As Figure 4-3 is normalised, the change in Ni value is representative of change in porosity. Due to the porosity's smaller percentage composition the change in porosity appears more significant. Given the nature of mass transport limitations in cells and the impact it can have, clearly for optimised operation cells need careful control of their initial environments for optimal long term performance.

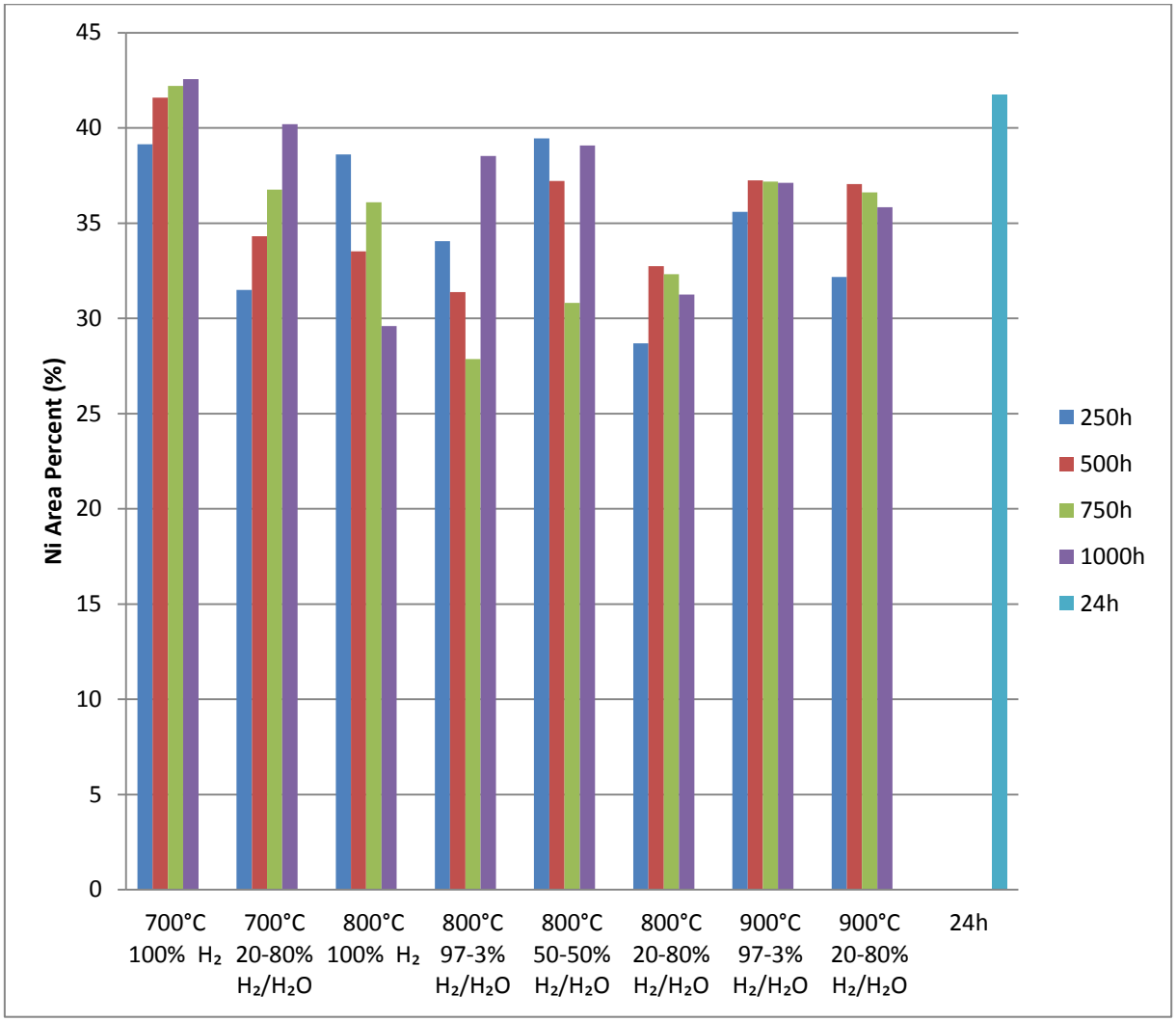

Figure 4-3 Normalised nickel area percentage for sample temperature and fuel regimes. Samples normalised relative to Zr mean value of 50% and porosity and nickel are adjusted proportionally.

For normalising the data relative to YSZ it is important to know if porosity and nickel content are inversely proportional. If the assumption of little to no porosity being present in the samples before reduction is correct then an intercept of 50 % Ni as the Y-axis should form a gradient through the proportional relationship. Figure 4-4 shows this graphically. From the linear trendlines generated from the data points, it shows

that it is definitely following the expected trend though not to the degree it theoretically should. The blue line shows the Ni vs. porosity values after being normalised to a constant YSZ value as seen in Figure 4-3, versus the as generated data points from the SEM and imaging analysis.

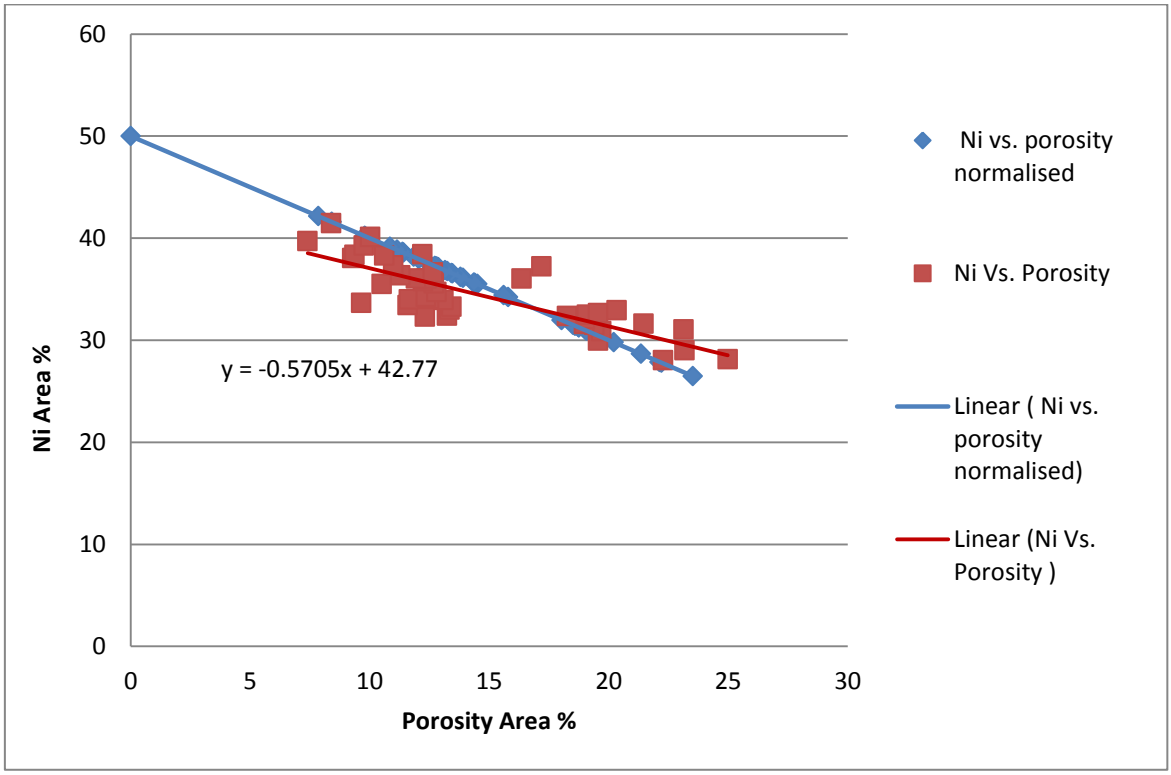

Figure 4-4 Suggested linear relationship between porosity and nickel content. Values have a linear line of best fit placed to highlight their trends. The as collected relationship between Ni and porosity is close to the expected normalised relationship.

Qualitatively, if there is a trend in the relative change in normalised Ni content then Table 4-1 describes it. For the majority of the data there is some degree of increase in Ni content percentage over time. It is possible that the shift in porosity is taking

place across the entirety of the cell, and isn't immediately apparent over the area of analysis in the sample. However analysis of microstructural variation did not lead to any noticeable differences regionally across the bulk of the cell. The table refers to larger quantities of Ni content percentage in the 1000h versus the 250h samples as an increase, less as a decrease, a consistent value as a constant and no clear trend (i.e. entirely irregular) as fluctuates.

Table 4-1 Relative change in Ni content for normalised sample sets with time. Fluctuating samples showed both increases and decreases in their analysis.

Temp(°C)/ Fuel(H_2/H_2O)l	100%	97%	50%	20%
700	Increase	N/A	N/A	Increase
800	Decrease	Fluctuates	Fluctuates	Increase
900	N/A	Constant	N/A	Increase

4.2 Nickel and Pore Radius Comparison and Analysis

Normal distributions taken from the histograms of the data for each test sample set produce mean values for the nickel and pore radii. These mean values are combined into the subsets for their set experimental parameters and presented in Figure 4-5 and Figure 4-6. Looking over the change in Ni particle radius there is a general trend apparent where the particle radius over time increases. This is less apparent in the pore radius graph.

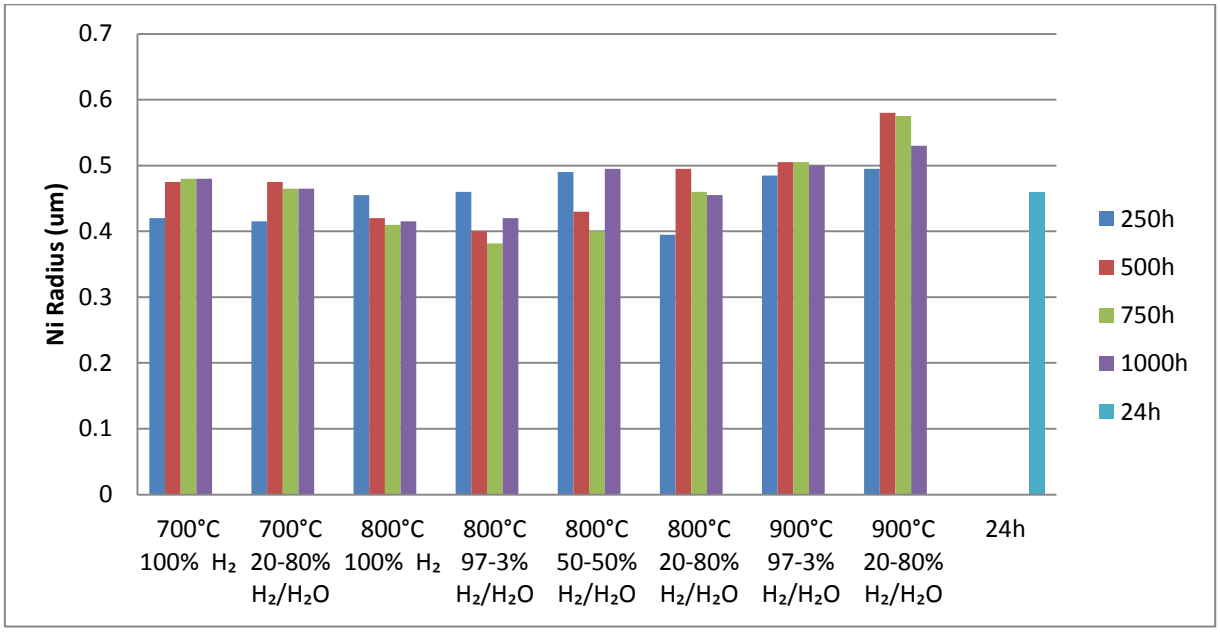

Figure 4-5 Mean Ni particle radius (μm) for samples sets. Each time frame shows the average of two samples. Each sample was evaluated through 12 images covering random sections of the sample.

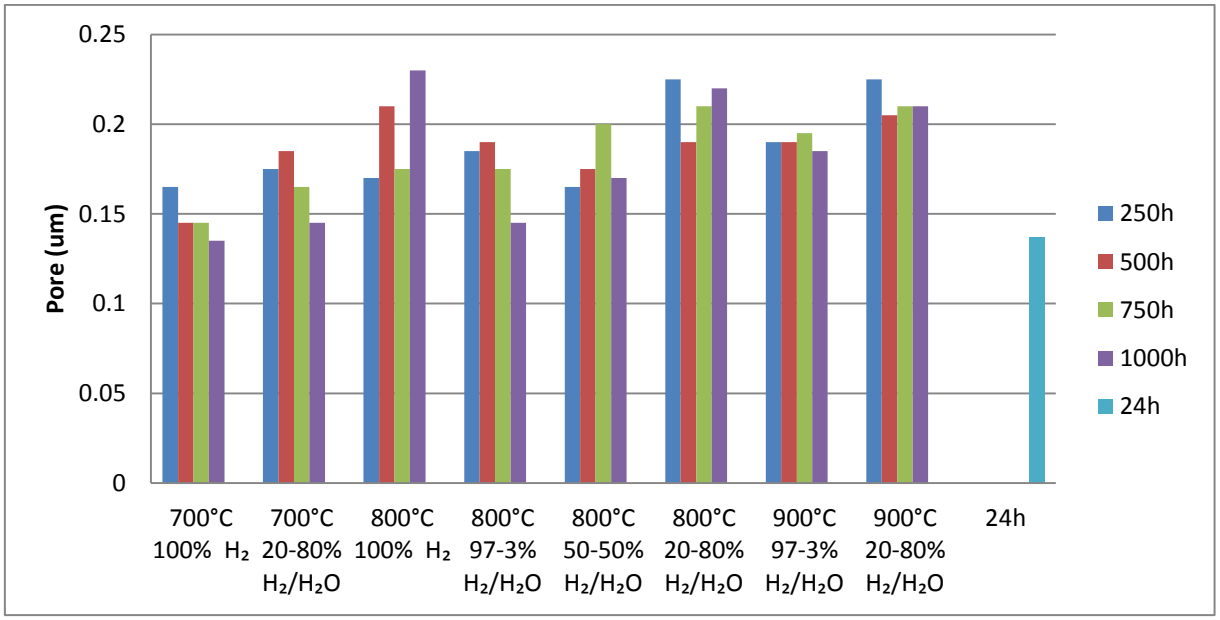

Figure 4-6 Mean Pore radius (μm) for samples sets. Each time frame shows the average of two samples. Each sample was evaluated through 12 images covering random sections of the sample.

Both nickel and pore radius, however, are affected by their respective area percentages as shown in Figure 4-7 and Figure 4-8. Both figures show a positive correlation between Ni radius and Ni area. The figures show the respective line of best fit for the sample points. Due to this, values determined straight from the imaging process may not fully represent the trend or change present in the samples. Because of this the data available will be normalised to the area percent. This can be done either by determining an overall mean value and subsequently adjusting based on deviation from this value, or a mean value is determine for the area percent of each sample set and used to see the trend over time for that specific group. The advantage of the latter process is for sample sets where the deviation from the mean content percentage value is large the relative progression over time is shown, whilst when choosing one set value to compare against the overall effects of temperature and steam content are more comparable. Due to the aim of the research a single normalised value was used to cross-compare the data.

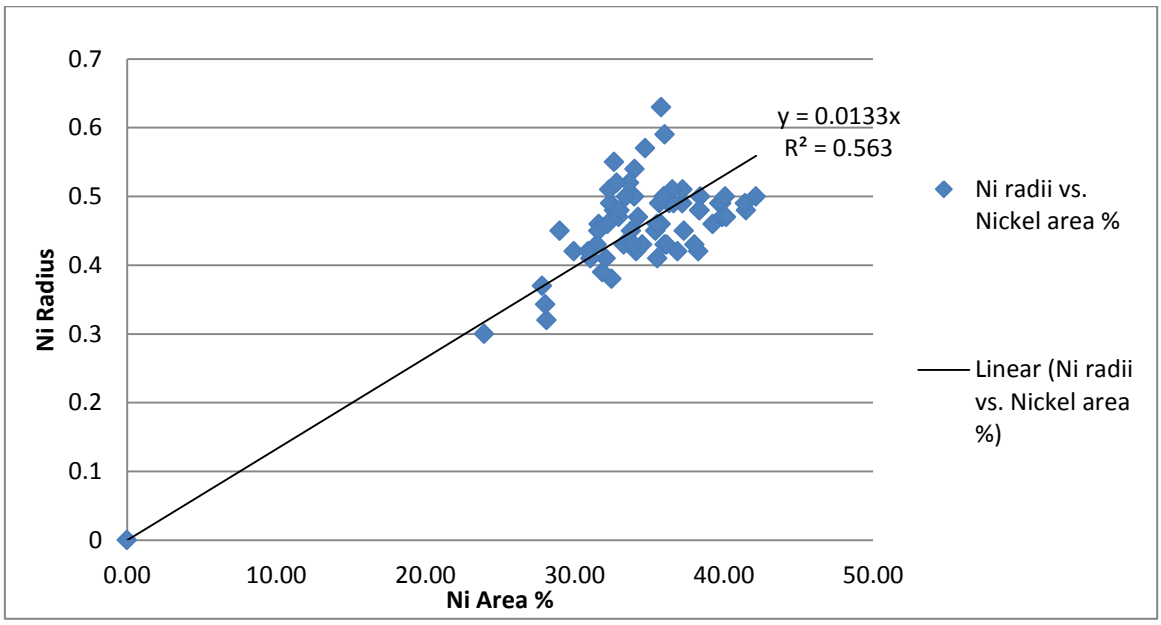

Figure 4-7 Correlation between Ni content and mean Ni particle radius. A linear line of best fit has been applied to the sample values for the mean Ni radius relative to its Ni content percentage.

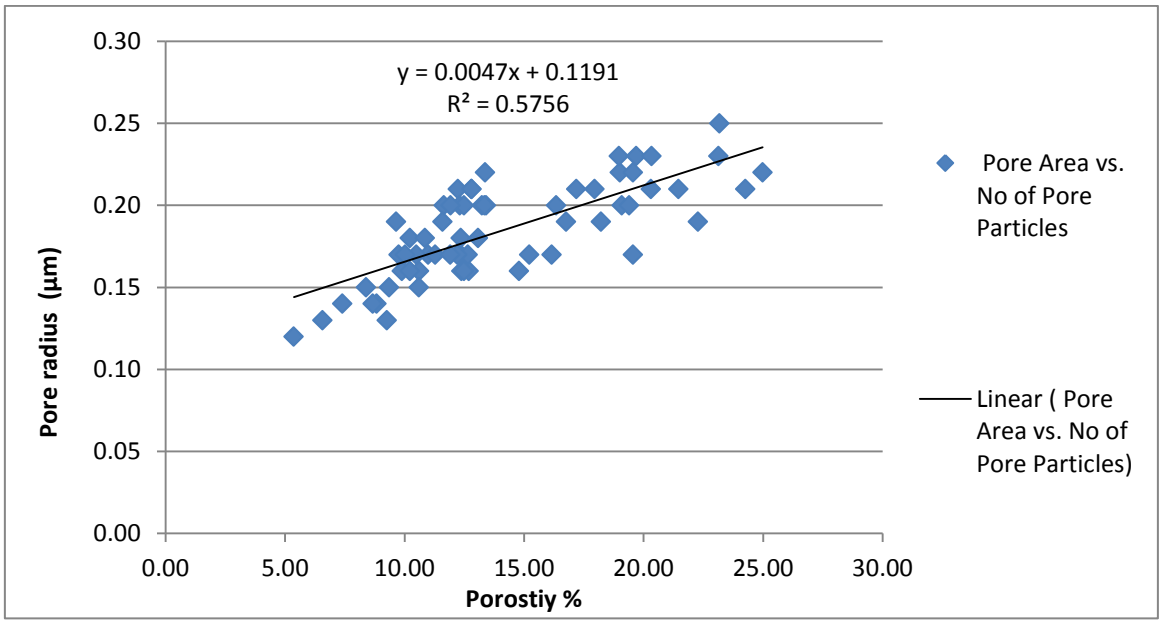

Figure 4-8 Correlation between porosity and mean pore radius. A linear line of best fit has been applied to the sample values for the mean pore radius relative to its porosity.

Looking at the normalised Ni radii from Figure 4-9, there is a trend for increasing mean particle radius over time, as well as a general trend for increasing Ni radius due to steam content and temperature. Figure 4-10 shows this trend via trendlines across the values present. This evidence corroborates with the understanding of the literature that the energy provided by the temperature and the coarsening effect of the steam both lead to larger particle radius.

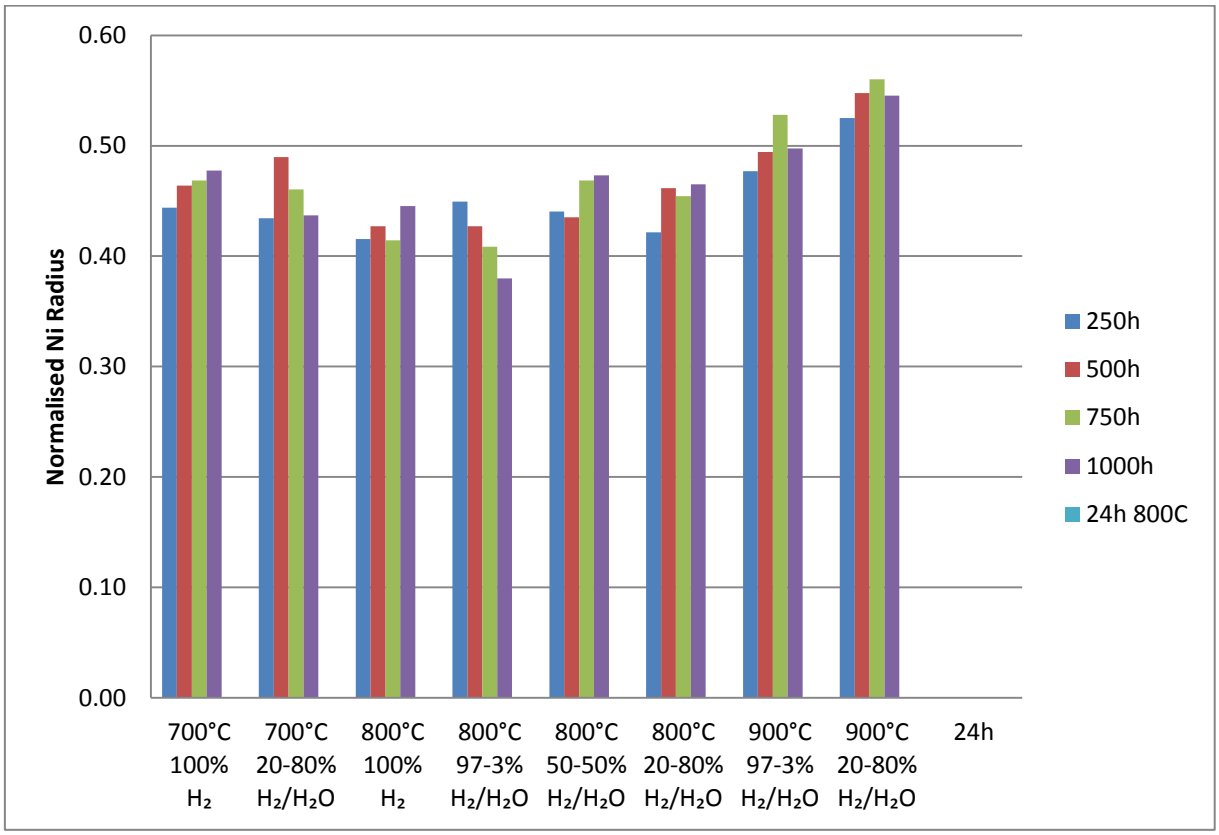

Figure 4-9 Ni particle radius normalised relative to their Ni content. Values are adjusted according to the relative amount of Ni greater or less than the average of 34 percent.

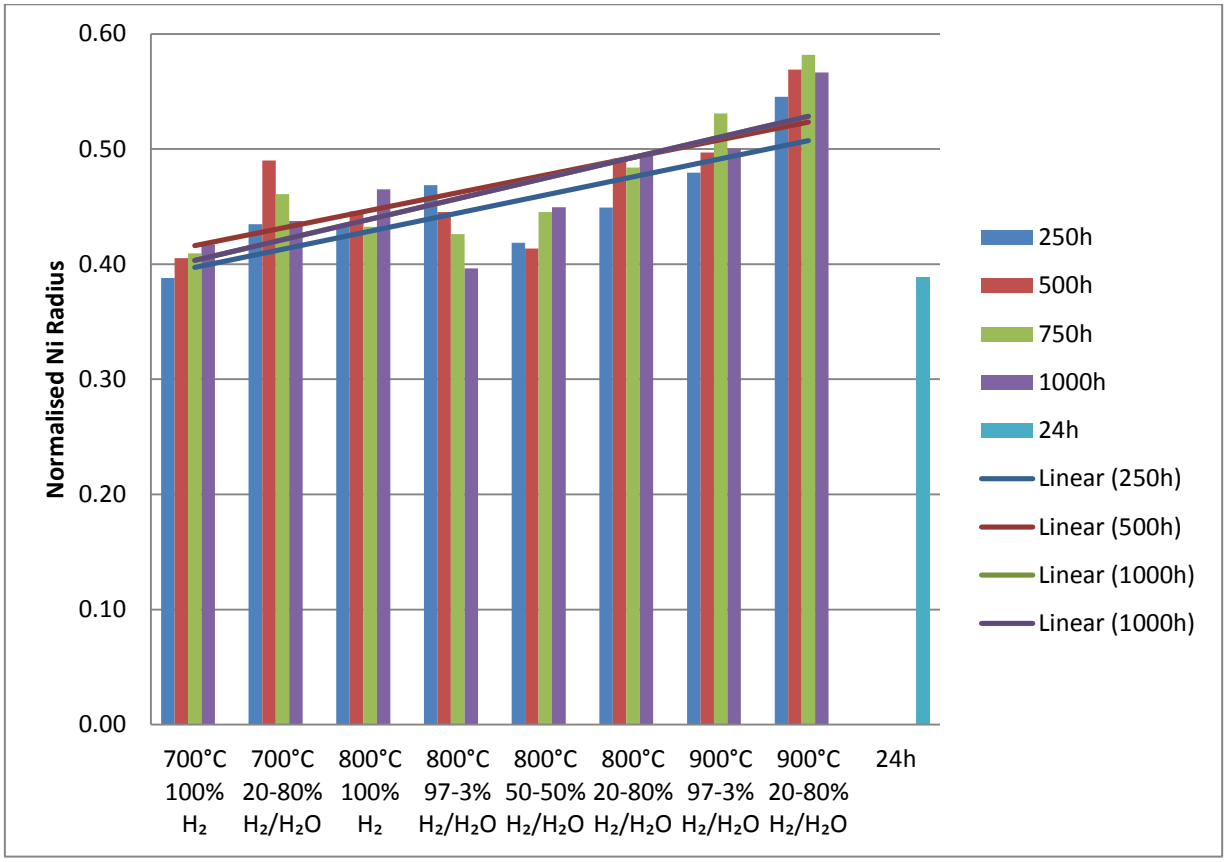

Figure 4-10 Graphic highlighting the general trend of effect of steam and temperature on Ni particle radius that have been normalised according to their Ni content.

The theory of particle coarsening is based around the consumption of smaller particles to create larger ones. This in theory should lead to a reduction in particle number over time and dependent on the environment in which they are exposed.

Figure 4-11 suggests that the number of particles is relatively independent of the respective area percent in the cell. Whilst there is a slight positive correlation, it is unlikely to be especially determinant in the number present. The relative lack of trend suggests that at least overall, the total number of pores can change irrespective of

the area change, which would mean that if there is a change in number of particles then it is due to a shift in the size distribution. Thus the number of pores has no influence on the area percentage, meaning the more pores present the smaller they are.

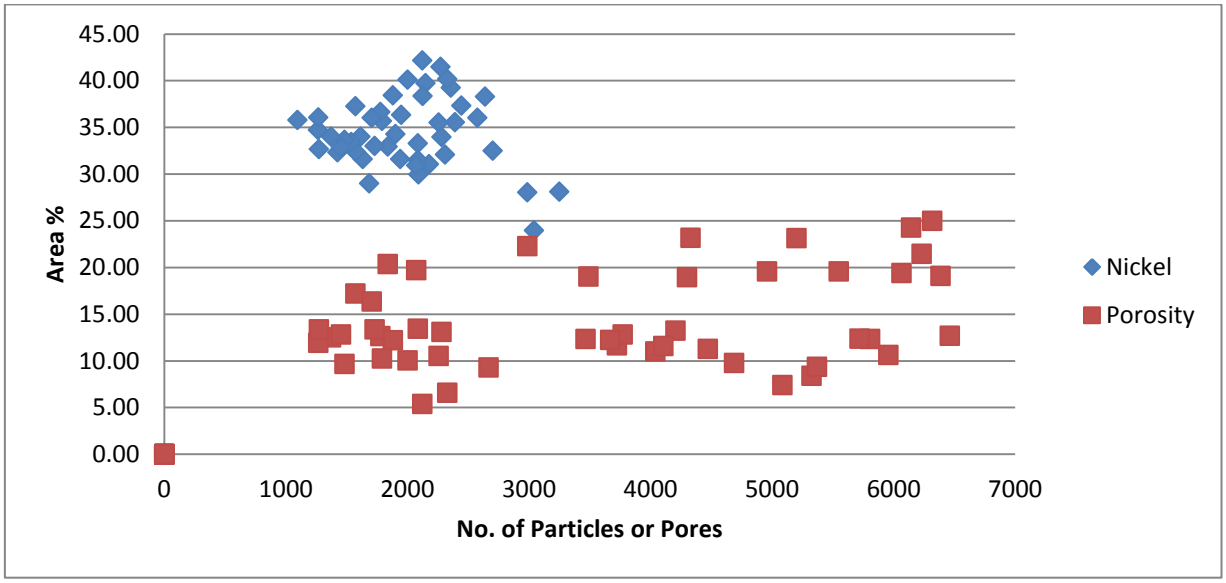

Figure 4-11 Number of Ni particles over Ni area and pores and porosity. The relative spread of samples indicates a lack of correlation between the two factors for both Ni particles and pores.

Plotting the variation in Ni particle change gives Figure 4-12, which highlights that the number of particles generally decreases as time goes on, which theoretically is what you'd expect of the microstructure. Only 800°C 97-3% H_2/H_2O shows an unexpected trend in particle size. The general slope downwards from the lowest temperature and steam content to the highest temperature and steam content samples is clearly visible. There appears to be a smaller number of particles present as temperature increases i.e. particle growth.

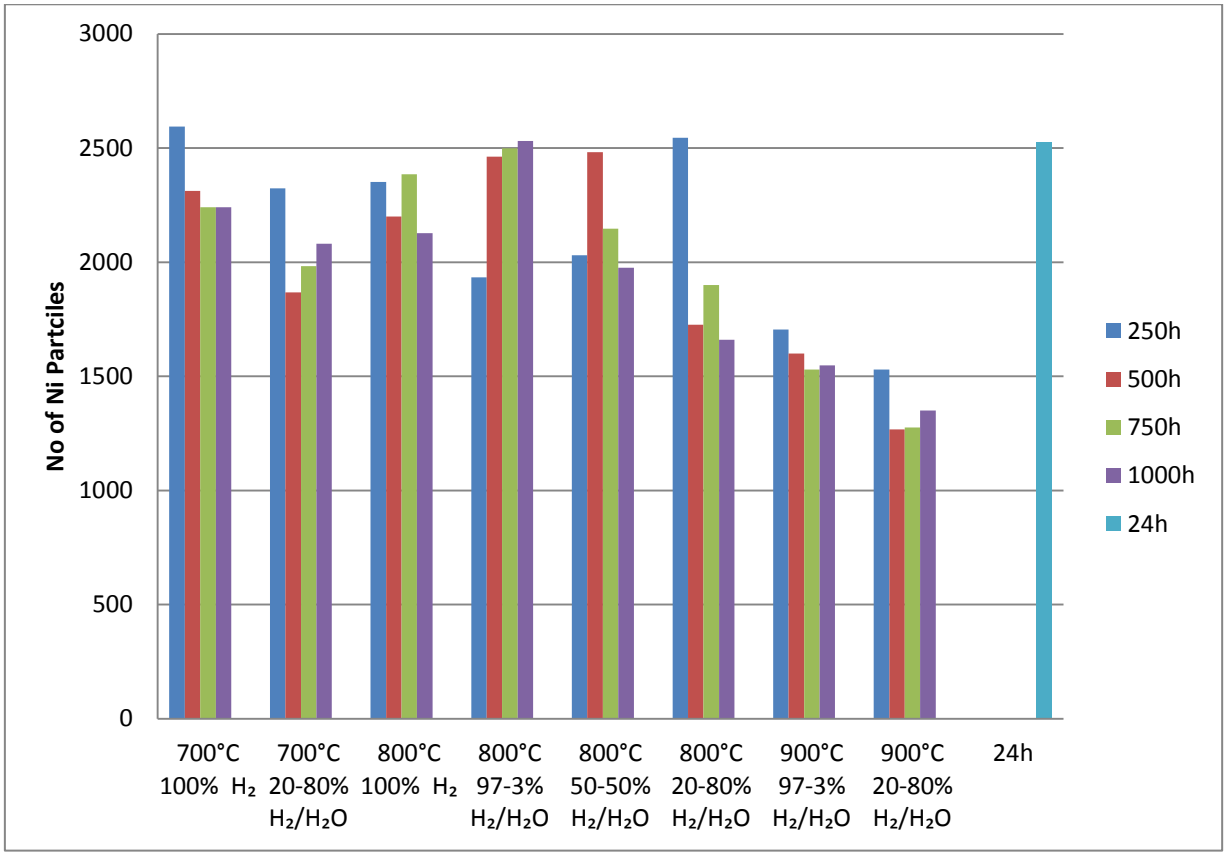

Figure 4-12 Number of Ni particle for given data set. Each time frame shows the average of two samples. Each sample was evaluated through 12 images covering random sections of the sample.

For pore numbers, similar trends to those present in the Ni particle distribution persist, but not as an exact parallel. Some samples have a significantly higher number of pores compared to the change in Ni particle number for the same subsets. Also there is often an increase in the number of pores visible. Compared to the area percentages, which should remain constant, the pores and nickel particles would behave differently. The nickel particles agglomerate due to the energy provided, to reduce surface energy. The porosity however is shaped by this movement, and cannot alter itself as such. Thus unlike the Ni particles which would see an eventual

elimination of small particles given the right conditions, small pore particles will always be present in the pore distribution. Equally large pore particles can be formed by the movement of smaller particles into larger ones. This explains why the pores do not follow a similar pattern to the Ni particles. It is worth noting that whilst the YSZ should remain relatively inert, very small pores [232, 233] may see collapse due to YSZ grains growing into the vacancies. Figure 4-14 shows the Ni particle number decreases with increasing mean Ni radii, whilst the pore radii is entirely independent of the pore number, as shown by the linear line of best fit.

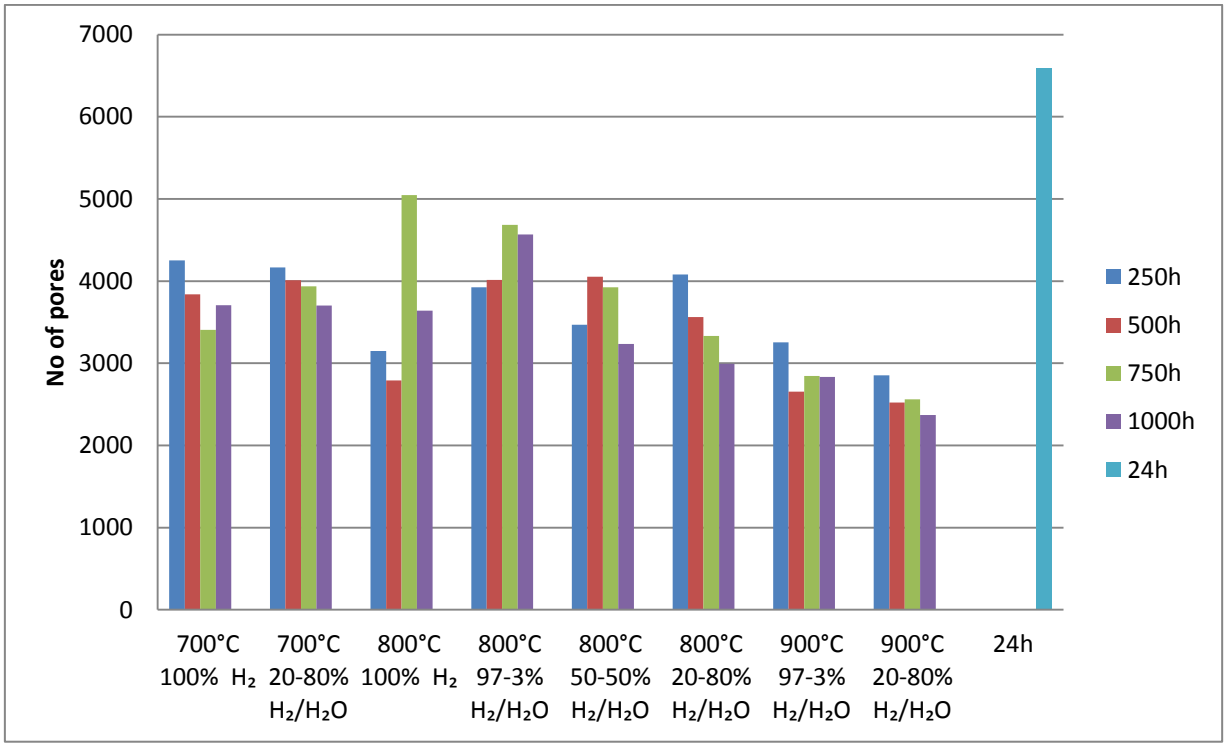

Figure 4-13 Number pores for given data set. Each time frame shows the average of two samples. Each sample was evaluated through 12 images covering random sections of the sample.

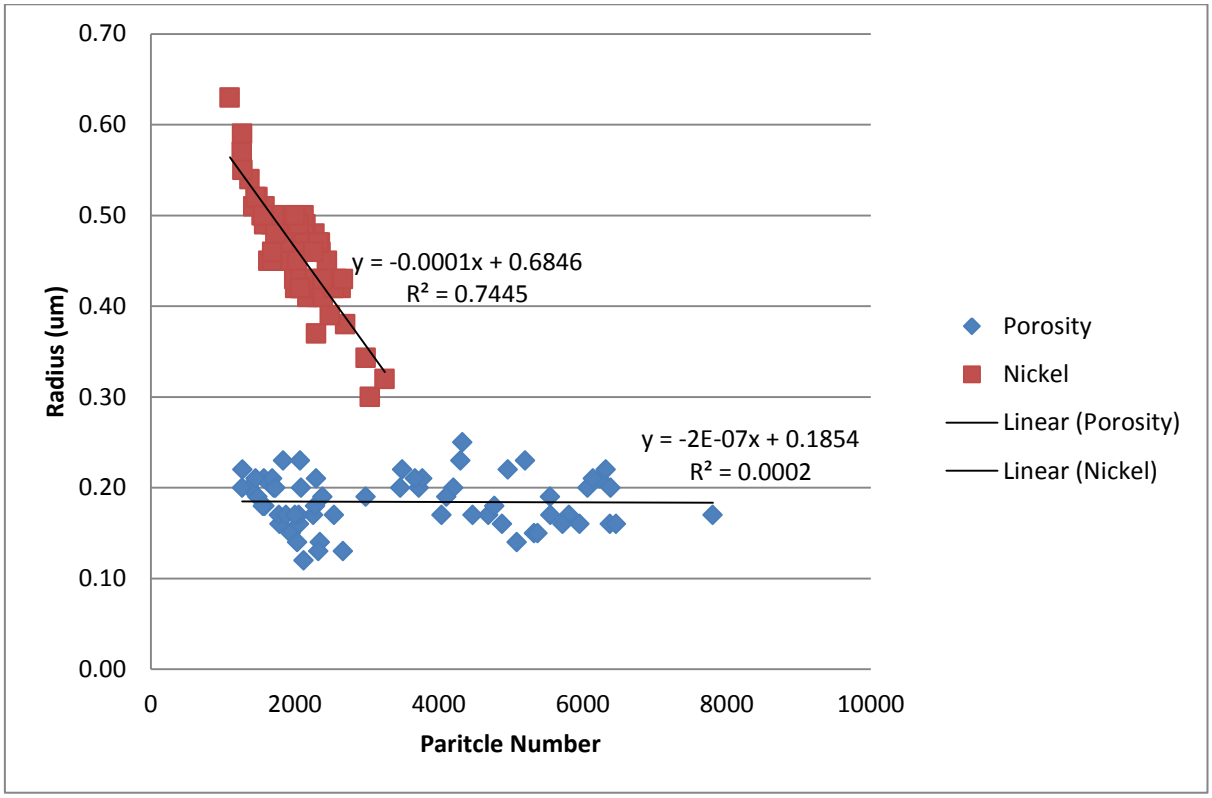

Figure 4-14 Comparison between mean nickel radius values (µm) and particle number and mean pore radius values (µm) and pore number. Linear lines of best fit have been applied to both sample sets showing a strong correlation for Ni and a weak/non-existent one for porosity.

Looking over the histograms presented in Figure 4-15 from the Ni particles in the sample set a clear trend can be seen wherein the number of relatively smaller particles (<0.1um), present in a high number in the 250h samples, disappear subsequently in the other sample times. This backs previous analysis regarding the change in particle number and how this effects the mean Ni values determined.

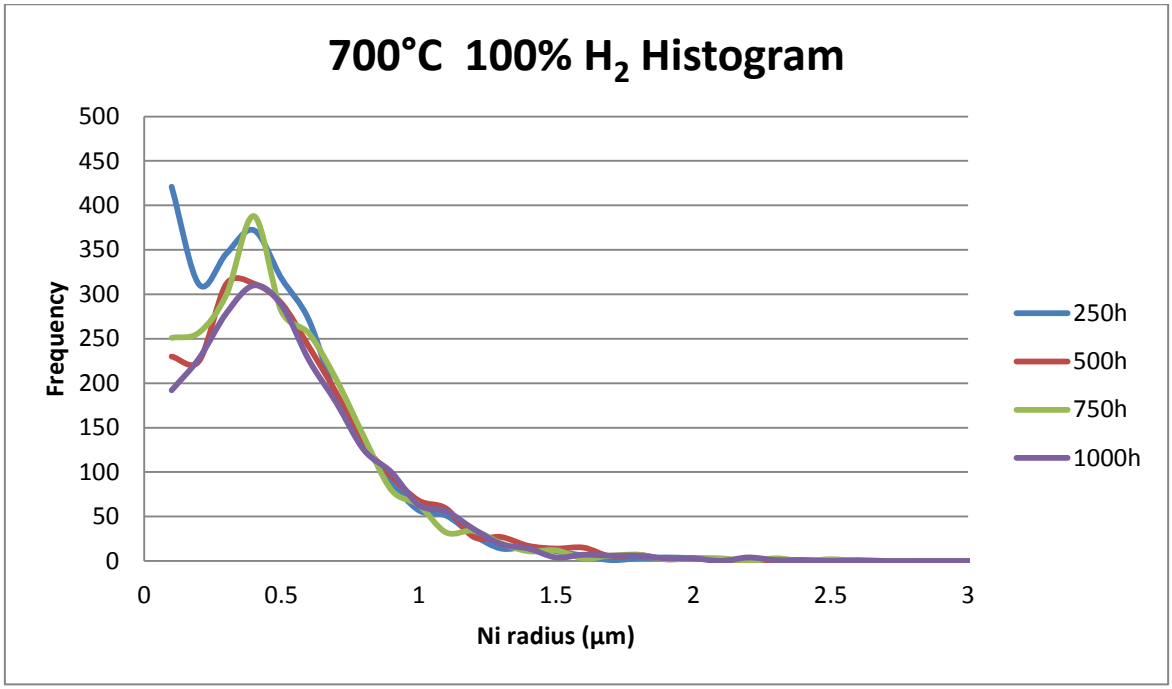

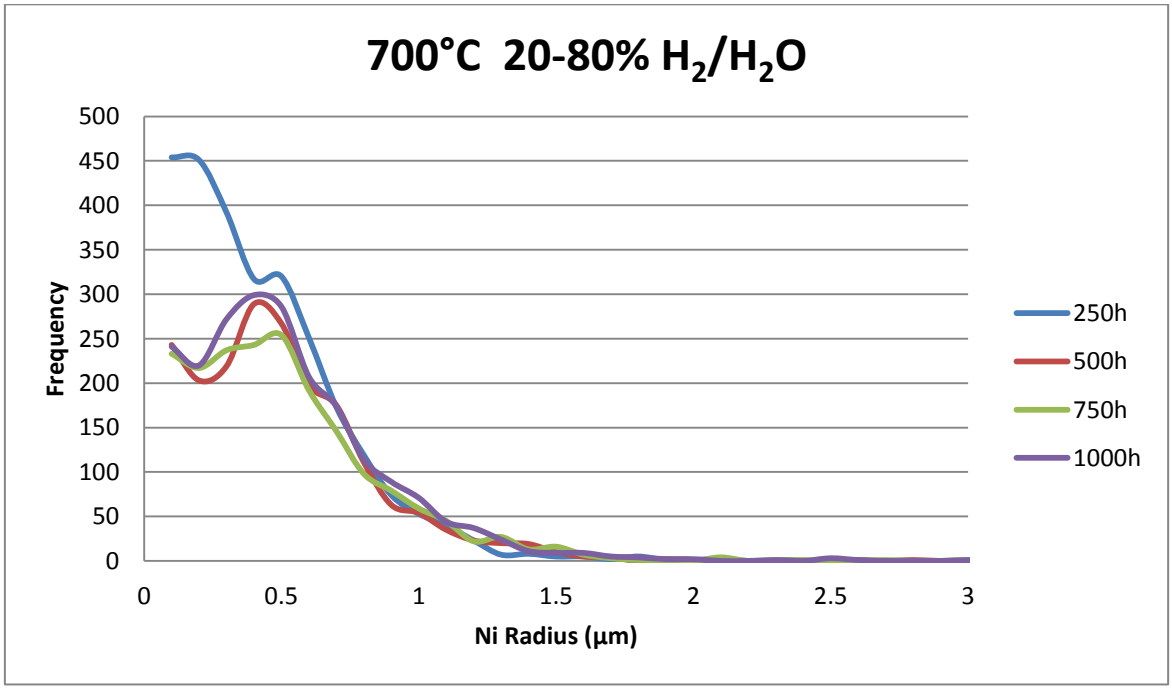

Figure 4-15 Example histograms of Ni particle radius, showing two samples and their relative size distributions for their 250, 500, 750 and 1000 hours samples.

Based on the value for the initial Ni particle radius at 250h versus the final radius at 1000h, Table 4-2 shows the relative increase or decrease for those values. Whilst the trend overall for the 4 values generated from each sample set are more insightful to the change in the anode, a numerical value can highlight differences between the microstructural changes for a given regime. Overall there is a more noticeable increase in mean radius for the 700°C and 800°C temperature ranges, whilst 900°C, which has already reached a larger mean particle radius by 250h, shows a modest increase over the 97-3% & 20-80% fuel regimes. It is also worth noting that the change for the 97-3% H_2/H_2O sample actually showed a negative growth, which was attributed most likely to different initial microstructures for the sample.

Table 4-2 Numerical changes in Ni particle radius from 250h to 1000h. the 800°C value shoes a decrease between 250h and 1000h.

Temp(°C)/ Fuel(H_2/H_2O)l	**100%**	**97-3%**	**50-50%**	**20-80%**
700	9.6%	N/A	N/A	6.9%
800	7.3%	-15.5%	9.5%	10.1%
900	N/A	2.8%	N/A	3.9%

To help further clarify the impacts of temperature and steam content on the Ni particle growth, Figure 4-16 compares the data points for a given temperature range against the different fuel compositions. The values have been adjusted according to their Ni content and subsequently normalised based on an initial radii value of 0.38 μm (derived from 24h reduction testing and analysis done). The figure clearly

highlights the expected resultant impact that both temperature and steam have a direct correlation to the mean Ni particle radii. With respect to the temperature the difference between 700°C and 800°C is less significant compared to 900°C. Given the increased rate of coarsening known to occur above 2/3rds of the melting point (which for nickel is 879°C), this is entirely expected. Given that this graph does not highlight the specific time points for these data points the accelerating effect of the steam on the nickel particles is less apparent but still clearly visible (especially for the 700°C and 900°C regimes). 800°C 97/3% H_2/H_2O had the unusual resultant behaviour with a general decrease over time, which the figure does not represent due to its presentation. Interestingly if compared solely against the pure hydrogen 800°C test, the data points mirror each other.

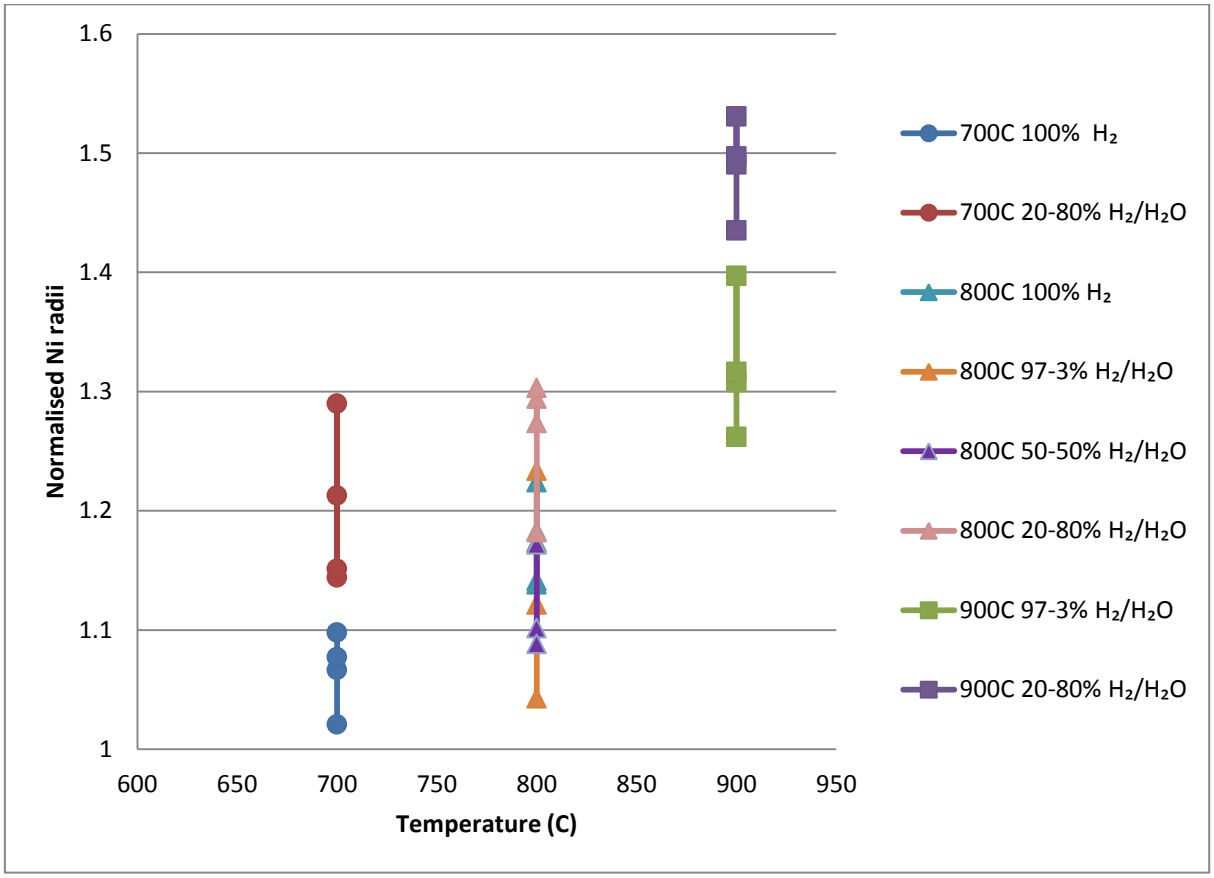

Figure 4-16 Ni particles normalised to 0.38µm radii over temperature setting. The value of 0.38 µm was determined from initially reduced samples average Ni particle radius. Note that the figure does not highlight which samples are largest and which are smallest of 250h, 500h, 750h and 1000h.

4.3 Conclusions

Data was collected from EDX imaging of sections of samples from each sample set. This data was analysed to give H_2/H_2O the percentage area of nickel, zirconia and the porosity. It was also examined to determine the total number of nickel particles and pores and their respective radii. The area percentage data was compared to see trends for sample sets and across increasing temperature and steam content. This

data was normalised to represent an average 50% YSZ content. The overall average was fairly similar across all samples, as unless there was a volatisation, the nickel should only have moved within the anode sample. However, some samples retained higher nickel content percentage than expected from an effectively reduced cell (50% NiO would give roughly 30% Ni). This could be an effect from polishing reducing the visible porosity, but was not shown to affect the Ni content or YSZ. Whilst porosity values showed more noticeable variation compared to the Ni content, no trend was applicable to the variation in the porosity and thus appeared to be constant.

Reasonably large standard deviations were present in the samples. Due to the experimental and time constraints only 1 run of a sample set was completed, though 2 specimens for each set of samples was tested further and analysed. This helped mitigate the effects of an individual sample producing particularly skewed data; however, it does less to prevent singular instances on an experiment-wide level having an impact which may have influenced the results, such as furnaces temporarily losing power.

Samples were analysed across random sections of the sample to ensure data represented the overall trend in microstructural change. Where samples had particularly dense regions unable to be imaged this constricted viable sections a bit but overall all samples were able to produce a distributed region of samples imaging.

The initial microstructure of the Ningbo samples is important for determining the long term microstructural change. Other samples with different microstructures or material compositions could likely meet different results than the samples tested here. One or

two samples had particular aberrant behaviour and attempts to repeat these experiments would likely highlight they are anomalous behaviour. However, if the same samples were tested in similar environments the overall growth trends and patterns present here should provide reproducible results.

Nickel particle radius shows a trend to increase in mean size with increasing temperature and/or steam content over time. Normalising the data relative to the nickel area percentage allows for a more accurate comparison of trends within groups, as well as across groups for the effects of temperature and steam on the anode microstructure. The change in Ni particle numbers corroborate with the trends seen for the Ni radius, as an increase in mean value should be facilitated by a decrease in the number of smaller Ni particle in favour of fewer larger particles.

The pore radius showed less comparable trends to the Ni particle radius, which ascribed to the fact the pore sizes are altered based on the Ni particles changes, leading to formation of large and small particles in remnants of previous Ni sites. Thus the mean trend of values does not follow a similar pattern to Ni particles in Ni-YSZ anodes.

CHAPTER 5 Particle Radius Modelling for TPB and Conductivity Predictions

As discussed in section 2.3, long term degradation in the anode is the result of agglomeration and coarsening of the Ni particles in a Ni-YSZ anode. The agglomeration occurs through sintering of the particles, which was predominately attributed to volume diffusion or migration of vacancies, at least for the initial sintering process. This is when the atoms move to occupy the vacancies due to the concentration difference between particles [295]. Coarsening is the result of Ostwald ripening, where larger particles grow at the expense of smaller ones, in an attempt to reduce surface energy. YSZ is known to inhibit both of these mechanisms[184], through non-wetting of the Ni particle, but to what extent can be dependent on the composition and size distribution of the particles in question.

By building on empirical data taken from literature and testing, models which describe the predicted change in mean Ni particle radius have been developed [237, 277, 284]. Both models by Nakajo et al and Gao et al (which is based on work by Vassen) have been recreated and compared with the available data. A particle packing based model developed by Chen et al [289] is used to predict microstructural parameters. This is combined with the Ni particle radius predicting models and produces values for the change in TPB length per unit volume and conductivity in the SOFC anodes. The complete combined modelling process can be combined with electrochemical performance data or used to outline accelerated testing for SOFC anode improvement.

5.1 Vassen Model

One of the earliest models used to predict Ni agglomeration in SOFC Ni-YSZ anodes was developed by Vassen et al [237], and has subsequently been used many times either in reference for values or to build upon the core derivations. It is based on surface diffusion of particles resulting in sintering and a progressive increase in mean Ni particle size.

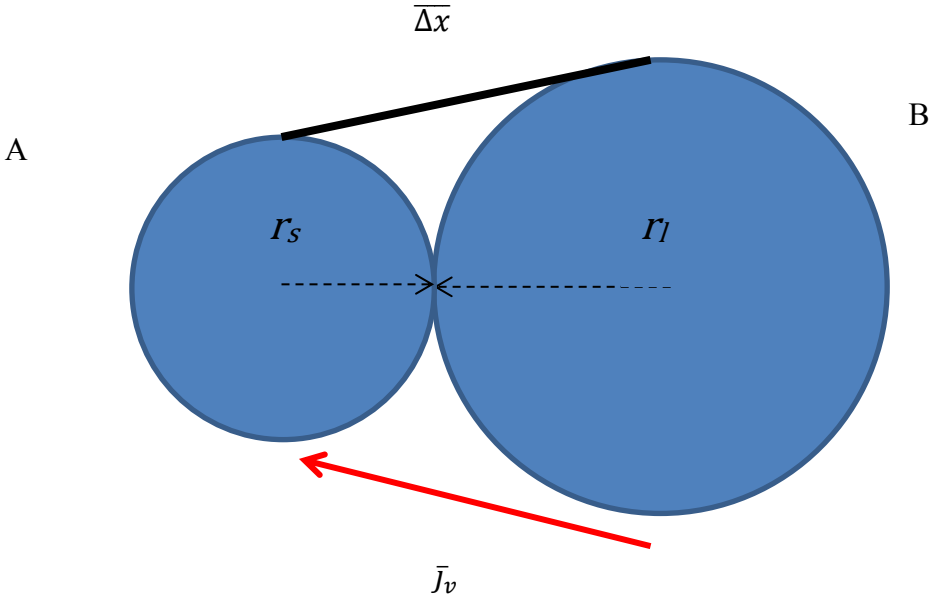

Figure 5-1 Geometric model of agglomeration process for two Ni particles. The flux $\bar{J}_v$ of vacancies travels from the larger B particle to the smaller A particle, simultaneously increase the size B.

In Figure 5-1 two nickel particles are shown, where due to a different curvature a pressure difference is created which causes a change in vacancy concentration leading to a flow of vacancies from the large particle to the small one. This vacancy

flow $\bar{J}$ is described by Fick's law of diffusion and is defined relative to this example in Equation 5-1

$$\bar{J} = D_{v,s}\frac{dC}{dx} \approx D_{v,s}\frac{\Delta C}{\overline{\Delta x}} = D_{v,s}\frac{C_f \Omega \gamma}{\Delta x k_B T}\left(\frac{1}{r_s} - \frac{1}{r_l}\right)$$

Equation 5-1

The vacancy surface diffusion coefficient is $D_{v,s}$, Δx is the diffusion distance, and the change/difference in vacancy concentration ΔC. This can be further expanded to include C_f, which is the vacancy concentration for a flat surface. k_B is the Boltzmann constant, Ω is the mean atomic (or molar) volume of the particle, γ is the surface energy), and $r_l$and r_s are the radius of the large and small Ni particles in question.

Due to thermodynamic instability caused by the concentration difference, the particles will attempt to reach equilibrium for which the particles will begin to join. The solubility of the Ni particles will be affected by their radii and is described by the Gibbs-Thomson relation [296], and allows for calculation of the vacancy concentration as shown in Equation 5-2. This relationship describes the solubility of the particle (Ni in this case) atoms in the lattice matrix, where ΔG is the change in Gibbs free energy, and ΔP is the change in pressure.

$$\Delta C = C_f \frac{\Delta G}{k_B T} = C_f \frac{\Omega \Delta P}{k_B T} = C_f \frac{\Omega \gamma}{k_B T}\left(\frac{1}{r_s} - \frac{1}{r_l}\right)$$

Equation 5-2

The distance between A and B, as shown in Figure 5-1, for the vacancy to diffuse Δx, is described in Equation 5-3. This takes into account the changing size of r_l and r_s as shown.

$$\Delta\bar{x} = \sqrt{(r_l + r_s)^2 + (r_l - r_s)^2} \qquad \textbf{Equation 5-3}$$

To help further facilitate the modelling, a description for a mean nickel radius r_{Ni} and the radius difference Δr are introduced. The mean radius is equal to $r_{Ni} = \frac{r_l + r_s}{2}$ and the radius difference is equal to the large particle radii minus the small particle $\Delta r = r_l - r_s$, as shown in Figure 5-1.For this model it is important that Δr is proportional to r_{Ni} for the duration of the growth. This indicates that the particle size distribution remains a similar shape during agglomeration. A constant for this proportionality, β, is presented in Equation 5-4. This value is assumed to be constant during the agglomeration process [237], and is a fitting proportionality parameter. This assumption is justified empirically due to the fact that the average particle radius difference is generally large when the average particle size is large.

$$\beta = \frac{(r_l - r_s)}{2r_{Ni}} \qquad \textbf{Equation 5-4}$$

The volume change which occurs via diffusion through a surface area with thickness $\delta_s$and circumference of $2\pi r_{Ni}$, and the equal volume change occurring in the large nickel particle, are shown in Equation 5-5 and Equation 5-6 respectively.

$$\frac{dV}{dt} = -\bar{J}_v \delta_s \Omega 2\pi r_{Ni}$$ **Equation 5-5**

$$\frac{dV}{dt} = 4\pi r_l^2 \frac{dr_l}{dt}$$ **Equation 5-6**

The atomic surface diffusion coefficient $D_s = D_{v,s} C_f \Omega$, combined with the previous equations used provide Equation 5-7, which evaluates the change in mean Ni radius over time.

$$\frac{dr_{Ni}}{dt} = \frac{\delta_s \Omega D_s \gamma}{2k_B T} \frac{1}{r_{Ni\infty}^3} \frac{\beta}{(1-\beta^2)(1+\beta^2)(1+\beta)^3}$$ **Equation 5-7**

This equation however does not take into account the limiting effect of the YSZ in the cermet. Vassen et al compared their work against finite element calculations and found it to be a reasonable match, but incorporated a growth restricting element to their model

$$\frac{dg(t)}{dt} = \frac{\delta_s \Omega D_s \gamma}{2k_B T} \frac{1}{r_{Ni\infty}^4} \frac{\beta(1+\beta)}{(1-\beta^2)(1+\beta^2)} \frac{1}{1-g(0)^3} \frac{1-g(t)}{g(t)^3}$$ **Equation 5-8**

This inclusion eventually inhibits the value for r_{Ni} to go beyond a max value $r_{Ni\infty}$. This growth restricting value $g(t)$ is defined in Equation 5-9, and uses the current value of r_{Ni} in its calculation to determine its dimensionless value.

$$g(t) = (1 + \beta)\frac{r_{Ni}}{r_{Ni\infty}}$$ **Equation 5-9**

5.2 Nakajo et al Ni radius predicting model

Nakajo et al [277] have developed a degradation model in an attempt to predict nickel particle growth in Ni-YSZ anodes. Using a modified equation developed by Vassen et al [237], Nakajo produced an equation to describe the rate of Ni particle growth dependant on temperature and steam/hydrogen composition.

5.2.1 Nickel particle radius predicting equation

The equation adjusts a normalised Ni particle radius over time to see the rate of growth (as Ni particle sizes vary from manufacturer to manufacturer). A slightly modified equation to the one presented in their work is shown in Equation 5-10 (the value $r_{Ni(0)}$ needed to be cubed, unlike the one presented in the publication).

$$r_{Ni}^2\frac{\partial r_{Ni}}{\partial t} = k_{0D_{an}} exp\left[-\frac{Ea_{D_{an}}}{R}\left(\frac{1}{T} - \frac{1}{T_{ref}}\right)\right]\frac{x_{H_2O}}{x_{H_2}^{0.5}}\frac{r_{Ni\infty}^3 - r_{Ni}^3}{r_{Ni\infty}^3 - r_{Ni(0)}^3}$$ **Equation 5-10**

here r_{Ni} is the Nickel particle radius, $r_{Ni\infty}$ is the max Ni particle radius, $r_{Ni(0)}$ is the initial particle radius, $k_{0D_{an}}$ is the anode degradation rate constant, T is the set-point temperature, T_{ref} is the reference temperature, R is the universal gas constant, $Ea_{D_{an}}$is the energy barrier for anode degradation and x_{H_2} and x_{H_2O} represent the hydrogen and steam partial pressures respectively. The paper acknowledges issues

in getting accurate comparative plots for samples with low H_2/H_20 ratios. An example of part of its flaw is highlighted in Figure 5-2, where for higher water content the model predicts reasonably well for the data available [297], however at lower water content (4% H_2O) it significantly overestimates the particle growth [277]. An attempt to improve this aspect of the model has been incorporated into this study. Values used specifically in this model taken from literature can be found in Table 5-1.

Table 5-1 Data values for Nakajo calculations.

Symbol	Description	number	reference
$Ea_{D_{an}}$	Activation energy of anode degradation (kJ mol^{-1})	15.15 gProms Determined	[277]
$k_{0D_{an}}$	Rate constant for Ni particle grain growth	1.05 x 10^{-3} gProms determined	[277]
T_{ref}	Reference temperature (K)	873	[277]
Ω	Volume Element (m^3)	1.09 x 10^{-29}	[237]

Values determined through gProms were based on experiments done with Ni-YSZ anode supported cells from two different sets of experiments. The results were subsequently compared against literature data. The conditions under which these tests took place are similar to those being investigated in this work.

5.2.2 Comparisons of Model with Literature and Experimental Data

Nakajo's model was compared against a number of available literature data points for Ni radius growth to show accuracy.

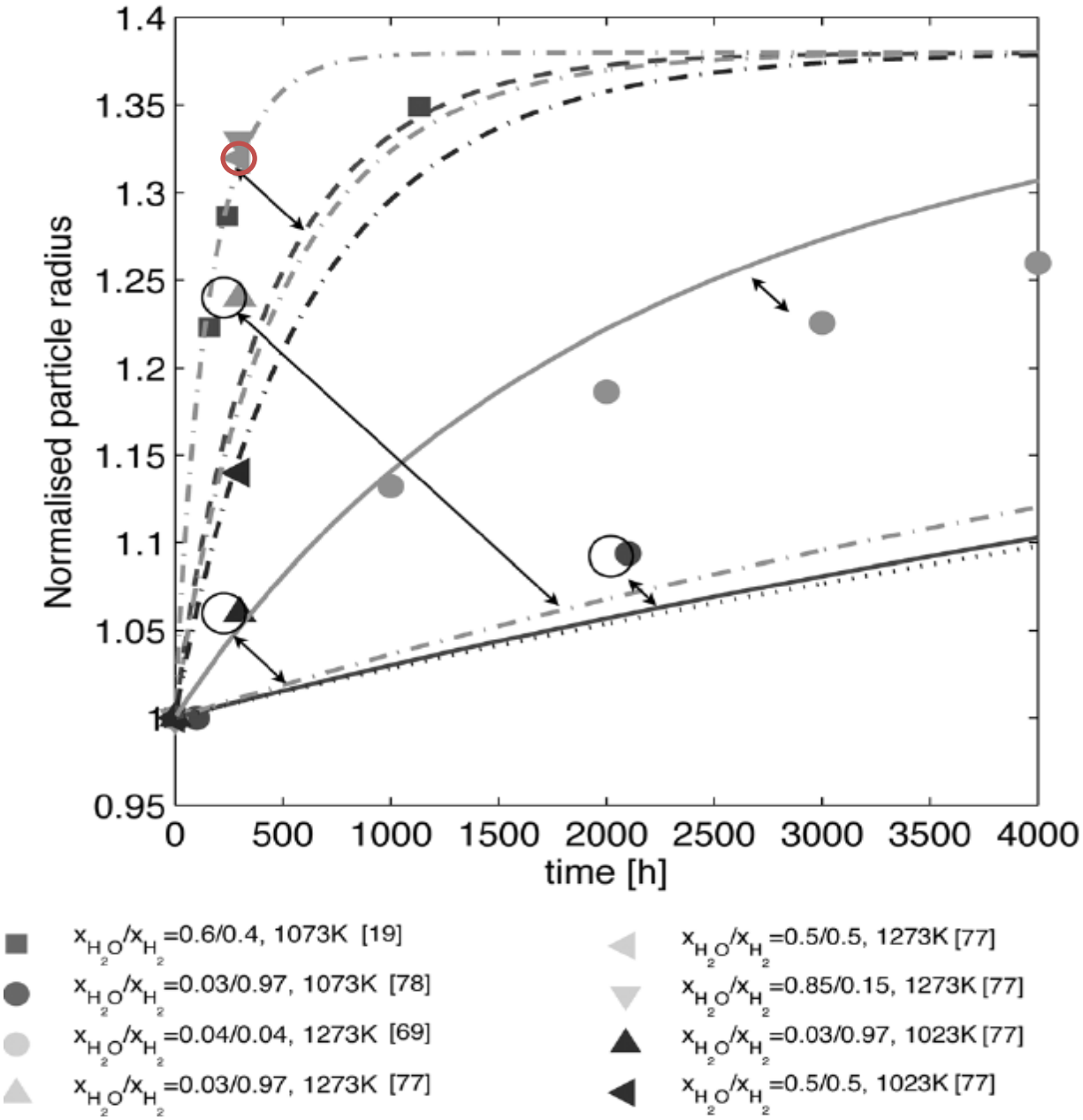

Figure 5-2 Nakajo et al's model for Ni particle increase compared to available literature, as presented in source [277]. 0.04/0.04 refers to a 4% H_2, 4% H_2O 92% Ar mixture.

Looking over Figure 5-2 it is important to highlight a number of issues. The referenced value for Thyden's [241] 1000°C 50/50% H_2/H_2O is not the ~1.32 shown

in Figure 5-2 (which was the lower of the two values generated and identified by a red circle), but an average value of 1.375. The author's explain that the model does not predict accurately for systems with low steam partial pressures. Noticeably in their results all of the 97/3% H_2/H_2O experiments [17, 241] are shifted away from their estimated radius (especially Thyden's 1273K experiment). In particular the model does not predict the effects of high temperature and low steam content, which it undervalues in terms of its accelerating affects.

Figure 5-3 shows how the data looks taking into some of the difference in referenced data points. It is worth noting that the value for Thyden's 1000°C 50/50% H_2/H_2O data point was formed of two values of which one showed a particularly high mean radius value. This heavily skews the normalised data point (~1.42 normalised radius), compared with the others generated from this study, which follow a trend of increasing mean value for higher temperature and or steam content. It also highlights that SOFC Ni-YSZ anode samples often have wide standard deviation due to their microstructure.

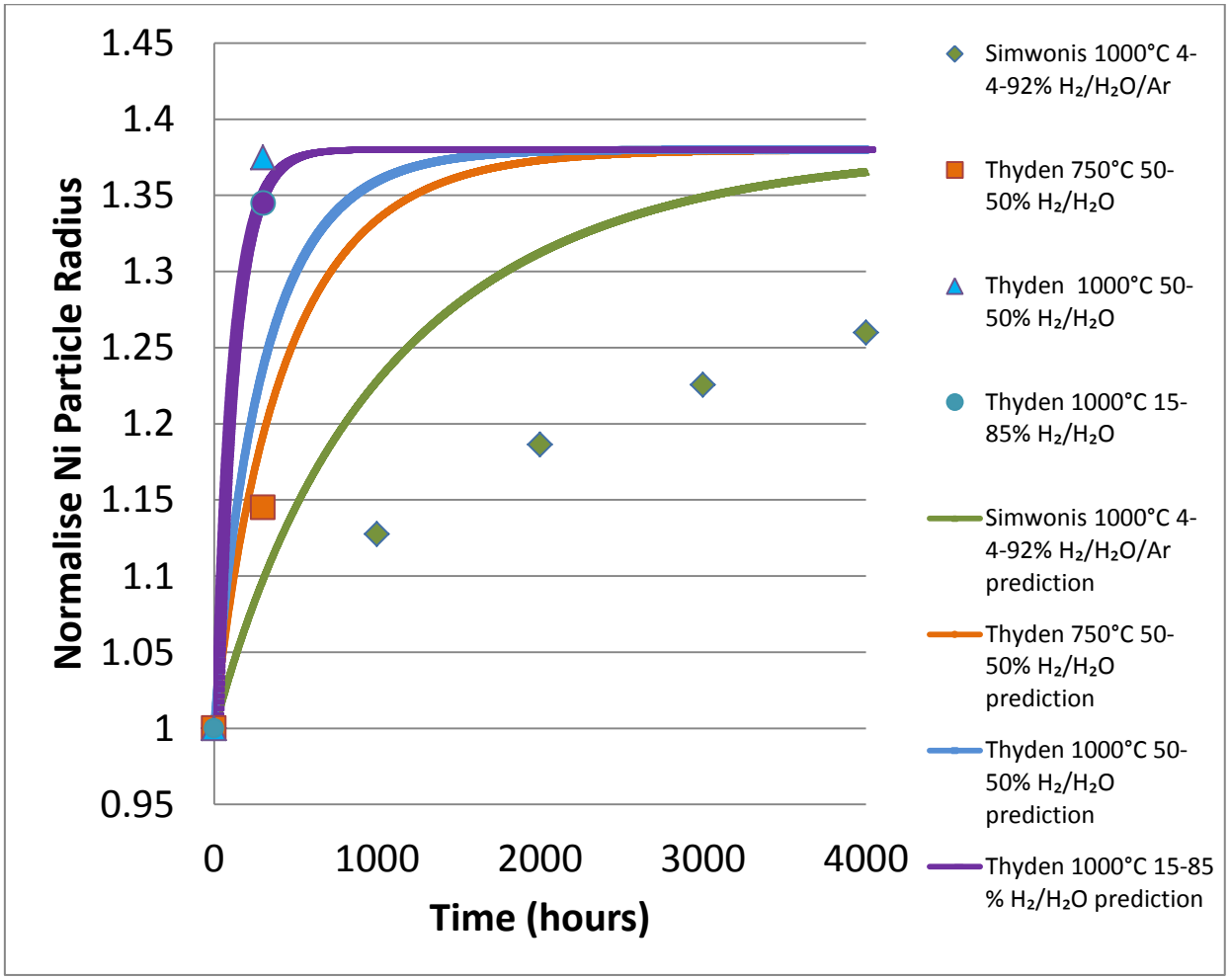

Figure 5-3 Comparison of Nakajo et al's model for normalised Ni radius predictions. Values are normalised to their initial particle radius

Based on the relative accuracy of the model for higher steam content experiments, an attempt to compare the Ningbo cells to the predicted outcomes defined by Equation 5-10 were compiled in Figure 5-4. It is immediately apparent that whilst providing a good fit for the 900°C 20%/80% H_2/H_2O test, the other tests are significantly overestimated. Various aspects regarding the model could attribute for this disparity. Firstly the model does not appear to appropriately consider the effects of temperature on the Ni sintering. It appears to be determined more by the effects of

steam, apparent through the relatively close curves shown for 700°C, 800°C and 900°C at 20%/80% H_2/H_2O, whilst the 50%/50% H_2/H_2O test is significantly lower, though no less inaccurate in its attempts to predict the rate of sintering. Secondly the limiting effect of YSZ could likely have an effect on the rate of Ni agglomeration (and not just the maximum mean radius). With no specific component in the equation to adjust for this, the difference in microstructures and total Ni volume percentage is ignored, meaning certain predictions may underestimate or overestimate. It is also worth noting that the experimental data does have a relatively large standard deviation and that the predictions, should it provide a similar curve to that shown, would be unlikely to match perfectly.

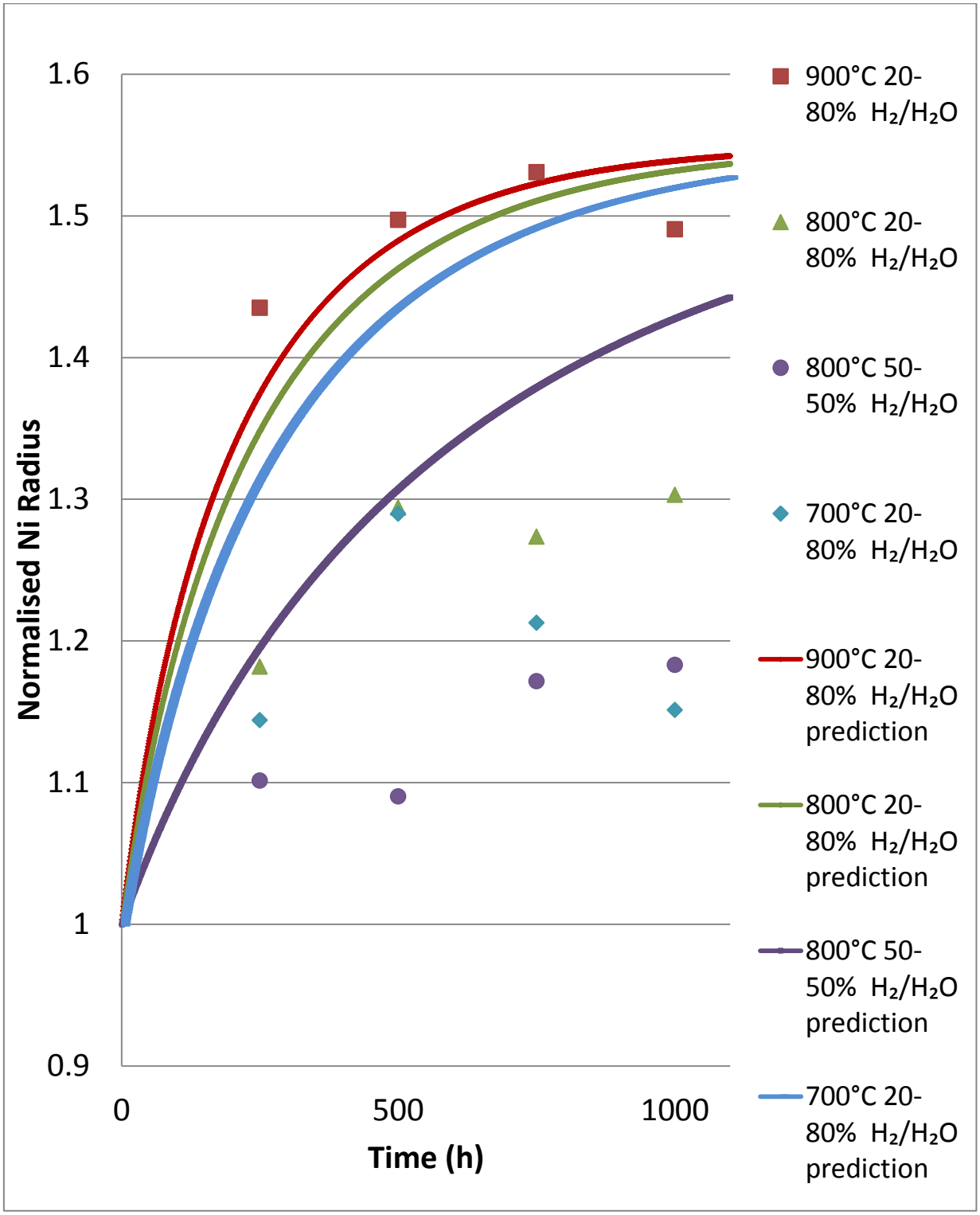

Figure 5-4 Experimental data versus Nakajo model equations. Samples normalised to 0.38 μm Ni particle radius. Note the relative inaccuracy in predicting Ningbo samples tested under varying conditions.

With the relative unsuitability of the model as taken from literature steps were then taken to bring the model more in line with the microstructural environment the Ningbo cells present in our own experiments. Initial attempts to tweak the model in small incremental ways did not adjust suitably for one data set without comprising the others. Due to the noticeable inability to account for the impact of temperature on the rate of change in mean Ni radius in the model, an attempt to correlate to the expected radii via an adjusted value for $Ea_{D_{an}}$ and an additional temperature component was incorporated. The adjusted model fits a 2nd order polynomial with temperature alongside a new value of $k_{0D_{an}}$ (0.00315) and $Ea_{D_{an}}$ (4.17 *10^6 J/mol^{-1}K^{-1}). The values were originally determined for the sample set under analysis, and thus were simply readjusted for the given experimental data, and were based off fitting. Equation 5-11 shows the adjusted equation used to model the mean Ni particle radius change shown in Figure 5-5.

$$r_{Ni}^2 \frac{\partial r_{Ni}}{\partial t} = k_{0D_{an}} exp\left[-\frac{Ea_{D_{an}} + (2.7T^2 - 6.7 \times 10^3 T)}{R\left(\frac{1}{T} - \frac{1}{T_{ref}}\right)} \right] \frac{x_{H_2O}}{x_{H_2}^{0.5}} \frac{r_{Ni\infty}^3 - r_{Ni}^3}{r_{Ni\infty}^3 - r_{Ni(0)}^3}$$

Equation 5-11

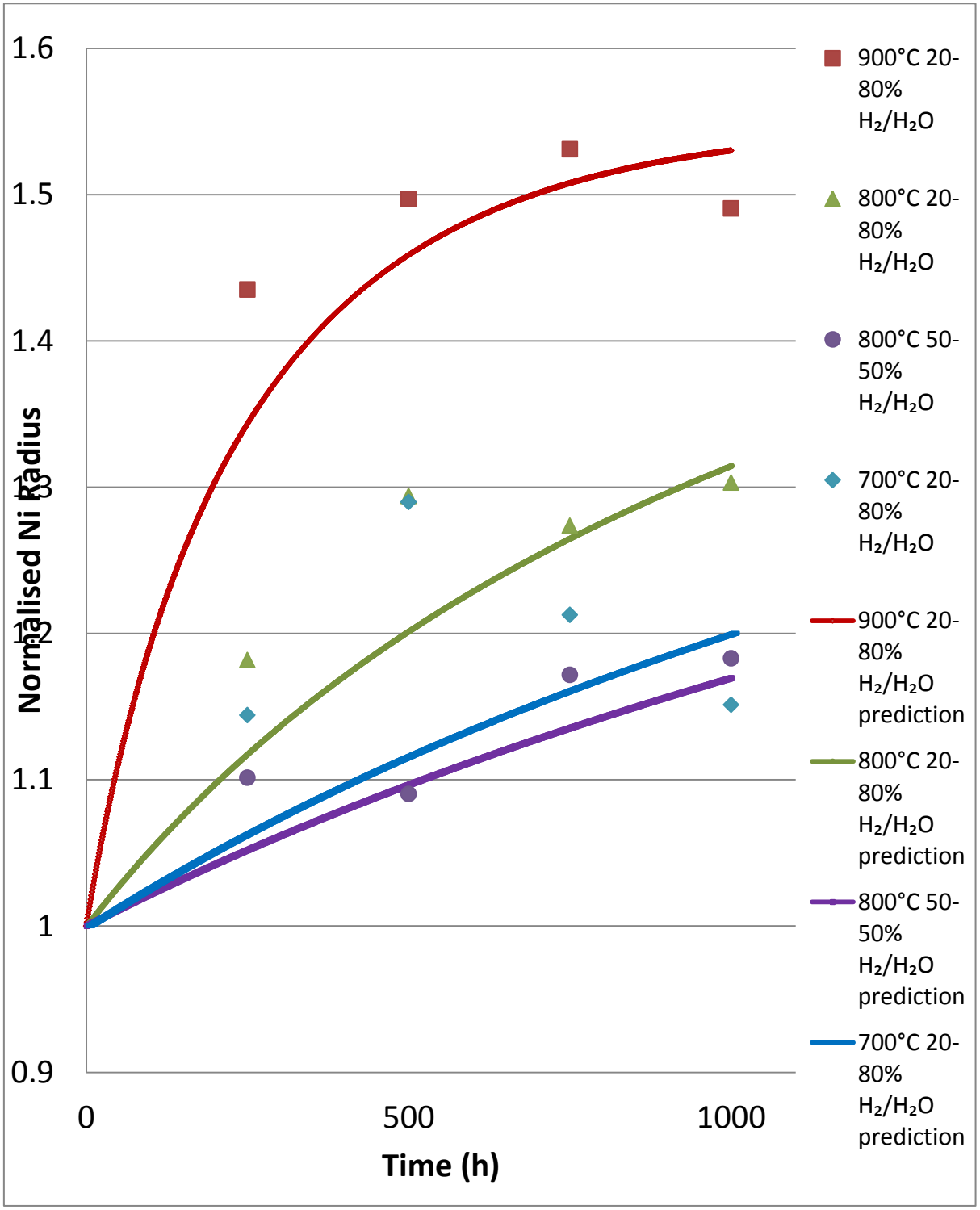

Figure 5-5 Experimental data versus Nakajo model adjusted for Ningbo cells. Samples normalised to 0.38 µm Ni particle radius. Note the superior fit to the sample data points compared to the unadjusted model equation.

Figure 5-5 shows the resultant modelling predictions versus their respective experimental data. Visually the comparison for the data versus prediction shows a good fit for 800C 50/50% and 20/80% H_2/H_2O samples. For all experiments a trend is visible wherein the first 250h data points show higher values then predicted. This suggests that a more rapid agglomeration is taking place in the first portion (<250h), at which point the agglomeration slows down, and could suggest a higher exponential order of fit. The data collected from 700°C 20%/80% H_2/H_2O shows significant divergence from the expected curve, with 500h especially being larger than expected. Assuming that the assumed value of $r_{Ni\infty}$ is correct, this model suggests that it would take a cell operating at 700°C 15,000h what the 900°C would take 2000h to achieve in Ni particle growth (with 20%/80% H_2/H_2O composition). These types of prediction could be valuable for developing accelerated testing experiments. Pure nickel metal has a melting point of 1728K, and coarsening is known to be more common [239] above 2/3rds of a metal's melting point. For pure nickel metal 2/3rds of 1728K is 1152K, thus ~879°C. This would mean that coarsening should be more noticeable for 900°C than 800°C or 700°C, which is apparent from the data collected.

5.3 Gao Ni Particle Radius Modelling

Gao et al [284] have developed a model based on the surface diffusion aspect of Ni transport limited by the YSZ backbone component of the cermet. The use of Fick's diffusion law, the Gibbs-Thomson relation for vacancy concentrations and percolation in the Ni network via coordination number theory are combined to produce the values. It has much of the same basis of Vassen's work on which it is based. This

work is based exclusively on a surface diffusion driven model, founded on the principal that grain boundary or bulk diffusion should be 3 orders of magnitude smaller than surface diffusion [282], and the evaporation-condensation mechanism will be negligible as the water pressure of Ni containing species is low for the suggested operation conditions (T<1000°C) [209].

5.3.1 Nickel Radius Predicting Equation

The model is based on certain assumptions, which include:

- Only testing with low water vapour content in the fuel is modelled to avoid potential effects of high steam content. Whilst the model may be suitable, steam influence was not specifically investigated as part of the work. The model does not include a specific steam factor in the prediction, unlike the Nakajo et al's model.
- The microstructure must be representable through random particle packing. Previous existing literature on the matter suggests this is a valid assumption, but novel design systems involving various microstructural setups such as core-shell structures [298], nanoparticle infiltrated cells, and nano-composites systems may be out of the scope of the model
- The existence of a stable YSZ backbone. A highly percolated network is key to the validity of the model, and if percolation is significantly lower than this it may change the manner or process in which the Ni particles agglomerate (or reduces the limiting factor the YSZ provides in the cell).

Similar to Equation 5-5 and Equation 5-6 from Vassen's modelling section, an equation evaluating the change in volume for a larger particle is shown in Equation 5-12 and Equation 5-13, with the notable difference of the inclusion of the n parameter, and the combination of parameters into one ΔS; which is the surface area of the vacancy diffusion.

$$\frac{dV_l}{dt} = 4\pi r_l^3 \frac{dr_l}{dt} = \sum |v_f| = n j_v \Delta S \Omega \qquad \textbf{Equation 5-12}$$

$$4\pi(1+\beta)^3 r_{Ni}^2 \frac{dr_{Ni}}{dt} = n j_v \Delta S \Omega \qquad \textbf{Equation 5-13}$$

$$\Delta S = 2\pi r_{Ni} \delta_s \qquad \textbf{Equation 5-14}$$

dV_l is the change in volume of the large particle, and n represents the average number of small particles contacting a large particle. It is based on particle packing theory which is discussed in more detail in section 5.4.

$$n = PT_{YSZ} \frac{Z_{Ni,Ni}}{2} \qquad \textbf{Equation 5-15}$$

$Z_{Ni,Ni}$ is the nickel coordination number (referred to as $Z_{ed,ed}$ later on to account for electronically conductive particles), and is divided in half as only the smaller particle contributes to diffusion flow. PT_{YSZ} is used to take into account the blocking effect of the YSZ backbone from further agglomeration of the Ni particles. It corresponds to

the probability of a Ni particle growth lifetime t_g larger than the set given time t i.e. $PT_{YSZ} = P(t_g > t)$. The probability that for λ at a time t, the particles will stop growing, would result in a constant value is shown in Equation 5-16

$$P(t < t_g + \Delta t \mid t_g > t) = \lambda \,.\Delta t \; (\Delta t > 0) \qquad \textbf{Equation 5-16}$$

Through using the nature of conditional probability Equation 5-16 can be used to derive a value for PT_{YSZ}:

$$PT_{YSZ}(t) = e^{-\lambda t} \qquad \textbf{Equation 5-17}$$

This value may be assumed to be constant [299] and when fully resolved as in [284] gives Equation 5-17, where the initial condition of $PT_{YSZ}(t = 0) = 1$ is used.

$$C_{rNi} = C_f exp\left(\frac{2\gamma\Omega}{k_B T}\frac{1}{r}\right) \approx C_f\left(1 + \frac{2\gamma\Omega}{k_B T}\frac{1}{r}\right) \qquad \textbf{Equation 5-18}$$

In Gao's model the value of C_{rNi} has an additional 2 multiplying their equation when compared against Vassen's derivation. Whilst not explicitly clarified why it is present, similar to when evaluating a value for PT_{YSZ}, it may be due to the fact that only the small particles are contributing to the diffusive flow. The difference in concentration is shown in Equation 5-19, similar to that in Equation 5-2.

$$\Delta C = C_{rs} - C_{rl} = C_f \frac{2\Omega\gamma}{k_B T}\left(\frac{1}{r_s} - \frac{1}{r_l}\right)$$ **Equation 5-19**

Using the same equation for Fick's law of diffusion as previously in Equation 5-1, and the previous addendums for Gao's model, provides Equation 5-20.

$$\bar{J}_v = D_{v,s} C_e \left(\frac{2\Omega\gamma}{k_B T}\right) \frac{r_{Ni}}{\left({r_{Ni}}^2 - \Delta {r_{Ni}}^2\right)\left({r_{Ni}}^2 - \Delta {r_{Ni}}^2\right)^{0.5}}$$
$$= \frac{2\Omega\gamma}{k_B T} \frac{\beta}{(1-\beta^2)(1-\beta^2)^{0.5} {r_{Ni}}^2}$$ **Equation 5-20**

Using Equation 5-20, Equation 5-15, Equation 5-14 , allows for Equation 5-12 to be rewritten into Equation 5-21.

$$\frac{dr}{dt} = C \frac{e^{-\lambda t}}{{r_{Ni}}^4}$$ **Equation 5-21**

Where C is defined in Equation 5-22. Solving Equation 5-20 results in the equation for evaluating the mean radius of Ni particles in a SOFC Ni-YSZ anode (Equation 5-23).

$$C = \frac{\delta_s \Omega D_s \gamma}{2 k_B T} \frac{\beta}{(1-\beta^2)(1+\beta^2)^{0.5}(1+\beta)^3} \overline{Z}_0 \frac{\eta_{Ni}}{\frac{\eta_{Ni}}{r_{Ni(0)}} + \frac{\eta_{YSZ}}{r_{YSZ}}}$$ **Equation 5-22**

$$r_{Ni} = \left(\frac{5C}{\lambda}\left(1 - e^{-\lambda t}\right) + {r_{Ni(0)}}^5\right)^{\frac{1}{5}}$$ **Equation 5-23**

In an attempt to reduce the number of fitting parameters used to determine the value for r_{Ni}, a reworking of Equation 5-23 was suggested.

$$r_{Ni} = \left[r_{Ni\infty}^5 - \left(\exp\left(-\frac{5C}{r_{Ni\infty}^5 - r_{Ni(0)}^5} \right) t \right) \left(r_{Ni\infty}^5 - r_{Ni(0)}^5 \right) + \right]^{\frac{1}{5}} \qquad \textbf{Equation 5-24}$$

$r_{Ni\infty}$ can be determined by calculating the value for the maximum radii of the large Ni particle r_l , and relating it to the β relationship $r_l = (1+\beta) r_{Ni\infty}$.

$$\frac{4\pi}{3} r_{l\infty}^3 = \frac{4\pi}{3} r_{l(0)}^3 + \left[\frac{\frac{\psi_{ed}}{r_{Ni}}}{\left(\frac{\psi_{ed}}{r_{Ni}} + \frac{\psi_{el}}{r_{YSZ}} \right)} \right] \frac{\bar{Z}}{2} \left(\frac{4\pi}{3} r_{l(0)}^3 + \frac{4\pi}{3} r_{s(0)}^3 \right) \qquad \textbf{Equation 5-25}$$

Where ψ_{ed} and ψ_{ed} are the volume fractions of solids in the anode. Equation 5-24 removes the need for another fitting parameter in λ, thus simplifying the fitting necessary through reduction of adjustable parameters in a theoretical model. Comparing of the two equations for r_{Ni} (Equation 5-23 and Equation 5-24) showed that the reduced adjustable parameter equation had very similar accuracy in terms of producing accurate estimations of nickel particle growth. Due to this the second equation has been selected in favour of the first.

Table 5-2 Data Values used in Gao modelling equations

Symbol	Description	Value	Reference
k_B	Boltzmann constant	1.38 x 10^{-23}	
δ_s	Thickness of inter-atomic spacing (2.5A)	2.5 x 10^{-10}	[237]
Ω	Volume Element (m^3)	1.09 x 10^{-29}	[237]
y	Surface energy (J m^{-2})	1.9	[237]
Z	Average coordination number, based off Sanyal	6.7	[288]

5.3.2 Comparisons of Models with Literature and Experimental Data

Through Equation 5-24 the model was compared to existing data [17, 19, 237] to ascertain its suitability for low/non-existent steam content Ni radius growth rates. Due to the adjustability of the β parameter for fitting to the data the models are capable of matching the experimental data with reasonable accuracy. Figure 5-6 and Figure 5-7 show the fitting of Tanasini et al [19], Faes et al [17] and Vassen et al's [237] experimental data with Equation 5-24, which shows strong correlation to the predicted data. The $r_{Ni\infty}$ values are determined via the fitting parameter and the initial radius of the nickel particles. Allowing a means to determine the expected change in radius and from further evaluation the expected change in performance.

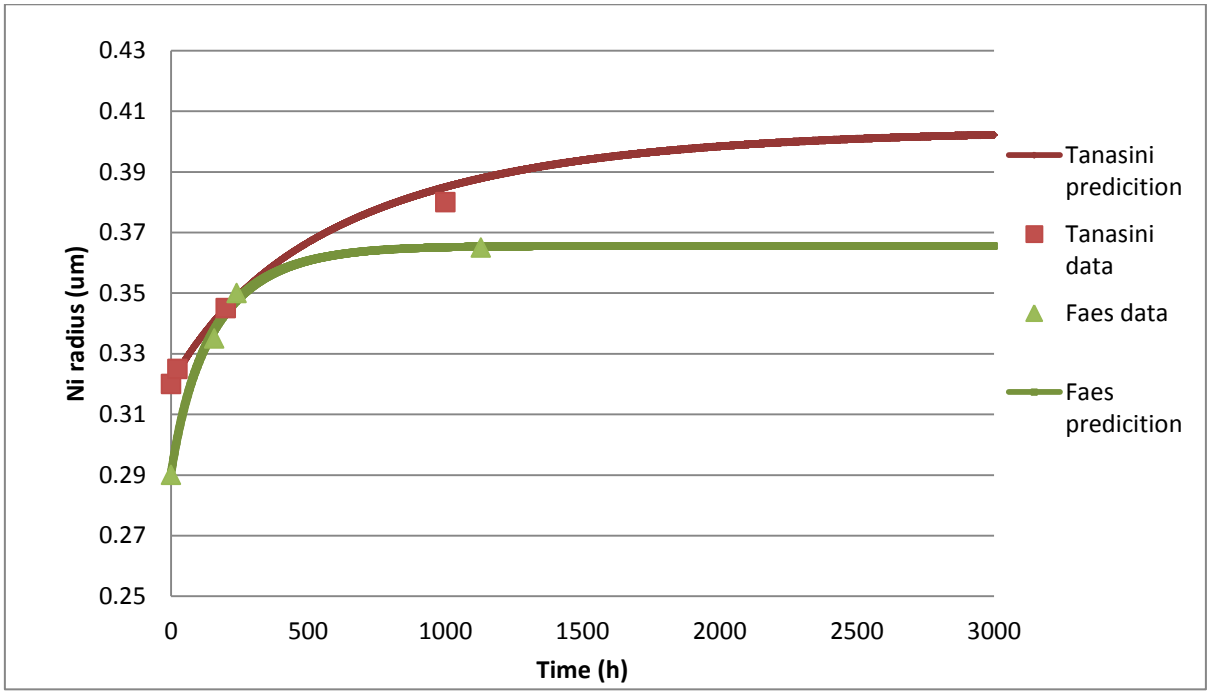

Figure 5-6 Gao model versus Faes and Tanasini data [17, 19]. The equation uses fitting parameters to produce a highly comparable prediction of the particle growth

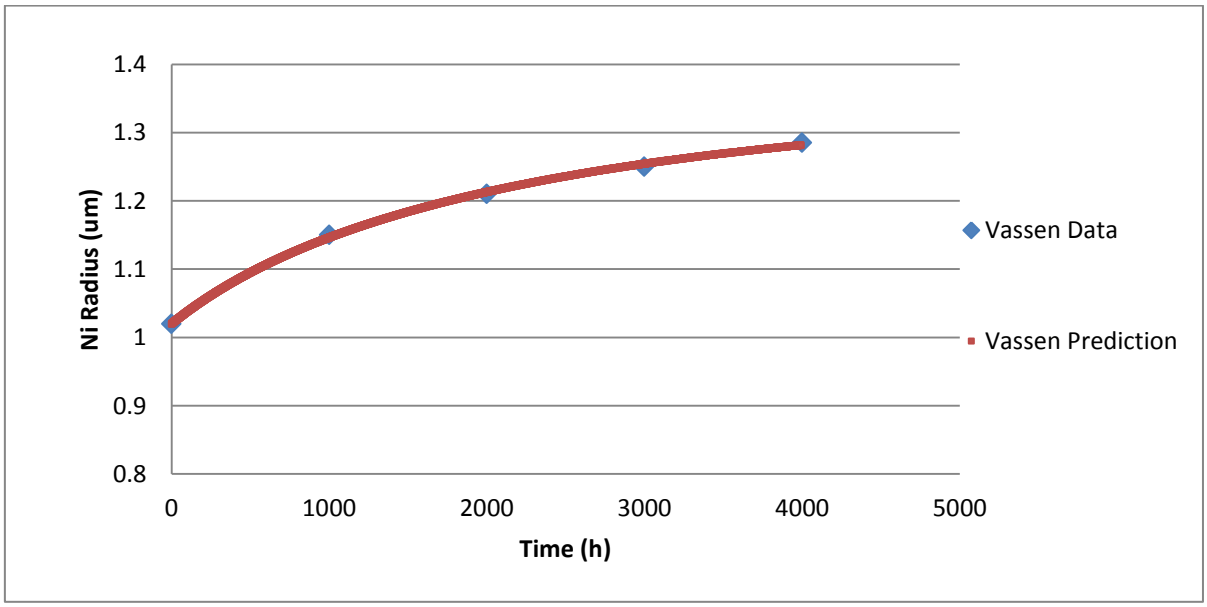

Figure 5-7 Gao model versus Vassen data showing Ni particle radius growth over time [237].

When the model is utilised for analysis of the experimental data from Ningbo cells, the initial attempt used a value of 0.9 for β, which was further adjusted to get a suitable fit with experimental data. The data as a whole has a number of points which deviate from the predicted model shape, with fitting parameters used to minimise deviations from the experimental data points. Table 5-3 shows the utilised fitting parameters for the experimental data. Whilst the value itself is a phenomenological parameter, it is of note that that the values for β are relatively high for the Ningbo cells compared to the comparison from literature as shown. Figure 5-8 shows the model predictions versus experimental data.

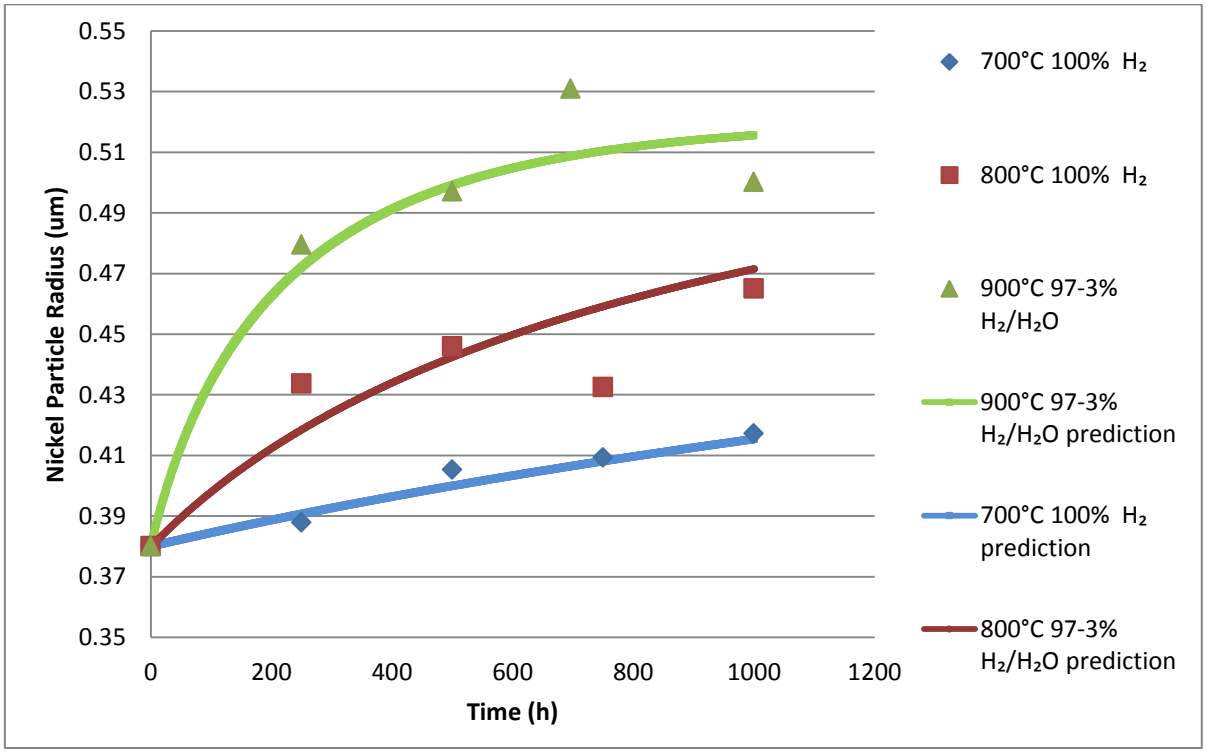

Figure 5-8 Gao model versus experimental data. Similar to other literature the equation does a good job of estimating the growth of the particles relative to their temperature and starting particle size.

Table 5-3 Fitting parameters used for various experiments.

Testing set [284]	β	Temperature (°C)
Tanasini	0.68	800
Faes	0.76	850
Vassen	0.94	1000
700°C 100%	0.8	700
800°C 100%	0.87	800
900°C 97%/3%	0.9	900

5.3.3 Conclusions on Radius Modelling Equations

Looking over the models available for nickel particle radius prediction, Gao et al's and the adjusted variant of Nakajo et al's both show suitability for anticipating long term radius change in the SOFC anode. Nakajo et al's model for higher steam content (Equation 5-10), initially underestimates the growth of the particles in the anode, but shows more accuracy as time goes on. The variability in the 700°C 20%/80% H_2/H_2O sample means any prediction is unlikely to match all data points, though it's final position at 1000h is reasonable given other data available. The Gao et al model for low/negligible steam content was compared with the experimental data from CHAPTER 4, and with suitably chosen fitting parameters shows a strong correlation to the experiment. The predictions highlight the differences in operating cells at 700°C, 800°C and 900°C, and in particular show the advantage to a slower expected rate of change in Ni particle radius for lower operating temperature SOFC anodes.

5.4 Chen et al Percolation Model for TPB Length and Conductivity Estimation

Determining microstructural change in SOFC anodes can be derived from anode cross-sectional image analysis. This, though giving a first idea of how this could impact on all performance, does not offer and immediate tool to estimate performance degradation. In order to evaluate this, further modelling is necessary. The previous work done by authors [286, 289, 300-303], to develop a predictive model which describes important values such as electronic conductivity or TPB length and density have been built through creating a set volume with a number of spheres of electronic and ionically conducting particles of potentially varying type and sizes. Looking at their number of contacts with adjacent particles, referred to as their co-ordination number Z, this can be used to create an appropriate physical setting to calculate a variety of parameters such as TPB length per unit volume. The optimal distribution of particles in the electrode is such that the particles connect to both the electrolyte surface and the current collection surface by a continuous chain of conducting particles. To establish whether the Ni or YSZ particles are connected in a continuous link from their given starting point (the electrolyte for ionically conducting particles, and the current collecting medium for electronically conducting particles) to the opposing end, the percolation probabilities need to be analysed. Percolation commonly refers to the flow of fluids through porous media, however in this case it describes the connected lattice of particles and their connectivity in a set model. Ni particles are here referred to as electrode particles as they are catalytically active (apart from being electronically conducting) whilst YSZ particles are referred to as electrolyte particles as they are ionically conducting.

Particle packing in a system can lead to 3 styles of packing, which can loosely be described as 1) low electrode particle loading, 2) equal particle loading, and 3) high electrode particle loading. These three loading types affect the probability of an A, B or C-type cluster, which have distinct networks that will determine their ability to provide effective TPB sites. A-type clusters extend through the entire width of the sample from the current collector to the dense electrolyte. B-type clusters extend from their respective start point but not the entire width of the sample. These types can contribute effective TPB sites, though they are not guaranteed to in the way A type are. C-type clusters are formed away from either starting point and are secluded from a possible connecting pathway. The probability that electrode particles (Ni in this case) will belong to an specific cluster type is known as the percolation probability of an electrode particle P_{ed}. The percolation probability P_{ed} of the electrode particles is dependent on the coordination number of the electrode particles with other electrode particles $Z_{ed,ed}$.

$$P_{ed} = \left[1 - \left(\frac{3.764 - Z_{ed,ed}}{2}\right)^{2.5}\right]^{0.4} \qquad \textbf{Equation 5-26}$$

Figure 5-9 gives an example of each type of cluster in an imaginary anode microstructure. However, it is still possible for two chains of ionic and electronically conducting particles to reach each other as well as having sufficient porosity to be a viable TPB point for reactions to take place without specifically reach their respective alternative surfaces, which can mean that B-types clusters can still contribute potentially, however for the analysis anything less than an A-type will not be deemed

usable. This percolation probability of an A-type cluster is determined through Equation 5-26, which is dependent on the average coordination number for each specific group of particles throughout the electrode.

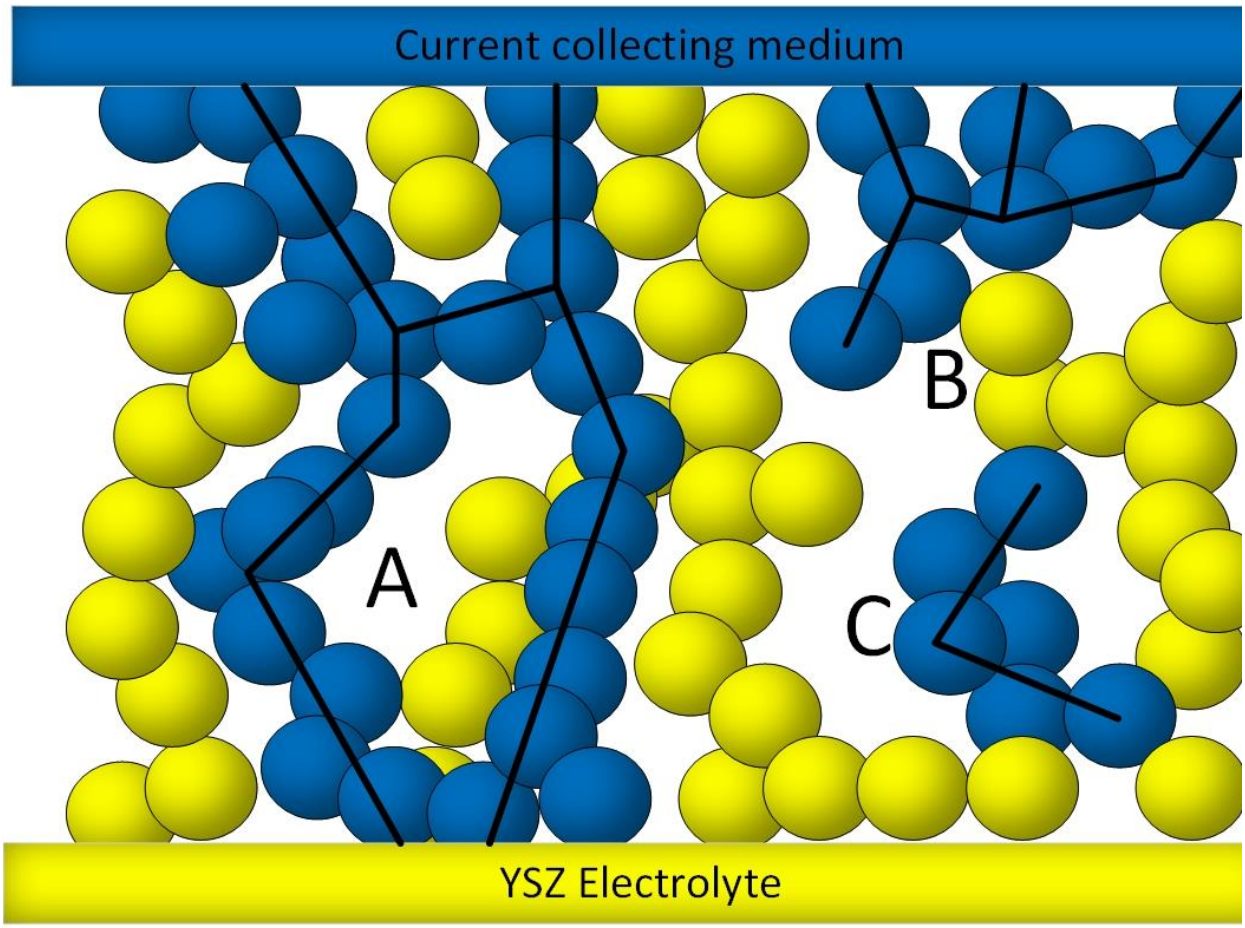

Figure 5-9 Anode microstructure type cluster example. A type represent fully percolated networks connecting the YSZ material with the current collecting medium. B and C types represent either un-connected networks or ones without contact to the YSZ electrolyte material.

Equation 5-27 shows the average coordination number $\bar{Z}$ of all particles within an M - component packed bed, where M is the total number of particle sizes present, Z_k is the coordination number and ζ_k is the particle number fraction for particle k, respectively. These are used to establish the suitable number for the entire packed bed, which as the average value is used in further equations to help describe/predict features based on the model number of contacts.

$$\overline{Z} = \sum_{k=1}^{M} \zeta_k Z_k \qquad \textbf{Equation 5-27}$$

The value of 6 for the average coordination number has been determined in literature to be an accurate input for modelling purposes, by comparison with physical simulations of packed bed distributions [301]. When determining if a particle loading is likely to produce A-type clusters, the minimum value of coordination number needed was shown to be 1.764 [303, 304], which with specific particle volume loadings and sizes can be used to determine the critical volume threshold needed to create A-type clusters. Higher levels of volume loading can lead to larger values for the coordination number Z which gradually increase the percolation probability, P_{ed}or P_{el}, of the electrolyte or electronically conducting particles

$$Z_{ed,ed} = \overline{Z} \frac{\frac{\psi_{ed}^{c}}{r_{ed}}}{\frac{\psi_{ed}^{c}}{r_{ed}} + \frac{\psi_{el}}{r_{el}}} = 1.764 \qquad \textbf{Equation 5-28}$$

$$Z_{el,el} = \overline{Z}\frac{\frac{\psi_{el}^{c}}{r_{el}}}{\frac{\psi_{el}^{c}}{r_{el}} + \frac{\psi_{ed}}{r_{ed}}} = 1.764$$ **Equation 5-29**

Equation 5-28 and Equation 5-29 describe the electrode and electrolyte material average coordination numbers respectively, and are analogous to each other. These can be used to find the critical threshold value for the respective volume loadings for a given particle size, and the effects of an increased percentage of ionically or electronically conductive material. These values are determined by the relative particle radii r_{ed} and r_{el} (nickel for electrode and YSZ for electrolyte), volume fractions ψ_{ed} and ψ_{el}, their respective percolation thresholds $\psi_{ed}^{c}$and ψ_{el}^{c} and the overall coordination number for all particles $\overline{Z}$.

$$\psi_{ed} = \frac{\frac{n_{ed_k}^{V} 4\pi r_{ed_k}^{3}}{3}}{\frac{\sum_{l=1}^{M} n_m^{V} 4\pi r_m^{3}}{3}} = \frac{n_{Ni_k}^{V} r_{Ni_k}^{3}}{\sum_{l=1}^{M} n_m^{V} r_m^{3}}$$ **Equation 5-30**

$$\psi_{ed} = \sum_{k=1}^{m} \psi_{ed_k}, \qquad \psi_{el} = \sum_{k=1}^{n} \psi_{el_k}$$ **Equation 5-31**

The volume fractions are determined by the number of Ni and YSZ particles per unit volume $n_{ed_k}^{V}, n_{el_k}^{V}$ and the relative radii of the specific particles $r_{Ni_k}^{3}$, $r_{YSZ_k}^{3}$.

$$n_k^V = \frac{(1-\Phi_g)\psi_k}{\frac{4}{3}\pi r_k^3}$$ **Equation 5-32**

$$\psi_{ed_k}^o = \frac{\psi_{ed_k}}{\psi_{ed}}, \qquad \psi_{el_k}^o = \frac{\psi_{el_k}}{\psi_{el}}$$ **Equation 5-33**

Equation 5-30 calculates the volume fractions of a specific material or particle, and is exclusive of porosity such that a 40%Ni, 40% YSZ, 20% pore distribution would be $\psi_{ed} = \psi_{el} = 0.5$. The total volume fraction of the electrode and electrolyte particles can be found through summing the respective particles as seen in Equation 5-31, which can then be used to find their relative particle volume percentage shown in Equation 5-33. The *k* notation refers to a particle of a specific size, and can also be used when evaluating the relative volume fraction of a specific particle size in non-binary systems $\psi_{ed_k}^o, \psi_{el_k}^o$. The number of particles per unit volume determined by Equation 5-32 is evaluated through the porosity Φ_g, the particle radius and the volume fractions.

To establish the value of coordination number, $Z_{ed,ed}$, $Z_{el,el}$ are used to evaluate the percolation probability. When looking to calculate the average coordination number for all m electrode particles Equation 5-34 uses the summation of the coordination number among the same type of particles and the number fraction ζ_{ed_k} of ed_k particles.

$$Z_{ed,ed} = \frac{\sum_{k=1}^{m}\sum_{k=1}^{m}\zeta_{ed_k} Z_{ed_k,ed_l}}{\sum_{k=1}^{m}\zeta_{ed_k}}$$ **Equation 5-34**

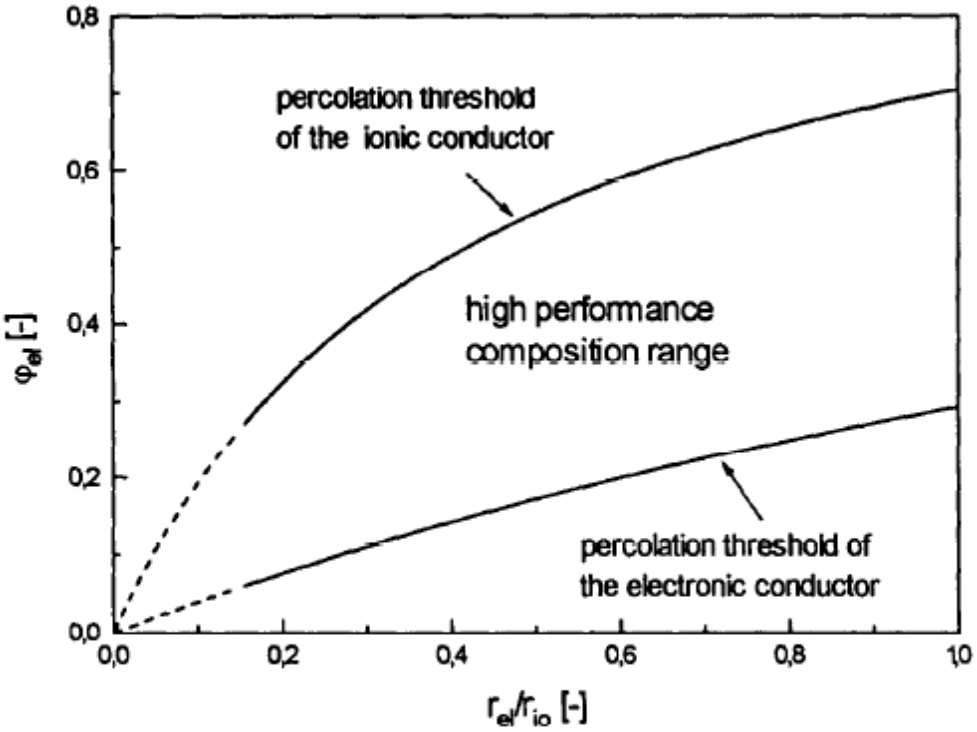

Figure 5-10 Percolation thresholds based on particles size ratio r_{el}/r_{io} and electrolyte volume fractions φ_{el} [303]. The upper bound represents compositions where high ionic percolation existing whilst the lower bound is for electronic percolation. The mid-region represents the optimal volume ratio to provide high percolation for both materials.

$$\zeta_k = \frac{n_{ed_k}^V}{\sum_{l=1}^{M} n_l^V} = \frac{\frac{\psi_{ed_k}}{r_k^3}}{\sum_{l=1}^{M} \frac{\psi_l}{r_l^3}} \qquad \textbf{Equation 5-35}$$

Equation 5-35 calculates the fraction of a certain type (or size within a type) of particle relative to the other particles present in the set unit volume. When combined

with Equation 5-34 an equation for electrode-electrolyte contact can be formed, which for a binary system produces Equation 5-36

$$Z_{ed,el} = 0.5\left(1 + \frac{r_{ed}^2}{r_{el}^2}\right)\bar{Z}\frac{\frac{\psi_{el}}{r_{el}}}{\sum_{ed=1}^{M}\frac{\psi_{ed}}{r_{ed}}} \qquad \textbf{Equation 5-36}$$

With the previous equations it is possible to establish parameters and variables for the model through which values for conductivity and TPB lengths can be estimated.

$$\sigma_{ed}^{ter,eff} = \sigma_{ed}^{ter,o}\frac{\sum_{k=1}^{n} 2r_{ed_k}S_{ed_k}}{\delta S} \qquad \textbf{Equation 5-37}$$

$$\sigma_{ed}^{tra,eff} = \sigma_{ed}^{tra,o}\left[\sum_{k=1}^{n}(1-\Phi_g)\psi_{ed_k}P_{ed}\right]^{\mu} \qquad \textbf{Equation 5-38}$$

Work by Chen et al [305] developed Equation 5-37 for YSZ calculations and estimates the effective inter-particle electronic conductivity where $\sigma_{ed}^{ter,o}$ is the intrinsic inter-particle conductivity, S_{ed_k} is the surface area fraction of all electrode particles (of size *k*), δ is the thickness of the boundary between particles and S is the geometric cross-sectional area of the composite electrode. Equation 5-38 estimates the effective intra particle electronic conductivity, where $\sigma_{ed}^{tra,o}$ is the intrinsic intra-particle electronic conductivity, Φ_g is the porosity and μ is the Bruggeman factor which accounts for tortuosity and is typically 1.5 [289] (as previously introduced in section 2.4.3).

The effective contact area between electrode particles per particle layers S_{edk}^{ter} is calculated by Equation 5-39, which is determined by the total number of electrode particles, the electrode-electrolyte coordination number, the electrode percolation probability, the overall geometrical surface area of the composite electrode and the cross-sectional surface area per contact $a_{ed,el}$.

$$S_{edk}^{ter} = \sum_{l=1}^{m} a_{edk,edl}(r_{edk}S)n_{edk}^{V}Z_{edk,edl}P_{ed} \qquad \textbf{Equation 5-39}$$

$$a_{ed,el} = \pi r_c^2 \qquad \textbf{Equation 5-40}$$

The parameter r_c is the neck radius formed by two particles with overlapping boundaries. The value is determined from Equation 5-41 by using the smallest of the two radii at any given point in time. θ is the contact angle of the particles as seen in Figure 5-11 .

$$r_c = sin\theta\big(min(r_k, r_l)\big) \qquad \textbf{Equation 5-41}$$

In both cases the equations are interchangeable for electrode and electrolyte particles. In certain cases by looking to calculate the dimensionless values of the inter and intra granular conductivities it can show the impact of certain physical properties or ratios of material sizes or loadings.

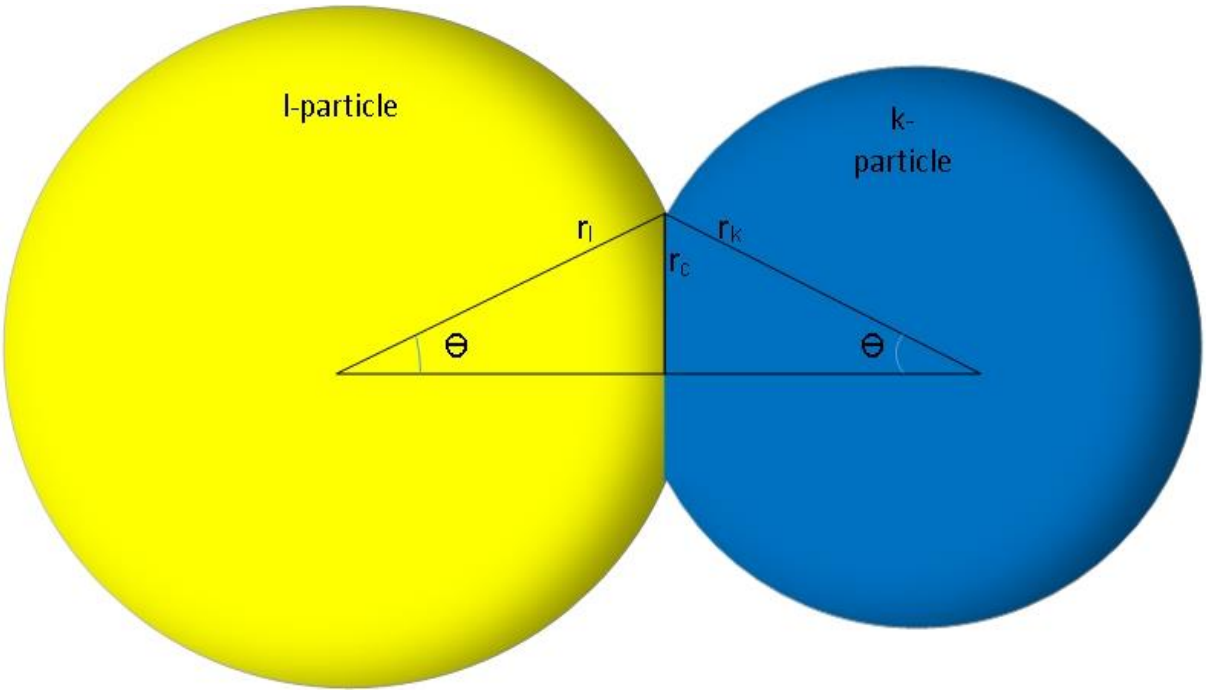

Figure 5-11 Example of k and l particles overlapping and visual of neck radius r_c.. and resultant contact angles θ produced.

The dimensionless effective electronic inter-particle conductivity $\tilde{\sigma}_{ed}^{ter,eff}$ and the dimensionless effective intra particle electronic conductivity $\tilde{\sigma}_{ed}^{tra,eff}$ are estimated through equations Equation 5-42 and Equation 5-43 . δ is the thickness of the grain boundary, which was estimated to be around 5nm for YSZ [306].

$$\tilde{\sigma}_{ed}^{ter,eff} = \frac{\sigma_{ed}^{ter,eff}}{\frac{\sigma_{ed}^{ter,o} r_{ed} sin^2\theta(1-\emptyset_g)}{\delta}}$$ **Equation 5-42**

$$\tilde{\sigma}_{ed}^{tra,eff} = \frac{\sigma_{ed}^{tra,eff}}{\sigma_{ed}^{tra,o}(1-\emptyset_g)^{\mu}} = [\psi_{ed} P_{ed}]^{\mu}$$ **Equation 5-43**

For a binary mixture, it is assumed that the TPB length per unit volume λ_{TPB}^{V} is the result of the contact perimeter between electrolyte and electrode particles and the total number of contact points per unit volume. λ_{TPB}^{V} has been shown to directly influence cell performance through adjustment of the ASR as seen in Figure 2-16. The value is determined as shown in Equation 5-44 . For systems with more than 2 particle size distributions, however, the percolation of the particles is critical to allow for complete transfer pathways (whether ionic or electronic), and so the effective TPB length per unit volume is often more useful for comparison and can be determined from Equation 5-45 . The contact perimeter between overlapping electrode and electrolyte $l = 2\pi r_c$ is multiplied with the number of particles and their respective coordination number with which they contact.

$$\lambda_{TPB}^{V} = l_{ed,el} n_{ed}^{V} Z_{ed,el} = l_{ed,el} n_{el}^{V} Z_{el,ed} \qquad \textbf{Equation 5-44}$$

$$\lambda_{TPB,eff}^{V} = \lambda_{TPB}^{V} P_{ed} P_{el} \qquad \textbf{Equation 5-45}$$

When dealing with multicomponent mixtures the overall equation remains functionally the same, but the variation introduced by the variety of particle sizes needs to be factored in to allow for accurate estimate of the effective TPB length per volume. If the volume fraction ψ_{ed}, ψ_{el} and the radii ratios among all particle types are fixed this generates Equation 5-46

$$\lambda_{TPB,eff}^{V} = \sum_{k=1}^{m}\sum_{l=1}^{m} l_{ed,el}\, n_{ed}^{V} Z_{ed,el} P_{ed} P_{el}$$ **Equation 5-46**

Similar to the conductivities, the dimensionless values for the TPB length per unit volume can be such that $\lambda_{TPB,eff}^{V}$ is only dependant on the porosity and the particle radii ratio. Which can be useful for comparing particle variation differences.

$$\tilde{\lambda}_{TPB,eff}^{V} = \frac{\lambda_{TPB,eff}^{V}}{\frac{(1-\emptyset_g)sin\theta}{r_{ed}^{2}}}$$ **Equation 5-47**

Table 5-4 Data values used in Chen model.

δ	Thickness of grain-boundary between particles (m)	5.4 nm (from YSZ)	[306]
Θ	Contact angle between two particles	15 taken almost arbitrarily	[303]
$\sigma^{tra,o}$	Intrinsic bulk material conductivity (Nickel) (S/m)	$7.8 * 10^{-4}$ (Ωm) *(Ts-293)*0.006	[307]
$\sigma^{ter,o}$	Intrinsic conductivity of the particle interface (S/m)	1 order of magnitude less than bulk	
r_{el}	Electrolyte particle (YSZ) radius	0.5 μm	Evaluated from image analysis
ψ_{ed}	Volume loading of Electronically conducting particles (Ni)	0.4	Based on Ningbo cells
ψ_{el}	Volume loading of ionically conducting particles (YSZ)	0.6	Based on Ningbo cells
$\bar{Z}$	Average coordination number	6	[289]

5.4.1 Non-dimensional Comparison of Model

As described in Equation 5-47 , the nondimensional equation for the TPB length per unit volume looks at the effects of the particle radii and their respective loading and its impact on percolation threshold, contacting points, etc. Figure 5-12 shows how the changing Ni particle radius at set operating conditions (800°C, 50%/50% Ni-YSZ mass loading, Ni_{∞}=1.3, Θ=15°, 50%/50% H_2/H_2O gas stream, Φ_g=0.2), as defined by Nakajo et al's model, are affected by different set electrolyte particle sizes (which like the Ni particles are normalised relative to their initial starting radius). Unsurprisingly the most effective system involves a balance of r_{ed}/r_{el} with the same particle size (in the case of Figure 5-12 this is r_{el} =1.3). This is do the particle packing allowing for a better percolated network when the particles are the same (or close to) size as each other. Notable the performance for $r_{el} = 1.1$ starts higher then drops progressively over time. This is due to the increase size difference between r_{ed} and r_{el} resulting in a reduction in percolation in the system.

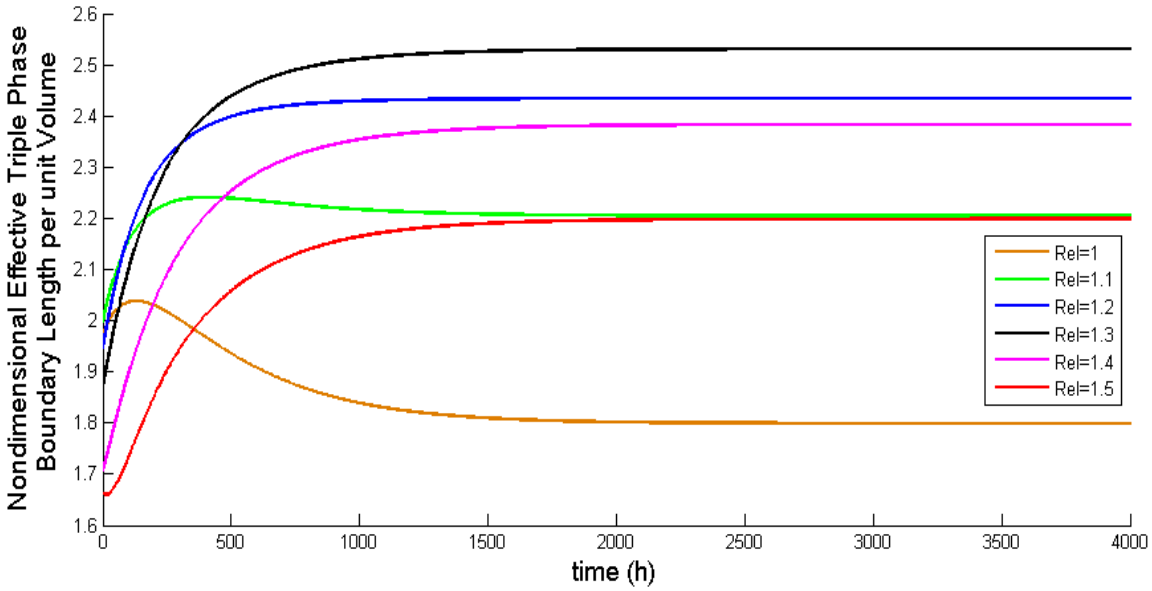

Figure 5-12 Nondimensional $\tilde{\lambda}^{V}_{TPB,eff}$ for varying set electrolyte particle sizes. The Ni radius has been set to 1.2 and highlights how at around the same size the performance is best but as the YSZ size gets larger or smaller you see a reuction in effective TPB length per unit volume.

The volume loading in the cell is important to allow for a sufficient percolation probability to provide pathways for ions and electrons. If the values for P_{ed} and P_{el} fall too low then the value for $\lambda^{V}_{TPB,eff}$ will eventually tend towards zero. In Figure 5-13 you can see this effect as for volume loadings which go to extremes in terms of minimal Ni or YSZ loading, their respective P_{ed} and P_{el} drop down as the Ni radius changes from smaller than the set electrolyte mean radius to larger than it. In reality it would be unlikely that the shift in particle radius due to agglomeration would cause a complete loss of percolation for all particles as per the model predictions, but the end result will likely mimic its performance.

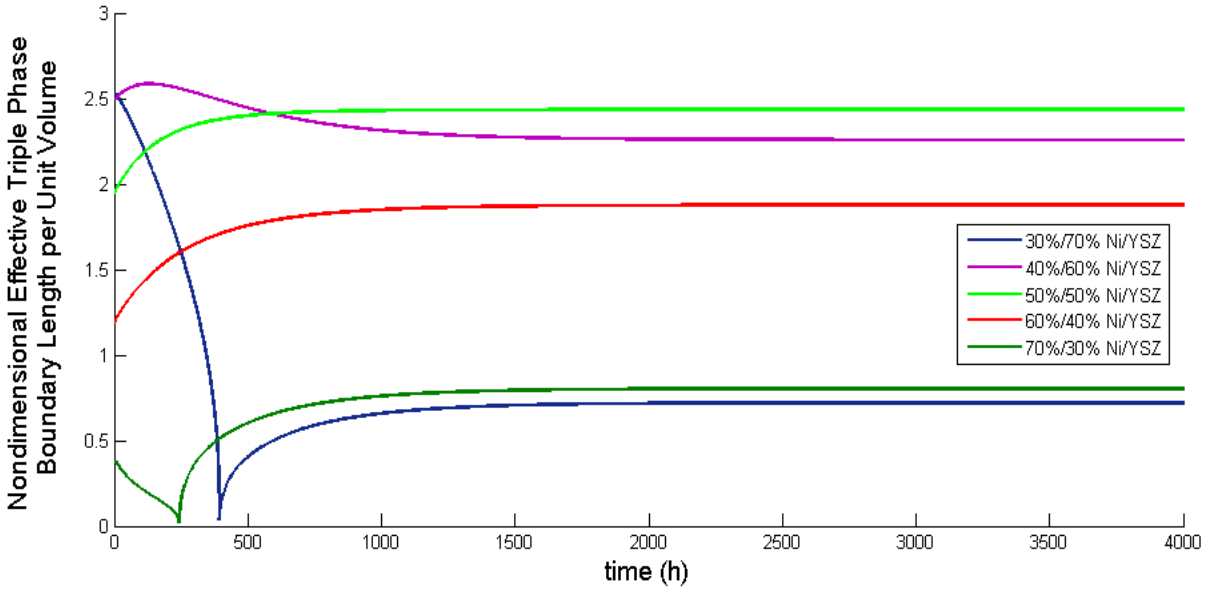

Figure 5-13 Nondimensional $\tilde{\lambda}^{V}_{TPB,eff}$ comparison of varying volume loadings. Samples with similar to slightly more YSZ show best performance with those samples heavily favouring one material showing reduced values. Not the drop of values to 0 in the extreme settings is a result of the percolation model as the Ni radius changes over time.

Looking at the effect of the max normalised Ni particle radius in Figure 5-14, it appears that the smaller the max particle size the more favourable the end $\tilde{\lambda}^{V}_{TPB,eff}$. Perhaps more interesting are the gaps between the max values, which is evenly spaced in terms of r_{∞}, but the values for $\tilde{\lambda}^{V}_{TPB,eff}$ can vary by as little as ~0.28 between 1.1 and 1.2, or ~0.5 for 1.2 to 1.3.

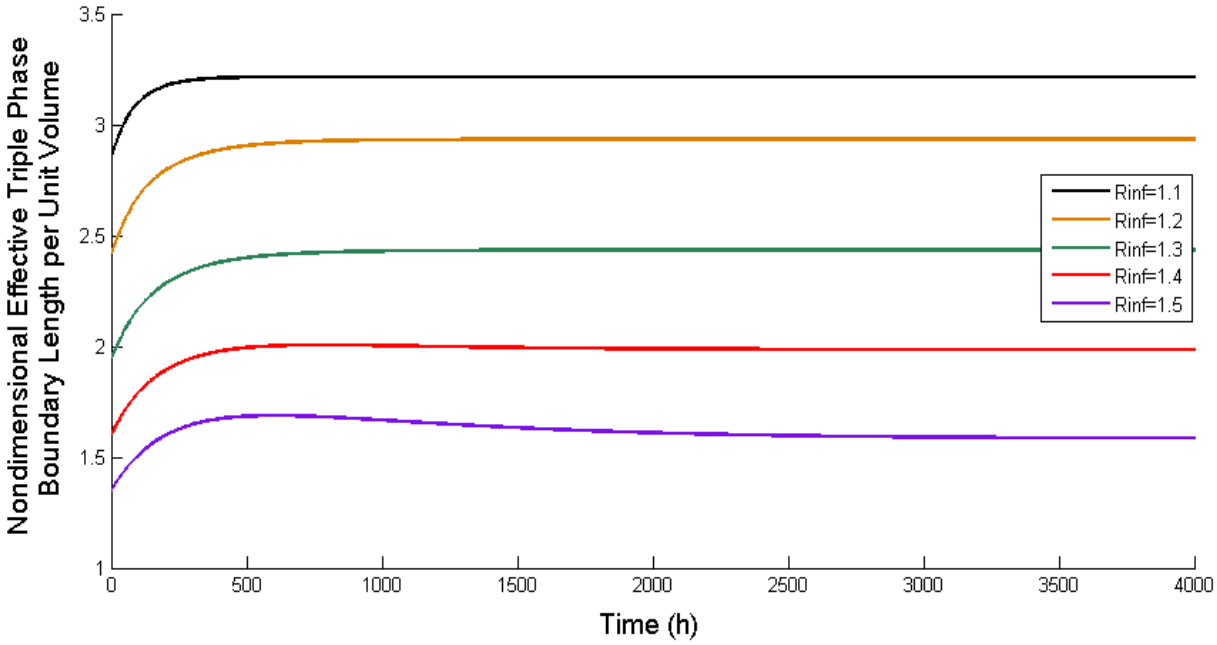

Figure 5-14 Nondimensional $\tilde{\lambda}^{V}_{TPB,eff}$comparison of different $r_{Ni\infty}$ values. This figure shows how a smaller value of $r_{Ni\infty}$ compared to the YSZ mean particle size results in the best possible $\tilde{\lambda}^{V}_{TPB,eff}$.

Due to percolation "incompleteness" the resistivity for Ni loadings below 40% results in an asymptotic increase in resistivity. Resistivity increases for Ni loadings of 60% and above is marginal compared to the % increase seen in lower Ni loadings (40%), as shown in Figure 5-15.

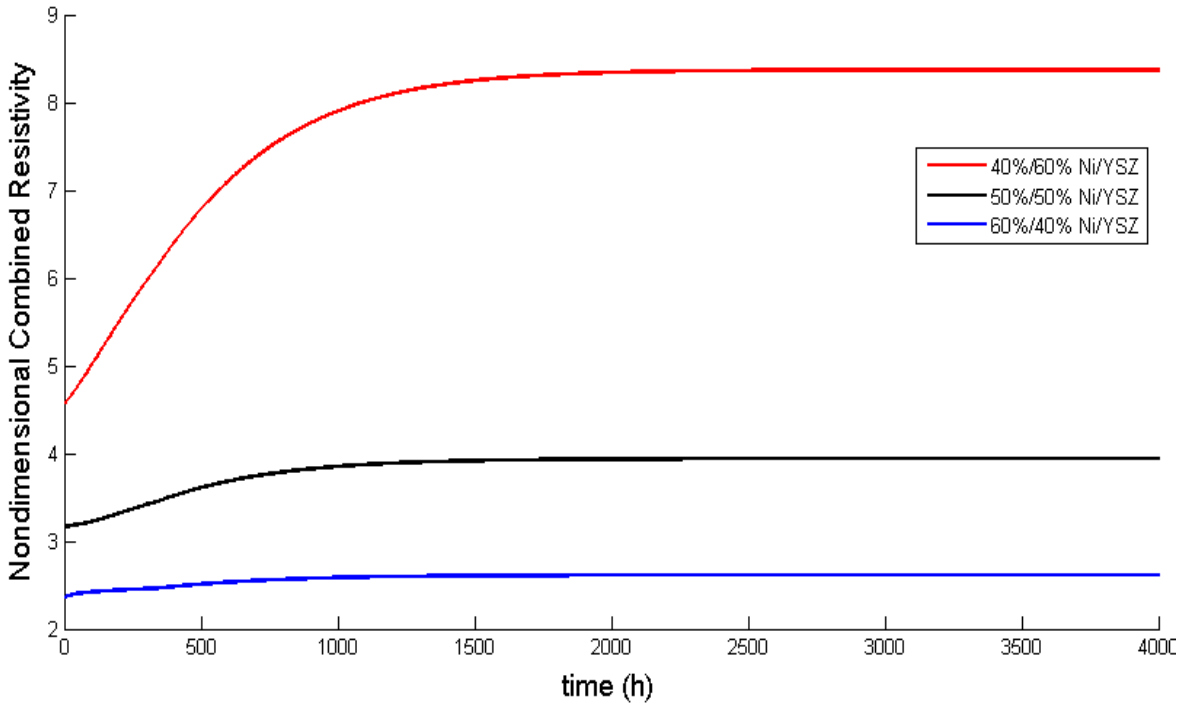

Figure 5-15 Variation of resistivity with varying volume loading. As expected a higher quantity of Ni reduces the overall resistivity in the sample, which particularly large relative increases above 50% loading.

5.4.2 Chen Model Combined with Gao and Nakajo model

Based on the relevant Ni particle radii predictions, the change in the predicted TPB length per unit volume and conductivity can be modelled to highlight long term loss in performance. Figure 5-16 and Figure 5-17 highlight the potential changes undergone in the Ni-YSZ anode microstructures as tested in CHAPTER 4. With regards to the relevant issues in the degradation of Ni-YSZ anodes the loss of TPB lengths for reactions to take place and the general loss of conductivity over time due to coarsening are contributing factors.

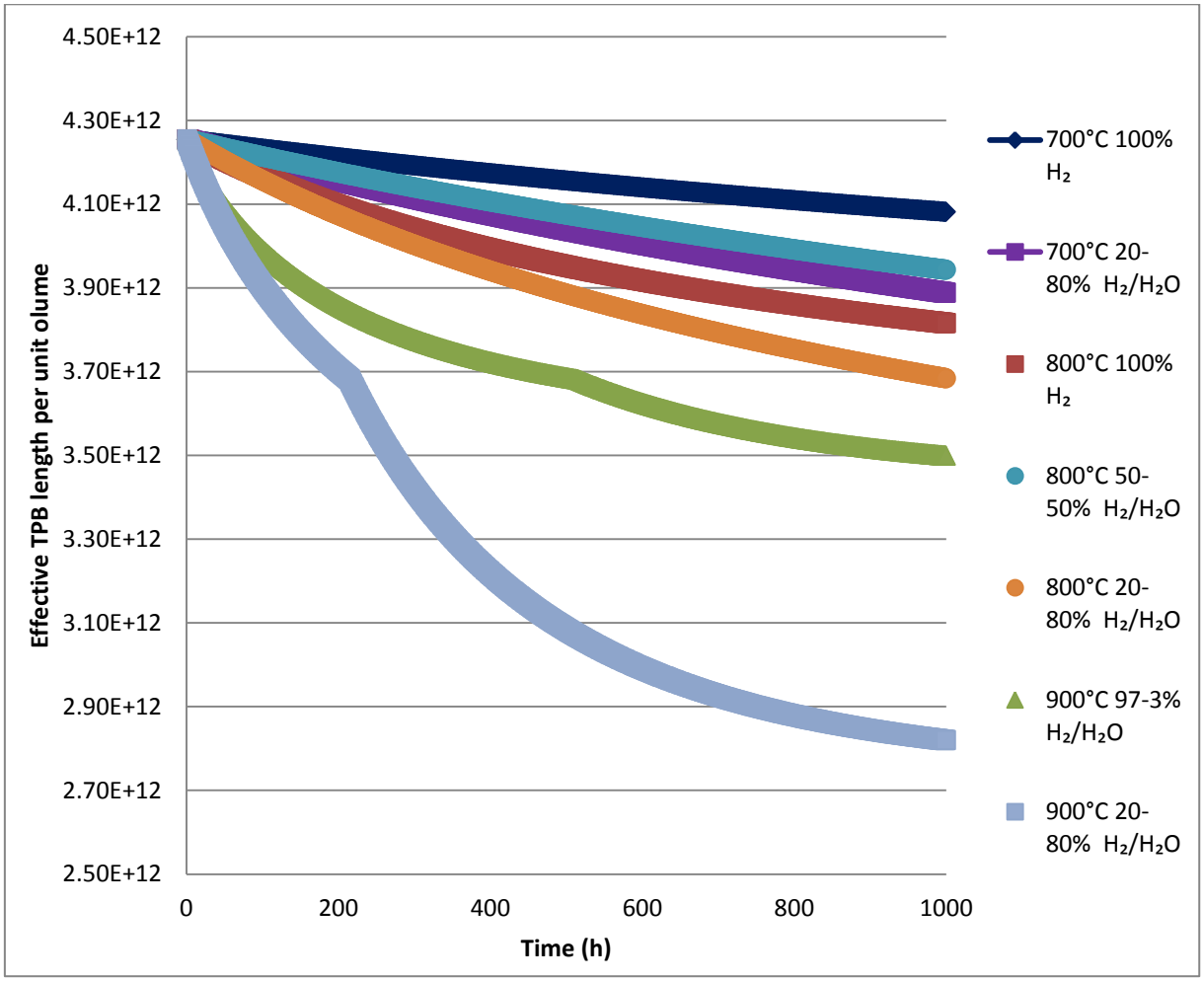

Figure 5-16 Relative effective TPB change based on Gao/Nakajo radius predictions and Chen percolation model. The drop seen in 900°C 20-80% H_2/H_2O and 900°C 97-3% H_2/H_2O is present in all Nakajo models and relates to the change in mean Ni particle radius to a value larger than the mean YSZ particle radius.

With regards to both figures, it is important to note that the two different models for particle radii growth have different $r_{Ni\infty}$. As it represents a maximum value for a mean value of the Ni particle distribution, it only offers a statistical statement, however derived (estimation for Nakajo and equation for Gao). For the Gao model compared with the experimental data, a lower set of $r_{Ni\infty}$ values are determined (equivalent of

0.52 μm versus the value of 0.59μm seen in Nakajo et al's model), leading to earlier peaks for reaching the max size and thus also reach their minimum plateaus for effective TPB lengths per unit volume and effective conductivity sooner as shown in Figure 5-12 to Figure 5-14 (in a given operational setting). These were not adjusted to show each model's potential predictive features.

Due to the fact that the experimental results for 800°C 97%/3% H_2/H_2O resulted in a negative growth rate, they were not included for comparison and although the 900°C 97%/3% H_2/H_2O experiments similarly have a small amount of steam present, the Gao model was used despite not taking into account the small presence of water. Due to accuracy of theoretical to experimental data the projections should be suitably comparable. The modelling equations for Chen's section build on an average coordination number of 6, whilst in Gao's model a value of 6.7 is used. Both values are defended in their respective works, so rather than trying to select one over the other, both values are used for their respective calculations. Principally the difference suggests a low number of contacts for Chen et al's calculations and thus an underestimate of derived parameters for values for TPB length per unit volume. Clearly the value has more importance in the particle packing model by Chen et al, as it influences every variable determined.

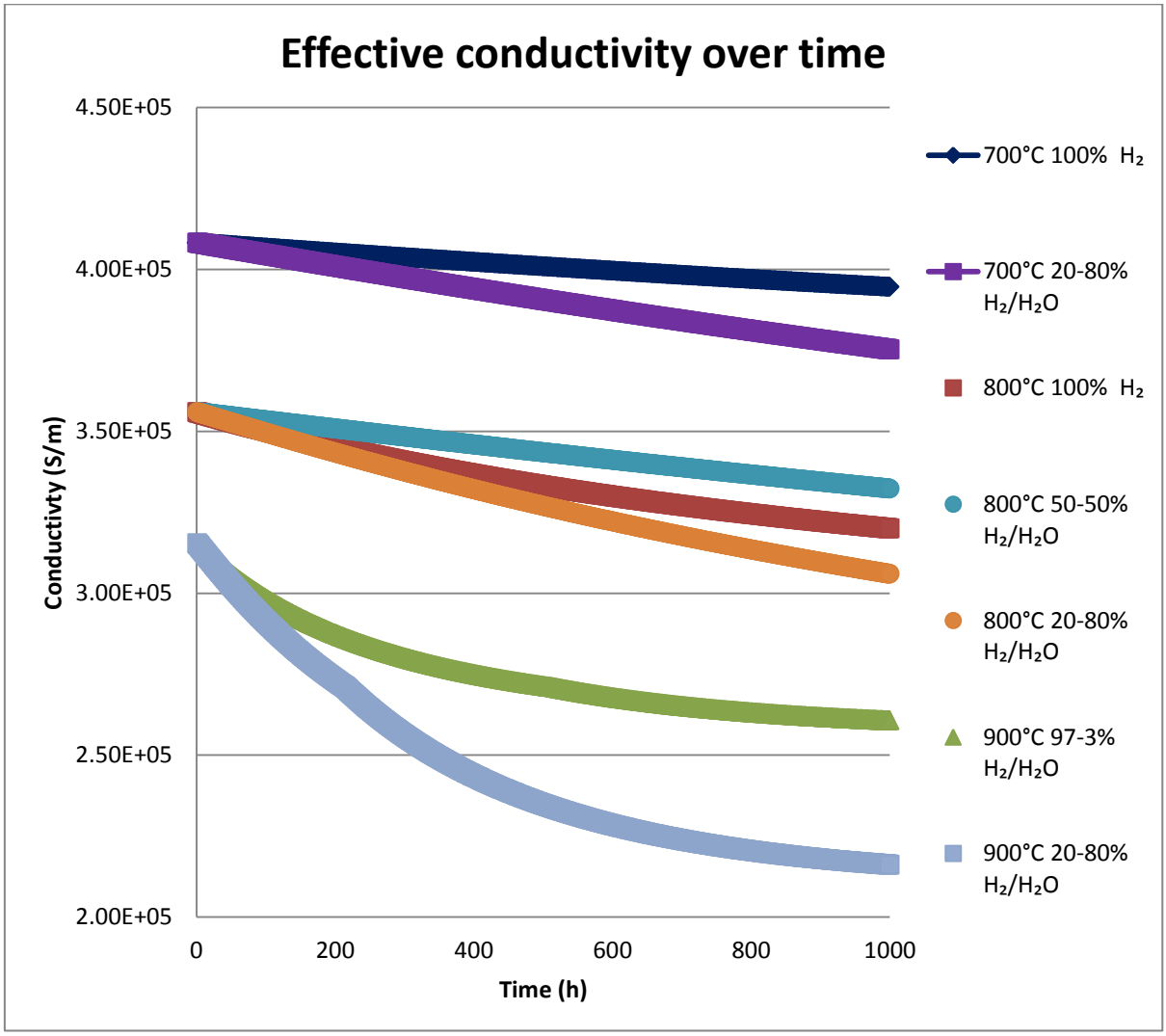

Figure 5-17 Relative effective conductivity (S/m) based on combined Gao/Nakajo radius predictions and Chen percolation model using equations Equation 5-37 & Equation 5-38.

Whilst Figure 5-17 shows that the relative electronic conductivity of Ni over time for given conditions has a strong dependence on the specified temperature, with lower temperatures clearly benefiting from higher initial conductivities and slower growth rates. Obviously this benefit works against the ionic conductivity which improves with increasing temperature. Normally the electronic conductivity is not the limiting factor

in anode performance, but over extend hours of operation could be an important factor to consider. The value for the conductivity chosen in this example is that of pure Ni, which may overestimate the overall conductivity.

5.5 Particle Radius Estimation and Parameter Evaluation Conclusion

Two models for predicting the nickel particle radii change in given temperature and fuel composition operating conditions have been combined to evaluate any possible regime undergone in a humidified hydrogen Ni-YSZ anode. This is further added to a particle packing model capable of predicting various parameters of the anode for a given mean particle size, allowing a time dependant model which can predict important parameters such as the change in TPB length per unit volume over time, which correlates directly to a loss of overall performance as previously mentioned. These models have their radii predictions compared to experimental data and show suitable accuracy for reliable recreations. These values are further used to predict their relative losses over time in conductivity and TPB lengths. Whilst the models clearly present a powerful tool when analysing very long term performance (especially in combination with microstructural data from shorter tests) , the importance of certain parameters used to fundamentally describe the changes inside of the anode benefit from accurate evaluation. Often times deciphering the values from available data is unclear and thus care has to be taken when adapting the model to different cell circumstances.

CHAPTER 6 Image Analysis and the Determination of Triple Phase Boundary (TPB) points

Due to the importance of TPB sites in fuel cell systems, a loss in the number of TPB points is relatable to the loss of electrochemical performance in the cell. A change in the number of TPB points directly impacts the overall TPB effectiveness i.e. those TPB points connected via a percolated network in the cell. Being able to generate viable means of calculating the number of TPB points presents an important tool for establishing the change in performance of a sample under analysis.

Utilisation of image analysis of experimental SEM images provides a means of establishing values for effective radius, x,y coordinates and material. This information can then be utilised to determine meaningful microstructural data. For example it provides values for Ni particle and pore contact angles, the number of TPB sites and the length of the distance between the overlapping intersection points, or overlap lengths, of Ni-pore contacts. Further observing the variation these parameters over time provides a means of assessing degradation/aging.

6.1 Microstructural

The electrochemical performance is directly linked to the microstructure of the anode [289]. As discussed previously in CHAPTER 2, the TPB points are a key microstructural feature for the electrochemical performance of the anode. However these are not the only microstructural features that affect the electrochemical

performance as only TPBs on a percolated network directly contribute to the electrochemical performance of the cell. In this section the image analysis is briefly discussed, highlighting the method used for generating the variables used in the analysis. A Laplacian adjacency matrix is constructed to establish contacts for the Ni particle and pores generated from the image analysis. The Laplacian adjacency matrix is then further processed to distinguish the Ni-Pore contacts in the image. From here a value for the Ni and pore contact angles θ and overlap length can be established. For the purposes of conciseness pores may be referred to as particles for the purpose of explaining how the data is collected.

6.1.1 Percolation

To allow for effective conduction of ions and electrons the Ni and YSZ particles must have sufficiently percolated networks throughout the anode. This means Ni particles connected to the interconnect surface, and YSZ particles connected to the electrolyte surface. Visual examples of percolated versus non-percolated particles can be seen in CHAPTER 5. The porosity must equally allow for connected pathways for delivery and removal of gas involved in the electrochemical process at the TPB sites.

2D imaging does not allow for an accurate mean of establishing the percolation in a system. Detailed 3D analysis is needed to develop a more precise idea of the effectiveness of TPB sites in terms of their connection to a percolated network. Thus percolation in the samples is not investigated and all values for TPBs are presented as imaged.

6.1.2 Image Analysis

The imaging process follows the method described in section 3.3, wherein SEM images are converted and generate values for further analysis such as the particle area. This process is applied to the Ni particles and pores in the sample, and the YSZ was treated as the background value. This was decided as the YSZ particles have a relatively un-circular shape, meaning the circle approach would be less appropriate for comparison. The Ni particles and pores are roughly circular and approximated as such to allow for an effective radius to be determined for each particle in an image. Also of the 3 phases in the system the YSZ was clearly the most connected of the phases, suggesting a high level of percolation and relatively even distribution through the system.

The data available from the microstructural analysis (CHAPTER 4) produced parameters describing the x,y centre coordinates as well as a radius and a material distinction (Ni or Pore). These parameters are further analysed by a programme. The programme aims to achieve a few steps .1) To represent the circles as defined by their given parameters, 2) establish whether the circles have an overlapping intersection with another circle or has no contacts, 3) then the circles which have intersections with particle not of the same material type are collected and presented in an array available for output into excel files for further analysis. This allows for calculation of the total number of TPB points as well as the overlap length of overlaps.

6.1.3 Laplacian Adjacency Matrix

A Lapacian adjacency matrix is used in graph theory to represent graphs without self loops. As such it is a useful tool in investigating interconnectivity and percolated networks between particles. Establishing if the particles are in contact is done through measuring the Euclidean distance d between the particles as shown in Figure 6-1, where r is the particle radius and $x\ and\ y$ are their respective coordinates. The evaluation of d is shown in Equation 6-1. If the value for d is less than the combined values for the particle radii they are in contact.

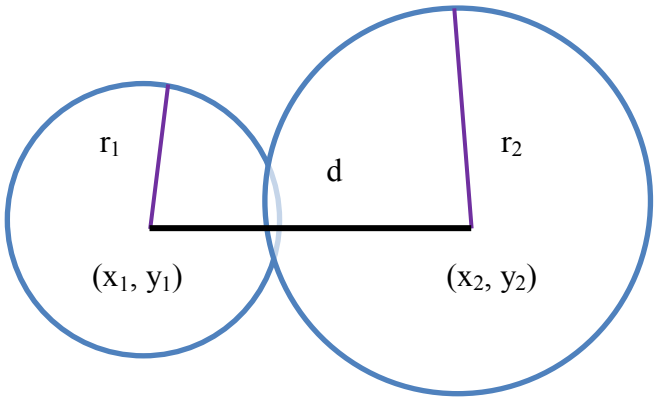

Figure 6-1 Diagram of Euclidean distance between two particles to determine if in contact. The respective x,y coordinates are used to determine if the distance d between the samples is less than or equal to the combined radius values.

$$d = \sqrt{(x_2 - x_1)^2 + (y_2 - y_1)^2}$$

Equation 6-1

If

$$d \leq r_1 + r_2 = contact$$

An example of the process for representing contact is shown in Figure 6-2, where a number of particles are in contact and one has no contacts. This is represented in a matrix which is then analysed to see whether the particle has contacts and if so what the contact angle is as well as the material contacting nature (different or the same). These lists are compiled and an average value for the Pore and Ni contact angle are produced, as well as the cumulative value of the TPB points and the overlap length.

a)

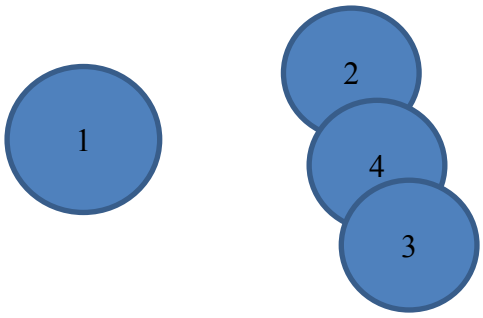

b)

	1	2	3	4
1	0	0	0	0
2	0	0	0	1
3	0	0	0	1
4	0	1	1	0

Figure 6-2 For determining the nature of contacting circles a Laplacian adjacency matrix was applied with a) example image of circular particles and b) the respective Laplacian adjacency matrix representing contacts.

It is worth noting that the sum of the rows is equivalent to double the number of contacts. For example in the above example, there are two contacts but would numerically be counted as four.

6.1.4 Identifying Nickel-Pore Contacts

For each circle created from the radii generated from the imaging analysis a material flag was ascribed. This value is used when identifying which particles have contact

with other particles (or pores), and in particular contact with a different material to its own.

6.1.5 Theta Value and Lengths

The contact angle is known to influence electrochemical performance [289], as this affects the TPB length. For determining the values of the contact angle and the overlap length, Figure 6-3 show a visual representation of the how the parameters are established.

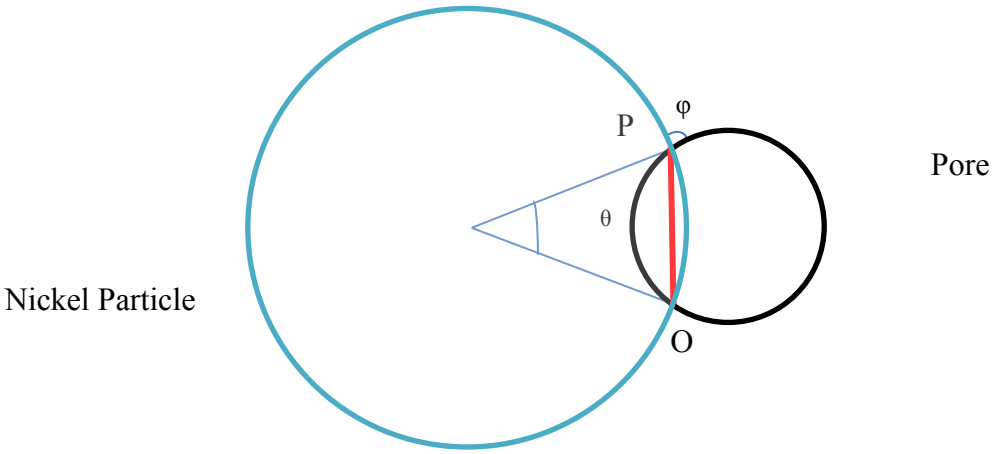

Figure 6-3 Diagram describing the nature of contact angle and overlap length. The distance between intersecting points P and O represent the overlap length for the pore and Nickel contact.

The contact angle θ, as defined as the arc created from the two intersection points, is evaluated as the whole contact angle, however it is important to note that the value used in literature previously by Costamagna [303] is half this value. For establishing the overlap length a straight line is drawn between the given intersection points and this value is then exported. In reality the Ni particle is not going to deform on contact

with a pore, but for any given interface the length of the intercept is going to be proportional to the arc, and thus serves as a useful analysis tool. Equation 6-2 describes the relationship, where $r_{Ni,eff}$ is the effective Ni particle radius, θ_{Ni}^{rad} is the contact angle in radians, and arc_{Ni} is the resultant arc length.

$$r_{Ni,eff}\theta_{Ni}^{rad} = arc_{Ni} \qquad \textbf{Equation 6-2}$$

The value φ represents the YSZ contact angle. It is known as the supplementary angle of the intersection angle. Figure 6-4 shows the variables used to establish the value for φ.

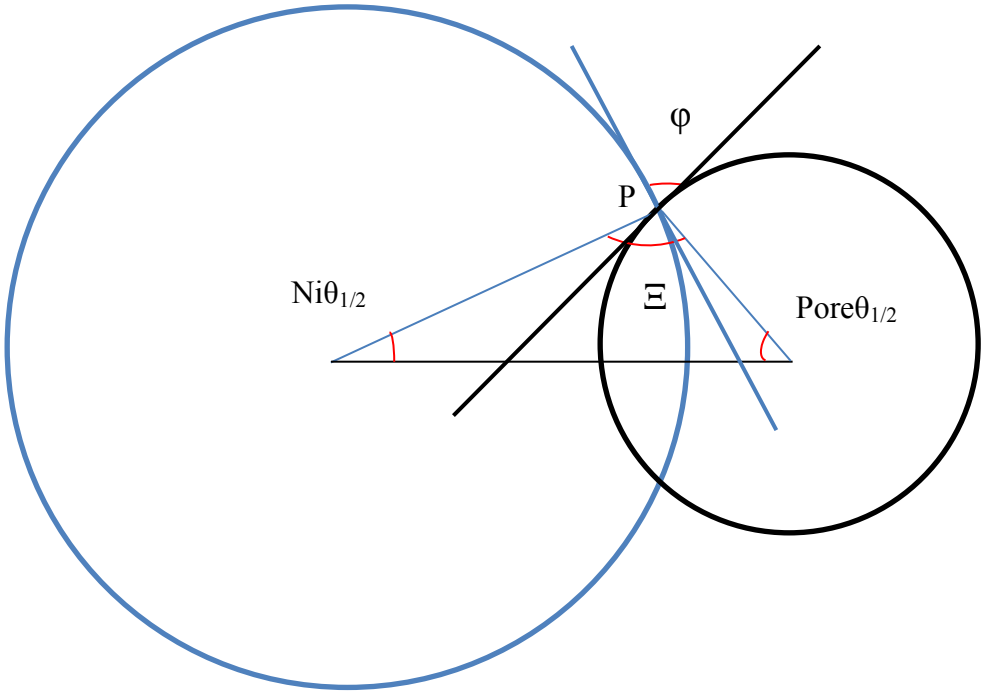

Figure 6-4 Diagram showing the radius of each circle to the intersecting point P and the tangent lines at those points. The resultant angles above and below are shown by φ and Ξ respectively.

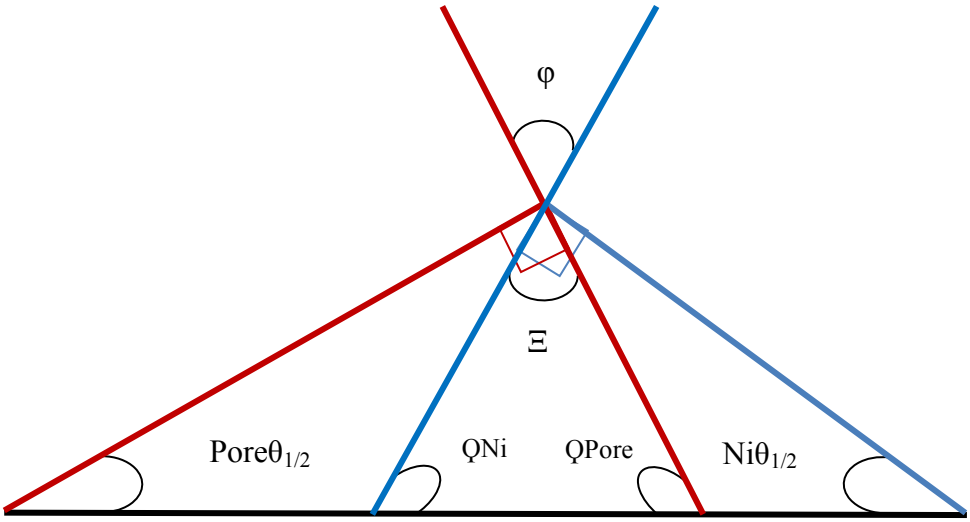

Figure 6-5 Depiction of triangle created by $Ni\theta_{1/2}$ and $Pore\theta_{1/2}$ and that created by the tangents to the radius at the point of intersection P.

As tangential lines perpendicular to the radius we know the that the right angles formed allow determination of the angles $\Qoppa Ni$ and $\Qoppa Pore$. As all the interior angles formed in a triangle are 180°, we can establish the combined values for intersection angles Ξ and thus φ. Equation 6-1 to Equation 6-7 show the process for this calculation.

$$\Qoppa Ni = 180 - 90 - Ni\theta_{1/2} \qquad \textbf{Equation 6-3}$$

$$\Qoppa Pore = 180 - 90 - Pore\theta_{1/2} \qquad \textbf{Equation 6-4}$$

$$\varphi = \Xi \qquad \textbf{Equation 6-5}$$

$$\Xi = 180 - \Omega Pore - \Omega Ni$$ **Equation 6-6**

$$\varphi = Ni\theta_{1/2} + Pore\theta_{1/2}$$ **Equation 6-7**

6.2 Comparisons of SEM and ImageJ Images with Image analysis Output

In both Figure 6-6 and Figure 6-7 , the circles being generated are those which share an overlapping circumference, so particles without contact are not included (though are calculated). The black and white image highlights more clearly the accuracy of the circles to represent the individual particles and pores. Visually it shows that certain particles which appear more oval in shape are likely to be wider than their respective radius and equally shorter on the alternative section. Whilst this could cause the process to falsely identify a contact or a non-contact with a pore and thus could alter the number of TPB points, it is assumed in the model that this aspect balances out over all images for comparison between data sets.

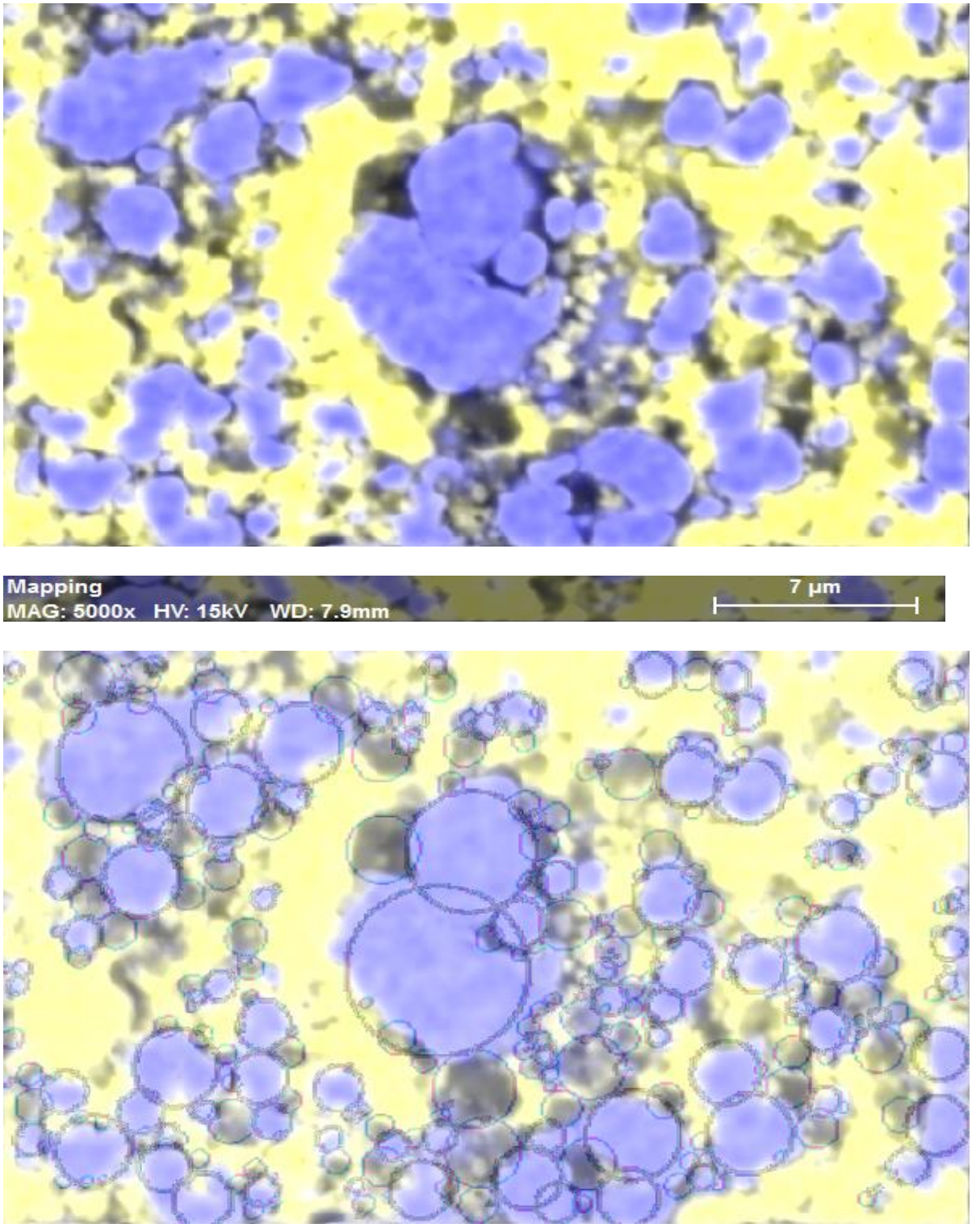

Figure 6-6 Comparison of original cropped SEM image and it with overlapping circles. Channels can be seen to form a collection of connected smaller pores often surrounding the nickel particles.

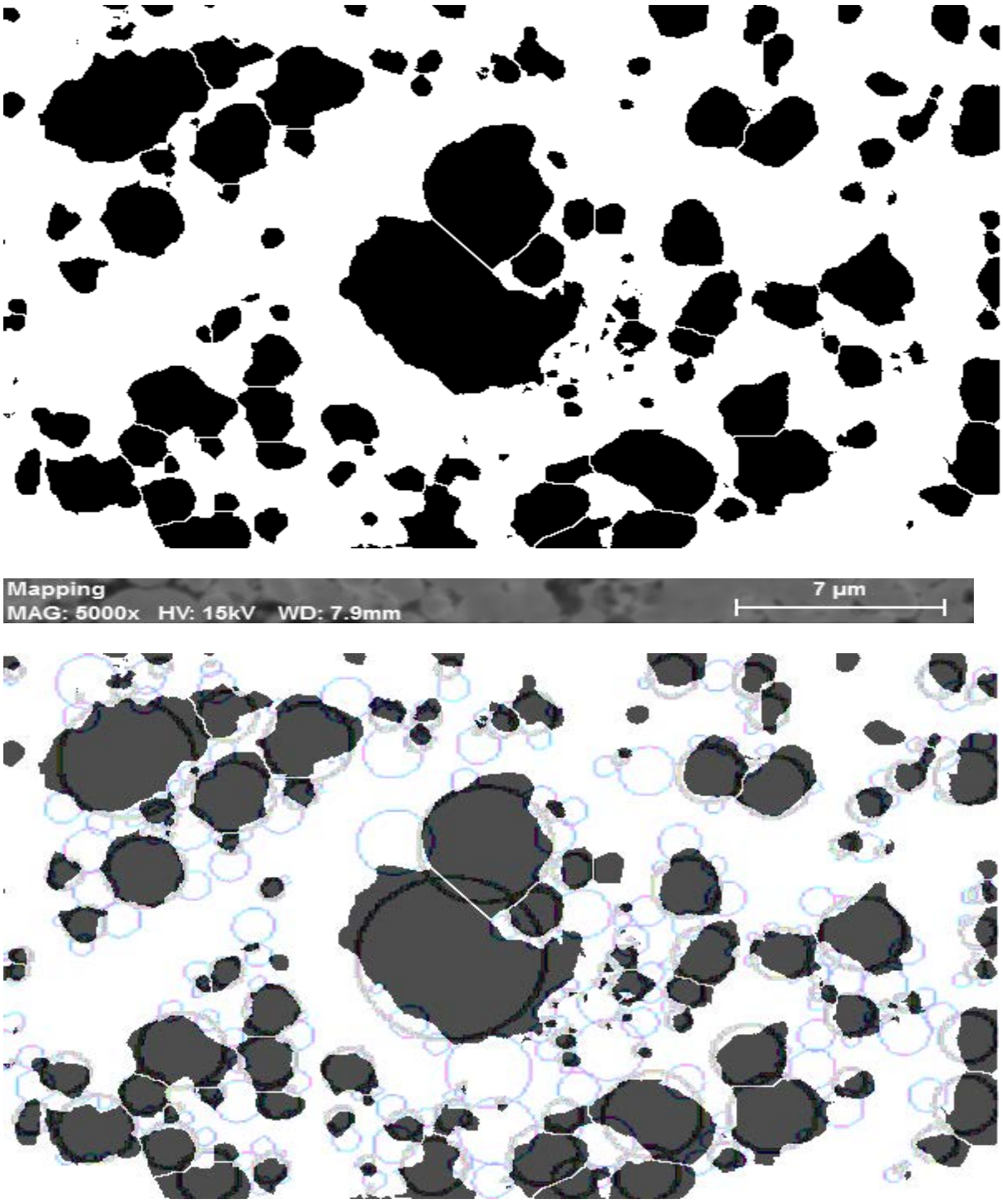

Figure 6-7 Comparison of colour thresholding, black and white creation of Ni particles (and pores with YSZ) and watershed image with circle-generation overlap model.

In figure 6.5 we see a total of 297 particle pore contacts out of a total of 496 Ni and pore particles. The particles with contacts are visible in the image.

6.3 TPB Identification

As discussed the YSZ forms the background for the images generated, and the Ni-pore interface defined by the circles generated through the effective radius values are overlapped onto this background. The Laplacian adjacency matrix is used to identify those particles in contact with other particles and through the material flag further identify which ones are in contact with a different material i.e. a pore-Ni contact. These contacts represent the TPBs in the image. As the particle is likely to have two intersection points for a given pore-Ni contact, each set of contacts was treated as 1 site for the sake of comparison within the data presented later on.

6.4 Modelling Results and Discussions

The data when analysed produced a selection of Ni and pore angles as well as their overlap length. In Figure 6-8 the variation in the nickel contact angle θ is plotted for the varying sample sets.

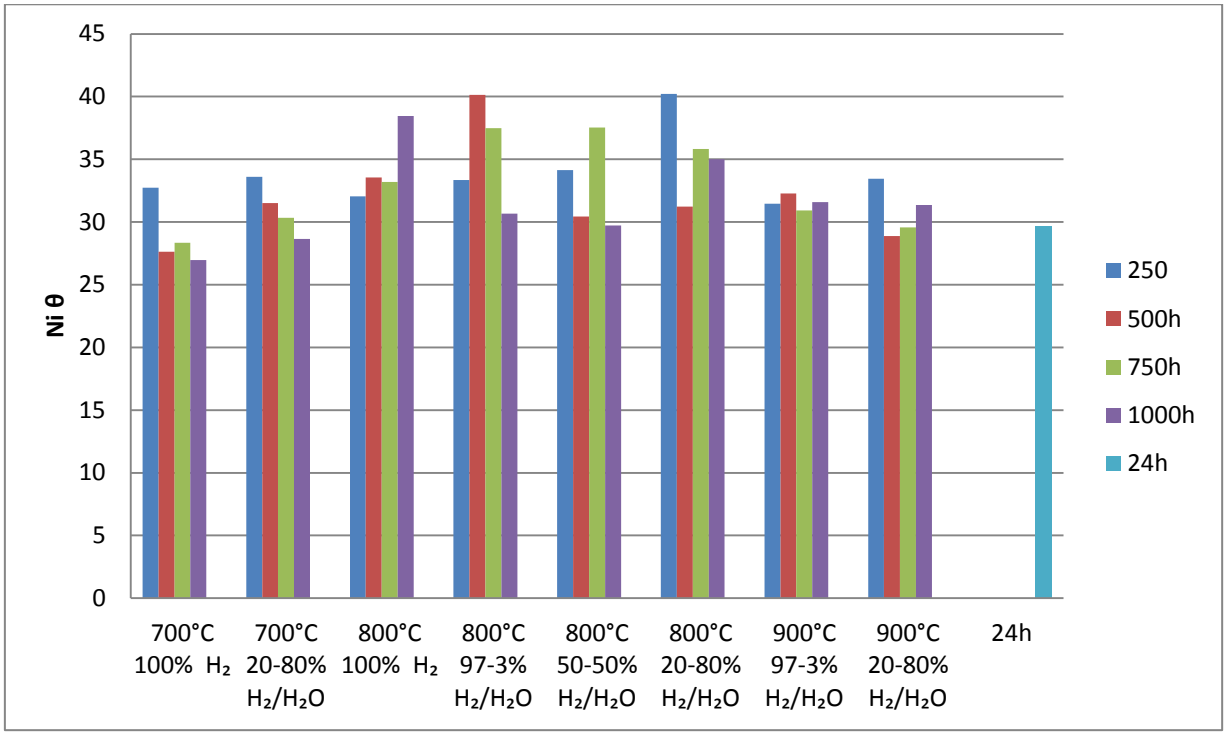

Figure 6-8 Mean Ni θ values for samples sets over time. Each time frame shows the average of two samples. Each sample was evaluated through 12 images covering random sections of the sample.

Whilst there is a slight trend in an initial decrease of θ after the 250 hours, there is no clear path taken by the contact angle in terms of change in a given temperature of fuel regime over time, due to the intra-variation between sample sets. To see if trends became more apparent, the values were adjusted according to their different Ni area percentage compared to the mean value, as shown in Figure 6-9. Equation 6-8 shows the method for adjusting the Niθ values.

$$\frac{Ni_\theta \times Average\ Ni\ area\ \%}{Sample\ Ni\ area\ \%} = Adj\ Ni_\theta$$ **Equation 6-8**

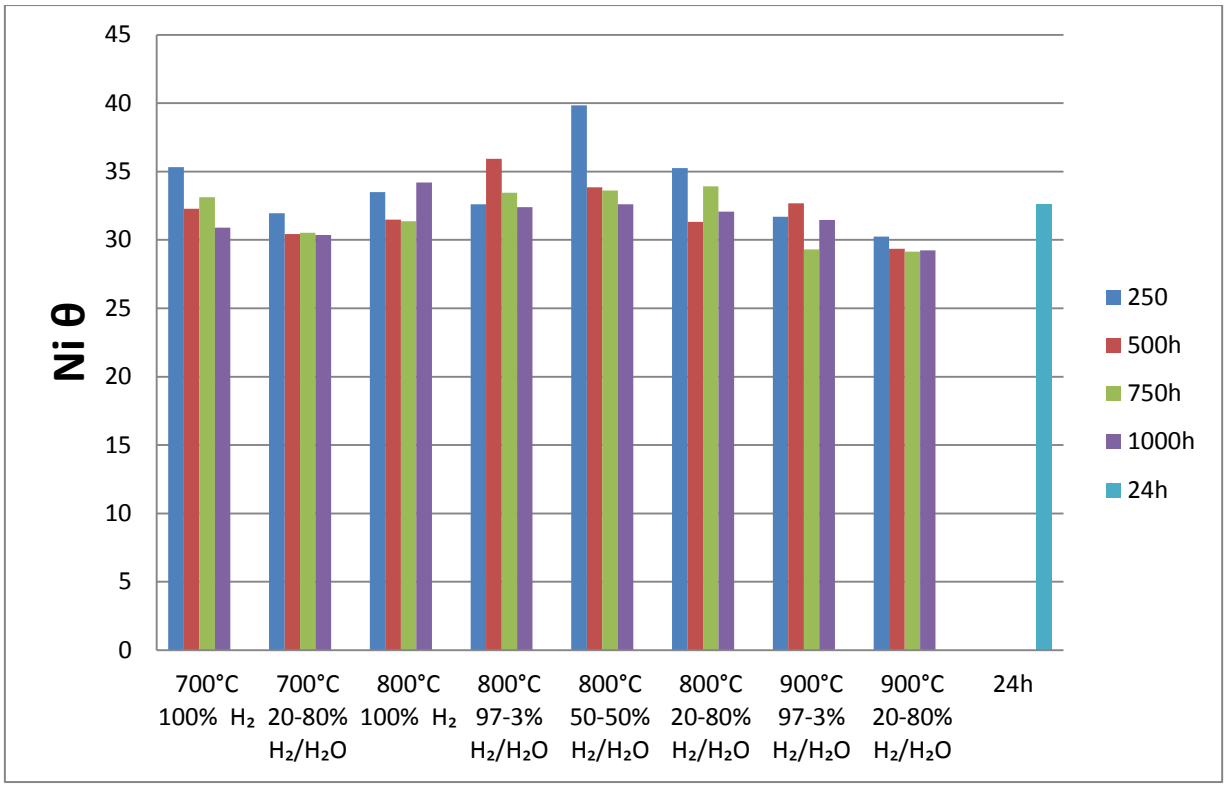

Figure 6-9 Mean Ni θ values adjusted for variation in Ni area percent for samples sets over time. Each time frame shows the average of two samples. Each sample was evaluated through 12 images covering random sections of the sample.

The figure shows smaller distribution between values, suggesting that the variation in Ni θ was simply to do with sample sections. Under the assumption that porosity cannot be further introduced, should the Ni contact angle remain constant then this would be due to a parallel growth or change in mean pore value relative to the Ni particle radius. It is however noted that there is a smaller downwards trends in contact angle size over time, especially after the first 250h. If there is a change in angle during the first 500h this is likely to be when change is undergone in the sample. When looking at the θ values for pores and that of nickel, the samples

generally show a trend where on value increase or decrease results in the opposite θ value, which suggests that the value for the YSZ contact angle φ remains constant.

Table 6-1 shows the mean θ values as well as their standard deviation and its relative size to the mean. The combined θ value is related to the value of YSZ's θ (the value is double φ) at the intersection points, and the small standard deviation is a sign of the relatively constant ratio between Ni θ and pore θ values.

Table 6-1 Mean θ values and relative standard deviation.

	Ni θ	pore θ	Combined θ	Ni θ/ Ni %
Mean	32.60	81.81	114.38	32.26
Std. dev	3.34	5.21	2.70	2.23
% dev	10.36	6.37	2.36	6.89

When looking at the data regarding number of TPB points and the overlap length of Ni and pore, it highlights that no definitive overall trend exist with the data as generated from the analysis. Many of the samples see a decline in TPB as expected but some samples in fact show an increase over time. Due to the nature of TPB points being related to the ratio of Ni volume and porosity, the values were adjusted according to this ratio, to better reflect the number of points between samples. Equation 6-9 describes this adjustment ratio

$$\left(\frac{Ni\ area\ \%}{Pore\ area\ \% + Ni\ area\ \%}\right) \times TPB = adj\ TPB \qquad \textbf{Equation 6-9}$$

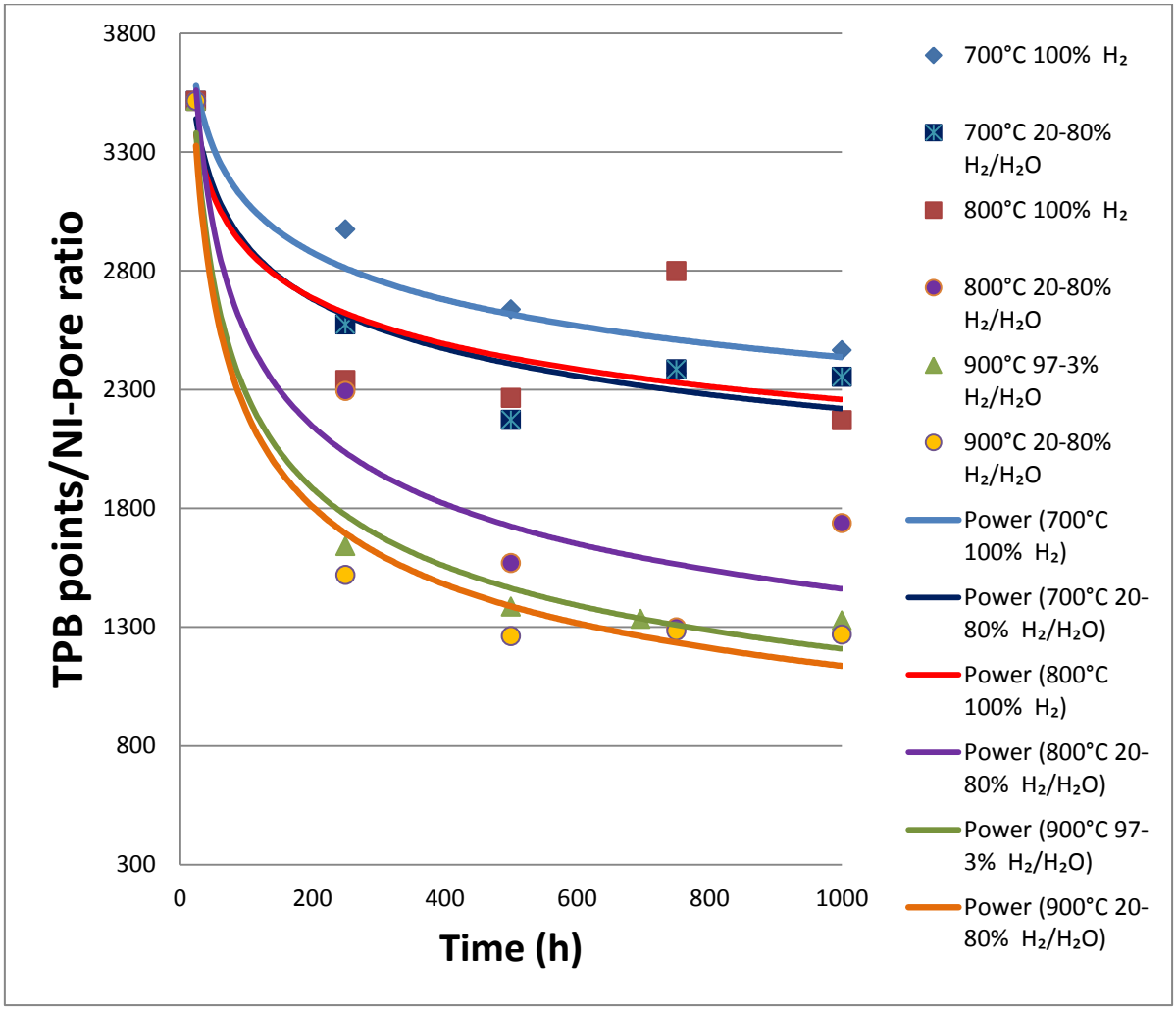

Figure 6-10 TPB points divided by respective Ni area %/porosity ratio over time for a given temperature (°C) and fuel composition (H_2/H_2O). The curve is a power law fitting of the data to show general trends.

The data presented in Figure 6-10 highlights the change over time for the number of TPB points. Power law trendlines have been applied to the data sets to suggest the presented decrease in TPB points over time for a given temperature and fuel regime. The graph is representative of the loss of performance in the Ni-YSZ anode, as highlighted in Figure 2-16. Compared to previous analysis of Ni particle radii and the

suggested change in TPB lengths according to modelling, these results suggest a closer relationship between the high and low steam content tests at 900°C.

The data in Figure 6-10 does not include the values for 800°C 50-50% H_2/H_2O and 800°C 97-3% H_2/H_2O runs. The 50-50% H_2/H_2O run was very irregular in the values generated for TPB points. This is likely a circumstance of when the extreme deviations are generated from a sample on similar run. The initial 250h test provided a particularly high mean value for the mean Ni particle radius, which is mirrored by the relatively low evaluation of TPB points. For 97-3% H_2/H_2O the trend is the same as that in the particle radius, the 250h and 1000h samples look to be reversed, with the highest mean radius and lowest number of TPB points present in the 250h samples rather than the 1000h.

Table 6-2 R^2 values relative to sample set for TPB points fitting curves.

Sample Set	700°C 100% H_2	700°C 20-80% H_2/H_2O	800°C 100% H_2	800°C 20-80% H_2/H_20	900°C 97-3% H_2/H_2O	900°C 20-80% H_2/H_2O
R^2	0.931	0.885	0.654	0.8529	0.972	0.952

The fitting curves generated in Figure 6-10 had respective R^2 values determined. Most show a high level of ability for the generated curve equations to take into account the variance of the data points to the curve. Whilst the values themselves look good with regards to validating the suggested curves it is important to note that these values do not inherently mean the curves are good fits for the data.

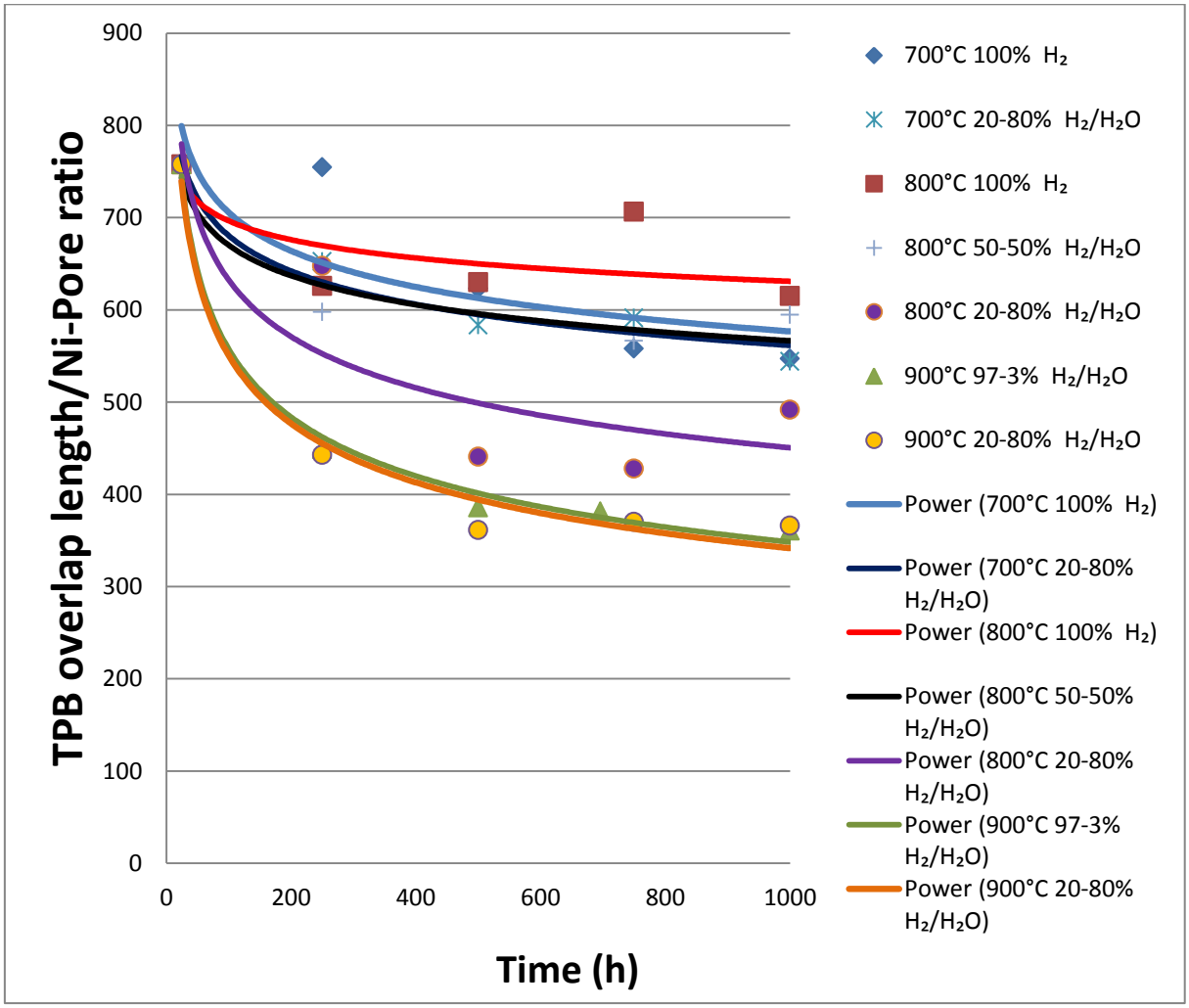

Figure 6-11 TPB overlap length adjusted according to Ni area percent vs. porosity ratio for a given temperature (°C) and fuel composition (H_2/H_2O). The curve is a power law fitting of the data to show general trends.

The final aspect of the analysis looks over the overlap length generated from the pore-Ni particle contact. Unlike the TPB points this is more likely to acknowledge the larger surface area available on larger particles-pore sites whilst still taking into account the actual number of points. It is however only a gauge to compare against, as the exact distance between a contact of Ni-Pore-YSZ is likely to impact the actual effectiveness of a given site. Figure 6-11 shows the plotting of the values adjusted to

take into account the Ni-Pore ratio as done previously. The figure has similar trends to that analysing TPB points, however, 800°C 100% H_2 presents a significantly higher value than expected. 800°C 50-50% H_2/H_2O however, in this analysis shows a trend more in keeping with the expected change over time, mirroring that seen in the 700°C 20-80% H_2/H_2O sample. The other curves follow an expected pattern over time, with the relative availability of effective TPB length decreasing over time. Similar to the previous analysis R^2 values were determined to highlight potential suitability for the given curves. Unsurprisingly 800°C 100% shows a weaker accounting for the variance then the other curves.

Table 6-3 R^2 values relative to sample set for TPB overlap length fitting curves.

Sample Set	700°C 100%H_2	700°C 20-80%H_2/H_2O	800°C 100%H_2	800°C 50-50% H_2/H_2O	800°C 20-80%H_2/H_20	900°C 97-3% H_2/H_2O	900°C 20-80%H_2/H_2O
R^2	0.948	0.688	0.654	0.895	0.770	0.989	0.964

6.5 Conclusions

An approach capable of analysing nickel and pore data containing x,y coordinates, radius and a material identifier and capable of providing an indication of the Ni and pore contact angles, TPB points and an overlap length for the pore-Ni interface is presented. Intra-variation between sample sets prevented ascertaining trends in the samples. To overcome this issue the mean Ni contact angles and TPB points/overlaps were adjusted according to their Ni content and Ni content/porosity ratio respectively. The Ni and pore contact angles from the experimental data have

been determined via this method. A mean Ni θ value of ~32° was determined, which matches closely with previous literature values [303]. An initial decrease in Ni θ is seen for some sample sets for 250h, however after this time the samples are fairly constant in their values. Ni and pore θ values when combined values (and thus the YSZ contact angle) showed very consistent values, suggesting that the ratio of pore size distribution to nickel particle distribution changes over time are proportional. This is likely caused by the YSZ microstructure influencing the change of the Ni particles and pores. An increase in temperature and/or steam content both correlated to a decrease in the number of TPB points and overlap lengths over time. Samples run at higher temperature and steam content can be used to predict the life microstructure change in samples meant to run at lower operating conditions and steam content in shorter time periods via this analysis technique.

CHAPTER 7 Conclusions and Further Work

7.1 Discussion of the Value of the Work Presented Here

The importance of understanding the microstructural changes in SOFC anodes and how this impacts on the long term performance of the cells, is a fundamental issue for the successful commercialisation of SOFCs. Comparative testing of the effects of steam content and temperature on the microstructural change is limited in availability in literature due to the necessity for long term testing. 3D analysis whilst more detailed and accurate in its presentation of microstructural information, is significantly more time consuming and dependant on costly equipment, and thus alternatives which offer accurate interpretations of the trends in microstructural change at less analytic effort supply potential alternative avenues for analysis. In particular for the development of new material compositions or differing microstructural parameters, the ability to test samples for relatively short durations for establishing the longer term projected performance has tangible cost and time saving benefits. By operating cells at higher temperature and steam compositions, estimations for the change in microstructure are feasible, and can be extrapolated back to more moderate operating conditions more realistically representing SOFC system operating conditions.

Samples were tested in varying degrees of steam content from 0% up to 80%, and temperatures of 700°C, 800°C and 900°C. The samples were cut, polished and imaged to create a portfolio of data to represent the microstructures in question. The

ImageJ software used to create black and white representations of the pores and nickel particles uses a thresholding method to present a suitably accurate description of the likely particle dimensions. These values were analysed to determine the particle size distributions present in the samples, and mean values for the nickel particle and pore sizes were determined. These were compared with the determined Ni area percentage and porosity, to draw conclusions on representative changes in the mean Ni radius over time for given test regimes. Ni particle radius growth rates were plotted against each other and temperature was seen to impact the rate of agglomeration for the Ni particles, as shown in Figure 4-9, in particular for those samples tested at 900°C. This was attributed to the fact that metals are known to coarsen more significantly above 2/3rds of their melting point, which for Ni is 879°C. Coarsening was accelerated by increasing the steam content, and all samples with 20-80% H_2/H_2O showed comparatively larger mean Ni particle size for the same time section compared to those with little to no steam content (0-3%). Porosity in some samples was lower compared to the expected value of ~15 area percent for the given Ni content.

By taking the x,y coordinates, radius and material identifiers from the microstructural analysis, a programme code capable of providing Ni and pore contact angles, TPB points, and an overlap length for the pore-Ni interface was developed. A method to determine the Ni and pore contact angles from the experimental data was achieved and a mean Ni θ value of ~32° was determined, which matches closely with previous experimental analysis [303]. A proportional change in Ni and pore size distribution over time was determined through comparison of the combined θ values. Data for the TPB points and the overlap length of the experimental samples was generated and

through adjustment relative to their Ni area percentage and porosity were analysed for trends. The TPB points, much like the Ni particle radii, showed a representative change over time, with the reduction in the number of Ni particles through diffusion of smaller particles into larger adjacent particles leading to a reduction in the total number of available TPB sites. The overlap length analysis provided another interesting insight into changes occurring in the SOFC anode, being able to more representatively show the changes occurring in the 800°C 50-50% H_2/H_2O sample compared simply to the number of sites. Temperature and steam content both correlated to a decrease in the number of TPB points and overlap lengths over time, however, the effect of steam was more noticeable below 900°C, where the effect of the temperature presented a more determinate role in overall change of TPB points and overlap.

Models for predicting Ni particle radius growth as well as microstructurally determined features such as conductivity and TPB length were presented in this work. Two models for predicting the nickel particle radius change for a given temperature and fuel composition were presented, allowing predictions of Ni growth rate dependant on the steam content to be established. The radius predictions are incorporated into a particle packing model capable of predicting various parameters of the anode for a given mean particle size, allowing for a time dependant model which can predict important parameters such as the change in TPB length per unit volume over time. The radius predictions were compared to experimental data and showed good correlation in their estimations of growth rates. The benefits of being able to predict various aspects of the anode performance change were described; however, it is important to note that different systems and material compositions can require

alternative values determined for various parameters presented to ensure model accuracy. As the model can perform with 2 dimensional data it allows for a less demanding analysis route compared to 3 dimensional models.

By running new samples or set ups through a higher temperature and steam combination, a better projection of the longer term performance is determinable in a shorter period of time. With more cell design moving towards lower temperature to reduce operating and equipment costs, the relative decrease in performance of anode components will take significantly longer at 700°C compared to 900°C to plateau in terms of Ni particle growth. Thus by utilising the models and reference data in this thesis a method for determining the rate of performance loss can be determined for samples. An example of the use of the model for effective TPB length per unit volume is shown in Figure 7-1. The sample run at 900°C and a fuel composition of 20-80% H_2/H_2O reached its plateau in terms of degradation in $1/10^{th}$ of the time taken for a sample at 700°C and 100% H_2 (roughly 1,600 hours versus 16,000 hours). Of course there are certain assumption and differences that need to be taken into account when making these comparisons. Firstly whilst it is assumed the steam only has an accelerating effect on the Ni particles, it is worth noting it could lead to other influencing factors such as increased loss of Ni mass due to volatilisation. This would likely show an increased value for the mean Ni particles as smaller particles would deplete at a faster rate. Also steam is generated during the reactions along the length of the anode and thus degradation is not likely to be consistent along its length, potentially altering when it reaches its plateau. Equally whilst comparatively there is only a 200°C difference between both tests, different mechanisms can dominate in different temperature regimes. For example the

increased coarsening seen above 2/3rd a metals melting point noted in CHAPTER 4. Both these points alone highlight that any comparison made between the testing conditions is only an indication of the relative performance. No data for a 16,000 hour test was attempted and thus its expected change is only a prediction. Any significant physical investment in using this procedure would ideally complete a test of this length to understand any other factors and the accuracy its ability to predict can provide.

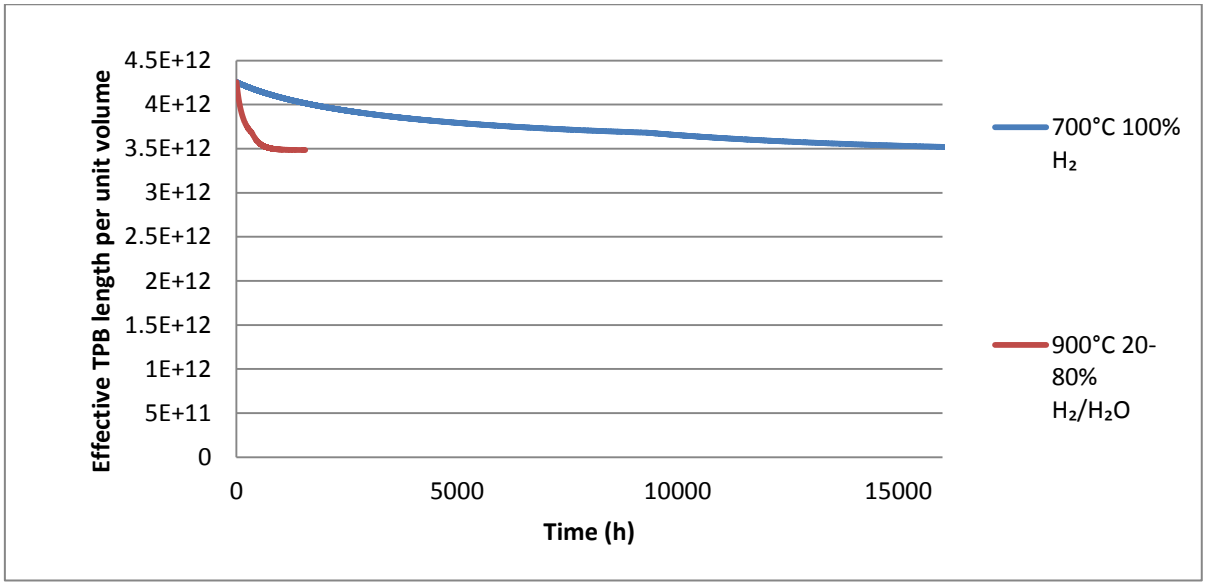

Figure 7-1 Example of TPB effective length modal predictions for use in accelerated testing. The significantly shorter time taken for the higher temperature and steam content testing to reach the plateau can be used to potentially predict longer term performance of a variety of samples.

7.2 Further Work

The nature of the work was to investigate the microstructural change occurring in the study experiments in order to allow for extrapolation of the change in performance in the cells. Comparison of these microstructural changes with long term electrochemical experiments both for performance data but also as a cross comparison of the microstructural change would be of benefit to the research. Due to the reactions taking place in the anode the specific amount of steam at a given location in a cell may vary, and comparisons between regions of cells may provide interesting insight into regional variations in cell degradation Certain parameters used in modelling in this thesis are based on relatively limited available data in literature. An in-depth analysis to determine the variables and how some of them are affected by the materials in question or their physical properties could benefit the accuracy of the model. Also seeing how different material compositions, especially with alternatives to YSZ or with doped Ni, perform to allow for integration with the model would add to the field of study. 3D tomography represents a tool for very detailed analysis of the microstructure in SOFCs, and if incorporated with 3D modelling tools can potentially allow for improvements in microstructural optimisation (relative to initial particle size distributions, pore former choice, etc.). The effects of contaminates in the fuel stream can have progressive degradation effects on the anode, and can affect the grain growth rate, volatisation, and TPB point changes considerably. Models capable of predicting the change in these parameters based on the level of contaminates would benefit from further testing done with respect to these variables. If combined with a model for cathode degradation, a complete description of the effects of degradation affecting the SOFC could be presented for

cell optimisation and testing. Lastly the ability of the thesis to adequately provide a detailed approach for accelerated testing were briefly described in the thesis, and further comparison of the predictions with significantly longer term (10,000+ hours) testing would allow for further validation of the work.

References

1. Kendall, K., *Introduction to SOFCs*, in *High-Temperature Solid Oxide Fuel Cells for the 21st Century (Second Edition)*. 2016, Academic Press: Boston. p. 1-24.
2. Delphi. *Delphi truck fuel-cell APU to hit road in 2012*. [cited 01/04/2017]; Available from: http://articles.sae.org/8222/.
3. NETL. *Solid Oxide Fuel Cells Technology Program Plan*. [cited 01/01/2015]; Available from: https://www.netl.doe.gov/File%20Library/Research/Coal/energy%20systems/fuel%20cells/Program-Plan-Solid-Oxide-Fuel-Cells-2013.pdf.
4. Yang, Z., et al., *Selection and Evaluation of Heat-Resistant Alloys for SOFC Interconnect Applications.* Journal of The Electrochemical Society, 2003. **150**(9): p. A1188-A1201.
5. Norman Bessette, D.P., Reginald Tyler, *Development of a Low-Cost 3-10 kW Tubular SOFC Power System- FY2011 Objectives.* 2011.
6. Shearing, P.R., D.J.L. Brett, and N.P. Brandon, *Towards intelligent engineering of SOFC electrodes: a review of advanced microstructural characterisation techniques.* International Materials Reviews, 2010. **55**(6): p. 347-363.
7. Mehmeti, A., et al., *Life cycle sustainability of solid oxide fuel cells: From methodological aspects to system implications.* Journal of Power Sources, 2016. **325**: p. 772-785.
8. Schmidt, M.S., et al., *Characterisation of the Ni/ScYSZ interface in a model solid oxide fuel cell anode.* Solid State Ionics, 2008. **179**(39): p. 2290-2298.
9. Schmidt, M.S., et al., *Effects of trace elements at the Ni/ScYSZ interface in a model solid oxide fuel cell anode.* Solid State Ionics, 2008. **179**(27–32): p. 1436-1441.
10. Schmidt, M.S., et al., *Three-phase-boundary dynamics at the Ni/ScYSZ interface.* Solid State Ionics, 2009. **180**(4–5): p. 431-438.
11. Fang, Q., et al., *Durability test and degradation behavior of a 2.5 kW SOFC stack with internal reforming of LNG.* International Journal of Hydrogen Energy, 2013. **38**(36): p. 16344-16353.
12. Shaikh, S.P.S., A. Muchtar, and M.R. Somalu, *A review on the selection of anode materials for solid-oxide fuel cells.* Renewable and Sustainable Energy Reviews, 2015. **51**: p. 1-8.
13. Kendall, K., *1 - Introduction to SOFCs*, in *High-Temperature Solid Oxide Fuel Cells for the 21st Century (Second Edition)*. 2016, Academic Press: Boston. p. 1-24.
14. Dodson, B. and H. Schwab, *Accelerated Testing - A Practitioner's Guide to Accelerated and Reliability Testing*. 2006, Society of Automotive Engineers, Inc.
15. Weber, A., et al., *Accelerated Lifetime Tests for SOFCs.* ECS Transactions, 2015. **68**(1): p. 1953-1960.
16. Simwonis, D., F. Tietz, and D. Stöver, *Nickel coarsening in annealed Ni/8YSZ anode substrates for solid oxide fuel cells.* Solid State Ionics, 2000. **132**(3–4): p. 241-251.
17. Faes, A., et al., *Nickel–Zirconia Anode Degradation and Triple Phase Boundary Quantification from Microstructural Analysis.* Fuel Cells, 2009. **9**(6): p. 841-851.
18. Nelson, G.J., et al., *Three-dimensional microstructural changes in the Ni–YSZ solid oxide fuel cell anode during operation.* Acta Materialia, 2012. **60**(8): p. 3491-3500.
19. Tanasini, P., et al., *Experimental and Theoretical Investigation of Degradation Mechanisms by Particle Coarsening in SOFC Electrodes.* Fuel Cells, 2009. **9**(5): p. 740-752.

20. Wincewicz, K.C. and J.S. Cooper, *Taxonomies of SOFC material and manufacturing alternatives.* Journal of Power Sources, 2005. **140**(2): p. 280-296.
21. Kilner, J.A., J. Druce, and T. Ishihara, *4 - Electrolytes A2 - Kendall, Kevin*, in *High-Temperature Solid Oxide Fuel Cells for the 21st Century (Second Edition)*, M. Kendall, Editor. 2016, Academic Press: Boston. p. 85-132.
22. Preux, N., A. Rolle, and R.N. Vannier, *12 - Electrolytes and ion conductors for solid oxide fuel cells (SOFCs)*, in *Functional Materials for Sustainable Energy Applications*. 2012, Woodhead Publishing. p. 370-401.
23. Arachi, Y., et al., *Electrical conductivity of the ZrO2–Ln2O3 (Ln=lanthanides) system.* Solid State Ionics, 1999. **121**(1–4): p. 133-139.
24. Kilner, J.A., *Fast oxygen transport in acceptor doped oxides.* Solid State Ionics, 2000. **129**(1–4): p. 13-23.
25. Kilner, J.A., *Fast anion transport in solids.* Solid State Ionics, 1983. **8**(3): p. 201-207.
26. Kim, D.J., *Lattice Parameters, Ionic Conductivities, and Solubility Limits in Fluorite-Structure MO2 Oxide [M = Hf4+, Zr4+, Ce4+, Th4+, U4+] Solid Solutions.* Journal of the American Ceramic Society, 1989. **72**(8): p. 1415-1421.
27. Navrotsky, A., *Thermochemical insights into refractory ceramic materials based on oxides with large tetravalent cations.* Journal of Materials Chemistry, 2005. **15**(19): p. 1883-1890.
28. Haering, C., et al., *Degradation of the electrical conductivity in stabilised zirconia system: Part II: Scandia-stabilised zirconia.* Solid State Ionics, 2005. **176**(3–4): p. 261-268.
29. Lee, D.S., et al., *Characterization of ZrO2 co-doped with Sc2O3 and CeO2 electrolyte for the application of intermediate temperature SOFCs.* Solid State Ionics, 2005. **176**(1–2): p. 33-39.
30. Politova, T.I. and J.T.S. Irvine, *Investigation of scandia–yttria–zirconia system as an electrolyte material for intermediate temperature fuel cells—influence of yttria content in system (Y2O3)x(Sc2O3)(11−x)(ZrO2)89.* Solid State Ionics, 2004. **168**(1–2): p. 153-165.
31. Yuan, F., et al., *Investigation of the crystal structure and ionic conductivity in the ternary system (Yb2O3)x–(Sc2O3)(0.11−x)–(ZrO2)0.89 (x = 0–0.11).* Journal of Alloys and Compounds, 2013. **549**: p. 200-205.
32. Tao, J., Y. Hao, and J. Wang, *The research of crystal structure and electrical properties of a new electrolyte material: Scandia and holmia stabilized zirconia.* Nippon Seramikkusu Kyokai Gakujutsu Ronbunshi/Journal of the Ceramic Society of Japan, 2013. **121**(1411): p. 317-325.
33. Mogensen, M., N.M. Sammes, and G.A. Tompsett, *Physical, chemical and electrochemical properties of pure and doped ceria.* Solid State Ionics, 2000. **129**(1–4): p. 63-94.
34. Andersson, D.A., et al., *Optimization of ionic conductivity in doped ceria.* Proceedings of the National Academy of Sciences of the United States of America, 2006. **103**(10): p. 3518-3521.
35. Deguchi, H., et al., *EXAFS study of doped ceria using multiple data set fit.* Solid State Ionics, 2005. **176**(23-24): p. 1817-1825.
36. Steele, B.C.H., *Appraisal of Ce1−yGdyO2−y/2 electrolytes for IT-SOFC operation at 500°C.* Solid State Ionics, 2000. **129**(1–4): p. 95-110.
37. Gödickemeier, M., et al., *Electrochemical characteristics of cathodes in solid oxide fuel cells based on ceria electrolytes.* Journal of the Electrochemical Society, 1997. **144**(5): p. 1635-1646.

38. Gödickemeier, M. and L.J. Gauckler, *Engineering of solid oxide fuel cells with ceria-based electrolytes.* Journal of the Electrochemical Society, 1998. **145**(2): p. 414-421.
39. De Souza, R.A. and J.A. Kilner, *Oxygen transport in La1−xSrxMn1−yCoyO3±δ perovskites: Part I. Oxygen tracer diffusion.* Solid State Ionics, 1998. **106**(3–4): p. 175-187.
40. Kilner, J.A. and R.J. Brook, *A study of oxygen ion conductivity in doped non-stoichiometric oxides.* Solid State Ionics, 1982. **6**(3): p. 237-252.
41. Ishihara, T., H. Matsuda, and Y. Takita, *Oxide Ion Conductivity in Doped NdAlO3 Perovskite-Type Oxides.* Journal of the Electrochemical Society, 1994. **141**(12): p. 3444-3449.
42. Stevenson, J.W., et al., *Influence of cobalt and iron additions on the electrical and thermal properties of (La,Sr)(Ga,Mg)O 3-δ.* Journal of the Electrochemical Society, 2000. **147**(9): p. 3213-3218.
43. Yasuda, I., et al., *Electrical conductivity and mechanical properties of alumina-dispersed doped lanthanum gallates.* Solid State Ionics, 2000. **135**(1–4): p. 381-388.
44. Choi, J.-J., et al., *Low temperature preparation and characterization of LSGMC based IT-SOFC cell by aerosol deposition.* Journal of the European Ceramic Society, 2012. **32**(1): p. 115-121.
45. Takahashi, T. and H. Iwahara, *Ionic conduction in perovskite-type oxide solid solution and its application to the solid electrolyte fuel cell.* Energy Conversion, 1971. **11**(3): p. 105-111.
46. Schober, T., J. Friedrich, and F. Krug, *Phase transition in the oxygen and proton conductor Ba2In2O5 in humid atmospheres below 300°C.* Solid State Ionics, 1997. **99**(1–2): p. 9-13.
47. Zhang, G.B. and D.M. Smyth, *Defects and transport of the brownmillerite oxides with high oxygen ion conductivity — Ba2In2O5.* Solid State Ionics, 1995. **82**(3): p. 161-172.
48. Fischer, W., G. Reck, and T. Schober, *Phase transition of Ba2in2O5 in humid air studied by in-situ X-ray powder diffraction*, in *Materials Science Forum*. 2000. p. 363-367.
49. Medvedev, D.A., et al., *Advanced materials for SOFC application: Strategies for the development of highly conductive and stable solid oxide proton electrolytes.* Progress in Materials Science, 2016. **75**: p. 38-79.
50. Green, M.A., A. Ho-Baillie, and H.J. Snaith, *The emergence of perovskite solar cells.* Nat Photon, 2014. **8**(7): p. 506-514.
51. Gill, J.K., O.P. Pandey, and K. Singh, *Ionic conductivity, structural and thermal properties of Ca2+ doped Y2Ti2O7 pyrochlores for SOFC.* International Journal of Hydrogen Energy, 2012. **37**(4): p. 3857-3864.
52. Kramer, S.A. and H.L. Tuller, *A novel titanate-based oxygen ion conductor: Gd2Ti2O7.* Solid State Ionics, 1995. **82**(1): p. 15-23.
53. Kumar, M., I.A. Raj, and R. Pattabiraman, *Y2Zr2O7 (YZ)-pyrochlore based oxide as an electrolyte material for intermediate temperature solid oxide fuel cells (ITSOFCs)—Influence of Mn addition on YZ.* Materials Chemistry and Physics, 2008. **108**(1): p. 102-108.
54. Matsumoto, H., T. Sakai, and Y. Okuyama, *Proton-conducting oxide and applications to hydrogen energy devices.* Pure and Applied Chemistry, 2013. **85**(2): p. 427-435.

55. Kendrick, E., M.S. Islam, and P.R. Slater, *Developing apatites for solid oxide fuel cells: Insight into structural, transport and doping properties.* Journal of Materials Chemistry, 2007. **17**(30): p. 3104-3111.
56. Jo, S.H., P. Muralidharan, and D.K. Kim, *Low-temperature sintering of dense lanthanum silicate electrolytes with apatite-type structure using an organic precipitant synthesized nanopowder.* Journal of Materials Research, 2009. **24**(1): p. 237-244.
57. Lacorre, P., et al., *Designing fast oxide-ion conductors based on La2Mo2O9.* Nature, 2000. **404**(6780): p. 856-858.
58. Marrero-López, D., et al., *Applicability of La2Mo2−yWyO9 materials as solid electrolyte for SOFCs.* Solid State Ionics, 2007. **178**(23–24): p. 1366-1378.
59. Georges, S., et al., *The LAMOX Family of Fast Oxide-Ion Conductors: Overview and Recent Results.* Journal of New Materials for Electrochemical Systems, 2004. **7**(1): p. 51-57.
60. Hattori, M., et al., *Effect of annealing on the electrical conductivity of the Y2O3–ZrO2 system.* Journal of Power Sources, 2004. **131**(1–2): p. 247-250.
61. Hattori, M., et al., *Effect of aging on conductivity of yttria stabilized zirconia.* Journal of Power Sources, 2004. **126**(1–2): p. 23-27.
62. Appel, C.C., et al., *Ageing behaviour of zirconia stabilised by yttria and manganese oxide.* Journal of Materials Science, 2001. **36**(18): p. 4493-4501.
63. Butz, B., et al., *Correlation between microstructure and degradation in conductivity for cubic Y2O3-doped ZrO2.* Solid State Ionics, 2006. **177**(37–38): p. 3275-3284.
64. Kondoh, J., et al., *Changes in Aging Behavior and Defect Structure of Y 2 O 3 Fully Stabilized ZrO2 by In2 O 3 Doping.* Journal of The Electrochemical Society, 2002. **149**(8): p. J59-J72.
65. Kondoh, J., et al., *Effect of Aging on Yttria-Stabilized Zirconia: I. A Study of Its Electrochemical Properties.* Journal of The Electrochemical Society, 1998. **145**(5): p. 1527-1536.
66. Liu, Y.L. and C. Jiao, *Microstructure degradation of an anode/electrolyte interface in SOFC studied by transmission electron microscopy.* Solid State Ionics, 2005. **176**(5–6): p. 435-442.
67. Andersen, T., et al., *Electrochemical removal of segregated silicon dioxide impurities from yttria stabilized zirconia surfaces at elevated temperatures.* Solid State Ionics, 2011. **190**(1): p. 60-66.
68. Andersen, T., et al., *Strontium zirconate as silicon and aluminum scavenger in yttria stabilized zirconia.* Solid State Ionics, 2011. **190**(1): p. 82-87.
69. Liu, W. and M. Flytzanistephanopoulos, *Total Oxidation of Carbon Monoxide and Methane over Transition Metal Fluorite Oxide Composite Catalysts.* Journal of Catalysis, 1995. **153**(2): p. 304-316.
70. Yano, M., et al., *Recent advances in single-chamber solid oxide fuel cells: A review.* Solid State Ionics, 2007. **177**(39–40): p. 3351-3359.
71. Yoo, K.B. and G.M. Choi, *Performance of La-doped strontium titanate (LST) anode on LaGaO3-based SOFC.* Solid State Ionics, 2009. **180**(11–13): p. 867-871.
72. Sfeir, J., *LaCrO3-based anodes: stability considerations.* Journal of Power Sources, 2003. **118**(1–2): p. 276-285.
73. Uchida, H., S.I. Arisaka, and M. Watanabe, *High performance electrode for medium-temperature solid oxide fuel cells: Control of microstructure of La(Sr)CoO3 cathodes with highly dispersed Pt electrocatalysts.* Journal of the Electrochemical Society, 2002. **149**(1): p. A13-A18.

74. Gil, V., C. Moure, and J. Tartaj, *Sinterability, microstructures and electrical properties of Ni/Gd-doped ceria cermets used as anode materials for SOFCs.* Journal of the European Ceramic Society, 2007. **27**(13–15): p. 4205-4209.
75. Pudmich, G., et al., *Chromite/titanate based perovskites for application as anodes in solid oxide fuel cells.* Solid State Ionics, 2000. **135**(1–4): p. 433-438.
76. Fuerte, A., et al. *Study of CuFe-Ce0.9Gd0.1O2-δ as IT-SOFC anode: Catalytic activity, thermal expansion, morphology, electrical conductivity and chemical compatibility*. in *ECS Transactions*. 2009.
77. Shaikh, S.S. and S.S. Bhoga, *Structural and electrical characterization of Ce 1-xCu xO 2-δ (x = 0.05-0.5) prepared by combustion technique.* Integrated Ferroelectrics, 2010. **119**(1): p. 66-73.
78. Shaikh, S.P.S., S.V. Moharil, and B.S. Nagrare, *A comparative study of copper-cermet anode material synthesized by different technique.* International Journal of Hydrogen Energy, 2012. **37**(8): p. 6853-6861.
79. Kim, H., et al., *Direct Oxidation of Liquid Fuels in a Solid Oxide Fuel Cell.* Journal of The Electrochemical Society, 2001. **148**(7): p. A693-A695.
80. Marina, O.A. and M. Mogensen, *High-temperature conversion of methane on a composite gadolinia-doped ceria–gold electrode.* Applied Catalysis A: General, 1999. **189**(1): p. 117-126.
81. De Marco, V., A. Grazioli, and V.M. Sglavo, *Production of planar copper-based anode supported intermediate temperature solid oxide fuel cells cosintered at 950 °C.* Journal of Power Sources, 2016. **328**: p. 235-240.
82. Park, S., J.M. Vohs, and R.J. Gorte, *Direct oxidation of hydrocarbons in a solid-oxide fuel cell.* Nature, 2000. **404**(6775): p. 265-267.
83. Mermelstein, J., M. Millan, and N. Brandon, *The impact of steam and current density on carbon formation from biomass gasification tar on Ni/YSZ, and Ni/CGO solid oxide fuel cell anodes.* Journal of Power Sources, 2010. **195**(6): p. 1657-1666.
84. Ramírez-Cabrera, E., A. Atkinson, and D. Chadwick, *The influence of point defects on the resistance of ceria to carbon deposition in hydrocarbon catalysis.* Solid State Ionics, 2000. **136**: p. 825-831.
85. da Costa, L.O.O., et al., *The study of the performance of Ni supported on gadolinium doped ceria SOFC anode on the steam reforming of ethanol.* International Journal of Hydrogen Energy, 2012. **37**(7): p. 5930-5939.
86. Souentie, S., et al., *Mathematical modeling of Ni/GDC and Au–Ni/GDC SOFC anodes performance under internal methane steam reforming conditions.* Journal of Catalysis, 2013. **306**(0): p. 116-128.
87. Fu, C.J., et al., *A promising Ni–Fe bimetallic anode for intermediate-temperature SOFC based on Gd-doped ceria electrolyte.* International Journal of Hydrogen Energy, 2011. **36**(21): p. 13727-13734.
88. Zhu, C., et al., *Solution combustion synthesis of Ce0.6Mn0.3Fe0.1O2 for anode of SOFC using LaGaO3-based oxide electrolyte.* International Journal of Hydrogen Energy, 2013. **38**(30): p. 13419-13426.
89. Ayawanna, J., et al., *Electrochemical Performance of Ni1-xCox-GDC Cermet Anodes for SOFCs.* Energy Procedia, 2013. **34**: p. 439-448.
90. Steinberger-Wilckens, R., et al., *Real-SOFC - A Joint European Effort to Improve SOFC Durability.* ECS Transactions, 2009. **25**(2): p. 43-56.
91. Badwal, S.P.S., F.T. Ciacchi, and D. Milosevic, *Scandia–zirconia electrolytes for intermediate temperature solid oxide fuel cell operation.* Solid State Ionics, 2000. **136–137**(0): p. 91-99.

92. Badwal, S.P.S., et al., *An investigation of conductivity, microstructure and stability of electrolyte compositions in the system 9 mol% (Sc2O3–Y2O3)–ZrO2(Al2O3).* Solid State Ionics, 1998. **109**(3–4): p. 167-186.
93. Sumi, H., et al., *Performance of nickel–scandia-stabilized zirconia cermet anodes for SOFCs in 3% H2O–CH4.* Solid State Ionics, 2004. **174**(1–4): p. 151-156.
94. Kishimoto, H., et al., *Rapid phase transformation of zirconia in the Ni-ScSZ cermet anode under reducing condition.* Solid State Ionics, 2008. **179**(35–36): p. 2037-2041.
95. Somalu, M.R., et al., *Fabrication and characterization of Ni/ScSZ cermet anodes for IT-SOFCs.* International Journal of Hydrogen Energy, 2011. **36**(9): p. 5557-5566.
96. Zhao, Y., et al., *Recent progress on solid oxide fuel cell: Lowering temperature and utilizing non-hydrogen fuels.* International Journal of Hydrogen Energy, 2013. **38**(36): p. 16498-16517.
97. Kolotygin, V.A., et al., *Functional properties of SOFC anode materials based on LaCrO3, La(Ti,Mn)O3 and Sr(Nb,Mn)O3 perovskites: A comparative analysis.* Solid State Ionics, 2013. **251**(0): p. 28-33.
98. Poetzsch, D., R. Merkle, and J. Maier, *Investigation of oxygen exchange kinetics in proton-conducting ceramic fuel cells: Effect of electronic leakage current using symmetric cells.* Journal of Power Sources, 2013. **242**(0): p. 784-789.
99. Jung, I., et al., *LSCM–YSZ nanocomposites for a high performance SOFC anode.* Ceramics International, 2013. **39**(8): p. 9753-9758.
100. McIntosh, S. and M. van den Bossche, *Influence of lattice oxygen stoichiometry on the mechanism of methane oxidation in SOFC anodes.* Solid State Ionics, 2011. **192**(1): p. 453-457.
101. Roushanafshar, M., et al., *Effect of hydrogen sulfide inclusion in syngas feed on the electrocatalytic activity of LST-YDC composite anodes for high temperature SOFC applications.* International Journal of Hydrogen Energy, 2012. **37**(9): p. 7762-7770.
102. Chourashiya, M.G. and L.D. Jadhav, *Synthesis and characterization of 10%Gd doped ceria (GDC) deposited on NiO-GDC anode-grade-ceramic substrate as half cell for IT-SOFC.* International Journal of Hydrogen Energy, 2011. **36**(22): p. 14984-14995.
103. Slater, P.R., D.P. Fagg, and J.T.S. Irvine, *Synthesis and electrical characterisation of doped perovskite titanates as potential anode materials for solid oxide fuel cells.* Journal of Materials Chemistry, 1997. **7**(12): p. 2495-2498.
104. Li, X., et al., *Electrical conductivity and structural stability of La-doped SrTiO 3 with A-site deficiency as anode materials for solid oxide fuel cells.* International Journal of Hydrogen Energy, 2010. **35**(15): p. 7913-7918.
105. Neagu, D. and J.T.S. Irvine, *Enhancing electronic conductivity in strontium titanates through correlated A and B-site doping.* Chemistry of Materials, 2011. **23**(6): p. 1607-1617.
106. Metcalfe, C., E. Lay-Grindler, and O. Kesler, *Characterization of Ni–YSZ anodes for solid oxide fuel cells fabricated by solution precursor plasma spraying with axial feedstock injection.* Journal of Power Sources, 2014. **247**(0): p. 831-839.
107. Jee, Y., et al., *High performance Bi-layered electrolytes via atomic layer deposition for solid oxide fuel cells.* Journal of Power Sources, 2014. **253**(0): p. 114-122.
108. Jiang, S.P., *A review of wet impregnation—An alternative method for the fabrication of high performance and nano-structured electrodes of solid oxide fuel cells.* Materials Science and Engineering: A, 2006. **418**(1): p. 199-210.
109. Liu, Z., et al., *Fabrication and modification of solid oxide fuel cell anodes via wet impregnation/infiltration technique.* Journal of Power Sources, 2013. **237**: p. 243-259.

110. Martins, R.F., et al., *Synthesis and characterization of NiO-YSZ for SOFCs.* Materials Research Bulletin, 2009. **44**(2): p. 451-456.
111. Larminie, J. and A. Dicks, *Fuel Cell Systems Explained (2nd Edition)*. 2003: John Wiley & Sons.
112. Zhang, H., et al., *Investigation of Sm0.5Sr0.5CoO3−δ/Co3O4 composite cathode for intermediate-temperature solid oxide fuel cells.* Journal of Power Sources, 2008. **185**(1): p. 129-135.
113. Mori, M., et al., *Thermal-Expansion Behaviors and Mechanisms for Ca- or Sr-Doped Lanthanum Manganite Perovskites under Oxidizing Atmospheres.* Journal of The Electrochemical Society, 2000. **147**(4): p. 1295-1302.
114. Mahato, N., et al., *Progress in material selection for solid oxide fuel cell technology: A review.* Progress in Materials Science, 2015. **72**: p. 141-337.
115. Jiang, S.P., *Development of lanthanum strontium manganite perovskite cathode materials of solid oxide fuel cells: a review.* Journal of Materials Science, 2008. **43**(21): p. 6799-6833.
116. Möbius, H.-H., *On the history of solid electrolyte fuel cells.* Journal of Solid State Electrochemistry, 1997. **1**(1): p. 2-16.
117. Kuo, J.H., H.U. Anderson, and D.M. Sparlin, *Oxidation-reduction behavior of undoped and Sr-doped LaMnO3: Defect structure, electrical conductivity, and thermoelectric power.* Journal of Solid State Chemistry, 1990. **87**(1): p. 55-63.
118. Hammouche, A., E.J.L. Schouler, and M. Henault, *Electrical and thermal properties of Sr-doped lanthanum manganites.* Solid State Ionics, 1988. **28**: p. 1205-1207.
119. Mah, J.C.W., et al., *Metallic interconnects for solid oxide fuel cell: A review on protective coating and deposition techniques.* International Journal of Hydrogen Energy, 2017. **42**(14): p. 9219-9229.
120. Shaigan, N., et al., *A review of recent progress in coatings, surface modifications and alloy developments for solid oxide fuel cell ferritic stainless steel interconnects.* Journal of Power Sources, 2010. **195**(6): p. 1529-1542.
121. Ishikawa, T., et al., *Optical spectroscopy of charge-ordering transition in La1/3Sr2/3FeO3.* Physical Review B, 1998. **58**(20): p. R13326-R13329.
122. Kawada, T. and T. Horita, *6 - Cathodes A2 - Kendall, Kevin*, in *High-Temperature Solid Oxide Fuel Cells for the 21st Century (Second Edition)*, M. Kendall, Editor. 2016, Academic Press: Boston. p. 161-193.
123. Doshi, R., et al., *Development of Solid-Oxide Fuel Cells That Operate at 500°C.* Journal of The Electrochemical Society, 1999. **146**(4): p. 1273-1278.
124. Simner, S.P., et al., *Performance Variability of La(Sr)FeO3 SOFC Cathode with Pt, Ag, and Au Current Collectors.* Journal of The Electrochemical Society, 2005. **152**(9): p. A1851-A1859.
125. Simner, S.P., et al., *Development of lanthanum ferrite SOFC cathodes.* Journal of Power Sources, 2003. **113**(1): p. 1-10.
126. Simner, S.P., et al., *Optimized Lanthanum Ferrite-Based Cathodes for Anode-Supported SOFCs.* Electrochemical and Solid-State Letters, 2002. **5**(7): p. A173-A175.
127. Simner, S.P., et al., *Interaction between La(Sr)FeO3 SOFC cathode and YSZ electrolyte.* Solid State Ionics, 2003. **161**(1): p. 11-18.
128. Wang, W.G. and M. Mogensen, *High-performance lanthanum-ferrite-based cathode for SOFC.* Solid State Ionics, 2005. **176**(5): p. 457-462.
129. Steele, B.C.H. and J.-M. Bae, *Properties of La0.6Sr0.4Co0.2Fe0.8O3−x (LSCF) double layer cathodes on gadolinium-doped cerium oxide (CGO) electrolytes.* Solid State Ionics, 1998. **106**(3): p. 255-261.

130. Mukerjee, S., et al. *Latest update on Delphi's solid oxide fuel cell stack for transportation and stationary applications*. in *ECS Transactions*. 2011.
131. Chen, Yu, and S.B. Adler, *Thermal and Chemical Expansion of Sr-Doped Lanthanum Cobalt Oxide (La1-xSrxCoO3-δ).* Chemistry of Materials, 2005. **17**(17): p. 4537-4546.
132. Kharton, V.V., et al., *Ceria-based materials for solid oxide fuel cells.* Journal of Materials Science, 2001. **36**(5): p. 1105-1117.
133. Yamamoto, O., *Solid oxide fuel cells: fundamental aspects and prospects.* Electrochimica Acta, 2000. **45**(15): p. 2423-2435.
134. Maric, R., et al., *Solid Oxide Fuel Cells with Doped Lanthanum Gallate Electrolyte and LaSrCoO3 Cathode, and Ni-Samaria-Doped Ceria Cermet Anode.* Journal of The Electrochemical Society, 1999. **146**(6): p. 2006-2010.
135. Horita, T., et al., *Stability at La0.6Sr0.4CoO3−d cathode/La0.8Sr0.2Ga0.8Mg0.2O2.8 electrolyte interface under current flow for solid oxide fuel cells.* Solid State Ionics, 2000. **133**(3): p. 143-152.
136. Tsoga, A., A. Naoumidis, and D. Stöver, *Total electrical conductivity and defect structure of ZrO2–CeO2–Y2O3–Gd2O3 solid solutions.* Solid State Ionics, 2000. **135**(1): p. 403-409.
137. Kobayashi, Y., et al., *Durability of a Segmented-in-Series Tubular SOFC with a (Ce, Sm)O 2 cathode interlayer: Influence of operating conditions.* Journal of the Electrochemical Society, 2014. **161**(3): p. F214-F225.
138. Kostogloudis, G.C., et al., *Chemical compatibility of alternative perovskite oxide SOFC cathodes with doped lanthanum gallate solid electrolyte.* Solid State Ionics, 2000. **134**(1): p. 127-138.
139. Matheswaran, P., M. Rajasekhar, and A. Subramania, *Assisted combustion synthesis and characterization of Pr0.6Sr0.4MnO3±δ nano crystalline powder as cathode material for IT-SOFC.* Ceramics International, 2017. **43**(1): p. 988-991.
140. Rim, H.-R., et al., *Characteristics of Pr1−xMxMnO3 (M = Ca, Sr) as cathode material in solid oxide fuel cells.* Materials Chemistry and Physics, 1998. **52**(1): p. 54-59.
141. Ralph, J.M., J.A. Kilner, and B.C.H. Steele, *Improving Gd-Doped Ceria Electrolytes for Low Temperature Solid Oxide Fuel Cells.* MRS Proceedings, 2011. **575**.
142. Takeda, Y., et al., *Gd1 − xSrxCoO3 for the electrode of solid oxide fuel cells.* Solid State Ionics, 1996. **86**: p. 1187-1190.
143. Yoon, H.S., et al., *Synthesis and characterization of Gd1−xSrxMnO3 cathode for solid oxide fuel cells.* Journal of Power Sources, 2001. **93**(1): p. 1-7.
144. Park, I., et al., *Enhanced performance of the Sm0.5Sr0.5CoO3−δ double layer porous cathode for solid oxide fuel cells.* Solid State Ionics, 2011. **184**(1): p. 35-38.
145. Deng, H., et al., *An ionic conductor Ce0.8Sm0.2O2−δ (SDC) and semiconductor Sm0.5Sr0.5CoO3 (SSC) composite for high performance electrolyte-free fuel cell.* International Journal of Hydrogen Energy, 2017.
146. Duong, A.T. and D.R. Mumm, *On the interaction of SSC and LSGM in composite SOFC electrodes.* Journal of Power Sources, 2013. **241**: p. 281-287.
147. Fukunaga, H., et al., *Reaction model of dense Sm0.5Sr0.5CoO3 as SOFC cathode.* Solid State Ionics, 2000. **132**(3): p. 279-285.
148. Martín, A.J., et al., *Chapter 15 - Recent Advances in Fuel Cells for Transport and Stationary Applications A2 - Gandía, Luis M*, in *Renewable Hydrogen Technologies*, G. Arzamendi and P.M. Diéguez, Editors. 2013, Elsevier: Amsterdam. p. 361-380.
149. Lee, H.Y., J.H. Jang, and S.M. Oh, *Cathodic Activity and Interfacial Stability of Y0.8Ca0.2Co1−x Fe x O3/YSZ Electrodes for Solid Oxide Fuel Cells.* Journal of The Electrochemical Society, 1999. **146**(5): p. 1707-1711.

150. Fontana, S., et al., *Metallic interconnects for SOFC: Characterisation of corrosion resistance and conductivity evaluation at operating temperature of differently coated alloys.* Journal of Power Sources, 2007. **171**(2): p. 652-662.
151. Zhu, W.Z. and S.C. Deevi, *Development of interconnect materials for solid oxide fuel cells.* Materials Science and Engineering: A, 2003. **348**(1): p. 227-243.
152. Zhu, W.Z. and S.C. Deevi, *Opportunity of metallic interconnects for solid oxide fuel cells: a status on contact resistance.* Materials Research Bulletin, 2003. **38**(6): p. 957-972.
153. Fergus, J.W., *Lanthanum chromite-based materials for solid oxide fuel cell interconnects.* Solid State Ionics, 2004. **171**(1): p. 1-15.
154. Antepara, I., et al., *Evaluation of ferritic steels for use as interconnects and porous metal supports in IT-SOFCs.* Journal of Power Sources, 2005. **151**: p. 103-107.
155. Fergus, J.W., *Metallic interconnects for solid oxide fuel cells.* Materials Science and Engineering: A, 2005. **397**(1): p. 271-283.
156. Wu, J. and X. Liu, *Recent Development of SOFC Metallic Interconnect.* Journal of Materials Science & Technology, 2010. **26**(4): p. 293-305.
157. Chen, L., et al., *Clad metals, roll bonding and their applications for SOFC interconnects.* Journal of Power Sources, 2005. **152**: p. 40-45.
158. Chen, X., et al., *Protective coating on stainless steel interconnect for SOFCs: oxidation kinetics and electrical properties.* Solid State Ionics, 2005. **176**(5–6): p. 425-433.
159. Jablonski, P.D. and D.E. Alman, *Oxidation resistance and mechanical properties of experimental low coefficient of thermal expansion (CTE) Ni-base alloys.* International Journal of Hydrogen Energy, 2007. **32**(16): p. 3705-3712.
160. Yang, Z., G.-G. Xia, and J.W. Stevenson, *Evaluation of Ni–Cr-base alloys for SOFC interconnect applications.* Journal of Power Sources, 2006. **160**(2): p. 1104-1110.
161. Qu, W., et al., *Yttrium, cobalt and yttrium/cobalt oxide coatings on ferritic stainless steels for SOFC interconnects.* Journal of Power Sources, 2006. **157**(1): p. 335-350.
162. Piccardo, P., et al., *ASR evaluation of different kinds of coatings on a ferritic stainless steel as SOFC interconnects.* Surface and Coatings Technology, 2007. **202**(4): p. 1221-1225.
163. Yokokawa, H., et al., *Thermodynamic considerations on Cr poisoning in SOFC cathodes.* Solid State Ionics, 2006. **177**(35-36): p. 3193-3198.
164. Sakai, N., et al., *Material transport and degradation behavior of SOFC interconnects.* Solid State Ionics, 2006. **177**(19-25): p. 1933-1939.
165. Hou, P.Y. and J. Stringer, *The effect of surface-applied reactive metal oxides on the high temperature oxidation of alloys.* Materials Science and Engineering, 1987. **87**: p. 295-302.
166. Orlovskaya, N., et al., *Structural evolution of La–Cr–O thin films: Part I. Microstructure and phase development.* Thin Solid Films, 2006. **515**(4): p. 1741-1747.
167. Zhu, J.H., et al., *LaCrO3-based coatings on ferritic stainless steel for solid oxide fuel cell interconnect applications.* Surface and Coatings Technology, 2004. **177–178**(0): p. 65-72.
168. Kim, J.-H., R.-H. Song, and S.-H. Hyun, *Effect of slurry-coated LaSrMnO3 on the electrical property of Fe–Cr alloy for metallic interconnect of SOFC.* Solid State Ionics, 2004. **174**(1–4): p. 185-191.
169. Choi, J.J., et al., *Oxidation resistance coating of LSM and LSCF on SOFC metallic interconnects by the aerosol deposition process.* Journal of the American Ceramic Society, 2007. **90**(6): p. 1926-1929.

170. Yang, Z.G., et al., *Evaluation of perovskite overlay coatings on ferritic stainless steels for SOFC interconnect applications.* Journal of the Electrochemical Society, 2006. **153**(10): p. A1852-A1858.
171. Gannon, P., Deibert, M., White, P., Smith, R., Chen, H., Priyantha, W., Lucas, J., et al, *Advanced PVD protective coatings for SOFC interconnects.* International Journal of Hydrogen Energy. **33(14)**: p. 3991-4000. .
172. PalDey, S. and S.C. Deevi, *Single layer and multilayer wear resistant coatings of (Ti,Al)N: a review.* Materials Science and Engineering: A, 2003. **342**(1–2): p. 58-79.
173. Brylewski, T., et al., *Screen-printed (La,Sr)CrO3 coatings on ferritic stainless steel interconnects for solid oxide fuel cells using nanopowders prepared by means of ultrasonic spray pyrolysis.* Journal of Power Sources, 2012. **208**(0): p. 86-95.
174. Wu, J., et al., *The performance of solid oxide fuel cells with Mn–Co electroplated interconnect as cathode current collector.* Journal of Power Sources, 2009. **189**(2): p. 1106-1113.
175. Wu, J., et al., *Pulse plating of Mn–Co alloys for SOFC interconnect applications.* Electrochimica Acta, 2008. **54**(2): p. 793-800.
176. Johnson, C., et al., *The effect of coating crystallization and substrate impurities on magnetron sputtered doped LaCrO3 coatings for metallic solid oxide fuel cell interconnects.* International Journal of Hydrogen Energy, 2009. **34**(5): p. 2408-2415.
177. Geng, S., et al., *Sputtered Ni coating on ferritic stainless steel for solid oxide fuel cell interconnect application.* International Journal of Hydrogen Energy, 2012. **37**(1): p. 916-920.
178. Xin, X., et al., *Development of the spinel powder reduction technique for solid oxide fuel cell interconnect coating.* International Journal of Hydrogen Energy, 2012. **37**(1): p. 471-476.
179. Shaigan, N., D.G. Ivey, and W. Chen, *Oxidation and electrical behavior of nickel/lanthanum chromite-coated stainless steel interconnects.* Journal of Power Sources, 2008. **183**(2): p. 651-659.
180. Shaigan, N., D.G. Ivey, and W. Chen, *Co/LaCrO3 composite coatings for AISI 430 stainless steel solid oxide fuel cell interconnects.* Journal of Power Sources, 2008. **185**(1): p. 331-337.
181. Jiang, S.P. and Y. Ramprakash, *H2 oxidation on Ni/Y–TZP cermet electrodes – polarisation behaviour.* Solid State Ionics, 1999. **116**(1–2): p. 145-156.
182. Shri Prakash, B., S. Senthil Kumar, and S.T. Aruna, *Properties and development of Ni/YSZ as an anode material in solid oxide fuel cell: A review.* Renewable and Sustainable Energy Reviews, 2014. **36**(0): p. 149-179.
183. Jiang, S.P., P.J. Callus, and S.P.S. Badwal, *Fabrication and performance of Ni/3 mol% Y2O3–ZrO2 cermet anodes for solid oxide fuel cells.* Solid State Ionics, 2000. **132**(1–2): p. 1-14.
184. Tu, H. and U. Stimming, *Advances, aging mechanisms and lifetime in solid-oxide fuel cells.* Journal of Power Sources, 2004. **127**(1–2): p. 284-293.
185. Faes, A., et al., *Design of experiment approach applied to reducing and oxidizing tolerance of anode supported solid oxide fuel cell. Part II: Electrical, electrochemical and microstructural characterization of tape-cast cells.* Journal of Power Sources, 2011. **196**(21): p. 8909-8917.
186. Sarikaya, A., V. Petrovsky, and F. Dogan, *Development of the anode pore structure and its effects on the performance of solid oxide fuel cells.* International Journal of Hydrogen Energy, 2013. **38**(24): p. 10081-10091.
187. Brown, M., S. Primdahl, and M. Mogensen, *Structure/Performance Relations for Ni/Yttria-Stabilized Zirconia Anodes for Solid Oxide Fuel Cells.* Journal of The Electrochemical Society, 2000. **147**(2): p. 475-485.

188. Kim, S.-D., et al., *Performance and durability of Ni-coated YSZ anodes for intermediate temperature solid oxide fuel cells.* Solid State Ionics, 2006. **177**(9–10): p. 931-938.
189. Sabolsky, E.M., et al., *In situ formation of a solid oxide fuel cell (SOFC) cermet anode by NiWO4 reduction.* Journal of Power Sources, 2013. **237**(0): p. 33-40.
190. Chen, K., et al., *Performance of an anode-supported SOFC with anode functional layers.* Electrochimica Acta, 2008. **53**(27): p. 7825-7830.
191. Opila, E.J., *Oxidation and Volatilization of Silica Formers in Water Vapor.* Journal of the American Ceramic Society, 2003. **86**(8): p. 1238-1248.
192. Hansen, K.V., K. Norrman, and M. Mogensen, *H 2 - H 2 O - Ni - YSZ Electrode Performance: Effect of Segregation to the Interface.* Journal of The Electrochemical Society, 2004. **151**(9): p. A1436-A1444.
193. Hauch, A. and M. Mogensen, *Ni/YSZ electrode degradation studied by impedance spectroscopy: Effects of gas cleaning and current density.* Solid State Ionics, 2010. **181**(15–16): p. 745-753.
194. Hauch, A., et al., *Ni/YSZ anode – Effect of pre-treatments on cell degradation and microstructures.* Journal of Power Sources, 2011. **196**(21): p. 8931-8941.
195. Mizusaki, J., et al., *Kinetic studies of the reaction at the nickel pattern electrode on YSZ in H2 H2O atmospheres.* Solid State Ionics, 1994. **70–71, Part 1**(0): p. 52-58.
196. Mizusaki, J., et al., *Kinetics of the Electrode Reaction at the H 2 - H 2 O Porous Pt/Stabilized Zirconia Interface.* Journal of The Electrochemical Society, 1994. **141**(6): p. 1674-1683.
197. Mizusaki, J., et al., *Preparation of Nickel Pattern Electrodes on YSZ and Their Electrochemical Properties in H 2 - H 2 O Atmospheres.* Journal of The Electrochemical Society, 1994. **141**(8): p. 2129-2134.
198. Utz, A., et al., *Studying the CO–CO2 characteristics of SOFC anodes by means of patterned Ni anodes.* Journal of Power Sources, 2011. **196**(17): p. 7217-7224.
199. Utz, A., et al., *Impurity features in Ni-YSZ-H2-H2O electrodes.* Solid State Ionics, 2011. **183**(1): p. 60-70.
200. Utz, A., et al., *Degradation and Relaxation Effects of Ni Patterned Anodes in H2 – H2O Atmosphere.* Journal of The Electrochemical Society, 2010. **157**(6): p. B920-B930.
201. Mukhopadhyay, M., et al., *Effect of anode configuration on electrical properties and cell polarization in planar anode supported SOFC.* Solid State Ionics, 2013. **233**(0): p. 20-31.
202. Mukhopadhyay, M., et al., *In-situ patterned intra-anode triple phase boundary in SOFC electroless anode: An enhancement of electrochemical performance.* International Journal of Hydrogen Energy, 2011. **36**(13): p. 7677-7682.
203. Mukhopadhyay, M., et al., *Engineered anode structure for enhanced electrochemical performance of anode-supported planar solid oxide fuel cell.* International Journal of Hydrogen Energy, 2012. **37**(3): p. 2524-2534.
204. Vlasov, A.N. and M.V. Perfiliev, *Ageing of ZrO2-based solid electrolytes.* Solid State Ionics, 1987. **25**(4): p. 245-253.
205. Hoganas, *Production of Sintered Components, Hoganas Handbook for Sintered Components*. 2013. p. 68-115.
206. Kuczynski, G.C., *The mechanism of densification during sintering of metallic particles.* Acta Metallurgica, 1956. **4**(1): p. 58-61.
207. Li, P., et al., *Dynamic nucleation and growth of Ni nanoparticles on high-surface area titania.* Surface Science, 2006. **600**(3): p. 693-702.

208. Basu, J. and R. Divakar, *In-situ electron microscopy investigation of reduction-induced microstructural changes in NiO.* Ceramics International, 2015. **41**(10, Part A): p. 12658-12667.
209. Pihlatie, M.H., et al., *Electrical conductivity of Ni–YSZ composites: Degradation due to Ni particle growth.* Solid State Ionics, 2011. **189**(1): p. 82-90.
210. Ananyev, M.V., et al., *Characterization of Ni-cermet degradation phenomena I. Long term resistivity monitoring, image processing and X-ray fluorescence analysis.* Journal of Power Sources, 2015. **286**(0): p. 414-426.
211. Aaberg, R.J., et al., *Morphological Changes at the Interface of the Nickel-Yttria Stabilized Zirconia Point Electrode.* Journal of The Electrochemical Society, 1998. **145**(7): p. 2244-2252.
212. Sehested, J., *Sintering of nickel steam-reforming catalysts.* Journal of Catalysis, 2003. **217**(2): p. 417-426.
213. Sehested, J., et al., *Sintering of nickel steam-reforming catalysts: effects of temperature and steam and hydrogen pressures.* Journal of Catalysis, 2004. **223**(2): p. 432-443.
214. Belton, G.R. and A.S. Jordan, *Gaseous hydroxides of cobalt and nickel.* The Journal of Physical Chemistry, 1967. **71**(12): p. 4114-4120.
215. Koch, S., et al., *Solid Oxide Fuel Cell Performance under Severe Operating Conditions.* Fuel Cells, 2006. **6**(2): p. 130-136.
216. Holzer, L., et al., *Microstructure degradation of cermet anodes for solid oxide fuel cells: Quantification of nickel grain growth in dry and in humid atmospheres.* Journal of Power Sources, 2011. **196**(3): p. 1279-1294.
217. Matsui, T., et al., *Performance Deterioration of Ni–YSZ Anode Induced by Electrochemically Generated Steam in Solid Oxide Fuel Cells.* Journal of The Electrochemical Society, 2010. **157**(5): p. B776-B781.
218. Matsui, T., et al., *Performance Deterioration of Ni-based Cermet Induced by Electrochemically-generated Steam in Anode.* ECS Transactions, 2009. **25**(2): p. 2023-2030.
219. Jiao, Z., et al., *Study on local morphological changes of nickel in solid oxide fuel cell anode using porous Ni pellet electrode.* Journal of Power Sources, 2011. **196**(3): p. 1019-1029.
220. Lee, Y.-H., et al., *Degradation of nickel–yttria-stabilized zirconia anode in solid oxide fuel cells under changing temperature and humidity conditions.* Journal of Power Sources, 2014. **262**(0): p. 451-456.
221. Khan, M.S., et al., *Effect of various sintering inhibitors on the long term performance of Ni-YSZ anodes used for SOFCs.* International Journal of Hydrogen Energy, 2015. **40**(35): p. 11968-11975.
222. *CRC Handbook of Chemistry and Physics*. 53rd ed. 1973, Cleveland: CRC Press.
223. Hidayat, T., et al., *The Kinetics of Reduction of Dense Synthetic Nickel Oxide in H2-N2 and H2-H2O Atmospheres.* Metallurgical and Materials Transactions B, 2009. **40**(1): p. 1-16.
224. Richardson, J.T., R. Scates, and M.V. Twigg, *X-ray diffraction study of nickel oxide reduction by hydrogen.* Applied Catalysis A: General, 2003. **246**(1): p. 137-150.
225. Sharma, R., *Kinetic measurements from in situ TEM observations.* Microscopy Research and Technique, 2009. **72**(3): p. 144-152.
226. Jeangros, Q., et al., *Energy-filtered environmental transmission electron microscopy for the assessment of solid–gas reactions at elevated temperature: NiO/YSZ–H2 as a case study.* Ultramicroscopy, 2016. **169**: p. 11-21.

227. Jeangros, Q., et al., *Measurements of local chemistry and structure in Ni(O)-YSZ composites during reduction using energy-filtered environmental TEM.* Chemical Communications, 2014. **50**(15): p. 1808-1810.
228. Jeangros, Q., et al., *Reduction of nickel oxide particles by hydrogen studied in an environmental TEM.* Journal of Materials Science, 2013. **48**(7): p. 2893-2907.
229. Jeangros, Q., et al., *A TEM study of Ni interfaces formed during activation of SOFC anodes in H2: Influence of grain boundary symmetry and segregation of impurities.* Acta Materialia, 2016. **103**: p. 442-447.
230. Zhu, X., et al., *Effects of Initial Reduction Temperature on the Microstructures and Performances of Ni/YSZ Anodes for Solid Oxide Fuel Cells.* Journal of The Electrochemical Society, 2013. **160**(10): p. F1170-F1174.
231. Mori, H., et al., *Investigation of the interaction between NiO and yttria-stabilized zirconia (YSZ) in the NiO/YSZ composite by temperature-programmed reduction technique.* Applied Catalysis A: General, 2003. **245**(1): p. 79-85.
232. Simonsen, S.B., et al., *NiO/YSZ Reduction for SOFC/SOEC Studied In Situ by Environmental Transmission Electron Microscopy.* Meeting Abstracts, 2014. **MA2014-02**(20): p. 981.
233. Simonsen, S.B., et al., *Environmental TEM study of the dynamic nanoscaled morphology of NiO/YSZ during reduction.* Applied Catalysis A: General, 2015. **489**: p. 147-154.
234. Simwonis, D., *Optimierung von Anoden der Hochtemperatur-Brennstoffzelle durch Korrelation von Herstellungsverfahren, Gefüge und Eigenschaften*
3678, in *Berichte des Forschungszentrums Jülich*. 1999, Forschungszentrum, Zentralbibliothek: Jülich. p. 124, VI S.
235. Iwai, H., et al., *Quantification of SOFC anode microstructure based on dual beam FIB-SEM technique.* Journal of Power Sources, 2010. **195**(4): p. 955-961.
236. Hagen, A., et al., *Degradation of Anode Supported SOFCs as a Function of Temperature and Current Load.* Journal of The Electrochemical Society, 2006. **153**(6): p. A1165-A1171.
237. Vaßen, R., D. Simwonis, and D. Stöver, *Modelling of the agglomeration of Ni-particles in anodes of solid oxide fuel cells.* Journal of Materials Science, 2001. **36**(1): p. 147-151.
238. Jiang, S.P., *Sintering behavior of Ni/Y2O3-ZrO2cermet electrodes of solid oxide fuel cells.* Journal of Materials Science, 2003. **38**(18): p. 3775-3782.
239. Iwata, T., *Characterization of Ni-YSZ Anode Degradation for Substrate-Type Solid Oxide Fuel Cells.* Journal of The Electrochemical Society, 1996. **143**(5): p. 1521-1525.
240. Monachon, C., et al., *Rapid Preparation and SEM Microstructural Characterization of Nickel–Yttria-Stabilized Zirconia Cermets.* Journal of the American Ceramic Society, 2008. **91**(10): p. 3405-3407.
241. Thydén, K., *Microstructural degradation of Ni-YSZ anodes for solid oxide fuel cells*, in *Riso National Laboratory for Sustainable Energy*. 2008, Technical University of Denmark (DTU).
242. Thydén, K., Y.L. Liu, and J.B. Bilde-Sørensen, *Microstructural characterization of SOFC Ni–YSZ anode composites by low-voltage scanning electron microscopy.* Solid State Ionics, 2008. **178**(39–40): p. 1984-1989.
243. SOFC-LIFE, *Deliverables D1.2 and D1.3 Description of the evolution with time of Ni agglomeration and volatilisation as functions of temperature, p(H2O), fuel and current density (ASC Matrix)*. 2013, Institute of High Temperature Electrochemistry (IHTE), Ekraterinburg, Russia.

244. Chen, G., et al., *Nickel volatilization phenomenon on the Ni-CGO anode in a cathode-supported SOFC operated at low concentrations of H2.* International Journal of Hydrogen Energy, 2012. **37**(1): p. 477-483.
245. W. Zhou, Z.L.W., ed. *Scanning Microscopy for Nanotechnology*. 2007, Springer-Verlag New York. 522.
246. Primdahl, S. and M. Mogensen, *Durability and thermal cycling of Ni/YSZ cermet anodes for solid oxide fuel cells.* Journal of Applied Electrochemistry, 2000. **30**(2): p. 247-257.
247. Münch, B. and L. Holzer, *Contradicting Geometrical Concepts in Pore Size Analysis Attained with Electron Microscopy and Mercury Intrusion.* Journal of the American Ceramic Society, 2008. **91**(12): p. 4059-4067.
248. Vivet, N., et al., *3D Microstructural characterization of a solid oxide fuel cell anode reconstructed by focused ion beam tomography.* Journal of Power Sources, 2011. **196**(18): p. 7541-7549.
249. Vivet, N., et al., *Effect of Ni content in SOFC Ni-YSZ cermets: A three-dimensional study by FIB-SEM tomography.* Journal of Power Sources, 2011. **196**(23): p. 9989-9997.
250. Clague, R., et al., *Stress analysis of solid oxide fuel cell anode microstructure reconstructed from focused ion beam tomography.* Journal of Power Sources, 2011. **196**(21): p. 9018-9021.
251. Kanno, D., et al., *Evaluation of SOFC anode polarization simulation using three-dimensional microstructures reconstructed by FIB tomography.* Electrochimica Acta, 2011. **56**(11): p. 4015-4021.
252. Shearing, P.R., et al., *Exploring microstructural changes associated with oxidation in Ni–YSZ SOFC electrodes using high resolution X-ray computed tomography.* Solid State Ionics, 2012. **216**(0): p. 69-72.
253. Shearing, P.R., et al., *Microstructural analysis of a solid oxide fuel cell anode using focused ion beam techniques coupled with electrochemical simulation.* Journal of Power Sources, 2010. **195**(15): p. 4804-4810.
254. Shearing, P.R., J. Gelb, and N.P. Brandon, *X-ray nano computerised tomography of SOFC electrodes using a focused ion beam sample-preparation technique.* Journal of the European Ceramic Society, 2010. **30**(8): p. 1809-1814.
255. Shearing, P.R., et al., *3D reconstruction of SOFC anodes using a focused ion beam lift-out technique.* Chemical Engineering Science, 2009. **64**(17): p. 3928-3933.
256. Tariq, F., et al., *3D imaging and quantification of interfaces in SOFC anodes.* Journal of the European Ceramic Society, 2014. **34**(15): p. 3755-3761.
257. Tetsuo Sakamoto, et al., *Development of an Ion and Electron Dual Focused Beam Apparatus for Three-Dimensional Microanalysis.* Japanese Journal of Applied Physics, 1998. **37**(4R): p. 2051.
258. Bansal, R.K., et al., *High-resolution three-dimensional reconstruction: A combined scanning electron microscope and focused ion-beam approach.* Journal of Vacuum Science & Technology B, 2006. **24**(2): p. 554-561.
259. Wilson, J.R., et al., *Three-dimensional reconstruction of a solid-oxide fuel-cell anode.* Nat Mater, 2006. **5**(7): p. 541-544.
260. Joos, J., et al., *Quantification of double-layer Ni/YSZ fuel cell anodes from focused ion beam tomography data.* Journal of Power Sources, 2014. **246**(0): p. 819-830.
261. Guan, Y., et al., *Lattice-Boltzmann modeling of gas transport in Ni-Yttria-stabilized zirconia anodes during thermal cycling based on X-ray computed tomography.* Electrochimica Acta, 2014. **121**(0): p. 386-393.

262. Shearing, P.R., et al., *Using Synchrotron X-Ray Nano-CT to Characterize SOFC Electrode Microstructures in Three-Dimensions at Operating Temperature.* Electrochemical and Solid-State Letters, 2011. **14**(10): p. B117-B120.
263. Julie, V., et al., *3D phase mapping of solid oxide fuel cell YSZ/Ni cermet at the nanoscale by holographic X-ray nanotomography.* Journal of Power Sources, 2013. **243**(0): p. 841-849.
264. Guan, Y., et al., *Analysis of the three-dimensional microstructure of a solid-oxide fuel cell anode using nano X-ray tomography.* Journal of Power Sources, 2011. **196**(4): p. 1915-1919.
265. Izzo, J.R., et al., *Nondestructive Reconstruction and Analysis of SOFC Anodes Using X-ray Computed Tomography at Sub-50 nm Resolution.* Journal of The Electrochemical Society, 2008. **155**(5): p. B504-B508.
266. Grew, K.N., et al., *Nondestructive Nanoscale 3D Elemental Mapping and Analysis of a Solid Oxide Fuel Cell Anode.* Journal of The Electrochemical Society, 2010. **157**(6): p. B783-B792.
267. Galinski, H., et al., *Ostwald Ripening and Oxidation Kinetics of Nickel Gadolinia Doped Ceria Anodes.* ECS Transactions, 2009. **25**(2): p. 2057-2060.
268. Rüger, B., et al., *3D Electrode Microstructure Reconstruction and Modelling.* ECS Transactions, 2009. **25**(2): p. 1211-1220.
269. Wilson, J.R., et al., *Effect of composition of (La0.8Sr0.2MnO3–Y2O3-stabilized ZrO2) cathodes: Correlating three-dimensional microstructure and polarization resistance.* Journal of Power Sources, 2010. **195**(7): p. 1829-1840.
270. Kenney, B., et al., *Computation of TPB length, surface area and pore size from numerical reconstruction of composite solid oxide fuel cell electrodes.* Journal of Power Sources, 2009. **189**(2): p. 1051-1059.
271. Lehnert, W., J. Meusinger, and F. Thom, *Modelling of gas transport phenomena in SOFC anodes.* Journal of Power Sources, 2000. **87**(1–2): p. 57-63.
272. Suwanwarangkul, R., et al., *Performance comparison of Fick's, dusty-gas and Stefan-Maxwell models to predict the concentration overpotential of a SOFC anode.* Journal of Power Sources, 2003. **122**(1): p. 9-18.
273. Cannarozzo, M., A.D. Borghi, and P. Costamagna, *Simulation of mass transport in SOFC composite electrodes.* Journal of Applied Electrochemistry, 2008. **38**(7): p. 1011-1018.
274. Matyka, M. and Z. Koza, *How to calculate tortuosity easily?* AIP Conference Proceedings, 2012. **1453**(1): p. 17-22.
275. Suzue, Y., N. Shikazono, and N. Kasagi, *Micro modeling of solid oxide fuel cell anode based on stochastic reconstruction.* Journal of Power Sources, 2008. **184**(1): p. 52-59.
276. Zalc, J.M., S.C. Reyes, and E. Iglesia, *The effects of diffusion mechanism and void structure on transport rates and tortuosity factors in complex porous structures.* Chemical Engineering Science, 2004. **59**(14): p. 2947-2960.
277. Nakajo, A., et al., *Electrochemical Model of Solid Oxide Fuel Cell for Simulation at the Stack Scale II: Implementation of Degradation Processes.* Journal of The Electrochemical Society, 2011. **158**(9): p. B1102-B1118.
278. Nakajo, A., et al., *Mechanical reliability and durability of SOFC stacks. Part I : Modelling of the effect of operating conditions and design alternatives on the reliability.* International Journal of Hydrogen Energy, 2012. **37**(11): p. 9249-9268.
279. Nakajo, A., et al., *Progressive activation of degradation processes in solid oxide fuel cells stacks: Part I: Lifetime extension by optimisation of the operating conditions.* Journal of Power Sources, 2012. **216**(0): p. 449-463.

280. Nakajo, A., et al., *Progressive activation of degradation processes in solid oxide fuel cell stacks: Part II: Spatial distribution of the degradation.* Journal of Power Sources, 2012. **216**(0): p. 434-448.
281. Nakajo, A., et al., *Mechanical reliability and durability of SOFC stacks. Part II: Modelling of mechanical failures during ageing and cycling.* International Journal of Hydrogen Energy, 2012. **37**(11): p. 9269-9286.
282. Chen, H.-Y., et al., *Simulation of coarsening in three-phase solid oxide fuel cell anodes.* Journal of Power Sources, 2011. **196**(3): p. 1333-1337.
283. Sun, X., et al., *Calculation of contact angles at triple phase boundary in solid oxide fuel cell anode using the level set method.* Materials Characterization, 2014. **96**(0): p. 100-107.
284. Gao, S., J. Li, and Z. Lin, *Theoretical model for surface diffusion driven Ni-particle agglomeration in anode of solid oxide fuel cell.* Journal of Power Sources, 2014. **255**(0): p. 144-150.
285. Abdeljawad, F., et al., *Connecting microstructural coarsening processes to electrochemical performance in solid oxide fuel cells: An integrated modeling approach.* Journal of Power Sources, 2014. **250**(0): p. 319-331.
286. Völker, B. and R.M. McMeeking, *Impact of particle size ratio and volume fraction on effective material parameters and performance in solid oxide fuel cell electrodes.* Journal of Power Sources, 2012. **215**(0): p. 199-215.
287. Zhao, F. and A.V. Virkar, *Dependence of polarization in anode-supported solid oxide fuel cells on various cell parameters.* Journal of Power Sources, 2005. **141**(1): p. 79-95.
288. Sanyal, J., et al., *A particle-based model for predicting the effective conductivities of composite electrodes.* Journal of Power Sources, 2010. **195**(19): p. 6671-6679.
289. Chen, D., et al., *Percolation theory to predict effective properties of solid oxide fuel-cell composite electrodes.* Journal of Power Sources, 2009. **191**(2): p. 240-252.
290. Wang, G., P.P. Mukherjee, and C.-Y. Wang, *Direct numerical simulation (DNS) modeling of PEFC electrodes: Part II. Random microstructure.* Electrochimica Acta, 2006. **51**(15): p. 3151-3160.
291. Goodwin, D.G., et al., *Modeling Electrochemical Oxidation of Hydrogen on Ni–YSZ Pattern Anodes.* Journal of The Electrochemical Society, 2009. **156**(9): p. B1004-B1021.
292. Vogler, M., et al., *Modelling Study of Surface Reactions, Diffusion, and Spillover at a Ni/YSZ Patterned Anode.* Journal of The Electrochemical Society, 2009. **156**(5): p. B663-B672.
293. Wang, X. and A. Atkinson, *Modeling Microstructure Evolution of Ni Cermet Using a Cellular Automaton Approach.* Journal of The Electrochemical Society, 2014. **161**(5): p. F605-F614.
294. Chen, Z., et al., *Analyses of microstructural and elastic properties of porous SOFC cathodes based on focused ion beam tomography.* Journal of Power Sources, 2015. **273**: p. 486-494.
295. Ebašek, N., *Cation Diffusion and Related Degradation Phenomena in La2NiO4+ for Oxygen Separation Membranes*, in *Department of Chemistry*. 2012, University of Oslo.
296. Baldan, A., *Review Progress in Ostwald ripening theories and their applications to nickel-base superalloys Part I: Ostwald ripening theories.* Journal of Materials Science, 2002. **37**(11): p. 2171-2202.
297. Faes, A., et al., *RedOx study of anode-supported solid oxide fuel cell.* Journal of Power Sources, 2009. **193**(1): p. 55-64.

298. Lim, C.-H. and K.-T. Lee, *Characterization of core-shell structured Ni-GDC anode materials synthesized by ultrasonic spray pyrolysis for solid oxide fuel cells.* Ceramics International, 2016. **42**(12): p. 13715-13722.
299. Deshpande, J.V., S.C. Kochar, and H. Singh, *Aspects of positive ageing.* Journal of Applied Probability, 1986. **23**(3): p. 748-758.
300. Suzuki, M. and T. Oshima, *Estimation of the Co-ordination number in a Multi-Component Mixture of Spheres.* Powder Technology, 1983. **35**(2): p. 159-166.
301. Suzuki, M. and T. Oshima, *Co-ordination number of a multi-component randomly packed bed of spheres with size distribution.* Powder Technology, 1985. **44**(3): p. 213-218.
302. Bouvard, D. and F.F. Lange, *Relation between percolation and particle coordination in binary powder mixtures.* Acta Metallurgica et Materialia, 1991. **39**(12): p. 3083-3090.
303. Costamagna, P., P. Costa, and V. Antonucci, *Micro-modelling of solid oxide fuel cell electrodes.* Electrochimica Acta, 1998. **43**(3–4): p. 375-394.
304. Kuo, C.-H. and P.K. Gupta, *Rigidity and conductivity percolation thresholds in particulate composites.* Acta Metallurgica et Materialia, 1995. **43**(1): p. 397-403.
305. Chen, X.J., et al., *Influence of microstructure on the ionic conductivity of yttria-stabilized zirconia electrolyte.* Materials Science and Engineering: A, 2002. **335**(1–2): p. 246-252.
306. Verkerk, M.J., B.J. Middelhuis, and A.J. Burggraaf, *Effect of grain boundaries on the conductivity of high-purity ZrO2□Y2O3 ceramics.* Solid State Ionics, 1982. **6**(2): p. 159-170.
307. Parkinson, R. *Properties and applications of electroless nickel*. Nickel Development Institute, 1995. pp. 1-37.

Appendix

Working out of Ni radius via Nakajo method

$$r_{gNi}^2 \frac{\partial r_{gNi}}{\partial t} = k_{0D_{an}} exp\left[-\frac{Ea_{D_{an}}}{R}\left(\frac{1}{T_s}-\frac{1}{T_{ref}}\right)\right]\frac{x_{H_2O}}{x_{H_2}^{0.5}}\frac{r_{g_{Ni\infty}}^3 - r_{g_{Ni}}^3}{r_{g_{Ni\infty}}^3 - r_{g_{Ni(0)}}}$$

$$K = k_{0D_{an}} exp\left[-\frac{Ea_{D_{an}}}{R}\left(\frac{1}{T_s}-\frac{1}{T_{ref}}\right)\right]\frac{x_{H_2O}}{x_{H_2}^{0.5}}$$

$$r_{gNi}(t) = \left(r_{g_{Ni\infty}}^3 - \exp\frac{-3Kt - 3Cr_{g_{Ni\infty}}^3 + 3Cr_{g_{Ni}}^3}{r_{g_{Ni\infty}}^3 - r_{g_{Ni(0)}}}\right)^{\frac{1}{3}}$$

To evaluate constant C we check limits

At time t=0, $r_{gNi} = r_{gNi(0)}$

$$r_{gNi}(t) = \left(r_{g_{Ni\infty}}^3 - \exp\frac{-3Cr_{g_{Ni\infty}}^3 + 3Cr_{g_{Ni(0)}}^3}{r_{g_{Ni\infty}}^3 - r_{g_{Ni(0)}}}\right)^{\frac{1}{3}}$$

$$r_{gNi}^3(t) = r_{g_{Ni\infty}}^3 - \exp\frac{-3Cr_{g_{Ni\infty}}^3}{r_{g_{Ni\infty}}^3 - r_{g_{Ni(0)}}} \; and \; \frac{+3Cr_{g_{Ni(0)}}^3}{r_{g_{Ni\infty}}^3 - r_{g_{Ni(0)}}}$$

$$r_{gNi}^3(t) = r_{g_{Ni\infty}}^3 + (r_{g_{Ni(0)}}^3 - r_{g_{Ni\infty}}^3)$$

$$r_{gNi}(t) = r_{g_{Ni(0)}}$$

At time t=∞ , $r_{gNi} = r_{g_{Ni\infty}}^3$

The exponential of -∞ is 0

$$r_{gNi}(t) = \left(r_{g_{Ni\infty}}^3\right)^{\frac{1}{3}}$$

This is only true when the value for r =1

Nakajo model with data used for Thyden 750°C 50-50 H_2/H_2O

```
clear all          % Remove data from the workspace
clc                % Clear screen

% System parameters

rinf=1.38;         % The Ni radius at infinite time
c1=1-rinf^3;       % Coefficient
k0=1.05e-3;        % Rate of reaction
Ea=15.15*10^3;     % Energy barrier (J/mol)
R=8.314;           % Universal gas constant (J/mol*K)
Ts=1023;           % Sample temperature (K)
Tref=873;          % Reference temperature (K)
chiH20=0.50;       % Molar fraction of H20
chiH2=0.50;        % Molar fraction of H2

tinit=0;           % Initial time value (h)
tend=4000;         % End time value (h)
tinc=1;            % Increment in time value (h)
t=[tinit:tinc:tend];     % Time vector

mu=1.5;  %Burggeman factor, for tortuosity (would possibly vary, but value used
is typically 1.5
Zavg=6;  %Overall average coordination number of all solid particles, often
given as 6.
rel=1.2; %Radius of ion conducting material (electrolyte YSZ) (normalised)
psied=0.75;   %Total solid volume fraction for electrode (electronic conducting
material)
psiel=0.25;   %Total solid volume fraction for electrolyte (ionic conducting
material)

delta=0.000000005;          %Thickness of inter-particle material (m), such as a
grain boundary. estimate of 5nm for literature.
theta=15;                   %Contact angle between two particles in degrees,
there is likely to be a max value for this, and whilst newly contacting
particles will have a smaller value
phig=0.20;                  %Porosity

s=0.00005;                      %Geometric cross-section area of composite
electrode (m^2), based of 1cm b 0.5cm sample
sigmainterintrinsiced=(1/((1/1282051)*(Ts-293)*(6*10^-3)));      %Intrinsic
conductivity of the particle interface of Ni, (S/m)
sigmaintraintrinsiced=(1/((1/12820512)*(Ts-293)*(6*10^-3)));      %Intrinsic
material conductivity of Ni, (S/m)
sigmaintraintrinsicel= 6.7;    %Intrinsic material conductivity of YSZ intra-
particle, from Chen paper (S/m) at 945C
sigmainterintrinsiced= 0.5;    %Intrinsic material conductivity of YSZ inter-
particle, from Chen paper (S/m) at 945C

    % Derived parameter
    K=k0*exp(-Ea/R*((1/Ts)-(1/Tref)))*chiH20/ sqrt(chiH2);

    figure(1)       % Creates figure or moves active figure to figure(1)
    hold on         % Does not over write figure

%Solve for r at time t
red=(rinf^3+(1-rinf^3)*exp(-3*K*t/(rinf^3-1))).^(1/3);  %Growth of radii of
electronically conducting particles, in this case the Nickel particles
```

```
r=(red/10000000);                                          %Reduction of normalised
particle radius (1-1.4) down to ~10nm length
psiced=((1.764/Zavg*psiel/rel)/(1-(1.764/Zavg)))*red;   %Percolation threshold
volume fraction for electrode (electronic conducting material)
psicel=((1.764/Zavg*psied./red)/(1-(1.764/Zavg)))*rel;  %Percolation threshold
volume fraction for electrolyte (ionic conducting material)
zetee=(psied./red.^3);                                     %Combined variables
zeted=((psiel./rel.^3) + (psied./red.^3));                 %Combined variables
zetaed=(zetee./zeted.^1);                                  %Particle number
fraction for electrode particles
zetael=(psiel/rel^3)./((psied./red.^3)+(psiel/rel^3));  %Particle number
fraction for electrolyte particles
combi=(psied./r);                                          %Combined value of
threshold volume divided by the radius, for ease of writing
combiel=(psiel/(rel/10000000));                            %Combined value of
threshold volume divided by electrolyte radius, for ease of writing

Zeded=0.5*(1+((rel^2)./(red.^2)))*Zavg.*((psied./r)./(((psied./r).^1)+(psiel./(r
el./10000000).^1)));                                       %Average number of
contacts electrode with neighbouring electrode particles
Zedel=Zavg.*psiel./rel./psied./red;                        %Average number of
contacts electrode have with neighbouring electrolyte particles, true for binary
component mixtures
Zeled=0.5*(1+((rel^2)./(red.^2)))*Zavg.*psied./red./psiel./rel.^1; %Average
number of contacts electrolyte with neighbouring electrode particles
Ped=(1-(((3.764-Zeded)/2).^2.5)).^0.4;                     %Percolation probability
of electronically conducting materials (Nickel) belonging to an A type cluster-
true for binary and multicomponent
Zelel=Zavg*((psiel/rel)./((psiel./rel)+(psied./red)));  %Average number of
contacts electrolytes have with neighbouring electrolyte particles
Pel= (1-(((3.764-Zelel)/2).^2.5)).^0.4;                    %Percolation probability
of ionically conducting materials (YSZ) belonging to an A type cluster


ra = (rel/10000000)*sind(theta);        %neck radius of electrolyte particles
rb=r*sind(theta);

    for i=1:length(rb)
      if  ra < rb(i)
          rc(i) = ra;
      else
          rc(i) = rb(i);                %rc is the shortest opposite length
(opposite to hypotenuse length)of the
      end                               %triangle formed by the contact angle
diamond formed by the two particles.
    end

aeded=pi*rc.^2;                                        %cross-sectional contact area
between a k-particle and a l-particle (m^2)
nved=((1-phig)*psied)./((4/3)*pi*r.^3);                %Number of Ni particles per
unit volume
stered=aeded.*(2*r*s).*nved.*(Zeded./2).*Ped;          %Effective contact surface
area between electrode particles per particle layer (m^2)



    for i=1:length(r)
        if r(i) > (rel/10000000)
           minredrel(i) = (rel/10000000);                  %Selects smallest
radius of either Red or Rel at given time
        else
```

```
            minredrel(i) = r(i);
    end
    end

sigmaintraeffed=sigmaintraintrinsiced.*(((1-phig)*psied.*Ped).^mu); %Effective
grain boundary conductivity (S/cm)
dimensionlesssigmaintraeffed=((psied.*Ped).^mu);
%Dimensionless effective intra electronic conductivity (through grain boundary),
sigmaintereffed=dimensionlesssigmaintereffed*sigmainterintrinsiced.*r*((sind(the
ta))^2)*(1-phig)/delta;   %Effective grain interior effective conductivity
(S/cm)
dimensionlesssigmaintereffed=(2*stered)/(s*((sind(theta))^2)*(1-phig));
%Dimensionless effective conductivity  through grain interior
lamdaVTPBeff=((3/2)*minredrel/r.^3)*(1-phig)*(sind(theta))*Pel.*Zedel.*Ped.
*psied;                        %Effective TPB length
dimensionlesslamdaVTPBeff= lamdaVTPBeff./(((1-phig)*sind(theta))./r.^2);
%Dimensionless effective TPB lengths per unit volume
```

Gao Model for thesis generated data

```
clear all       % Remove data from the workspace
clc             % Clear screen

% System parameters

y=1.9;                                  %Surface Energy (Jm-2)%
Omega=(1.09*10^-29);                    %Volume element/volume of a vacancy (m3)%
ds=2.5*(10^-10);                        %thickness of surface through which diffusion
takes place%
kb=1.38*(10^-23);                       %Boltzmann constant% (previously multiplied
by for some reason? hours maybe(60^-2)*(60^-2))
Z0=6.7;                                 %Initial Coordination Number
psiel=0.6;                              %Total solid volume fraction for electrolyte
(ionic conducting material)
psied=0.4;                              %Total solid volume fraction for electrode
(electronic conducting material)
rel=0.5*(10^-6);                        %ysz particle radius%
r0= 0.38*(10^-6);                       %initial particle radius%
k0=1.05e-3;                             % Rate of reaction
Ea=15.15*10^3;                          % Energy barrier (J/mol)
R=8.314;                                % Universal gas constant (J/mol*K)
Ts=1173;                                % Sample temperature (K)
Tref=873;                               % Reference temperature (K)
chiH20=0.97;                            % Molar fraction of H20
chiH2=0.03;                             % Molar fraction of H2
mu=1.5;                                 %Burggeman factor, for tortuosity (would
possibly vary, but value used is typically 1.5
Zavg=6;                                 %Overall average coordination number of all
solid particles, often given as 6.
delta=0.000000005;                      %Thickness of inter-particle material (m),
such as a  grain boundary. estimate of 5nm for literature.
s=0.00005;                              %Geometric cross-section area of composite
electrode (m^2), based of 1cm by 0.5cm sample
phig=0.2;                               %Porosity
sigmaintraintrinsicel= 6.7;             %Intrinsic material conductivity of YSZ
intra-particle 945°C
```

```
sigmainterintrinsicel= 0.05;       %Intrinsic material conductivity of YSZ
inter-particle 945°C
sigmainterintrinsiced=(1/((1/1282051)*(Ts-293)*(6*10^-3)));       %Intrinsic
conductivity of the particle interface of Ni, (S/m)
sigmaintraintrinsiced=(1/((1/12820512)*(Ts-293)*(6*10^-3)));      %Intrinsic
material conductivity of Ni, (S/m)
theta=15;                %Contact angle between two particles in degrees, there
is likely to be a max value for this, and whilst newly contacting particles will
have a smaller value


tinit=0;                           % Initial time value (h)
tend=4000;                         % End time value (h)
tinc=1;                            % Increment in time value (h)
t=[tinit:tinc:tend];               % Time vector

Ds=exp(0.0127*Ts - 37.345);        %Adjusted value for Ni radius evaluation
B=0.9;                             %Attributed empirically determined value
appropriate for given cells
rl0=(1+B)*r0;                      %Maximum Ni particle radius
rs0=(1-B)*r0;                      %Minimum Ni particle radius



C=((Ds*y*Omega*ds)./(2*kb*Ts)).*(B/((1-
(B^2)).*((1+(B^2)).^0.5)*((1+B).^3))).*Z0.*(psied/((psied/r0)+(psiel/rel)));

rlinf=(((4/3*pi*(rl0^3))+
(((psied/r0)/((psied/r0)+(psiel/rel)))*(Z0/2)*(4/3*pi*(rl0^3)+(4/3*pi*(rs0^3))))
)/((4/3)*pi))^(1/3);
rinf=(rlinf)/(1+B);
red=((rinf^5)-((exp((-5*C*t)/((rinf^5)-(r0^5)))).*((rinf^5)-r0^5))).^(1/5);



psiced=((1.764/Zavg*psiel/rel)*red)/(1-(1.764/Zavg));   %Percolation threshold
volume fraction for electrode (electronic conducting material)
psicel=((1.764/Zavg*psied./red)*rel)/(1-(1.764/Zavg));  %Percolation threshold
volume fraction for electrolyte (ionic conducting material)
zetee=(psied./red.^3);                          %Combined variables
zeted=((psiel./rel.^3) + (psied./red.^3));      %Combined variables
zetaed=(zetee./zeted.^1);                       %Particle number fraction for
electrode particles
zetael=(psiel/rel^3)./((psied./red.^3)+(psiel/rel^3));    %Particle number
fraction for electrolyte particles

Zedel=0.5*(1+((red.^2)./(rel.^2)))*Zavg.*((psiel./rel)./(psied./red));
%Average number of contacts electrode have with neighbouring electrolyte
particles, true for binary component mixtures
Zeled=0.5*(1+((rel^2)./(red.^2)))*Zavg.*((psied./red)./(psiel./rel)); %Average
number of contacts electrolyte with neighbouring electrode particles
Zeded=Zavg*((psied./red)./((psied./red)+(psiel./rel)));  %Average number of
contacts electrode with neighbouring electrode particles
Ped=(1-(((3.764-Zeded)/2).^2.5)).^0.4;                  %Percolation probability
of electronically conducting materials (Nickel) belonging to an A type cluster-
true for binary and multicomponent
Zelel=Zavg*((psiel/rel)./((psiel./rel)+(psied./red)));  %Average number of
contacts electrolytes have with neighbouring electrolyte particles
Pel= (1-(((3.764-Zelel)/2).^2.5)).^0.4;                 %Percolation probability
of ionically conducting materials (YSZ) belonging to an A type cluster
```

```
   ra = rel*sind(theta);
   rb=red*sind(theta);

    for i=1:length(rb)
      if  ra < rb(i)
          rc(i) = ra;
      else
          rc(i) = rb(i);                                  %rc is the shortest
opposite length (opposite to hypotenuse length)of the
      end                                                 %-triangle formed by the
contact angle diamond formed by the two particles.
    end

    aeded=pi*rc.^2;                                          %cross-sectional
contact area between a k-particle and a l-particle (m^2)
    nved=((1-phig)*psied)./((4/3)*pi*red.^3);                 %Number of Ni
particles per unit volume
    stered=aeded.*(2*red*s).*nved.*(Zeded./2).*Ped;           %Effective contact
surface area between electrode particles per particle layer (m^2)



    for i=1:length(red)
        if red(i) > rel
           minredrel(i) = rel;                  %Selects smallest radius of
either Red or Rel
        else
           minredrel(i) = red(i);
        end
    end



sigmaintraeffed=sigmaintraintrinsiced.*(((1-phig)*psied.*Ped).^mu); %Effective
grain boundary conductivity (S/cm)
dimensionlesssigmaintraeffed=((psied.*Ped).^mu);
%Dimensionless effective intra electronic conductivity (through grain boundary),
sigmaintereffed=dimensionlesssigmaintereffed*sigmainterintrinsiced.*red*((sind(t
heta))^2)*(1-phig)/delta;   %Effective grain interior effective conductivity
(S/cm)
dimensionlesssigmaintereffed=(2*stered)/(s*((sind(theta))^2)*(1-phig));
%Dimensionless effective conductivity  through grain interior
lamdaVTPBeff=((3/2)*minredrel/red.^3)*(1-phig)*(sind(theta))*Pel.*Zedel.*Ped.
*psied;                      %Effective TPB length
dimensionlesslamdaVTPBeff= lamdaVTPBeff./(((1-phig)*sind(theta))./r.^2);
%Dimensionless effective TPB lengths per unit volume
sigmaefftotal=(1./((1./sigmaintraeffed)+(1./sigmaintereffed)));
%Effective total conductivity
```